DTU Library

A Numerical Model for a Floating TLP Wind Turbine

Kumari Ramachandran, Gireesh Kumar Vasanta

[Link back to DTU Orbit](#)

A numerical model for a floating TLP wind turbine

Gireesh Kumar V Ramachandran

Department of Wind Energy
Technical University of Denmark
Lyngby, Denmark

THIS THESIS IS DEDICATED TO MY BELOVED FRIEND KISHORE A.P, WHO LEFT BEHIND
A LARGE VOID WHICH CAN NEVER BE BRIDGED

Abstract

A numerical model is developed for a TLP configuration of a floating offshore wind turbine. The platform dynamics and hydrodynamic forces are derived and implemented in an advanced aero-elastic code, Flex5, to compute the hydro-aero-servo-elastic loads and responses on the floater and the wind turbine. This is achieved through three steps. In the first step, an independent 2D code with fourteen degrees of freedom (DOFs) is developed and the responses are verified for load cases concerning steady and spatially coherent turbulent wind with regular and irregular waves. In the second step, the 2D code is augmented with three more DOFs. A three-dimensional wave model with directional spreading is derived and implemented to obtain 3D code. Comparison of the 3D responses with that of the 2D shows a good agreement. The 3D code is tested for load cases using steady and turbulent wind with 3D irregular waves. In addition, the effect of wind-wave misalignment is investigated. Further, in the third step, the 3D platform dynamics and wave loading are implemented into Flex5, resulting in a fully coupled hydro-aero-servo-elastic code. The implementation is tested to make the model reliable and robust. In addition, the responses are compared to that of the 3D code responses, which shows a good agreement, in general. The extended Flex5 code is used to carry out a parametric study to investigate the influence of various configurations on the responses when subjected to different sea states and a potential configuration is recommended. The potential configuration is subjected to sea states with more narrow wave spectrum with collinear and oblique wave heading and a swell case. The responses are compared with that of the baseline configuration and recommendations are suggested for future work.

Resumé

En numerisk model er udviklet til en TLP konfiguration af en flydende offshore vindmølle. Platform dynamikken og de hydrodynamiske kræfter udledes og implementeres i en avanceret aero-elastisk kode, Flex5, for at beregne de hydro-aero-servo-elastiske belastninger og strukturelle respons. Dette opnås gennem tre trin. I det første trin, udvikles en uafhængig 2D kode med fjorten grader af frihed (DOFs), og responsen er verificeret for lasttilfælde med bå de konstant vind og kohæ rent turbulens med regelmæssige og uregelmæssige bølger. I det andet trin, udvides 2D-koden med yderligere tre DOFs. En tre-dimensionel bølgemodel med retningsbestemt spredning udledes og implementeres for at opnå en 3D-kode. Sammenligning mellem 2D og 3D resultater viser god overensstemmelse. 3D-koden testes for lasttilfælde med konstant og turbulent vind med 3D uregelmæssige bølger. Desuden undersø ges indflydelsen af forskelle i vind- og bølgeretning. I det tredje trin, implementeres platform dynamikken og bølge belastning for 3D i Flex5, hvilket resulterer i en fuldt koblet hydro-aero-servo-elastisk kode. Implementeringen testes for at gøre modellen pålidelig og robust. 3D resultater fra Flex5 sammenlignes med resultater fra 3D koden udviklet i andet trin, hvilket viser god overensstemmelse generelt. Den udvidede Flex5 kode anvendes til at udføre et parametrisk studie for at undersøge indflydelsen af forskellige konfigurationer under forskellige tilstande, og en potentiel konfiguration anbefales. Den anbefalede konfiguration udsættes for belastningstilstande med smallere bølgespektrum for kollineære og skråt indkommende bølger og et dø nninge tilflde. Den strukturelle respons sammenlignes med baseline konfigurationen og anbefalinger for det fremtidige arbejde gives.

Guru Brahma, Guru Vishnu, Gururdevo Maheshwara
Guru Sakshat Parabrahma, Tasmai Shree Gurave Namaha!!

This thesis is submitted in partial fulfilment of the Ph.D. degree from the Technical University of Denmark. The work was performed at the Fluid Mechanics Section of Department of Wind Energy at the Technical University of Denmark, in the period February 2009 to June 2012. The study has been performed under the supervision of Professor Jens Nørkær Sørensen as main supervisor, Associate Professor Henrik Bredmose and Professor Dr.(Techn.) Jørgen Juncher Jensen as co-supervisors. I owe my deepest gratitude to my supervisors for their excellent guidance, motivation and support throughout the entire project. I am grateful to the fruitful discussions we had and invaluable suggestions given by Stig Øye. I thank all the faculty members of the Fluid Mechanics section for the inspiring courses and discussions and Ruth and Marianne for their support.

This research was carried out as part of the Statkraft Ocean Energy Research Program (SOERP), sponsored by Statkraft. This support is gratefully acknowledged. I also thank for the support and feedback from Jørgen Krokstad and Øyvind Kristiansen as part of SOERP. I thank the Otto Mønsted fond for the travel support for OMAE conference.

I thank my colleagues and friends for their continuous support for having a great international work place ambience and to adapt me to a new culture and life. I would like to express my most sincere thanks to my family and close friends for their patience and tireless support.

Finally, I thank the Almighty for giving me enough strength to sail through turbulent times and carrying me along the wind in the right direction and showering all the success and happiness in my life, without which nothing would have been possible and I pray for this continued light and wind for ever.

Gireesh Kumar V Ramachandran

Copenhagen, June 2012

List of Symbols

$(V0)_1$	Free stream wind velocity defined in system 1
$[\mathbf{C}]$	Damping matrix
$[\mathbf{K}]$	Stiffness matrix
$[\mathbf{M}]$	Mass matrix
$[T]_{ij}$	Transformation matrix from system i to j
α	Angle of attack
$\alpha 1$	Power law exponent
β	Blade twist angle
χ	angle between the wind velocity in the wake and the rotational axis of the rotor
$\ddot{()}$	Second derivative of the variable
Δf	Incremental frequency
ΔL_i	Change in length of the ith tendon
Δt	Time step
δ	Logarithmic decrement
$\dot{()}$	First derivative of the variable
$\dot{x}_t$	Tower longitudinal structural velocity
η	Surface elevation
η_1	Platform surge displacement
η_2	Platform sway displacement
η_3	Platform heave displacement
η_4	Platform roll displacement
η_5	Platform pitch displacement
η_6	Platform yaw displacement
η_a	Wave amplitude
$\frac{\partial P}{\partial \theta}$	Aerodynamic power sensitivity
γ	Peak enhancement factor for JONSWAP spectrum
λ	Wave length
$(f_n)_{heave}$	Natural frequency in the heave DOF

$(f_n)_{pitch}$	Natural frequency in the pitch DOF
$(f_n)_{roll}$	Natural frequency in the roll DOF
$(f_n)_{surge}$	Natural frequency in the surge DOF
$(f_n)_{sway}$	Natural frequency in the sway DOF
$(f_n)_{yaw}$	Natural frequency in the yaw DOF
$\{F_c\}$	Connection force between tower bottom and foundation top
$\mathbf{a_{ij}}$	Transformation matrix from system i to j
$\mathbf{n}$	Normal vector
$\mathbf{V_b}$	Blade structural velocity vector
$\mathbf{V_f}$	Induced velocity vector due to the platform movement
$\mathbf{V_{rel}}$	Relative velocity vector seen by the blade
$\mathbf{V_t}$	Tower structural velocity vector
$\mathbf{W_{qs}}$	Quasi-static induced velocity vector
$\mathbf{W}$	Rotor induced velocity vector
ω	Rotor speed in radians/s
Ω_0	Rotor rated speed
ω_{1e}	Blade first edge-wise natural frequency
ω_{1f}	Blade first flap-wise natural frequency
ω_{2f}	Blade second flap-wise natural frequency
$\omega_{\varphi n}$	Controller frequency
ω_t	Tower natural frequency
ϕ	Inflow angle
$\phi_{i,y}^{1e}$	First edge-wise mode shape of Blade i in the y direction
$\phi_{i,y}^{1f}$	First flap-wise mode shape of Blade i in the y direction
$\phi_{i,y}^{2f}$	Second flap-wise mode shape of Blade i in the y direction
$\phi_{i,z}^{1e}$	First edge-wise mode shape of Blade i in the z direction
$\phi_{i,z}^{1f}$	First flap-wise mode shape of Blade i in the z direction
$\phi_{i,z}^{2f}$	Second flap-wise mode shape of Blade i in the z direction
ρ	Sea water density
ρ_a	Air density
σ	Standard deviation
$\sigma(r)$	Solidity ratio as function of r

τ	Convective time constant
τ_1	Time constant for dynamic wake model
τ_2	Time constant for dynamic wake model
θ_0	angle where the blade is deepest into the wake
θ_c	Blade cone angle
θ_n	Random phase angle
θ_p	Blade pitch angle
θ_t	Nacelle tilt angle
θ_w	Rotor azimuthal position
θ_y	Rotor yaw angle
ζ	Critical damping ratio
$\zeta_{\varphi n}$	Controller damping coefficient
$\{\mathbf{F_g}\}$	Generalized force
a	Axial induction factor
a'	Tangential induction factor
a_c	Critical axial induction factor
A_{ij}	Hydrodynamic added mass matrix
a_n	Frequency dependent wave amplitude
A_{tend}	Area of cross section of the tendon
B	Number of blades
Bi	i^{th} Blade
c	Chord length
C_a	Added mass coefficient
C_{Dz}	Hydrodynamic drag coefficient in the heave direction
C_D	Hydrodynamic drag coefficient in the surge direction
C_d	Aerodynamic drag coefficient
$C_{l,dyn}$	Dynamic value of aerodynamic lift coefficient
$C_{l,fs}$	Aerodynamic lift coefficient for fully separated flow
$C_{l,inv}$	Aerodynamic lift coefficient for inviscid flow
C_l	Aerodynamic lift coefficient
C_M	Inertia coefficient
C_n	Normal force coefficient

C_T	Thrust coefficient
C_t	Tangential force coefficient
c_t	Damping coefficient of tower
D	Aerodynamic drag force per unit length
$D(\phi)$	Direction dependent PSD
d_e	Length of spokes
D_f	Diameter of floater
d_{tend}	Diameter of the tendon
D_t	Diameter of tower
dF_i	Incremental force/moment in the ith DOF
dM	Incremental rotor torque
dr	Incremental blade radii
DS	Directional wave spectrum
dT	Incremental rotor thrust
dz	Incremental height
E_{tend}	Young's modulus of the tendon
F	Prandtl's correction factor
f	Frequency
$F_{b,f}$	Buoyancy force contribution from floater
$F_{b,t}$	Buoyancy force contribution from tower
F_b	Buoyancy force
$F_{G,f}$	Gravity force contribution from floater
$F_{G,t}$	Gravity force contribution from turbine
F_{gi}	Generalized force in the ith DOF
F_G	Total gravity force
f_g	Glauert's correction factor
F_i	Hydrodynamic force/moment in the ith DOF
F_i^{Hydro}	i^{th} component of the hydrodynamic load
F_i^{Lines}	i^{th} component of the applied load from mooring lines
F_{moori}	Mooring force in the ith tendon
f_p	Peak wave frequency
f_s	Flow separation function

F_w	Rotor thrust from wind
g	Acceleration due to gravity
h	Platform height
H_s	Significant wave height
H_t	Tower height
h_t	Tower submergence
h_w	Water depth
I_D	Drive train inertia
J_4	Effective mass moment of inertia in the roll DOF
J_5	Effective mass moment of inertia in the pitch DOF
J_6	Effective mass moment of inertia in the yaw DOF
k	Wave number
K_{ij}	Impulse response function of the radiation problem
K_I	Controller integral constant
K_P	Controller proportional constant
k_t	Spring stiffness coefficient of tower
KC	Keulegan-Carpenter number
L	Aerodynamic lift force per unit length
L_0	Initial length of tendons
L_i	Instantaneous length of the ith tendon
L_s	Shaft length
$m(x)$	Blade mass distribution over length
m_1	Effective mass in the surge direction
m_2	Effective mass in the sway direction
m_3	Effective mass in the heave direction
M_{aero}	Rotor torque
m_f	Mass of floater
M_{gen}	Generator torque
m_n	Mass of nacelle
m_{ts}	Equivalent tower top mass
m_t	Mass of tower
N_{gear}	Gearbox ratio

p	Static pressure
p_b	Excess dynamic pressure at the bottom face of the platform
P_n	Normal force per unit length
P_t	Tangential force per unit length
p_t	Excess dynamic pressure at the top face of the platform
r	Radial position along the blade from the blade root
$r1_t$	Radius of the tower
s	Spreading parameter
$S_\eta(f)$	Power spectral density of surface elevation
T	Wave period
t	Time
T_0	Total pretension in the tendons
T_i	Instantaneous tension in the ith tendon
T_p	Peak wave period
T_y	Shear force at a beam section in the y direction
T_z	Shear force at a beam section in the z direction
u	Water particle horizontal velocity
u_B	Floater velocity
U_m	Maximum wave velocity
u_{res}	Resultant velocity
v	Water particle y direction velocity
$V(z)$	Wind speed at height z, above the ground
V_θ	Tangential velocity component
V_r	Radial velocity component
Vb_y	Tangential component of the blade structural velocity
Vb_z	Normal component of the blade structural velocity
w	Water particle vertical velocity
W_0	Mean induced velocity
x_b	x coordinate of the centre of buoyancy
x_G	x coordinate of the centre of mass
y_b	y coordinate of the centre of buoyancy
y_G	y coordinate of the centre of mass

z_0	Roughness length
z_r	Reference height above the ground
W_n	Normal component of the induced velocity
W_t	Tangential component of the induced velocity

List of Tables

List of Figures

Contents

CHAPTER 1

Introduction

As the world is moving towards greener energies, the wind energy is getting more and more focus. Much research has been done on onshore wind turbines for the last three to four decades. More recently a fair amount of research is being done on bottom mounted offshore wind turbines. As an outcome of the research, the onshore and bottom mounted offshore wind turbines have been produced industrially and many projects were implemented commercially. The commercial implementation of these types of wind turbines helped to substantially increase the amount of knowledge from practical life. The offshore wind industry started in 1991 when the first offshore wind farm was implemented in Vindeby, Denmark. However, the market growth started only after a decade when the next offshore wind farm was constructed in Middelgrunden, Denmark followed by one of the largest offshore wind farms Horns Rev. The last decade has seen a steady growth in offshore wind industry both in terms of installations (or capacity additions) and in terms of intense research and development.

As the energy demand goes high, it needs to be looked farther into the sea, where the wind potential is substantially high, Suzuki (1994) and Knauer (2006). Though the farther sea looks promising, there are several challenges such as deep waters, combined wind, wave and sea current loads, power transmission etc.,. Depending on the geographic locations, the offshore wind potential varies. The offshore wind energy arena can be divided into three types of water depths viz. shallow, moderate or transitional and deep waters, Jonkman (2007). In Europe, a considerable amount of wind potential is available in the shallow waters, however, coastal regions of Norway, Portugal, Italy and Spain have got deep waters. Most of the potential available in the UK is in the transitional water depths. In addition, most of the offshore potential in the US, Manwell et al. (2001) and Japan, Kosugi et al. (2002), Henderson et al. (2002) and Kogaki et al. (2003), are in the deep waters. Manwell *et al.* points out that a cost effective technology to extract deep water offshore wind energy needs to be developed. For each of the water depths, different types of solutions are proposed. Some of the examples are monopile foundation for shallow waters, jacket structure for transitional depths and floating foundations for deep waters, which is illustrated in Figure 1.1. The transitional and deep water solutions are still under research, commercial viabilities are still under investigation.

The offshore wind energy interest is ignited by the following reasons:

- High annual average and less turbulent wind speeds

- Scarcity of land and saturation of available wind potential in the land

- Problems concerned with the noise and visual impact of large wind turbines

The main disadvantages of the deep water solutions are the prohibitively higher costs, still premature technologies, especially on proper control algorithms, and additional complex rigid body motions.

Though in the 90's certain amount of work was done to expedite the floating offshore wind turbine concepts, Halfpenny (1991), none of them were conclusive about the prospects.
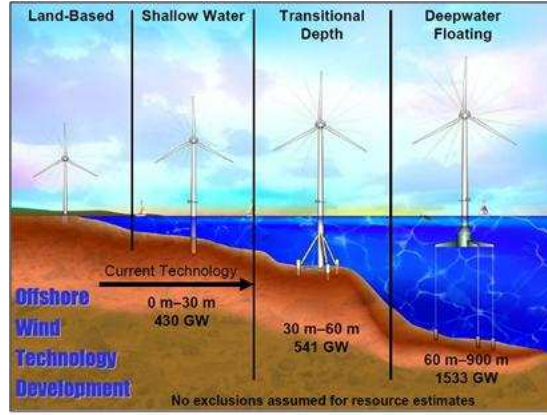
FIGURE 1.1: Classification of offshore technologies based on water depth, Jonkman (2007)

However, in the early 2000, Henderson and Vugts (2001) came up with more focus on these concepts as the offshore wind energy market was picking up the momentum by the installation of Middelgrunden wind farm. They pointed out that the cost reduction of TLP concept (one fifth) from early 90's to 2000's in the offshore oil and gas industry may also be applicable for deep water offshore wind energy. Still the cost was prohibiting the further prospects of the concepts.

However, in the later 2000's a renewed interest in floating wind turbines was achieved because of the new oil and gas tax regulations in some countries and a subsequent research funding. This paved the way for investigating the feasibility of a range of concepts, Lee et al. (2005), Chen et al. (2006), state of the art numerical tools, Jonkman (2007), International Energy Agency's initiative on code comparison projects, Jonkman et al. (2010), and demonstration projects by the industry such as Blue H, Hywind and WindFloat. Focussed research in each of the aspects or sub-systems of the floating wind turbines and innovative design tools to predict the loads and responses accurately can improve the prospects of floating offshore wind turbines and can become an economically and industrially feasible solution for future energy needs.

1.1 Classification of deep water solutions

The deep water solutions can either be single unit floater or multi unit floater systems. Single unit floaters are the platforms with single wind turbine systems, whereas multi unit floaters are the platforms with more than one wind turbine on it. It can be a series of wind turbines on a pontoon and the pontoons may be rotated for the wind turbine rotors to be aligned with the wind direction. The rotatable platform systems are known as weather waning systems because of its capability to adjust to the wind directions to capture maximum wind and to minimize wake effects. A typical example of a multi unit floater is the WindSea concept. Henderson and a group of researchers, Henderson et al. (1999), studied the response of multiple unit floater concepts in the frequency domain and its influence on cost and some suggestions for cost reduction etc., Henderson et al. (2000) extended their studies for considering multiple unit floating systems for different environmental conditions at different locations. In that study, they carried out a simple loads analysis by considering the wind turbine as a rigid structure and came up with a cost reduction matrix. They also presented an excellent environmental conditions comparison matrix for different seas. In a subsequent paper with Vugts, Henderson and Vugts (2001), Henderson points out about the

prospects of floating wind energy solutions with some suggestions for a prospective solution. In 2002, Henderson et al. (2002) reported the work of categorically assessing the resources available in Japanese waters along with suggestions for potential deep water solutions. A range of concepts along with the accessories such as mooring, anchoring, transmission systems were discussed in detail. Present challenges and future prospects were also explained. Henderson and Patel (2003) reported the procedures followed for the development of an analytical tool for modelling the floating wind turbine loads and the fatigue damage estimation due to the vessel motion. Analysis was presented for a comparison of loads and fatigue damage for some of the components (blade, tower, shaft etc.,) of onshore wind turbine and floating wind farm. Computations were carried out for a multiple unit floating offshore structure. Aerodynamic loads were calculated using the standard Blade Element Momentum theory with rigid blades and tower. In a further paper in 2003, Henderson et al. (2003) reviewed various concepts suitable for water depths ranging from 50 m onwards. Advantages and disadvantages of the concepts are listed along with some cost considerations. The following figure shows a cost analysis for offshore wind turbine concepts dependent on water depths.
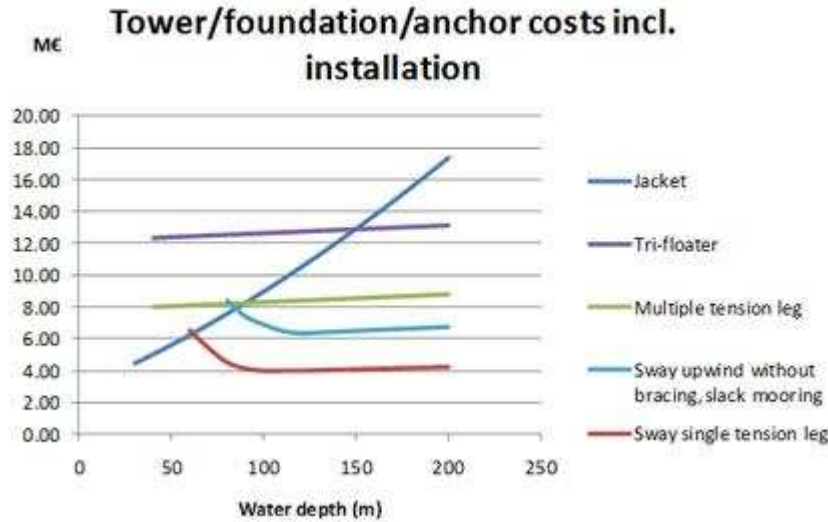
FIGURE 1.2: Cost analysis dependent on water depths, figure courtesy Sway, Norway

The single unit floater systems are classified based on the method by which they achieve the static stability. A schematic of different types of static stability methods is shown in Figure 1.3(a). Hence the single floater systems can be broadly classified as ballast (for example, spar buoy), mooring lines (for example, TLP) and buoyancy type (for example, barge) concepts, see Butterfield (2005). These are illustrated in Figure 1.3(b). In addition to these, there are also hybrid concepts such as taut leg, Sclavounos et al. (2010), semi submersible types etc., see Roddier et al. (2001). Each of the concepts has its own advantages and disadvantages. In a recent paper, Henderson and Witcher (2010) brings out the current status of floating offshore wind energy by reviewing the working principles, advantages and disadvantages along with detailed descriptions of classical floating concepts. The review also shows the present state of the art along with identification of design space based on stability, vertical and pitch motions, fatigue loading and cost considerations. The need for special turbine control systems is emphasized. Based on the review, the TLP concept is shown to have a wider market as it is suitable for water depths between 50 m and 300 m. The Figure 1.2 also shows that TLP concept has a steadier cost across the water depths.
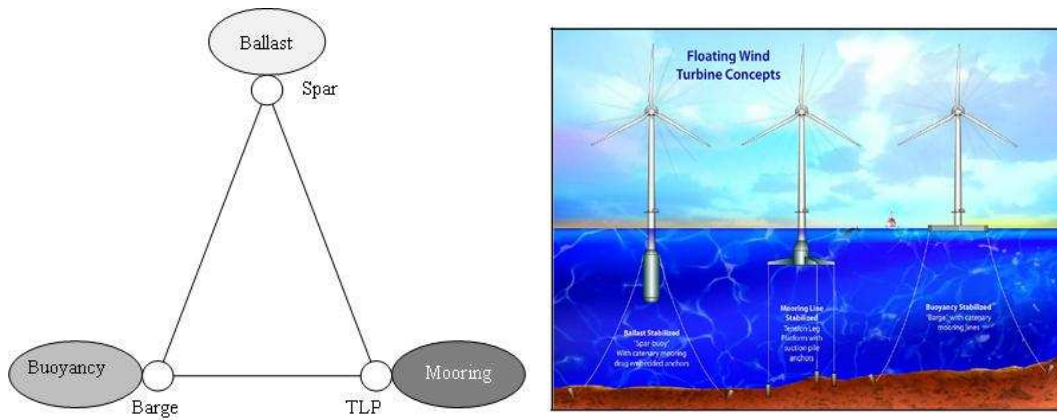
FIGURE 1.3: (a) Static stability methods and (b) Classification of deep water solutions based on stability, Jonkman (2007)

1.1.1 Spar

A spar buoy is a very long cylinder platform protruding out of the mean water surface. The wind turbine is installed on top of this cylinder. The cylinder needs to be ballasted enough to lower the centre of gravity below the centre of buoyancy in order to achieve stability. The buoyancy force will be in balance with the gravity force and the restoring is achieved by means of the vertical distance between the centres of buoyancy and the gravity. The spar buoy will also be equipped with mooring lines for station keeping. The location of fairlead position of the mooring lines is critical.

A typical example of Spar buoy type is the Hywind concept, developed by Statoil Hydro, Norway. The prototype was installed with a Siemens 2.3 MW wind turbine approximately 12 km southeast of Karmøy island, Norway. The water depth at this location is approximately 220 m. This concept is designed for water depths ranging from 120 m to 700 m. The Hywind prototype is shown in Figure 1.4(a).

 Nielsen et al. (2006a) and Nielsen et al. (2006b) made an integrated dynamic analysis of Hywind floating wind turbine concept using two independent codes viz. HywindSim and Simo-Riflex. Out of these, the existing softwares Simo and Riflex were coupled to analyse dynamics of rigid and floating bodies, whereas HywindSim is an inhouse MATLAB/Simulink simplified code for the same purpose. Both of the codes use WAMIT for hydrodynamic loads and the mooring line forces are computed quasi-statically in HywindSim. The Simo-Riflex coupled model benefits the advantages of both SIMO and RIFLEX programs. The RIFLEX program is based on nonlinear finite element formulation for flexible structures and hence catenary moorings are modeled effectively. The wind turbine loads were modeled as a table lookup set up for thrust coefficients in both of the codes. The coupled responses were compared with that of model scale experiments. The authors emphasize the need for special control algorithm in order to actively damp the wind induced tower motion at higher wind speeds (beyond rated wind speed). In a further paper, Skaare et al. (2007a) and Skaare et al. (2007b) extended the previous work by coupling the Simo-Riflex code with an advanced aero-elastic code HAWC2. The wind turbine was modeled in HAWC2, whereas the substructure including mooring was modeled in Simo-Riflex. The information such as reaction forces and mass matrices from the HAWC2 are exchanged with the interface point displacement, velocity, acceleration etc., from Simo-Riflex through a DLL routine. Responses for a set of test cases were obtained and compared with that of the model scale tests to validate the coupling method. Further, some instabilities in the tower pitch motion were recognized at

above rated wind speed due to the negative damping caused by the conventional blade pitch control strategy. These can be controlled by incorporating a special pith control algorithm.

Larsen and Hanson (2007) studied the instability mechanism due to negative damping associated with floating offshore wind turbines. The cause for instability was identified as the control frequency being less than the lowest structural natural frequency. This was studied using HAWC2 code coupled with SIMO/RIFLEX. The analysis found that while the wind turbine is operating above rated wind speed, the platform motion causes the relative velocity to switch up and down the rated wind speed. Since a variable speed variable pitch regulated wind turbine adopts a control technique of pitching the blades above rated power to keep the rpm constant, the controller tries to pitch the blades faster according to the change in wind speed, giving rise to an instability condition. The study also demonstrates the need for special control algorithm to avoid the instability. Aerodynamic torque in the high wind speed region was expressed by means of a proportional, integral and differential gain terms of a PID control algorithm.

Karimirad et al. (2009) predicted the dynamic responses of a catenary moored spar floating wind turbine subjected to extreme environmental conditions. The wind turbine was in parked condition and the responses were computed using a coupled system of DeepC for hydrodynamics, HAWC2 for wind turbine dynamics. The mooring line stiffness was computed using SIMO/RIFLEX and the values were supplied externally to HAWC2 using DLL. Hydrodynamic loads were computed using Morison's equation and are compared with that of a panel method. Subsequent to this, Karimirad and Moan (2010) reported the relevance of hydrodynamic and aerodynamic damping on the dynamic responses of catenary moored spar wind turbine. A quasi-static coupled model (HAWC2 and DeepC) was used for the computation. The hydrodynamic damping is attributed to the quadratic drag component, which is also proportional to the body velocity through Morison's equation, as given below.

$$dF = \rho C_m A \dot{u}_r + \rho A \dot{u}_W + 0.5 \rho C_D D u_r |u_r|$$
$$u_r = u_W - u_B \tag{1.1}$$

In the equation, the first term corresponds to the added mass contribution, wherein the relative motion of water particle and the structure is taken into account. The second term corresponds to the Froude-Krylov force contribution. The last term corresponds to the viscous quadratic drag contribution, which is nonlinear in nature. The equation (1.1) is a semi-empirical relation for incremental inline force (force per unit length), which is valid when the characteristic diameter of the body is much smaller than the wave length. The incremental force is integrated over the height of the structure upto the free surface in order to obtain the total force and corresponding bending moment. Case studies were conducted to demonstrate the influence of the drag coefficient. Aerodynamic damping was implemented by means of the blade relative velocity including the platform rigid body velocity components. It was found that the high frequency platform motion is severe for electrical power (induces more fluctuation) and hence reducing the platform frequency could help in obtaining steadier electrical power. Since the present computations were using a land based wind turbine control technique, implementation of a more specific control algorithm could also improve the power production. Karimirad and Moan (2011a) implemented an extrapolation procedure to determine the extreme responses based on the data from one hour simulations. The spar buoy type wind turbine is subjected to operational and extreme loading based on a joint probability distribution of wind and wave climate. The coupled responses were obtained using a quasi-static coupled model of HAWC2 and DeepC. In a recent paper, Karimirad and Moan (2011b) considered the wave and wave-wind induced dynamic responses of a catenary moored spar wind turbine. The analysis was carried out for operational and extreme conditions for a set of environmental conditions. The hydrodynamic loads

from HAWC2 and DeepC were compared. It was observed that Naess method reduces uncertainties in extreme value prediction. Further, the wave loads were found to cause extreme responses during extreme conditions, whereas wind loads induced responses were critical during operational conditions.

In a recent publication, Ormberg et al. (2011) details the development of a coupled tool to predict the dynamic loads and responses of a floating wind turbine. The RIFLEX code was extended by incorporating a Blade Element routine to calculate the aerodynamic loads and a control algorithm to regulate the power. The hydrodynamic loads were computed using WAMIT. Structural part of the model was implemented using a detailed finite element approach. The system of equations were solved using a nonlinear time domain integration scheme. The coupled model was used to compute the loads and responses for a number of test cases and the model was bench-marked against other analysis tools, which is reported in Luxcey et al. (2011).

FIGURE 1.4: (a) Hywind prototype, figure courtesy StatoilHydro and (b) Blue H prototype, figure courtesy Blue H

1.1.2 TLP

TLP achieves stability through the pretension in the tension legs. Since the structure is having positive buoyancy, the additional buoyancy needs to be balanced by applying equal pretension in the mooring lines to achieve stability. Ballasting can also be used partly to achieve stability. One of the such types is the Blue H concept, installed in Italian waters. The Blue H prototype is shown in Figure 1.4(b).

 Chen (2005) and Chen et al. (2006) studied three deepwater floater concepts viz. NREL TLP, Dutch Trifloater and Japanese SPAR for 5MW horizontal axis wind turbine in 2D. The static and dynamic responses for NREL TLP and Dutch Trifloater were compared. Focus was given to 2D NREL TLP for the dynamic and aeroelastic coupled analysis. The aeroelastic tool used was HAWC. For coupling with HAWC, linear regular wave forcing was used. The HAWC responses show good agreement with 2D computations using a MATLAB

implementation. However, the power was found to be fluctuating largely and tower top and bottom shear force and bending moments were found to be larger than that of onshore wind turbine. The need of special control or damping mechanisms were suggested for future studies. This study is one of the first attempts to couple the hydrodynamics and platform dynamics with wind turbine aeroelastic computation.

Lee et al. (2005) reported the coupled dynamic responses of TLP and spar buoy in the time and frequency domain. In the time domain MSC ADAMS and FAST codes were used, whereas in the frequency domain, SML (SWIM-MOTION-LINES) code was used. The responses were studied for different sea states and its sensitivity for different frequency ranges suggesting that both of the concepts are feasible ones. A fully coupled dynamic model in frequency domain for tension leg and catenary moored wind turbine was formulated by Sclavounos et al. (2008) using the LINES, WAMIT and FAST codes. Linear theory was employed assuming rigid blades and tower. A set of environmental conditions were considered for a series of candidates and were evaluated based on rms acceleration of nacelle. In addition, a cost study was also carried out. Sclavounos et al. (2010) used WAMIT to estimate hydrodynamic loads from linear waves and for nonlinear waves, an in-house code was used. For mooring lines, the LINES code was used and for wind turbine loads, FAST was used. The estimated loads and responses were used to compare the anchor capacity, tendon pretension, frequency sensitivity and economic aspects of two floating concepts viz. Tension Leg Platform (TLP) and Taught Leg Buoy (TLB) for 3MW and 5MW wind turbines. The coupled model does not take into account the fully coupled effects of rotor-floater dynamics interaction and flexibility of blades and tower. Focus was given to fatigue loads on floaters and mooring lines. Based on the responses for a set of sea states, it was proposed that TLP is a preferred floater for water depths greater than 50 m, whereas for water depths between 30 to 50 m, TLB is recommended.

1.1.3 Barge

For Barge type floaters, the stability is achieved by means of its large water-plane area. It is a shallow-drafted platform. Some ballasting may be required to achieve the desired draft. Mooring lines are used for station keeping purpose. Since the platform has sufficient restoring without the mooring lines, it is easier to assemble the platform with the wind turbine and float it out to the location of installation.

In the area of development of coupled hydro-aero-servo-elastic code, considerable amount of work has been done by Jonkman, Jonkman (2007). One of the first publications by Jonkman and Sclavounos (2006) attempted to make an integrated tool by assuming the platform rotations to be small and using a linearized hydrodynamic description. The computations were carried out in the time domain. The wave induced forces were computed using Morison's equation. It was intended to extend the code to consider nonlinear waves, presence of sea current, study of Vortex induced Vibration (VIV) etc., In a subsequent paper, Jonkman and Buhl (2007a), the simulations capabilities have been enhanced to deal with all kinds of floating platforms. Further, the time domain coupled responses of barge were verified with that of the frequency domain response and the quasi-static mooring line responses were bench marked. The coupled areoelastic code was used to study the loads and responses of a barge with a 5MW wind turbine under extreme conditions and the observations were reported in Jonkman and Buhl (2007b). The loads and responses were compared with that of a land based wind turbine. The analysis shows that under extreme conditions, the barge is subjected to large motions, in particular pitch, which brings higher loads to the tower and blades. One of the load cases showed a yaw instability. Design modifications were suggested to reduce the platform motion and eliminate the instability which would provide a cost-effective design. In a later paper, Jonkman (2008), Jonkman attempted to reduce

the large pitch motion of the barge, by introducing barge pitch damping by means of a feedback control and pitch-to-stall rotor speed regulation strategy. However, both of the methods were not fully successful. It is important to note that the instability occurs above rated wind speed. Jonkman summarised all the above methods and results in the PhD thesis, Jonkman (2007), which gives a complete picture of the work done so far on coupling the hydrodynamics and aero-elastic codes and provides suggestions for further improvements. The total external load on the support platform was expressed as in equation (1.2), where A corresponds to hydrodynamic added mass matrix, F_i^{Hydro} is the ith component of the hydrodynamic load and F_i^{Lines} is the ith component of the applied load from mooring lines. The hydrodynamic loads were expressed using the equation (1.3). Suggestions for further work include using the code to analyze other floating wind turbine concepts, introduction of hydrodynamic second order effects such as slowly varying drift force and sum-frequency effect into the Hydrodyn code, incorporating potential loading from VIV and sea ice, replacing the quasi-static mooring system with a dynamic model etc., Recommendations were also made to carry out studies on a TLP and spar systems and also with higher capacity wind turbines.

$$F_i^{Platform} = -A_{ij}\ddot{q}_j + F_i^{Hydro} + F_i^{Lines} \qquad (1.2)$$

$$F_i^{Hydro} = F_i^{Waves} + \rho g V_0 \delta_{13} - C_{ij}^{Hydrostatic} q_j - \int_0^t K_{ij}\left(t - \tau\right) \dot{q}_j\left(\tau\right) d\tau \qquad (1.3)$$

In (1.3), the first term attributes to the wave diffraction problem, the second and third terms attribute to the hydrostatic problem and the last term and the added mass contribution constitute the radiation problem. K_{ij} in the last term is known as the impulse response function of the radiation problem. This can be found out by applying a suitable transformation to the the frequency dependent solution obtained from codes such as WAMIT, as shown in (1.4).

$$K_{ij}\left(t\right) = -\frac{2}{\pi} \int_0^\infty \omega \left[A_{ij}\left(\omega\right) - A_{ij}\left(\infty\right)\right] sin\left(\omega t\right) d\omega$$

$$or \qquad (1.4)$$

$$K_{ij}\left(t\right) = \frac{2}{\pi} \int_0^\infty B_{ij}\left(\omega\right) cos\left(\omega t\right) d\omega$$

The wave diffraction, hydrostatic and radiation problems and the mooring line equations are solved separately within the scope of the linearization assumptions.

1.1.4 Hybrid concepts / Semisubmersible

Hybrid concepts utilize certain features of the stability achieving mechanisms from two or more classical concepts in order to achieve stability.

Semisubmersibles float on the mean water surface. Stability is achieved by means of ballasting and mooring systems. One of such types is the WindFloat concept by Principle Power Corporation, USA. The WindFloat prototype is shown in Figure 1.5.

FIGURE 1.5: WindFloat, figure courtesy Principle Power

1.2 Deep water challenges

In order to make the deep water offshore wind energy a feasible solution, there are manyfold challenges to be dealt with. A preliminary cost study can be found in Musial and Butter-field (2004), which predicts the cost of energy production from a TLP concept would fall substantially by the year 2025. A study carried out by Wayman et al. (2006) suggests that the TLP would be a cost-effective one. Apart from the cost issue, the following challenges need to be solved.

1.2.1 Right solution

Many solutions for the deep water wind turbines are still under consideration. Out of these, a few were described above. However, from the literature, it is noticed that the best solution is still a subjective one, because all of the solutions are highly site dependent. In addition to the floater concept, it could also be on the type of wind turbine, say pitch or stall or active stall regulated, two or three bladed, with tubular or lattice tower or it could also be possible to have a completely different solution, say vertical axis wind turbine like the DeepWind concept, as described by Vita et al. (2010). It is also imperative to ask whether a conventional onshore turbine design is compatible for the selected floating solution or not. Henderson and Patel (1998) carried out studies on the influence of platform motion on the wind turbine loads (both extreme and fatigue) at different components. The analytical model is position dependent, based on which the weighting functions were derived. The weighting functions are used to establish a relation of the platform motion to any component. This was proved for one of the components, whereas for the other components such as nacelle, it still needs to be proved.

1.2.2 Complex loading pattern

Deep water wind turbines are subjected to complex combination of wind, wave and current loading. The wave loading is basically nonlinear and three dimensional in nature. There are a number of theories, which describe the wave loading based on the environmental conditions, wave steepness, slenderness of the structure under wave loading etc., The principle followed for the present work is described in detail in Chapter 3. The presence of a sea

current will change the wave length and consequently the wave number. The wind and wave misalignment will be a usually occurring load case. In addition, there are still research happening on the kind of wind velocity profile and turbulence model which can best describe the wind conditions in the sea along with wake effects in wind-farm.

Loads and load cases are the corner stone for the whole design process of wind turbines and hence prediction of loads are the key element for a cost-effective design. In the case of onshore wind turbines, these loads are predicted using sophisticated aero-servo-elastic codes, which are time tested and validated. However, offshore wind turbines, floating turbines in particular, pose additional complex combination of aerodynamic, hydrodynamic, gravitational and and other loads during transportation and installation. Though attempts are made to augment the existing codes to include these complexities, validation is yet to be done. The numerical tools need to be validated enough to assess the strengths and weaknesses of different floating concepts and associated loads and load cases. Hence, sufficiently accurate and validated state of the art numerical code would be one of the first challenges to be resolved in the case of deep water wind turbine challenges.

In the present research, it is attempted to address this part of the challenge rather than proposing any particular configuration or solution. However, the TLP configuration is used to derive the equations of motion and building the numerical tool. This can be generalized for other configurations as well with relevant modifications.

1.2.3   Standards / guidelines

At present, the standards / guidelines available are for the onshore and bottom fixed offshore wind turbines. For bottom fixed offshore wind turbines, the standard used for design is IEC 61400-3, IEC (2009) and the guidelines are DNV J101, DNV (2011) and Germanischer Lloyd guidelines for wind turbines, GL (2007). However, there are no standard or guidelines available for floating offshore wind turbines. These are under development.

1.2.4   Material selection

Research is still being done on the selection of floater material. Concrete and steel are the conventional materials, however, a cost effective solution is still being finalized.

1.2.5   Mooring system

Based on the mooring system, the floating offshore wind turbine structures can be classified as catenary mooring, taut leg mooring and tension leg mooring systems. Examples of concepts that utilize catenary mooring systems are spar buoys, tri-floater concept, pill box design etc., Vertical tension leg is a sub set of taut leg system.

1.2.6   Anchors

Based on the applications and load carrying capacity, there are different anchoring systems available such as gravity based, drag embedded, driven pile, suction, drilled and grouted and torpedo embedded anchors. The right one needs to be selected based on the soil conditions, which determine the load capacity of the anchors. Out of these, the vertically loaded anchors are more expensive due to their deep embedment in order to maximize the pull out load.

1.2.7   Cabling

Though cabling for the power transmission is a proven area in the case of bottom mounted wind turbines, this needs a serious consideration in the case of deep water solutions. The main reasons for the challenge is that these units are placed far offshore and the moving units itself pose challenges for the power transmission. The first point has impact on the cost and transmission losses aspects. Today most of the power transmission are done through High Voltage Direct Current (HVDC) conversion. One of the solutions for the transmission issue is to have load centres in the sea, which is already in use in Danish waters.

1.2.8   Transportation and installation

Transporting the floating offshore wind turbine units to its specified sites and then installing the machines is a great challenge. A number of methods are suggested in the literature. However, these need to be proved in real conditions to finalize the right method. Unlike the bottom fixed wind turbines, the use of specialized vessels for installation can be eliminated by assembling the turbines at shore or at an offshore platform and then the assembled pieces can be float out to the locations. This can considerably reduce the installation costs because of the elimination of expensive installation vessels and reduced delay time associated with weather window dependency.

1.2.9   Operation and maintenance

The operation and maintenance aspect for the deep water solutions are complicated compared to their onshore counterparts. Research is being done to identify various solutions / techniques to make it possible cost effectively. One of the methods is to have a reliable design and another one is the implementation of condition monitoring techniques. Despite of these, there will still be problems related to changing the electronic chips / switches and the major issues could arise when a replacement of major component is needed such as blades or gearbox or generator, which needs dismantling and reassembling of the tower top machinery. These challenges are yet to be resolved.

1.2.10   Measurement data

Unlike onshore wind energy development, the measured met-ocean data at the relevant height are limited. The measurement stations such as those of the FINO projects, FINO (2011), provide certain confidence for offshore developments. However, the lack of measurement data for deep water areas pose one of the main challenges. In addition to the wind, wave and current data, we also require the bathymetry. Further challenges include the estimation of correct wind velocity distribution in the sea and also the wind and wave joint probability density function.

1.2.11   Other logistical considerations

Many other logistical considerations such as environmental impact, ship transport, icing, earthquake effects etc., need to be dealt with. These are some of the areas need to be assessed site specifically. These technical considerations will lead to the administrative processes for the projects seeking permits for offshore wind energy development. These are mainly dependent on the kind of policies adopted by different countries. Hence the growth rate for offshore wind energy is not only dependent on technological advancements, but it also has a dependence on policy matters.

1.3   Brief review on the aero-elastic tools

A brief review on the presently available hydro-aero-servo-elastic tools is presented here. The most widespread aero-elastic tools for onshore wind turbines are as follows:

- Flex5, developed by Stig Øye of Technical University of Denmark (DTU), Øye (1996).

- HAWC2 (Horizontal Axis Wind Turbine Code), developed by Risø-DTU, Larsen and Hansen (2007).

- Bladed, developed by GL Garrad Hassan, Garrad and Hassan (2010).

- FAST, developed by National Renewable Energy Laboratory (NREL), Jonkman and Buhl (2005).

- PHATAS (Program for Horizontal Axis Wind Turbine Analysis and Simulation), developed by Energy Research Centre of the Netherlands (ECN), Lindenburg (2005).

Out of the above codes, Flex5, HAWC2, Bladed and PHATAS are commercial codes and FAST is an open source code, which are exclusively made for wind turbines. All these codes compute the loads in time domain. All of these make use of Blade element momentum theory with necessary corrections to represent the rotor aerodynamics. For the aerodynamics purpose, FAST utilizes AeroDyn, Laino and Hansen (2002). In addition to these codes, there are also a few more general purpose codes such as MSC ADAMS (Automatic Dynamic Analysis of Mechanical Systems, developed by MSC), SIMPACK, which can be used for the aero-elastic loads computation. While HAWC2, Bladed and ADAMS use a multibody formulation, Flex5 uses a modal formulation and FAST uses a mixed form (modal and multibody). In multibody formulation, the user has the flexibility to model or formulate different geometry / shapes.

1.4   Present Work

1.4.1   Motivation and Objectives

In the last decade, considerable amount of work has been done by many researchers across the world to extend the existing aero-elastic codes to compute bottom-fixed offshore wind turbine loads and recently for floating offshore wind turbines, Larsen and Hansen (2007), Jonkman (2007), Karimirad (2011). A complete review of the status of the coupling of aero-elastic codes with offshore codes can be found in Cordle and Jonkman (2011) for floating offshore wind turbines. By taking into account each of the modeling capabilities, there are only a limited number of codes, which can compute the complete coupled behaviour accurately. Further, validation against measurements are essential.

From Cordle and Jonkman (2011), it can be noted that though Flex5 is a widely used aero-elastic code for the design analysis of onshore and bottom-fixed offshore wind turbines, there is no reported results available for floating offshore wind turbines. In this perspective, coupling the platform dynamics with Flex5 code is appropriate. More detailed description about Flex5 can be found in Chapter 6. The study is highly motivated by the need of the industry for floating wind turbines.

The goal is achieved by deriving the equations of motion for the coupled system dynamics along with hydrodynamic and aerodynamic loading using first principles and implementing the equations of motion to obtain a simplified code. Upon obtaining confidence on the simplified code, the Flex5 code is augmented with relevant platform dynamics and three-dimensional hydrodynamic loading model.
The main objectives of the thesis are as follows:

- Development of an independent 2D and 3D numerical tool which can capture the coupled dynamics of a TLP floating wind turbine

- Extension of Flex5, to estimate the loads and responses of a TLP floating wind turbine

- Investigating the instabilities involved in a TLP floating wind turbine

- Parametric study to identify the critical load cases

As a first step, equations of motion are derived for a two-dimensional configuration and implemented. In 2D, a simplified coupling procedure is followed first and later the full coupling is implemented. The coupled responses are validated through a series of test cases. In the next step, the two-dimensional code is extended to a three-dimensional code. The three-dimensional coupled responses are compared with that of two-dimensional responses and a satisfactory comparison was obtained. Upon obtaining the three-dimensional coupled responses, the platform dynamics and wave load procedures are coupled with Flex5. The responses are compared with that of the three-dimensional code.

Finally, the augmented Flex5 code is used to carry out a parametric study, which evaluates various configurations subjected to a set of load cases and the configuration performance is assessed. The parametric study also reveals the extreme external conditions, which can form some of the load cases. In addition, the influence of the floating wind turbine control parameters are bench-marked against the onshore controller parameters.

1.4.2 Structure of the thesis

The text is organised as follows. In Chapter 2, the problem specification is provided along with the model description and a systematic derivation of aerodynamic loads. The unsteady Blade Element Momentum (BEM) theory is briefly described for the derivation of aerodynamic loads.

Chapter 3 describes the formulation and implementation of wave kinematics computation procedures. Linear irregular two-dimensional and three-dimensional waves are considered. Irregular waves are formulated using the JONSWAP spectrum with an amplification factor of 3.3. The wave loads are determined using Morison's equation.

A two-dimensional coupling procedure is detailed in Chapter 4. Both simplified and full coupling procedures are detailed and results are presented for a set of load cases. The characteristics of the responses are discussed.

In Chapter 5, a three-dimensional coupling procedure is modeled along with three-dimensional wave loading with directional spreading. A set of load cases similar to that of the two-dimensional case are computed and the responses are compared with that of the two-dimensional cases. The similarity and differences are pointed out and discussed in detail. Some of the instabilities noticed are investigated and possible remedies are recommended.

The three-dimensional platform dynamics along with wave load procedure is coupled to Flex5 and the coupling procedure along with the results are detailed in Chapter 6. A set of load cases are computed and the results are compared with that of the previous results.

In Chapter 7, a parametric study is carried out to evaluate the performance of the baseline configuration subjected to a set of load cases. Based on the analysis, alternative configurations are suggested and evaluated. Further, recommendations are made for a potential configuration.

In Chapter 8 the conclusions from the research are enlisted along with future areas of work.

Model Description and Aerodynamic Loading

In this chapter, the problem specification is provided with a detailed description on the aerodynamic loading formulation.

2.1 Problem specification

As described in Chapter 1, a Tension Leg Platform configuration of the floating offshore wind turbine solution is being investigated. The platform configuration is chosen as described in Joensen et al. (2007). The dimensions considered for the configuration are listed in Table 2.1. Data from the NREL 5MW reference wind turbine is used, see Jonkman et al. (2009). A schematic drawing of the floating TLP wind turbine is shown in Figure 2.1.

TABLE 2.1: TLP Dimensions.

Floater	Diameter(D_f)	16 m	Spoke length (d_t)	22 m
	Height (h)	10 m	Mass (m_f)	2E5 kg
Turbine	Hub height (H_t)	100 m	Tower submergence (h_t)	15 m
	Rotor diameter (D)	126 m	Tower bottom diameter (D_t)	6 m
	Tower bending rigidity (EI_t)	$4.05E11$ Nm^2	Nacelle mass (m_n)	3.5E5 kg
	Tower mass (m_t)	3.47E5 kg	Blade mass (m_b)	17740 kg
Tendons	Initial length (L_0)	175 m	Young's modulus (E_{tend})	210E9 N/m^2

Wind and wave climate for a placement on the west coast of Norway were chosen in the present study. The coastal location is shown in Figure 2.2, and the environmental parameters are listed in Table 2.2. The selected wind and wave climatic conditions are found on the web site www.waveclimate.com. No further work was done to investigate site specific conditions. The peak period was selected as the lowest period from the range of peak periods for the selected wave height using the following equation,(DNV (2011)),

$$11.1\sqrt{H_s/g} \le T_p \le 14.3\sqrt{H_s/g} \tag{2.1}$$

where T_p is the peak period and H_s is the significant wave height.

Floating offshore wind turbines are subjected to environmental loading conditions arising from wind, wave and sea current. The aerodynamic loading from the wind is formulated in the next section.
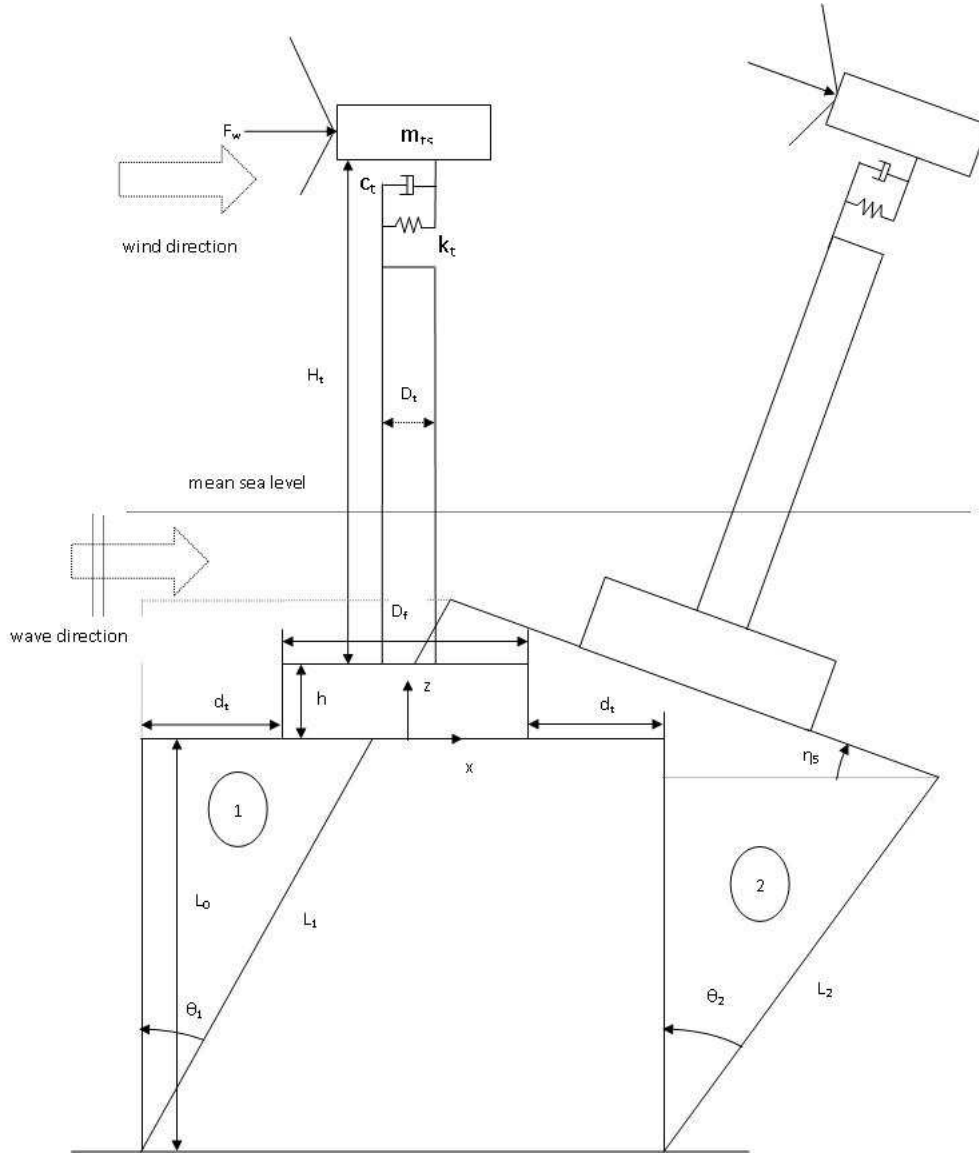
FIGURE 2.1: Configuration schematic

TABLE 2.2: Wind and wave climate for North Sea.

wave conditions	
Significant wave height	7 m
Peak period	10 s
Water depth	200 m
wind conditions	
Annual average wind speed	10 m/s
Predominant wind direction	West and South-West
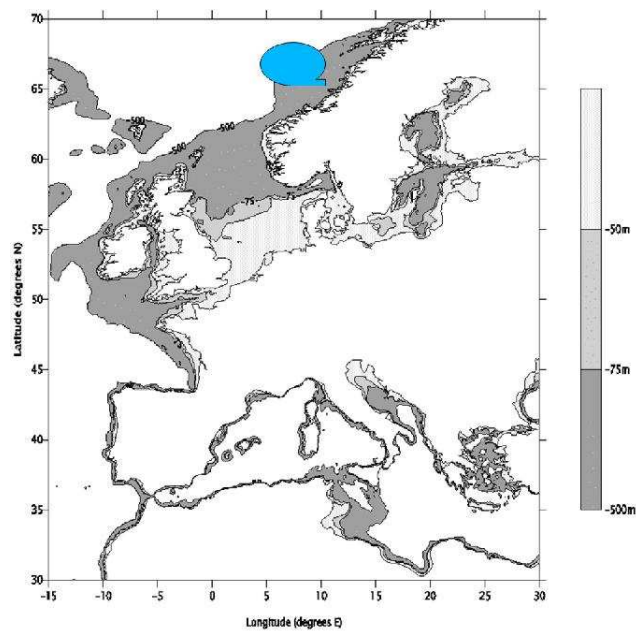
FIGURE 2.2: Geographical location, Henderson et al. (2000)

2.2   Aerodynamic loads

The wind turbine rotor as well as the whole structure is subjected to wind loads, which are time dependent. Wind loading on the rotor is usually modeled by means of unsteady Blade Element Momentum (BEM) theory, Hansen (2008). The fundamental equations are derived using one-dimensional momentum theory for a rotor disc. For this purpose, the rotor is divided into N annular elements having a length dr, located at radial position r from the rotor centre. The fundamental assumptions for the annular elements are given below:

- No radial flow dependency between the elements.

- The force exerted by the blades onto the flow is constant in each of the annular elements, which is consistent with the assumption of an infinite number of blades.

The infinite number of blades assumption is corrected by means of Prandtl's tip loss factor for a finite number of blades. As the vortex system in the wake of a rotor with a finite number of blades is different from that of a rotor with infinite number of blades, the Prandtl's tip loss factor needs to be applied in the equations for incremental thrust and torque, which is explained in section 2.2.5.

The unsteady BEM takes into account the rotor induced velocity and the temporal and spatial variation of wind velocity. The spatial variation of wind velocity is a consequence of the blade tangential velocity variation along the radial positions due to the change of azimuthal position and the variation of free stream wind velocity along the blade length due to a wind shear profile. However, to obtain the aero-elastic loads, the aerodynamic model needs to interact with a structural model, wherein the relative velocity seen by the blade is a resultant of the wind and structural velocities. Hence, a structural model of the wind turbine needs to be coupled with the unsteady BEM such that the calculation of the aerodynamic loads are based on the relative velocity seen by the blade (through the angle of attack) and the relative velocity is dependent on the structural velocity, which is a consequence of the aerodynamic loading.

Since the blades and tower are considered as flexible, the structural velocity consists of the velocity of vibrating blades and tower. In the case of floating wind turbines, in addition to the above variables, induced velocity from the platform movement also need to be taken into account.

Formulation and implementation of the aerodynamic loads through BEM is explained in the following sections.

2.2.1   Coordinate System

The coordinate system followed for the development of aerodynamic loads is shown in Figure 2.3. The word *coordinate system* is abbreviated to *system* from here onwards. System 1 corresponds to the inertial coordinate system, placed at the sea bed. System 2 is located at the floater bottom, 3 at the intersection point of floater top and tower bottom, 4 at the tower top, 5 is placed on the main shaft, located at the main bearing and finally system 6 is placed at the blade root.

The hydrodynamic forces and the equations of motion for the complete system are derived with respect to system 2, whereas system 3 represents the beginning of the wind turbine. All the systems are moving along with the platform except system 1. Transformation from system 1 to 2 shall take into account the platform rotations viz. roll, pitch and yaw. The change from system 2 to 3 is the swapping of the x and z axes. System 4 takes into account the nacelle tilt and yaw angles. System 5 is rotating along with the shaft and takes into

account the azimuthal positions. System 6 is rotating along with the blade and takes into account the blade cone angle.
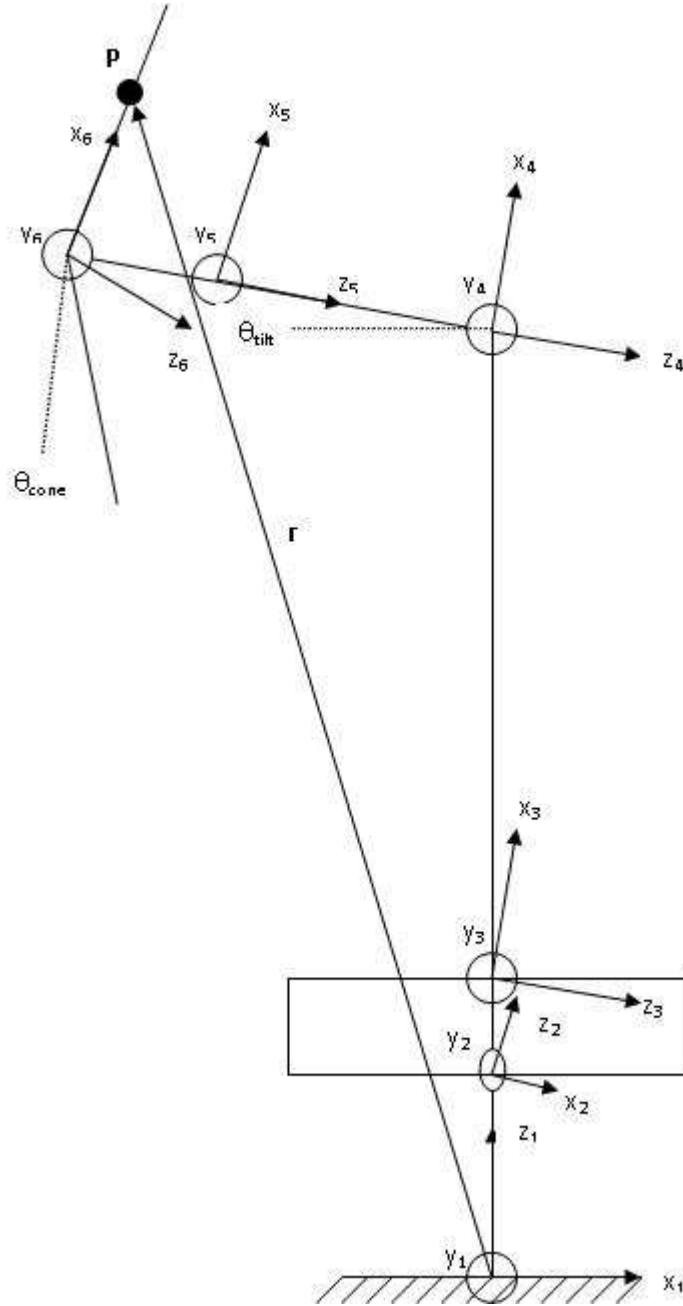
FIGURE 2.3: Coordinate system for floating offshore wind turbine.

2.2.2   Transformation Matrices

Transformation matrices are derived for moving from one system to the other. The systems 1 and 2 are related with a transformation matrix, which takes into account rotations about the x axis (roll), the y axis (pitch) and the z axis (yaw). Hence, rotations about x, y and z

axes give rise to the following transformation matrices.

$$\mathbf{R_{x1}} = \begin{pmatrix} 1 & 0 & 0 \\ 0 & \cos\eta_4 & \sin\eta_4 \\ 0 & -\sin\eta_4 & \cos\eta_4 \end{pmatrix} \tag{2.2}$$

$$\mathbf{R_{y1}} = \begin{pmatrix} \cos\eta_5 & 0 & -\sin\eta_5 \\ 0 & 1 & 0 \\ \sin\eta_5 & 0 & \cos\eta_5 \end{pmatrix} \tag{2.3}$$

$$\mathbf{R_{z1}} = \begin{pmatrix} \cos\eta_6 & \sin\eta_6 & 0 \\ -\sin\eta_6 & \cos\eta_6 & 0 \\ 0 & 0 & 1 \end{pmatrix} \tag{2.4}$$

These rotations give rise to the final transformation matrix from system 1 to 2 as shown below,

$$\mathbf{a_{12}} = \mathbf{R_{z1}R_{y1}R_{x1}} \tag{2.5}$$

where $\mathbf{a_{12}}$ represents the final transformation matrix from system 1 to 2, η_4, η_5 and η_6 are floater roll, pitch and yaw rotations respectively.

Moving from system 2 to 3 is possible by using the following transformation matrix.

$$\mathbf{a_{23}} = \begin{pmatrix} 0 & 0 & 1 \\ 0 & 1 & 0 \\ 1 & 0 & 0 \end{pmatrix} \tag{2.6}$$

Transformation from system 3 to 4 can be done by a rotation about x axis, which takes into account the yaw angle, subsequently rotating about y axis to account for rotor tilt angle. About z axis, no rotations are present and hence the transformation matrices are described below.

Rotation about x axis is given by,

$$\mathbf{a_1} = \begin{pmatrix} 1 & 0 & 0 \\ 0 & \cos\theta_y & \sin\theta_y \\ 0 & -\sin\theta_y & \cos\theta_y \end{pmatrix} \tag{2.7}$$

Rotation about y axis is given by,

$$\mathbf{a_2} = \begin{pmatrix} \cos\theta_t & 0 & -\sin\theta_t \\ 0 & 1 & 0 \\ \sin\theta_t & 0 & \cos\theta_t \end{pmatrix} \tag{2.8}$$

Rotation about z axis is given by,

$$\mathbf{a_3} = \begin{pmatrix} 1 & 0 & 0 \\ 0 & 1 & 0 \\ 0 & 0 & 1 \end{pmatrix} \tag{2.9}$$

Hence the final transformation matrix from system 3 to 4 is,

$$\mathbf{a_{34}} = \mathbf{a_3 a_2 a_1} \tag{2.10}$$

where θ_y and θ_t are nacelle yaw and tilt angles respectively. The coordinate system is chosen in such a way that in order to have the nacelle nose-up configuration, a negative tilt angle is required.

The transformation matrix from system 4 to 5 can be obtained by rotating the coordinate system about the z axis giving rise to the following equation. No other rotation is allowed since the shaft is assumed to be stiff.

$$\mathbf{a_{45}} = \begin{pmatrix} \cos\theta_w & \sin\theta_w & 0 \\ -\sin\theta_w & \cos\theta_w & 0 \\ 0 & 0 & 1 \end{pmatrix} \tag{2.11}$$

where θ_w is the rotor azimuthal position.

System 6 is used to represent the rotor blade, wherein the local x axis is aligned along the length of the blade, y axis along the blade chord length and z axis is normal to the blade, pointing along the main shaft. Moving from system 5 to 6 shall take into account the blade cone angle and hence the transformation matrix is given in the following equation.

$$\mathbf{a_{56}} = \begin{pmatrix} \cos\theta_c & 0 & -\sin\theta_c \\ 0 & 1 & 0 \\ \sin\theta_c & 0 & \cos\theta_c \end{pmatrix} \tag{2.12}$$

where θ_c is the blade cone angle. Similar to tilt angle, a negative cone angle needs to be chosen.

2.2.3 Coordinate positions

The coordinates for each position is expressed in terms of the transformation matrices as follows. The subscript in the vector represents the coordinate system.

A point in system 2 can be expressed in system 1 as given below.

$$\mathbf{r_1} = \mathbf{a_{21}}\mathbf{r_2} \tag{2.13}$$

where $\mathbf{r_2}$ is the coordinate vector of the point in system 2 and $\mathbf{a_{21}}$ is the transformation matrix from system 2 to 1.

Similarly, points in system 3, 4, 5 and 6 can be expressed to the immediate lower system as detailed in the following equations.

$$\mathbf{r_2} = \mathbf{a_{32}}\mathbf{r_3} \tag{2.14}$$

$$\mathbf{r_3} = \mathbf{a_{43}}\mathbf{r_4} \tag{2.15}$$

$$\mathbf{r_4} = \mathbf{a_{54}}\mathbf{r_5} \tag{2.16}$$

$$\mathbf{r_5} = \mathbf{a_{65}}\mathbf{r_6} \tag{2.17}$$

Hence, a point in system 6 can be expressed in system 1 using the above transformations, which is given below.

$$\mathbf{r_1} = \begin{cases} \mathbf{a_{21}a_{32}a_{43}a_{54}a_{65}r_6} \\ \\ \mathbf{a_{12}}^T\mathbf{a_{23}}^T\mathbf{a_{34}}^T\mathbf{a_{45}}^T\mathbf{a_{56}}^T\mathbf{r_6} \end{cases} \tag{2.18}$$

A point, P, on the blade can be expressed in the inertial coordinate system (system1) using the following vector.

$$\mathbf{r_{P1}} = \begin{pmatrix} x_p \\ y_p \\ z_p \end{pmatrix} = \mathbf{r_{fb1}} + \mathbf{r_{ft1}} + \mathbf{r_{t1}} + \mathbf{r_{s1}} + \mathbf{r_{b1}} \tag{2.19}$$

where $\mathbf{r_{fb1}}$ is the coordinate vector for platform bottom point in system 1, $\mathbf{r_{ft1}}$ is the coordinate vector for platform top point in system 1, $\mathbf{r_{t1}}$ represents the tower coordinate, $\mathbf{r_{s1}}$ is the shaft coordinate and $\mathbf{r_{b1}}$ is the blade coordinate in system 1.

The floater bottom and top positions are given in the following expressions,

$$\mathbf{r_{fb1}} = \begin{pmatrix} 0 \\ 0 \\ L_0 \end{pmatrix} \tag{2.20}$$

$$\mathbf{r_{ft1}} = \mathbf{a_{21}} \begin{pmatrix} \eta_1 \\ \eta_2 \\ h + \eta_3 \end{pmatrix} \tag{2.21}$$

where L_0 is the initial length of the tendons, h is the floater height and η_1, η_2 and η_3 are the floater translational displacements viz. surge, sway and heave degrees of freedom respectively.

The coordinates of the tower, shaft and blade are given s follows,

$$\mathbf{r_{t1}} = \mathbf{a_{21}a_{32}} \begin{pmatrix} H_t \\ 0 \\ 0 \end{pmatrix} \tag{2.22}$$

$$\mathbf{r_{s1}} = \mathbf{a_{21}a_{32}a_{43}} \begin{pmatrix} 0 \\ 0 \\ -L_s \end{pmatrix} \tag{2.23}$$

$$\mathbf{r_{b1}} = \mathbf{a_{21}a_{32}a_{43}a_{54}a_{65}} \begin{pmatrix} r \\ 0 \\ 0 \end{pmatrix} \tag{2.24}$$

where H_t is the tower height, L_s is the shaft length, r is the radial position along the blade from the blade root.

The wind velocity defined in the blade coordinate system is given by,

$$(\mathbf{V0})_6 = \mathbf{a_{56}a_{45}a_{34}a_{23}a_{12}}(\mathbf{V0})_1 \tag{2.25}$$

where $(\mathbf{V0})_1$ is the free stream wind velocity defined in the inertial system (system 1).

The velocity triangle seen by the blade is shown in Figure 2.4.
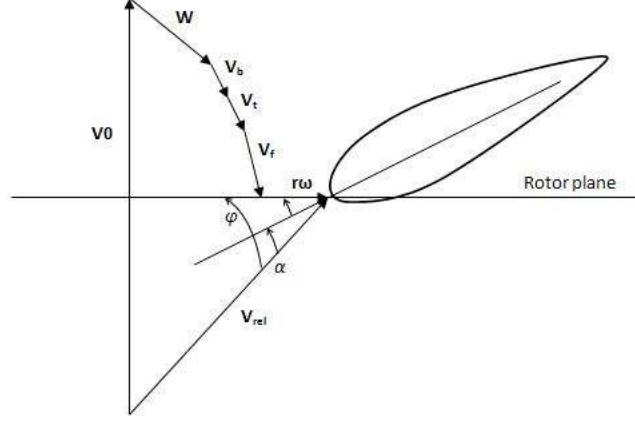
FIGURE 2.4: Velocity triangle seen by the blade

From the figure, the relative velocity seen by the blade in the blade coordinate system can be computed as given below.

$$(\mathbf{V_{rel}})_6 = (\mathbf{V0})_6 + (\mathbf{W})_6 + (\mathbf{V_b})_6 + (\mathbf{V_t})_6 + (\mathbf{V_f})_6 \tag{2.26}$$

where W is the rotor induced velocity, V_f is the induced velocity due to the platform movement, V_t is the tower structural velocity, V_b is the resultant of blade structural and tangential velocity components. The subscript 6 shows that all the variables are computed in system 6. This is done by evaluating the velocity components in its own systems and transferring to the blade system.

The critical step in BEM is the computation of induced velocity, $\mathbf{W}$, which is done by means of a dynamic wake model. The dynamic wake model is explained in section 2.2.4. The induced velocity due to the platform movement, V_f , has two components in the blade system. The first component corresponds to the platform rigid body translational velocity, whereas the second component corresponds to the translational velocity components due to the platform angular velocity, which is detailed in the following equation.

$$(\mathbf{V_f})_6 = \begin{pmatrix} \dot{\eta}_1 \\ \dot{\eta}_2 \\ \dot{\eta}_3 \end{pmatrix}_6 + (\mathbf{r_f})_6 \times \begin{pmatrix} \dot{\eta}_4 \\ \dot{\eta}_5 \\ \dot{\eta}_6 \end{pmatrix}_6 \tag{2.27}$$

where $(\mathbf{r_f})_6$ is the vector from platform to a point on the blade under consideration, evaluated in system 6 by applying appropriate transformation. Similarly, the platform translational and angular velocities are also expressed in system 6 by applying the corresponding transformations.

The tower velocity has only one component, which is in the z direction corresponding to the tower longitudinal degree of freedom. The tower velocity, which is measured in its system and transformed to system 6 is given below.

$$(\mathbf{V_t})_6 = \begin{pmatrix} 0 \\ 0 \\ \dot{x}_t \end{pmatrix}_6 \tag{2.28}$$

where $\dot{x}_t$ is the tower longitudinal structural velocity.

The blade velocity V_b evaluated in its own system is given by the following equation,

$$(\mathbf{V_b})_6 = \begin{pmatrix} 0 \\ r\omega \cos\theta_c + Vb_y \\ Vb_z \end{pmatrix}_6 \tag{2.29}$$

where ω is the rotor speed in radians/s, θ_c is the blade cone angle, Vb_y and Vb_z are the tangential and normal components of the blade structural velocity, which is computed using the blade mode shapes in flapwise and edgewise directions. The x component of the velocity vector is zero because of the absence of blade extensional degree of freedom.

When starting a simulation, the initial rotor induced velocity is assumed to be zero.

The angle between the relative velocity and the rotor plane, known as the inflow angle, ϕ, is computed from the velocity triangle as given below.

$$\tan\phi = \left(\frac{V_{rel}(z)}{-V_{rel}(y)} \right)_6 \tag{2.30}$$

The angle of attack, α, is the angle between the relative velocity and the airfoil chord line, which is the difference between the inflow angle and the local pitch angle as given below.

$$\alpha = \phi - (\beta + \theta_p) \tag{2.31}$$

where the local pitch angle is the summation of blade twist angle, β, and the blade pitch angle, θ_p.

The lift and drag forces per unit length are computed using the following equations.

$$L = \frac{1}{2}\rho_a c V_{rel}^2 C_l \tag{2.32}$$

$$D = \frac{1}{2}\rho_a c V_{rel}^2 C_d \tag{2.33}$$

where ρ_a is the air density, which normally takes the value of 1.225 kg/m^3 at standard conditions (IEC), c is the blade chord length at a given radial position, and C_l and C_d are the lift and drag coefficients, respectively.

From the lift and drag force distributions, the normal and tangential forces per unit length on the rotor are computed as follows.

The normal force per unit length is given by,

$$P_n = L\cos\phi + D\sin\phi \tag{2.34}$$

The tangential force per unit length is given by,

$$P_t = L\sin\phi - D\cos\phi \tag{2.35}$$

The normal and tangential force distributions are integrated over the blade length and summed for the three blades to obtain the total normal and tangential forces.

2.2.4   Computation of induced velocity - Dynamic wake model

Because of the flow over the three dimensional rotor, the vortex system formed on the blades generate a downwash, referred to as the induced velocity, with a normal and a tangential component. The induced velocity does not react immediately to a change in aerodynamic loads, but with a time delay. This is computed through a dynamic wake model. Many engineering models exist for the computation of dynamic wake. These models predict the time delay using an exponential decay function with appropriate time constants. The model proposed by Øye (1991) is used here. In this model, a filter is utilized for the induced velocity, which consists of two first order differential equations as follows.

$$W_{int} + \tau_1 \frac{dW_{int}}{dt} = W_{qs} + k\tau_1 \frac{dW_{qs}}{dt} \tag{2.36}$$

$$W + \tau_2 \frac{dW}{dt} = W_{int} \tag{2.37}$$

The quasi-static value of the induced velocity is written as:

$$W_{qs} = \begin{pmatrix} W_x^{qs} \\ W_y^{qs} \\ W_z^{qs} \end{pmatrix}$$

$$W_y^{qs} = W_t = \frac{-BL\sin\phi}{4\pi\rho_a rF |V0 + f_g \mathbf{n}\,(\mathbf{n}\cdot\mathbf{W})|} \tag{2.38}$$

$$W_z^{qs} = W_n = \frac{-BL\cos\phi}{4\pi\rho_a rF |V0 + f_g \mathbf{n}\,(\mathbf{n}\cdot\mathbf{W})|}$$

where W_n and W_t represent the normal and tangential components of the induced velocity, B represents the number of blades, r, radius to the blade element under consideration and F corresponds to Prandtl's correction factor, which is explained in section 2.2.5. Glauert's correction factor in the equation is f_g and the normal vector $\mathbf{n}$ is in the direction of drive train, which is the vector, $(0, 0, -1)$.

The two time constants, which are calibrated, using a simple vortex method, is given below:

$$\tau_1 = \frac{1.1}{(1 - 1.3a)} \frac{R}{V0} \tag{2.39}$$

$$\tau_2 = \left(0.39 - 0.26 \left(\frac{r}{R}\right)^2\right)\tau_1 \tag{2.40}$$

where R is the rotor radius. General expression for the axial induction factor is:

$$a = \frac{|V0| - |V'|}{|V0|} \tag{2.41}$$

However, the axial induction factor is not allowed to exceed a value of 0.5, which is explained in section 2.2.5.

The simultaneous differential equations are solved analytically by assuming the right hand sides of the equations to be constant, giving rise to the following scheme:

- Calculate the quasi-static induced velocity at the current time step using the equation (2.38).

- Estimating the right hand side of the equation (2.36) using backward difference scheme is given below.

$$H = W_{qs}^i + k\tau_1 \frac{W_{qs}^i - W_{qs}^{i-1}}{\Delta t} \tag{2.42}$$

where $k = 0.6$, Δt is the time step, the superscripts i and $i - 1$ represent the present and previous time position respectively.

- Solving the equation (2.36) analytically gives rise to the following equation.

$$W_{int}^i = H + \left(W_{int}^{i-1} - H\right) exp\left(\frac{-\Delta t}{\tau_1}\right) \tag{2.43}$$

- Solving the equation (2.37) analytically, will compute the induced velocity at current time step using the following equation.

$$W^i = W_{int}^i + \left(W^{i-1} - W_{int}^i\right) exp\left(\frac{-\Delta t}{\tau_2}\right) \tag{2.44}$$

Application of the dynamic time filter is necessary for the induced velocity in order to capture the time domain behaviour of the loads and power when the thrust is changed, say by pitching the blades.

The dynamic wake implementation is validated against the trend of Figure (9.8) in Hansen (2008). The same kind of figure from the present implementation is shown in Figure 2.5. The validation is not a quantitative comparison, as both of the wind turbines used to obtain the results are different. The reference figure is for a 2MW wind turbine subjected to a wind speed of 8.7 m/s, whereas the present implementation is for a 5MW wind turbine subjected to 10 m/s wind speed. It is observed that the trends in both of the figures are the same, especially with a small time constant of 2.5 to 5 s.
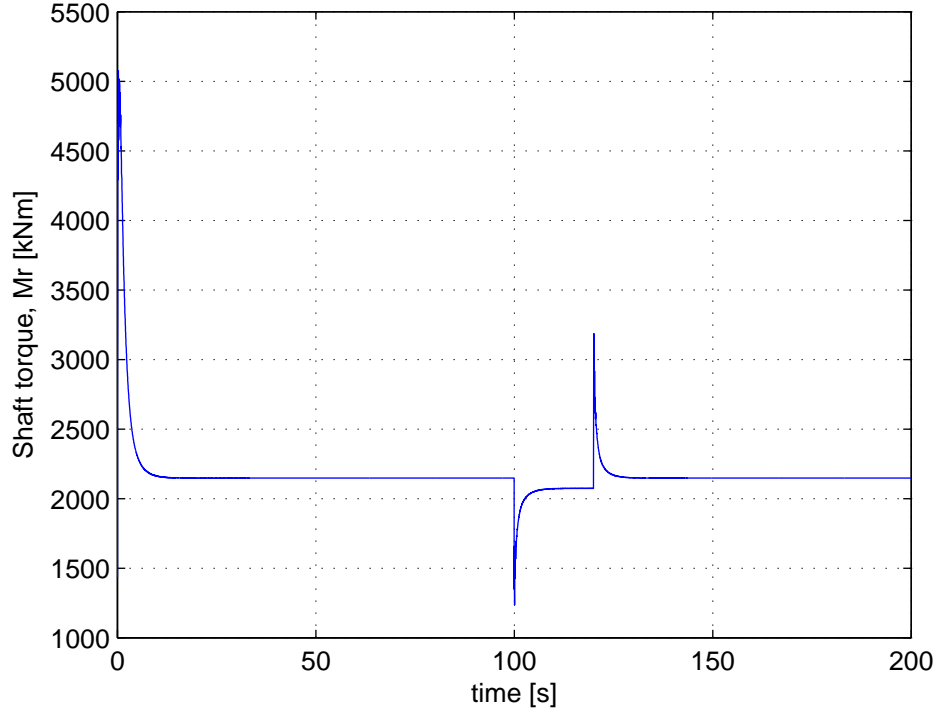
FIGURE 2.5: Rotor shaft torque variation at a wind speed of 10 m/s when a step pitch input is given

2.2.5 Correction factors

As explained, the BEM method is derived for an infinite bladed disc. In order to apply the governing equations for a finite number of blades rotor, appropriate correction factors need to be applied. All such correction factors are explained in this section.

Prandtl's tip loss factor corrects the assumption of an infinite number of blades. The correction factor is applied to the incremental thrust and torque as given in the following equations.

$$dT = 4\pi r \rho_a V0^2 a(1-a)F dr \tag{2.45}$$

$$dM = 4\pi r^3 \rho_a V0\omega(1-a)a'F dr \tag{2.46}$$

where a and a' are the axial and tangential induction factors respectively. Prandtl's tip loss factor, F is given below.

$$F = \frac{2}{\pi}\cos^{-1}(e^{-f}) \tag{2.47}$$

where

$$f = \frac{B}{2}\frac{R-r}{r\sin\phi} \tag{2.48}$$

Using the expressions for dT and dM, the following equations for the axial and tangential induction factors are derived.

$$a = \frac{1}{\frac{4F \sin^2 \phi}{\sigma C_n} + 1} \tag{2.49}$$

$$a' = \frac{1}{\frac{4F \sin \phi \cos \phi}{\sigma C_t} - 1} \tag{2.50}$$

where solidity ratio, $\sigma(r) = \frac{c(r)B}{2\pi r}$, normal force coefficient, $C_n = C_l \cos \phi + C_d \sin \phi$ and tangential force coefficient, $C_t = C_l \sin \phi - C_d \cos \phi$.

When the value of axial induction factor becomes high (approximately larger than 0.4), the simple momentum theory breaks. For wind turbines, the situation of axial induction factor going beyond 0.4 is often experienced. To have a constant mass flow rate, the control volume at the rotor disc needs to be increased (or expanded), which means the velocity is decreased. When the wake vortices are large, the streamlines are not smooth and hence the Bernoulli's equation is no longer valid. Hence, the Glauert's correction is applied to take into account this effect. Though several empirical relations between the thrust coefficient and axial induction factor exist, the equation proposed by Spera (1994) is used here.

$$C_T = \begin{cases} 4a(1-a)F & for \;\; a \leq a_c \\[2mm] 4\left(a_c^2 + (1-2a_c)\,a\right)F & for \;\; a > a_c \end{cases} \tag{2.51}$$

where critical axial induction factor, $a_c = 0.2$.

Using the conventional equation for thrust coefficient, plugging the expression for incremental thrust and comparing the thrust coefficient expression with the above equation gives rise to the axial induction factor, as given below.

For $a \leq a_c$,

$$a = \frac{1}{\frac{4F \sin^2 \phi}{\sigma C_n} + 1} \tag{2.52}$$

For $a > a_c$,

$$a = \frac{1}{2}\left[2 + K\left(1 - 2a_c\right) - \sqrt{\left(K\left(1 - 2a_c\right) + 2\right)^2 + 4\left(Ka_c^2 - 1\right)}\right] \tag{2.53}$$

where

$$K = \frac{4F \sin^2 \phi}{\sigma C_n} \tag{2.54}$$

2.2.6 Dynamic stall

From the velocity triangle shown in Figure 2.4, the angle of attack is a function of relative velocity and local pitch angle. The angle of attack changes dynamically during every revolution either because of the change in relative velocity or because of pitching the blade over time. When the angle of attack takes a step change, the aerodynamic loads do not respond at the same time, but with a time delay, which is assumed to be proportional to the ratio

of chord to the relative velocity seen at the blade section, $(c/Vrel_6)$. Prior to the stall, the steady airfoil data is sufficient to capture the loadings, whereas, this effect also need to be captured in the stalled and post stalled regions.

In the post stall region, if a steady airfoil data are used, increasing the angle of attack causes the lift to decrease, giving rise to a negative slope in the angle of attack vs. lift coefficient curve. This negative slope can lead to self-induced vibrations and the wind turbine might experience large blade flapwise moments. However, these large bending moments do not appear in practice, Øye (1991). This problem can be dealt by implementing a dynamic stall model.

The response of the aerodynamic load is dependent on whether the boundary layer is attached or partly separated. For attached flow, the time delay is estimated using the Theodorsen theory for unsteady lift and aerodynamic moment. Many models are suggested in the literature to take into account of the dynamic effect. The Beddoes-Leishman model takes into account the attached flow, leading edge separation, compressibility effects and also corrects the drag and moment coefficients.

The model suggested by Øye (1991) is used here. In the Øye model, the dynamic stall is modeled through a separation function, f_s. For wind turbines, trailing edge separation is assumed to be most important phenomenon in terms of dynamic airfoil data, however, effects in the linear region may also be important. For trailing edge stall, the degree of stall can be described through f_s, a function that takes the value zero at leading edge separation and unity at trailing edge separation. Hence the dynamic value of lift coefficient is expressed as follows,

$$C_{l,dyn} = f_s C_{l,inv}(\alpha) + (1 - f_s)C_{l,fs}(\alpha) \tag{2.55}$$

where $C_{l,inv}$ is the lift coefficient for inviscid flow without any separation (an extrapolation of static airfoil data in the linear region), $C_{l,fs}$ is the lift coefficient for fully separated flow (for example, flow over a flat plate with sharp leading edge). The rate of change of degree of stall is expressed below,

$$\frac{df_s}{dt} = \frac{f_s^{st} - f_s}{\tau} \tag{2.56}$$

Integrating the above equation, the unsteady separation function is obtained.

$$f_s(t + \Delta t) = f_s^{st} + (f_s(t) - f_s^{st}) \exp\left(\frac{-\Delta t}{\tau}\right) \tag{2.57}$$

where f_s^{st} is the value of f_s that reproduces the static airfoil data as given below,

$$f_s^{st}(\alpha) = \frac{C_{l,st}(\alpha) - C_{l,fs}(\alpha)}{C_{l,inv}(\alpha) - C_{l,fs}(\alpha)} \tag{2.58}$$

$$\tau \simeq A\frac{c}{Vrel_6} = 4\frac{c}{Vrel_6} \tag{2.59}$$

where τ is a convective time constant, here taken as the time for the air to move four times the chord length down stream. This dynamic model is only applied to the lift coefficient data. Steady airfoil data is used for the drag and moment coefficients. Depending on the angle of attack, the lift will vary. Using unsteady data, stabilizes the solution. Applying a dynamic stall model, the airfoil data is always chasing the static value at a given angle of attack that is also changing in time.

The dynamic stall model is implemented in the computations and verified using Figure 9.9 in the text book by Hansen (2008). This is done by generating the steady lift curve from the reference figure and corresponding inviscid and fully separated lift coefficients by empirical expressions. From these three lift values, the separation function is computed for each angle of attack. In this way, the curve in the reference figure is reproduced using the dynamic stall implementation. A time constant of $\tau = 0.08s$ is used in the computation.

The dynamic stall loop is generated for the following sinusoidal variation of the angle of attack.

$$\alpha = 15 + 2\sin(12.57t) \tag{2.60}$$

An initial condition of $f_s(0) = f_s^{st}$ is used. The resulting curve, which is the same as that of Figure 9.9 of Hansen (2008) is shown in Figure 2.6.
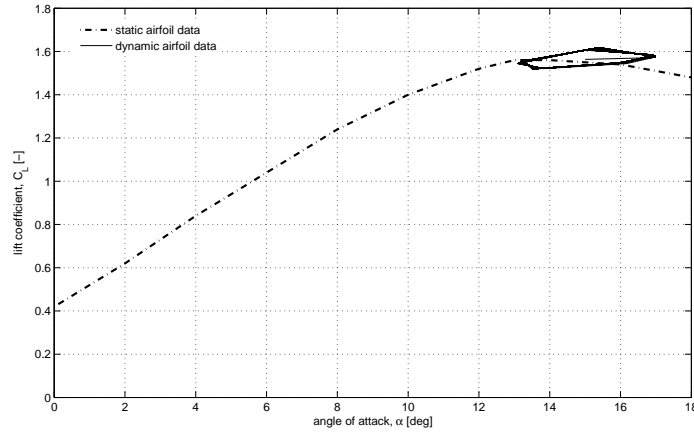
FIGURE 2.6: Validation of dynamic stall implementation

2.2.7   Tower shadow model

The presence of tower distorts the incoming wind flow. Since the tower is a blunt body, the wind flow over the tower can be represented using potential flow theory. In polar coordinates, the incoming axial wind velocity has two components viz. radial and tangential as shown in Figure 2.7. The expressions for radial and tangential velocity components are given in the following equations.

$$V_r = V0\left(1 - \left(\frac{r1_t}{r}\right)^2\right)\cos\theta \tag{2.61}$$

$$V_\theta = -V0\left(1 + \left(\frac{r1_t}{r}\right)^2\right)\sin\theta \tag{2.62}$$

where $r1_t$ is the radius of the tower and θ is the angle made by the radial vector with the horizontal.

As a consequence of tower shadow, the relative velocity drops, which is reflected as a drop in the rotor thrust with a periodicity of three times the rotor frequency (3p). An example
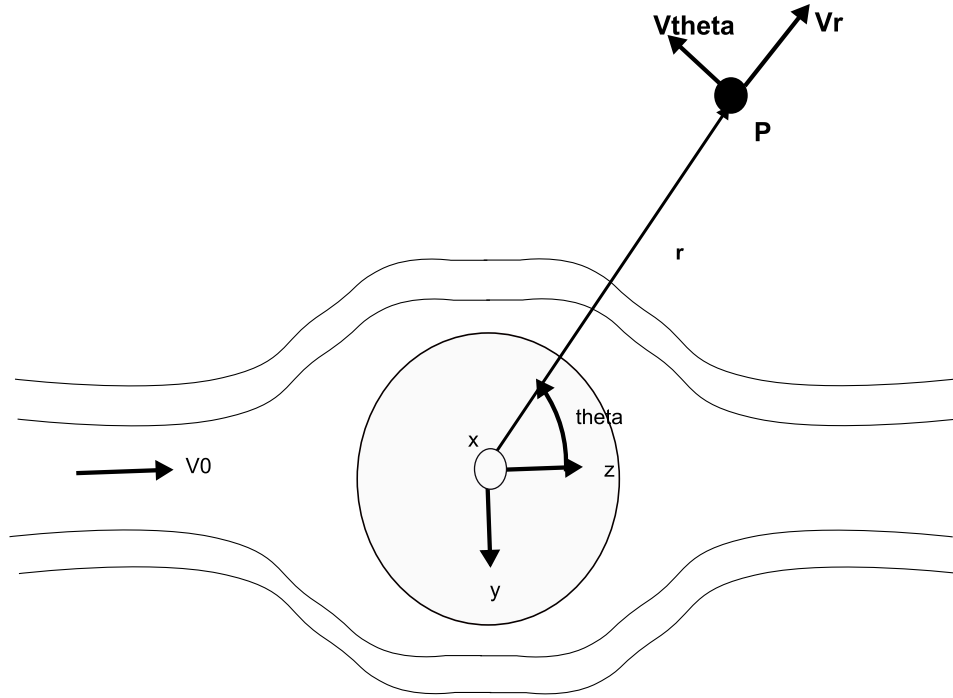
FIGURE 2.7: Influence of tower on incoming flow

of the tower shadow implementation is shown in Figure 2.8. The drop in the rotor thrust is attributed to the presence of tower shadow, otherwise, the rotor thrust would have been a constant line.
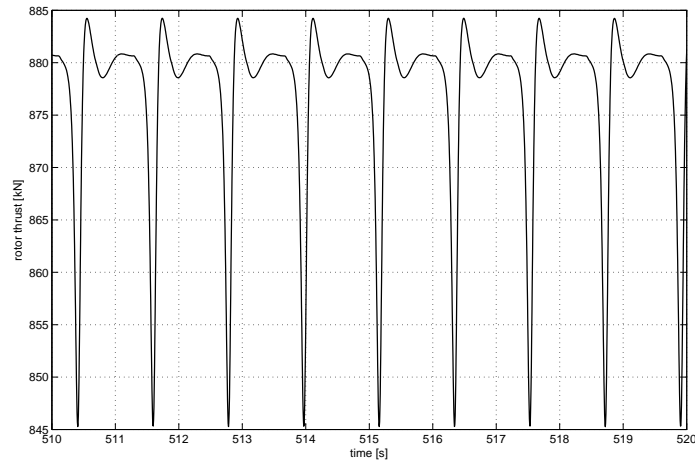
FIGURE 2.8: Example of the presence of tower shadow

2.2.8 Dynamic yaw

Presence of a nacelle yaw, which is the misalignment between the free stream wind velocity and the rotor plane, induces a velocity component along the blade length at the inner part

of the blade. At this condition, a part of the rotor will be in wake. This flow situation is three dimensional by nature, resulting in a different normal velocity to the rotor plane, as compared to the free stream velocity. This will change the average level of induced velocity. The influence of these differences can be taken into account by redistributing the rotor loads azimuthally by implementing a dynamic yaw model.

The normal component of the induced velocity in the drive train coordinate system is transformed to the blade coordinate system as given below.

$$(W_n)_6 = \begin{pmatrix} 0 \\ 0 \\ W_z \end{pmatrix} \tag{2.63}$$

$$(W_n)_5 = a_{56}^T (W_n)_6 \tag{2.64}$$

$$V' = (V0)_5 + (W_n)_5 = \begin{pmatrix} V0_x \\ V0_y \\ V0_z + W_{5z} \end{pmatrix} \tag{2.65}$$

The wake skew angle is given by the following equation.

$$\cos \chi = \frac{\mathbf{n} \cdot \mathbf{V'}}{|\mathbf{n}||\mathbf{V'}|} \tag{2.66}$$

where the wake skew angle, χ, is the angle between the wind velocity in the wake and the rotational axis of the rotor, $\mathbf{n}$ is the normal vector in the direction of the rotational axis.

The wake skew angle is assumed to be constant along the blade radius and can be approximately equal to the angle computed at 70 % of the blade radial position, $r/R = 0.7$,

$$\tan \theta_0 = \left(\frac{V0_y}{V0_x} \right)_6 \tag{2.67}$$

$$\theta_{wing}(t + \Delta t) = \theta_{wing}(t) + \omega \Delta t \tag{2.68}$$

where θ_0 is the angle where the blade is deepest into the wake, θ_{wing} is the azimuthal position of the rotor and ω is the rated rpm of the rotor in rad/s. Hence, the induced velocity at the new azimuthal position at time $(t + \Delta t)$ is given by,

$$W = W_0 \left(1 + \frac{r}{R} \tan \left(\frac{\chi}{2} \right) cos(\theta_{wing} - \theta_0) \right) \tag{2.69}$$

where W_0 is the mean induced velocity obtained from the dynamic wake model.

2.2.9   Wind shear model

The wind velocity field seen by the wind turbine varies both spatially and temporally. A schematic drawing of such a wind field is shown in Figure 2.9. The mean spatial variation of the flow field can be represented by means of a wind shear profile. The effect of wind shear is an increase of mean wind velocity along the height above the ground following either a logarithmic or a power law. At neutral atmospheric stability conditions, the wind shear models recommended by IEC are power law and logarithmic profiles as given in the following equations.

fluctuating component

mean component
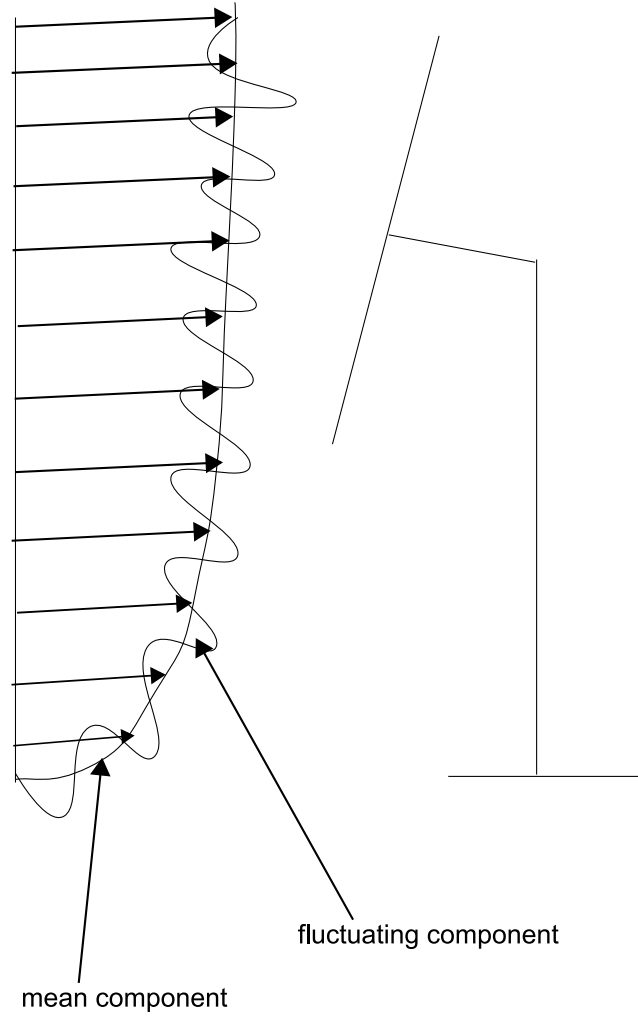
FIGURE 2.9: Spatial and temporal variation of wind velocity

$$V(z) = V(z_r) \left(\frac{z}{z_r} \right)^{\alpha 1} \tag{2.70}$$

$$V(z) = V(z_r) \frac{ln\left(\frac{z}{z_0} \right)}{ln\left(\frac{z_r}{z_0} \right)} \tag{2.71}$$

where $V(z)$ is the wind speed at height z, the height above ground, z_r is the reference height above ground used for fitting the profile, z_0 is the roughness length and $\alpha 1$ is the wind shear or power law exponent having a value of approximately 0.2 onshore, 0.14 or less in the ocean.

2.2.10   Turbulence

The turbulence available in the wind flow is represented through various models. In Figure 2.9, the fluctuating part on top of the mean flow is the turbulence component. In other

words, the instantaneous velocity in any direction is the sum of its mean value and a fluctuating component. The fluctuating component can be obtained from different turbulence models. When the wind turbine is experienced with the wind flow, the turbulence available in the ambient flow is distorted by the rotation of rotor giving rise to a requirement for rotational sampling of the flow. The classical method of treating the turbulence is to use any standard wind spectrum, IEC (2009), such as Kaimal or von Kàrmàn or Davenport spectrum. The turbulence models suggested by Paul Veers (1988), Mann (1994) and Øye takes into account the spectral moments and coherence of the turbulence.

In this thesis, two models are used viz. a spatially coherent Mann model and Øye model. The Mann model is used for the two-dimensional and three-dimensional codes, whereas the Øye model is used for Flex5 coupling.

2.3   Summary

In this chapter, the problem is described along with a configuration selection and representative dimensions. Having defined the problem, the unsteady BEM is described in detail along with some of the implementation test cases. In the next chapter, the hydrodynamic loads will be described in detail.

Hydrodynamic Loading

In this chapter, the hydrodynamics part of the problem is formulated and the implementation is described. For the water depth under consideration, wave load theory for deep waters is applicable. This is explained through the wave kinematics development for two-dimensional regular and irregular and three-dimensional irregular waves and finally the hydrodynamic force computation.

3.1 Two dimensional linear regular wave theory

The most simple description of the surface waves is by means of regular Airy wave theory. The surface waves are assumed as smooth sinusoidal or cosine shaped waves with a certain amplitude and time period. Motion of the water particles depend on the vertical and horizontal positions and time. For finite water depth, the wave particles take a circular orbital shape and the wave period and wave length are related through the dispersion relation, as shown below.

$$\omega^2 = gk \tanh(kh_w) \tag{3.1}$$

where ω is the angular wave frequency, g is the acceleration due to gravity, k is the wave number and h_w is the water depth.

The coordinate system is chosen at the mean water surface with positive x axis along the wave propagation direction and z axis pointing upwards, which is consistent with the coordinate system followed for the platform bottom point. This means that, the sea bed is at $z = -h_w$, the water depth. However, the hydrodynamic forces and moments are computed about the platform bottom point. The velocity potential is shown in the following equation:

$$\phi(x, z, t) = -\frac{\omega \eta_a}{k} \frac{\cosh(k(z + h_w))}{\sinh(kh_w)} \sin(\omega t - kx) \tag{3.2}$$

where the wave amplitude, $\eta_a = \frac{H}{2}$.

The surface elevation, η, can be computed using the following equation.

$$\eta = \eta_a \cos(\omega t - kx) \tag{3.3}$$

The wave kinematics are computed from the velocity potential using linear Airy wave theory assuming the wave steepness, $\frac{H}{\lambda}$, is small. Hence, the wave kinematics are given in the following equations.

Water particle horizontal velocity,

$$u = \omega \eta_a \frac{\cosh(k(z + h_w))}{\sinh(kh_w)} \cos(\omega t - kx) \tag{3.4}$$

35

Water particle vertical velocity,

$$w = -\omega\eta_a \frac{\sinh\left(k\left(z + h_w\right)\right)}{\sinh\left(kh_w\right)} \sin\left(\omega t - kx\right) \tag{3.5}$$

Water particle horizontal acceleration,

$$\dot{u} = -\omega^2\eta_a \frac{\cosh\left(k\left(z + h_w\right)\right)}{\sinh\left(kh_w\right)} \sin\left(\omega t - kx\right) \tag{3.6}$$

Water particle vertical acceleration,

$$\dot{w} = -\omega^2\eta_a \frac{\sinh\left(k\left(z + h_w\right)\right)}{\sinh\left(kh_w\right)} \cos\left(\omega t - kx\right) \tag{3.7}$$

The implementation of wave kinematics is checked through a simple example for the environmental conditions defined. As the maximum wave height for a wave climate with significant wave height of $H_s = 7\ m$ is $H_m = 1.86 H_s = 13.02\ m$ for a 3 hours realization, a wave height of 13.02 m and a wave period of 10 s are used for the computation. An example of surface elevation and wave kinematics, computed at mean water level is shown in Figure 3.1.
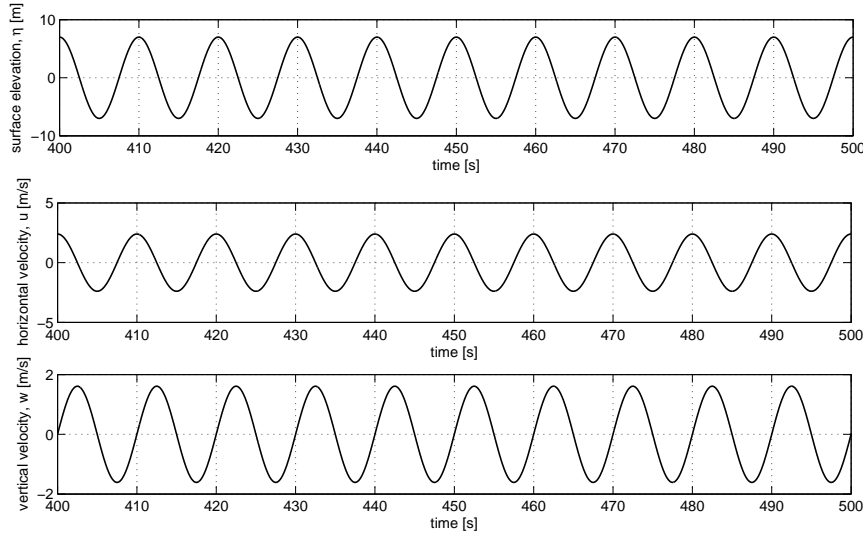
FIGURE 3.1: Two dimensional regular wave kinematics

3.2   Two dimensional linear irregular wave theory

The wave kinematics so far discussed is for regular waves, which in their pure form are not commonly seen in the ocean environment. Instead, the waves can be considered as composed of many regular waves with different frequencies and amplitudes, which are known as irregular waves. The concept of irregular waves is a realistic representation of the actual waves, and can be expressed by means of statistical quantities.

The wave climate used for irregular waves in the present study has a significant wave height of 7 m and a peak period of 10 s. The energy available in the wave is represented by means of a wave spectrum, which contains a wide range of frequencies. Out of the many spectra

proposed, two of the widely used ones are Pierson-Moskowitz spectrum and Joint North Sea Wave Project (JONSWAP) spectrum. As the JONSWAP spectrum usually represents the measured frequency spectrum fairly well for the North Sea, the JONSWAP spectrum with a peak enhancement factor of 3.3 is used, and is shown in Figure 3.2.
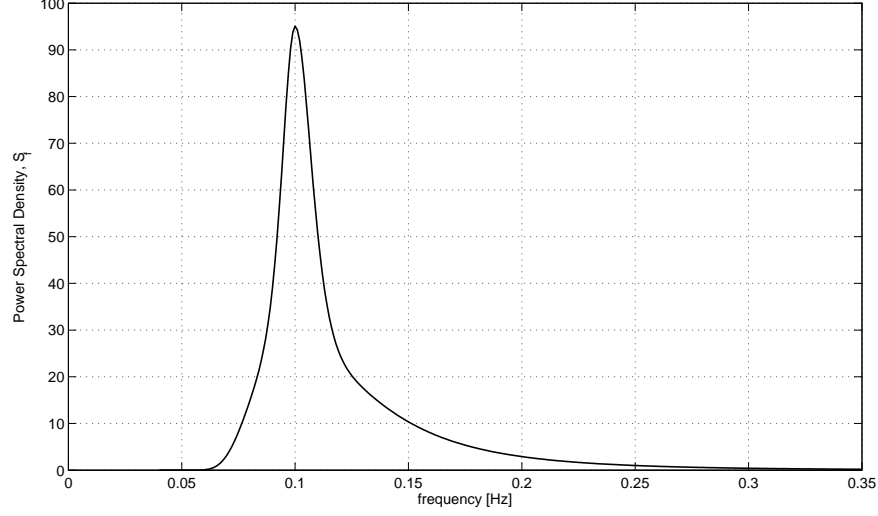
FIGURE 3.2: JONSWAP Spectrum

A set of uniformly distributed frequencies with a frequency resolution of 0.001 Hz is chosen. This corresponds to a maximum computation time duration of 1000 s before repetition. The spectrum is constructed using frequency cut offs between 0.04 Hz and 0.35 Hz, as the wave energy outside this frequency range is negligible. The resulting spectrum is centered around the peak wave frequency, f_p of 0.1 Hz, as specified. The power spectral density is given by the following equation.

$$S_\eta(f) = \frac{\alpha g^2}{(2\pi)^4 f^5} \exp\left(-\frac{5}{4}\left(\frac{f}{f_p}\right)^{-4}\right) \gamma^b \tag{3.8}$$

where

$$\alpha = 3.32285 H^2 f_p^4 \tag{3.9}$$

$$\gamma = 3.3 \tag{3.10}$$

$$b = \exp\left(-\frac{(f - f_p)^2}{2\sigma^2 f_p^2}\right) \tag{3.11}$$

$$\sigma = \begin{cases} 0.07 & \text{for } f \leq f_p \\ 0.09 & \text{for } f > f_p \end{cases} \tag{3.12}$$

For each of the frequency, the wave amplitude is computed from the power spectral density of the wave spectrum. The wave number is calculated from the wave dispersion relation.

Using these parameters, the surface elevation time series is computed using the following equation,

$$\eta(x,t) = \sum_n a_n \cos\left(\omega_n t - k_n x + \theta_n\right) \tag{3.13}$$

where a_n represents frequency dependent wave amplitude, θ_n represents the random phase angle, which lies between 0 and 2π radians. The phase angles are used to make the surface elevation random. The randomness in the phase angle is introduced using a random number generator, however, to obtain reproducible results, a seed number of 0 is used.

The frequency dependent wave amplitude is given in the following equation.

$$a_n = \sqrt{2S_\eta(f)\Delta f} \tag{3.14}$$

Implementation of the surface elevation is validated using the simple relation of significant wave height and standard deviation, as shown in below, Sumer and Fredsøe (2006).

$$H_s = 4\sigma_\eta \tag{3.15}$$

From the actual implementation, the standard deviation is 1.75 m, whereas the standard deviation from equation (3.15) is also 1.75 m. Hence the implementation is validated. Further, the implementation is validated by comparing the surface elevations from the present model and that in a reference Bredmose and Jacobsen (2010). The reference time series data is obtained from the same code used in the reference and was compared with the time series data of the present implementation. The comparison is shown in Figure 3.3, wherein both surface elevations match. The comparison is for a specific realization of a focused wave group with a focus time of 60 s.
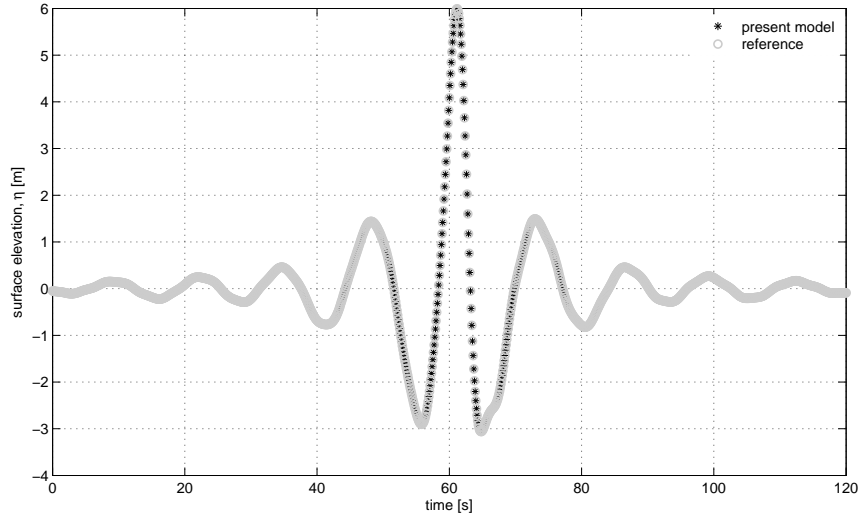
FIGURE 3.3: Two dimensional irregular wave - surface elevation validation

As used for regular waves, Linear wave theory is used to compute the wave kinematics, which gives rise to the horizontal and vertical velocity components as shown in the following equations.

$$u(x, z, t) = \sum_{n=1}^{N} a_n \omega_n \frac{\cosh\left(k_n\left(z + h_w\right)\right)}{\sinh\left(k_n h_w\right)} \cos\left(\omega_n t - k_n x + \theta_n\right) \tag{3.16}$$

$$w(x, z, t) = \sum_{n=1}^{N} -a_n \omega_n \frac{\sinh\left(k_n\left(z + h_w\right)\right)}{\sinh\left(k_n h_w\right)} \sin\left(\omega_n t - k_n x + \theta_n\right) \tag{3.17}$$

An example of the time series plots of surface elevation, horizontal and vertical velocities are shown in Figure 3.4.
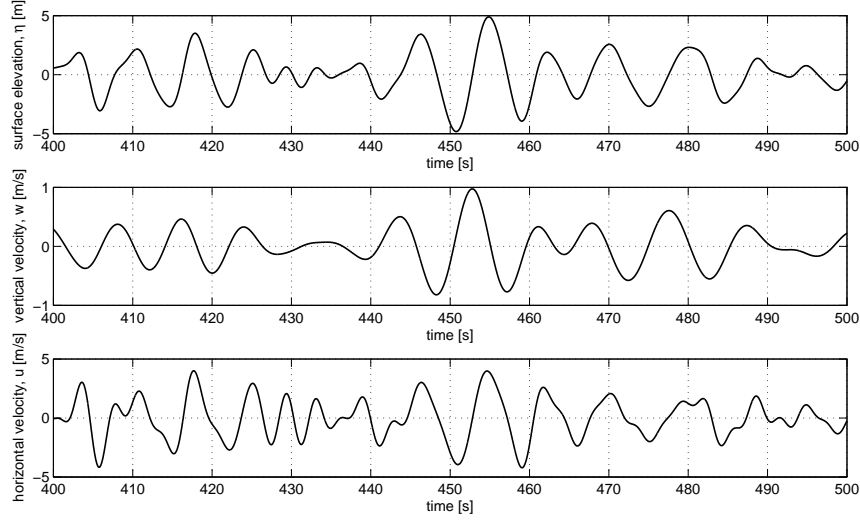
FIGURE 3.4: Two dimensional irregular wave kinematics

Using the wave kinematics, the wave induced forces are computed by means of Morison's equation.

3.3 Three-dimensional linear irregular wave theory

The complete three-dimensional description of the ocean environment is obtained with irregular wave theory with directional spreading. The wave is having a predominant direction along with a spreading centered around this direction. While $\pm\pi$ will cover the entire directions, significant energy is only concentrated around $\pm\pi/2$ direction and the rest of the directions are neglected. These waves are composed of finite number of regular waves with different frequencies and directions.

Wave kinematics are derived using the linear wave theory. Similar to the two-dimensional irregular waves, the wave amplitudes are derived based on a wave spectrum. However, the spectrum needs to take into account the directional spreading of waves and hence it becomes both frequency- and direction-dependent spectrum. For the frequency-dependent spectrum, the JONSWAP spectrum, as described in section 3.2 is used. The frequency resolution and the cut off frequencies remain the same. The directional spectrum takes the form of a cosine-power distribution, as shown in the following equation.

$$D(\phi) = \begin{cases} \frac{2}{\pi}\cos^2(\phi - \theta_0) & \text{for} \quad -\pi/2 \le \phi \le \pi/2 \\[2mm] 0 & \text{elsewhere} \end{cases} \tag{3.18}$$

where ϕ represents the range of directions between $-\pi/2$ to $\pi/2$ for a wave heading of $\theta_0 = 0$. The wave heading angle is the mean of the range of directions under consideration. Based on any wave heading, the range of directions can be selected. The general form of the cosine-power is with a power of $2s$, where s represents the degree of spreading around the mean direction. In this computation, $s = 1$ is used as shown in (3.18) .

The power spectral density of the directional wave spectrum is the product of both frequency- and direction- dependent spectral components, which is given in the following equation.

$$DS\,(f, \phi) = S_\eta(f)D(\phi) \tag{3.19}$$

where $S_\eta(f)$ is the frequency-dependent spectral function, as defined in equation (3.8). The resulting wave spectrum is shown in Figure 3.9. In the figure, the spectrum is concentrated in the frequency axis around the peak wave frequency of $0.1\ Hz$ and in the directional axis around the wave heading direction of $0°$, which is expected.
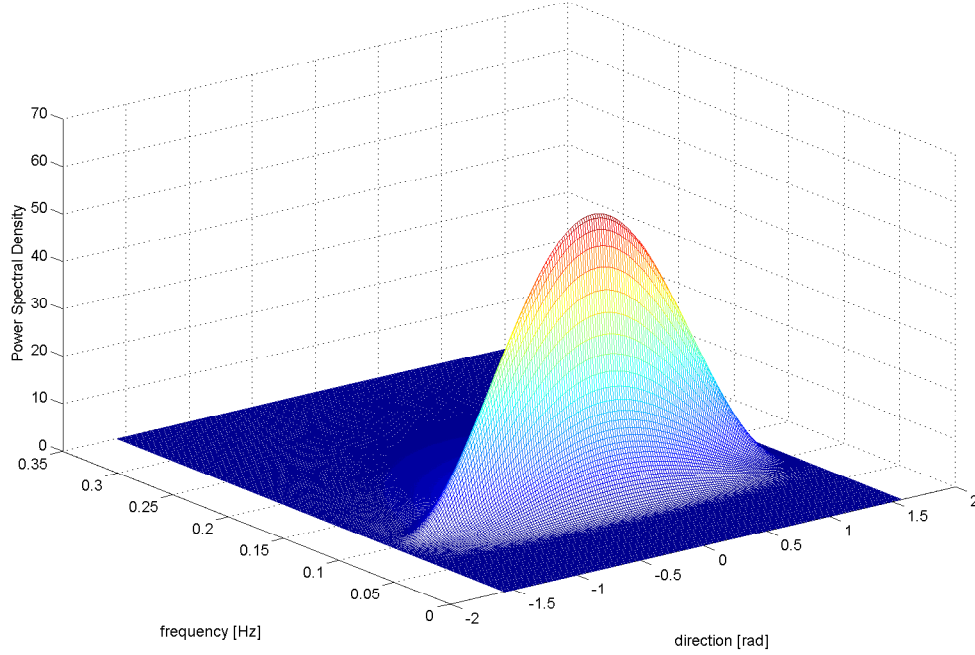
FIGURE 3.5: Three dimensional wave spectrum

The frequency- and direction-dependent wave amplitude and surface elevation are defined as in the following equations.

$$a_{np} = \sqrt{2DS\,(f, \phi)\,\Delta f \Delta\phi} \tag{3.20}$$

$$\eta(x, y, t) = \sum_{n=1}^{N} \sum_{p=1}^{M} a_{np} \cos\left(\omega_n t - k_n \cos(\phi_p)x - k_n \sin(\phi_p)y + \theta_{np}\right) \tag{3.21}$$

where n and p correspond to the frequency and direction components and θ_{np} represents random phase angle, which lies between 0 and 2π radians, depending on both frequency ω_n and direction ϕ_p.

The time series velocity components are computed from the following linear formulae:

$$u(x, y, z, \phi, t) = \sum_{n=1}^{N} \sum_{p=1}^{M} a_{np} \cos(\phi_p)\omega_n \frac{\cosh\left(k_n\left(z + h_w\right)\right)}{\sinh\left(k_n h_w\right)}$$
$$\cos\left(\omega_n t - k_n \cos(\phi_p)x - k_n \sin(\phi_p)y + \theta_{np}\right) \tag{3.22}$$

$$v(x, y, z, \phi, t) = \sum_{n=1}^{N} \sum_{p=1}^{M} a_{np} \sin(\phi_p)\omega_n \frac{\cosh\left(k_n\left(z + h_w\right)\right)}{\sinh\left(k_n h_w\right)}$$
$$\cos\left(\omega_n t - k_n \cos(\phi_p)x - k_n \sin(\phi_p)y + \theta_{np}\right) \tag{3.23}$$

$$w(x, y, z, \phi, t) = \sum_{n=1}^{N} \sum_{p=1}^{M} -a_{np}\omega_n \frac{\sinh\left(k_n\left(z + h_w\right)\right)}{\sinh\left(k_n h_w\right)}$$
$$\sin\left(\omega_n t - k_n \cos(\phi_p)x - k_n \sin(\phi_p)y + \theta_{np}\right) \tag{3.24}$$

where u, v and w are water particle velocities in x, y and z directions respectively.

A time series example of surface elevation, x, y and z components of the velocity are shown in Figure 3.6.

The wave kinematics are Delta stretched, ISO (2005) from 25 m below mean sea level, as described in the next section.
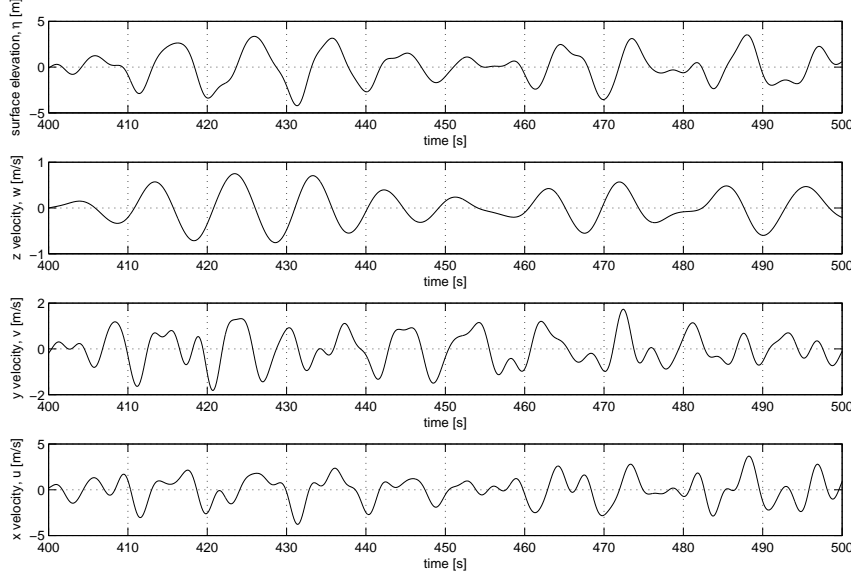
FIGURE 3.6: 3D wave kinematics

3.4   Delta stretching method

The linear wave theory is valid only upto the mean sea level, whereas the instantaneous sea surface is unsteady. For surface protruding structures, the wave kinematics at the instantaneous water surface above mean sea level need to be computed, in order to obtain a reasonably good estimate of the wave induced forces and moments. This is achieved by means of certain modifications carried out on the linear wave theory. These modifications are widely known as stretching methods, which have been suggested by different researchers. Some of these stretching methods are Wheeler stretching, Wheeler (1970), linear extrapolation, Forristall (1981), and Delta stretching, ISO (2005) and Rodenbusch and Forristall (1986). All these empirical models assume small wave steepness. For a detailed review on the stretching methods, the reader may consult, Gudmestad (1993), and for a comprehensive error analysis of the models, Xü (1995).

As given in Forristall (1981), linear extrapolation overestimates the horizontal velocity and Wheeler stretching underestimates it. Delta stretching provides an empirical average between the two other schemes. In the case of Wheeler stretching, the kinematics are stretched from the sea bed upto the mean sea level. The kinematics are mapped to the stretched numerical height, which will be used for further force computations. An example of the Wheeler stretched height is shown in the following figure.

In the case of Delta stretching, the wave kinematics are stretched from a reference height. The usual kinematics is followed upto this reference height and from there on, the kinematics is mapped to a stretched numerical height. The reference height is chosen as half of the significant wave height, $h' = \frac{H_s}{2}$, below the mean sea level, ISO (2005). Stretching is done only on the wave crest, not on the wave trough. Hence the necessary and sufficient condition for Delta stretching to be applied is that the surface elevation needs to be positive and the height under consideration needs to be above the reference height. Otherwise, the usual wave kinematics is followed. The stretching is done from the reference height upto a level of $\Delta\eta$, which is usually above the mean sea level. The empirical parameter Δ for Delta
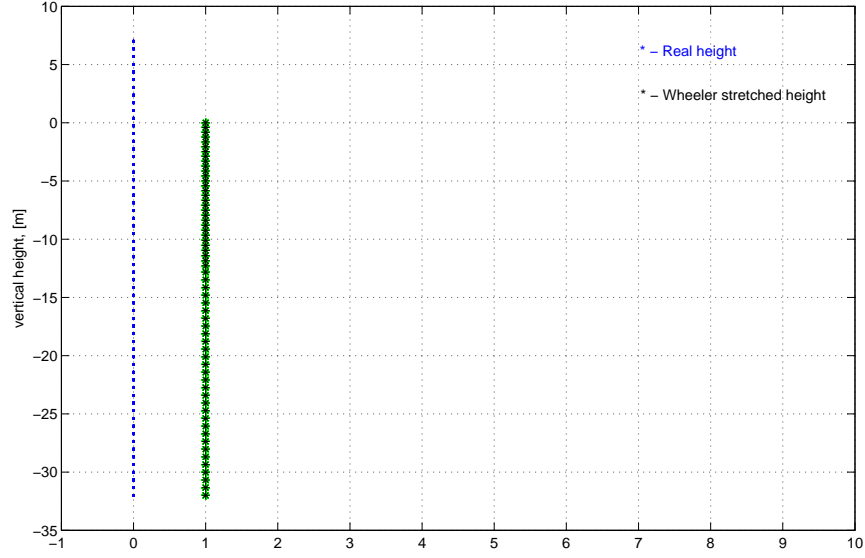
FIGURE 3.7: Wheeler stretched height

stretching is chosen as 0.3. Hence the maximum stretched height can go upto 30% of surface elevation, η, above the mean sea level. An example of the Delta stretched height is shown in the Figure 3.8.
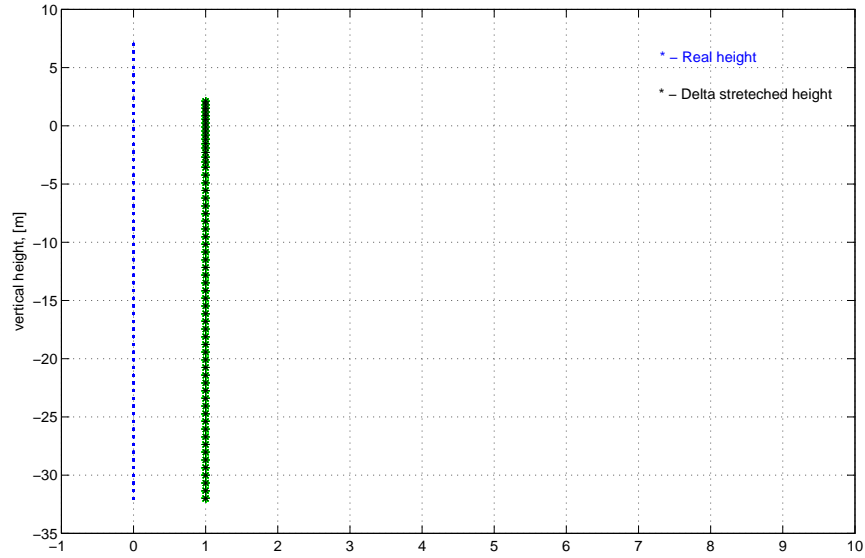
FIGURE 3.8: Delta stretched height

From the figure, it can be noticed that the stretched height is above the mean water level. The limiting cases of Delta stretching are obtained by using $\Delta = 0$ gives rise to Wheeler

stretching and $\Delta = 1$ gives rise to linear extrapolation. The mathematical representation of Delta stretching is illustrated below.

The coordinate mapping is given below.

$$z' = \begin{cases} (z + h')\frac{h' + \Delta\eta}{h' + \eta} - h' & \text{for } z > -h' \text{ and } \eta > 0 \\ \\ z & \text{otherwise} \end{cases} \tag{3.25}$$

If $z' < 0$, ie., below mean sea level, the wave velocities are written as follows.

$$u = \omega\eta_a \frac{\cosh{(k(z' + h_w))}}{\sinh{kh_w}} \cos{(\omega t - kx)} \tag{3.26}$$

$$w = -\omega\eta_a \frac{\sinh{(k(z' + h_w))}}{\sinh{kh_w}} \sin{(\omega t - kx)} \tag{3.27}$$

If $z' > 0$, ie., in the range of mean sea level to the instantaneous water surface, the wave velocities are Taylor expanded using the z' coordinate, yielding,

$$u = \omega\eta_a \left(\frac{\cosh{kh_w}}{\sinh{kh_w}} + kz' \right) \cos{(\omega t - kx)} \tag{3.28}$$

$$w = -\omega\eta_a \left(1 + kz' \frac{\cosh{kh_w}}{\sinh{kh_w}} \right) \sin{(\omega t - kx)} \tag{3.29}$$

The same method can be also extended to two- and three-dimensional irregular waves. An example of the vertical variation of horizontal velocity is shown in Figure 3.9. In the figure, the step change in horizontal velocity is because of the delta stretching.
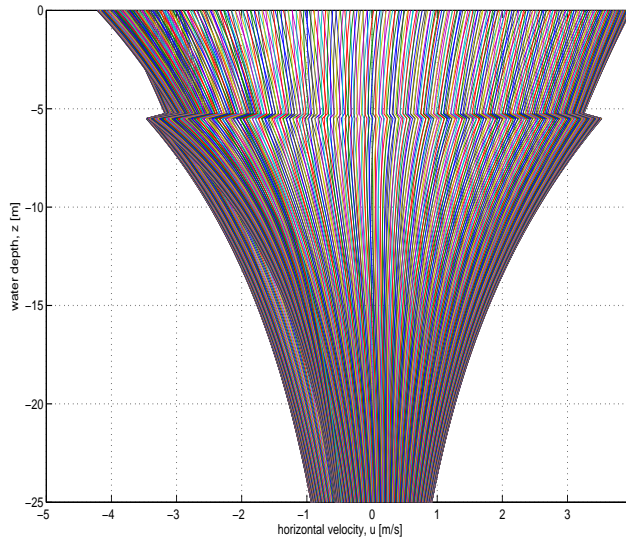
FIGURE 3.9: Vertical variation of horizontal velocity

3.5 Effect of wave diffraction and hydrodynamic force coefficients

The mean wave length in the wave environment under consideration is approximately 150 m. Hence, the ratio of characteristic diameter of the structure to the wave length is approximately 0.13, which is less than 0.2. This condition justifies that the effect of diffraction can be neglected and hence Morison's equation is used for computing the hydrodynamic forces with the following force coefficients.

The Keulegan-Carpenter Number (KC) for the floater configuration can be computed as follows.

$$KC = \frac{U_m T}{D} \tag{3.30}$$

where U_m is the maximum wave velocity, T is the wave period and D is the diameter of the structure. Hence, for the floater, $KC = 1.25$ and for the tower, $KC = 2.5$. Since the KC numbers are less than 7, the structure is considered to be in the inertia dominated regime and hence the hydrodynamic force coefficients can be taken as those given below.

The hydrodynamic added mass coefficient for a cylinder in surge direction is the standard value of $C_a = 1.0$, chosen from DNV (2011) and in the heave direction, it is 0.64, Sumer and Fredsøe (2006), as the added mass effect from the water around the bottom of the cylinder is considered similar to that of a circular disc moved perpendicularly to its own plane. For this situation, the reference volume for C_a is the volume of a sphere with same diameter as the disc. Similarly, the drag coefficient in the surge direction for a cylinder in this KC range is then to be $C_D = 1.0$, DNV (2011) and in the heave direction, the bottom of the platform is considered to act like a rectangular box, for which, $C_{Dz} = 2.0$, Sumer and Fredsøe (2006). In addition, the inertia coefficient follows the relation of $C_M = 1 + C_a$.

The pitch and roll added masses are computed using the following procedure.

The pitch added mass is considered to have contributions from accelerating the fluid in the lateral direction (side-wise) and the fluid in the top and bottom faces of the floater. For obtaining the first component, the floater is discretized perpendicular to the X-Z plane, giving rise to circular discs with diameter same as the floater diameter. The discretization is shown in the Figure 3.10. The flow direction is along the X axis.

Front view   Top view

Flow direction
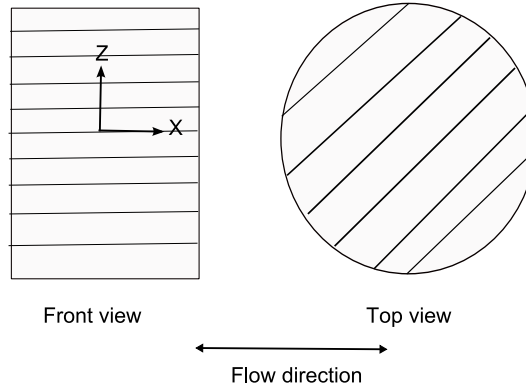
FIGURE 3.10: Floater discretization for side-wise pitch added mass

This will generate a pitch added mass, which is represented using the following equation.

$$I_{pitch1} = 2\rho C_{a1} A1 \int_0^R z^2 dz \tag{3.31}$$

where area of circular cross-section, $A1 = \pi R^2$, and for each section, the added mass coefficient, $C_{a1} = 1$, Sumer and Fredsøe (2006). The added mass and area of cross-section are constant for all the elements and z is the perpendicular distance from the centre of the floater to the section under consideration. Hence the side-wise contribution of pitch added mass is obtained as $I_{pitch1} = 1.7131E7 \ kgm^2$.

Similarly, the added mass contribution in the longitudinal direction is obtained by discretizing the floater perpendicular to the X-Y plane, giving rise to rectangular sections with floater height and varying lateral dimension. The discretization is shown in the Figure 3.11. The flow direction is along the Z axis.

Top View   Cross sectional view   Flow direction
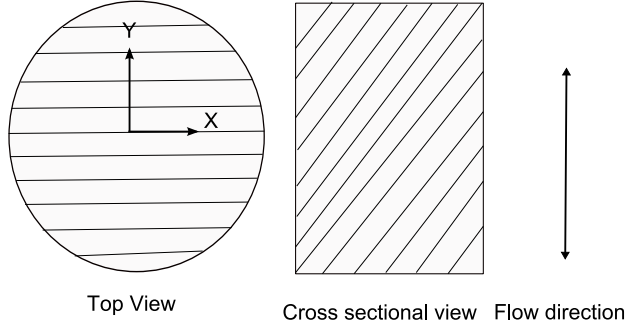
FIGURE 3.11: Floater discretization for longitudinal pitch added mass

This will generate a pitch added mass in the longitudinal direction, which is represented using the following equation.

$$I_{pitch2} = 2\rho \int_0^R C_{a2}(y) A2(y) y^2 dy \tag{3.32}$$

where $A2(y)$ is the area of rectangular section, which varies along the y axis of the floater, unlike the previous case, the added mass coefficient, C_{a2}, is also varying based on the width to height ratio, Sumer and Fredsøe (2006), and hence these variables are kept inside the integration symbol. The cross-sections are at a distance of y from the floater centre. Hence the longitudinal contribution of pitch added mass is obtained as $I_{pitch2} = 3.2259E7 \ kgm^2$.

The total pitch added mass can be computed as $I_{pitch} = I_{pitch1} + I_{pitch2} = 4.939E7 \ kgm^2$.

Similarly, the roll added mass can also be computed because of the floater symmetry.

3.6   Hydrodynamic force

The hydrodynamic forces are expressed by considering the relative movement of the structure with respect to the oscillatory motion of water particles and are given by the following equations, Morison et al. (1950).

In the surge direction, the force per unit length becomes

$$dF_1 = C_a \rho A \left(\dot{u} - \ddot{\eta}_{1f} \right) dz + \rho A \dot{u} dz + C_D \frac{1}{2} \rho D_f u_{res} \left(u - \dot{\eta}_{1f} \right) dz \tag{3.33}$$

In the sway direction, the force per unit length becomes

$$dF_2 = C_a \rho A \left(\dot{v} - \ddot{\eta}_2 \right) dz + \rho A \dot{v} dz + C_D \frac{1}{2} \rho D_f u_{res} \left(v - \dot{\eta}_2 \right) dz \tag{3.34}$$

In the heave direction, the total force becomes

$$F_3 = \frac{4}{3}\pi \left(\frac{D_f}{2}\right)^3 \rho C_{az} \left(\dot{w} - \ddot{\eta}_3\right) + \frac{\pi}{4} \left(D_f^2 p_b - \left(D_f^2 - D_t^2\right) p_t\right) +$$
$$\frac{\pi}{8} D_f^2 \rho C_{Dz} |w - \dot{\eta}_3| \left(w - \dot{\eta}_3\right) \tag{3.35}$$

While in the roll and pitch directions, the moment per unit length as measured from the bottom point of the floater ($z = 0$) are given in the following equations.

The incremental roll moment is given by,

$$dF_4 = C_a \rho A \left(\dot{v} - \ddot{\eta}_2\right)(-z)dz + \rho A \dot{v}(-z)dz + C_D \frac{1}{2} \rho D_f u_{res} \left(v - \dot{\eta}_2\right)(-z)dz \tag{3.36}$$

The incremental pitch moment is given below.

$$dF_5 = C_a \rho A \left(\dot{u} - \ddot{\eta}_{1f}\right) zdz + \rho A \dot{u} zdz + C_D \frac{1}{2} \rho D_f u_{res} \left(u - \dot{\eta}_{1f}\right) zdz \tag{3.37}$$

where the magnitude of the resultant velocity is expressed as, $u_{res} = \sqrt{\left(u - \dot{\eta}_{1f}\right)^2 + \left(v - \dot{\eta}_2\right)^2}$, sea water density, $\rho = 1025 \ kg/m^3$, cross-sectional area of the platform, A, platform surge, sway and heave displacements η_{1f}, η_2 and η_3 respectively, platform and tower bottom diameters D_f and D_t, z and dz represent the vertical distance from the platform bottom to a point under consideration and the incremental vertical distance. The $\dot{()}$ and $\ddot{()}$ represent first and second derivatives of the variable with respect to time.

The excess dynamic pressure at bottom and top faces of the platform are p_b and p_t, which can be expressed using the following general equation, Sumer and Fredsøe (2006).

$$p^+ = p + \rho g z = \rho g \frac{H}{2} \frac{\cosh k \left(z + h_w\right)}{\cosh k h_w} \cos \left(\omega t - kx\right) \tag{3.38}$$

The above equation is for a regular wave with straight forward generalization for irregular two- and three-dimensional waves.

The wave induced yaw moment is considered to be zero, $F_6 = 0$. In equations (3.33) to (3.37), the first term is the added mass contribution, the second term is the Froude-Krylov force and the third term is the quadratic viscous drag contribution. In equations (3.33), (3.34), (3.36) and (3.37), the relative velocities and accelerations are computed by neglecting the pitch induced surge and roll induced sway contributions, as these quantities are very small considering the dimensions of the floater.

The total horizontal force acting on the structure is found out by integrating the incremental force from bottom of the structure to the top in the positive z direction. Delta stretching is applied to the wave kinematics before computing the wave induced forces. The total force is computed by dividing the structure into 40 equidistant segments vertically and summing the forces corresponding to each element. A convergence study was also carried out by doubling the discretization (80 elements), which has no influence on the final results. This horizontal force becomes the external forcing function in the equation of motion in the surge direction for the platform. The computer implementation of this forcing function in the equations of motion is done slightly differently by grouping the structural acceleration term from the external forcing function into the mass matrix of the equations of motion. A similar methodology is also applicable for the sway force. The integration of incremental roll and pitch moments to obtain the total moments is also done the similar way as the force integration is carried out.

The total vertical force on the structure is depicted in Equation (3.35). In the equation, the Froude-Krylov force is the resultant of the excess dynamic pressure differences at the bottom and top faces of the platform. As far as the added mass force is concerned, in the vertical direction, the added mass is assumed as a spherical shape with a diameter equal to the platform diameter. The computer implementation is exactly the same way as that in the surge case. The drag force takes into account the relative motion between the vertical component of the wave velocity and that of the structure.

The implementation of surge force equation is validated with a result in reference Bredmose and Jacobsen (2010). The same dimensions and flow conditions used in the reference paper is adopted for the validation purpose. This computation is for a force on a vertical cylinder of 5 m diameter, which is placed at 20 m water depth, subjected to a focused wave group of a JONSWAP spectrum with a peak period of 13 s. The focus time is 60 s. The comparison of the surge force is shown in Figure 3.12. From the figure, it is observed that both of the surge force quantities compare well and hence the force implementation is validated.
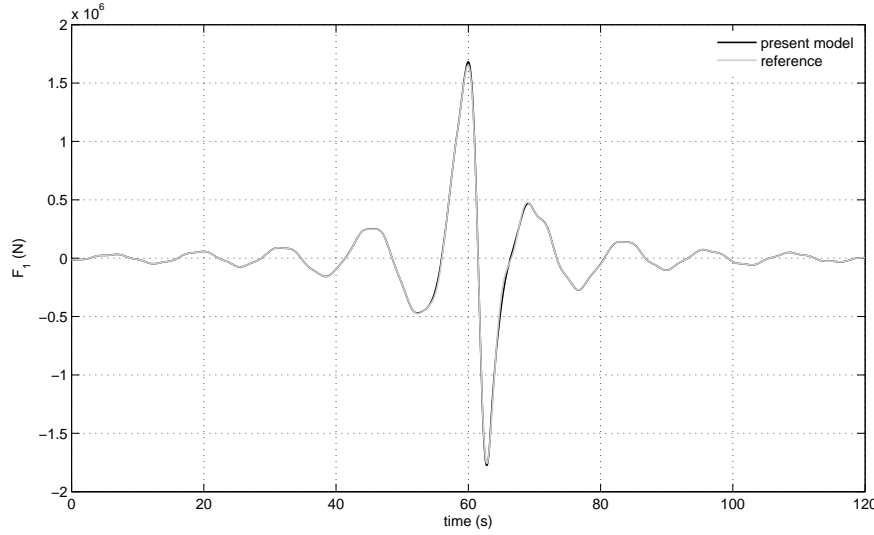
FIGURE 3.12: Surge force validation

3.7 Summary

In this chapter, the hydrodynamics part of the problem is described in detail giving focus on regular and irregular waves. The kinematics and force quantities derived in the chapter is used for the coupled formulation and analysis of the problem. In the next chapter, two-dimensional coupling and implementation of the problem will be explained along with results and observations.

CHAPTER 4

Two Dimensional Coupling

In this chapter, the problem is formulated in a two dimensional space. Initially a comprehensive model of the wind turbine along with aerodynamic loading module is formulated using the method of virtual work and unsteady BEM for an onshore wind turbine. Subsequently, the platform dynamics is formulated along with hydrodynamic loading in 2D space. Finally, the coupling is carried out in two stages. In the first step, the aerodynamic load is applied externally to the platform dynamics module, which is known as semi-coupled model. In the final step, all the modules are formulated in an integrated approach giving rise to a fully coupled model. The implementation of the models are tested for a number of load cases, observations are made and conclusions are drawn.

4.1 Semi-coupled model

The wind turbine dynamics along with aerodynamic module is derived first using the method of virtual work and unsteady BEM. Further, the platform dynamics in plane motion is formulated based on the force equilibrium. Linear Airy wave theory is applied for the waves. Hydrodynamic loads are modelled by means of Morison's equation using two dimensional linear irregular wave theory as explained in Chapter 3, section 3.2. Finally, the coupling procedure is explained along with test cases and observations.

4.1.1 Wind turbine model

The NREL 5-MW reference wind turbine is modeled using eleven degrees of freedom, which are detailed in Table 4.1. Tower and nacelle are modeled as lumped masses, connected through a spring and damper, whereas, the blades are modeled as elastic beams with distributed stiffness and mass properties using the three lowest eigen modes. Procedure followed for computation of the blade mode shapes is explained below.

TABLE 4.1: Wind turbine degrees of freedom

	Degrees of freedom	Number of DOF
Tower	longitudinal	1
Shaft	Azimuthal position	1
Blade	First and second flap for each blade	6
Blade	First edge for each blade	3
	Total	**11**

The twist, rigidity and mass distribution along the blade length are shown in Figures 4.1, 4.2 and 4.3, Jonkman et al. (2009). The blade mode shapes are computed analytically by

considering the mass and stiffness distribution, Hansen (2008). Blade beam model is shown in Figure 4.4.
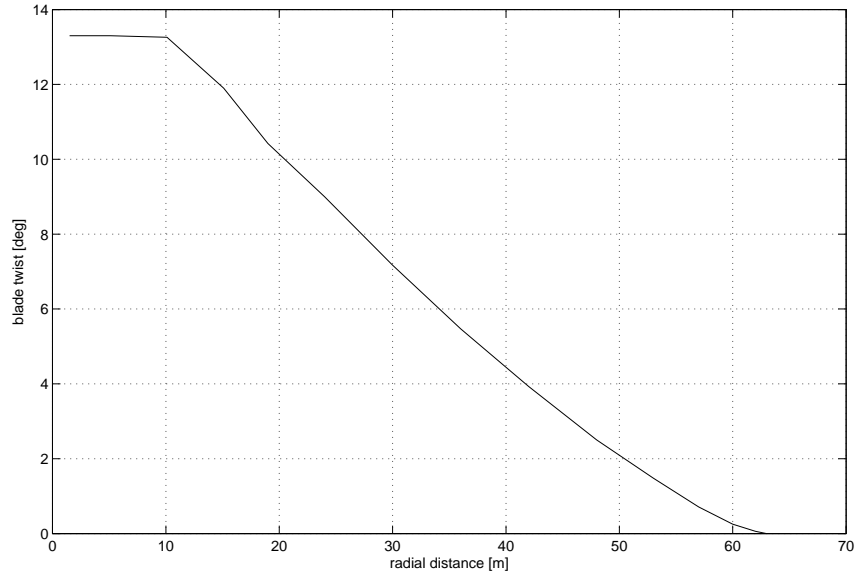
FIGURE 4.1: Blade twist distribution
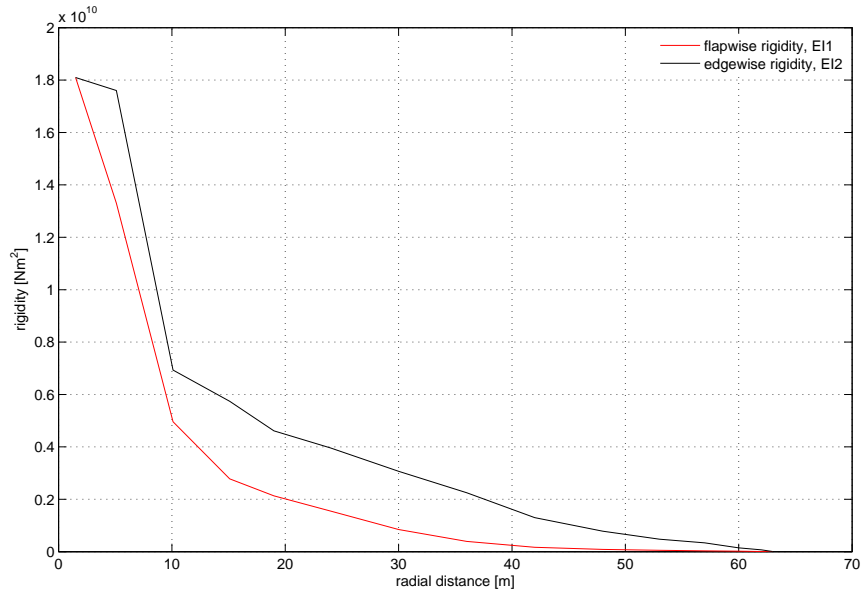
FIGURE 4.2: Blade stiffness distribution

For computing mode shapes, the beam is not subjected to any external loads and considering one element and applying Newton's second law implies the following two equations in y and z directions.
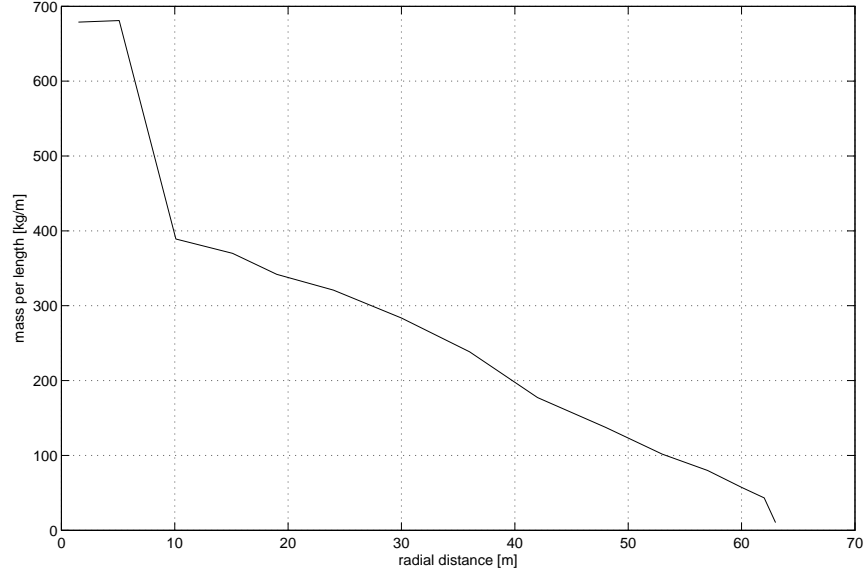
FIGURE 4.3: Blade mass distribution
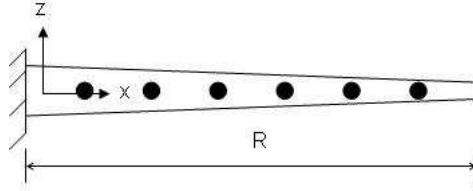
FIGURE 4.4: Blade beam model

$$\frac{dT_z}{dx} = m(x)\ddot{u}_z(x)$$

$$\frac{dT_y}{dx} = m(x)\ddot{u}_y(x)$$

(4.1)

where T is the shear force at a section of the beam. For an eigen mode, the deflection type is of the form, $u = A\sin(\omega t)$, which implies that the acceleration will be, $\ddot{u} = -\omega^2 u$. Substituting this in the above equation will give rise to the following equations.

$$\frac{dT_z}{dx} = -m(x)\omega^2 u_z(x)$$

$$\frac{dT_y}{dx} = -m(x)\omega^2 u_y(x)$$

(4.2)

Considering the right hand sides of the above equations as external loads to a static beam

bending equation, namely, $p_z = m(x)\omega^2 u_z(x)$ and $p_y = m(x)\omega^2 u_y(x)$. Since the deflections are not known a priori, the equations need to be solved iteratively.

To begin the iteration, the static deflection at the blade tip is used, which gives rise to the frequency equation as follows.

$$\omega^2 = \frac{p_z^N}{u_z^N m^N} \tag{4.3}$$

where the superscript N denotes the quantities at the blade tip. Using this frequency, a new loading is computed at all discrete points as in the following equation.

$$
\begin{aligned}
p_z^i &= \omega^2 m^i \frac{u_z^i}{\sqrt{\left(u_z^N\right)^2 + \left(u_y^N\right)^2}} \\
p_y^i &= \omega^2 m^i \frac{u_y^i}{\sqrt{\left(u_z^N\right)^2 + \left(u_y^N\right)^2}}
\end{aligned}
\tag{4.4}
$$

Corresponding to these loads, new deflections are computed and the steps are repeated until the frequency converges. The deflections corresponding to the converged frequency are known as first flapwise modes, $\phi_f^{1f} = u_z^{1f}$ and $\phi_e^{1f} = u_y^{1f}$.

In order to obtain the first edgewise deflection shapes, the flapwise deflection contributions are subtracted from the total deflection as depicted in the following equation and the same procedure as in the first flapwise deflection is followed.

$$
\begin{aligned}
u_z^{1e} &= u_z - const_1 u_z^{1f} \\
u_y^{1e} &= u_y - const_1 u_y^{1f}
\end{aligned}
\tag{4.5}
$$

The constant $const_1$ is computed by satisfying the orthogonality condition as in the following equation.

$$\int_0^R u_z^{1f} m u_z^{1e} dx + \int_0^R u_y^{1f} m u_y^{1e} dx = 0 \tag{4.6}$$

Combining the equations (4.5) and (4.6) will give rise to the constant as follows.

$$const_1 = \frac{\int_0^R u_z^{1f} m u_z dx + \int_0^R u_y^{1f} m u_y dx}{\int_0^R u_z^{1f} m u_z^{1f} dx + \int_0^R u_y^{1f} m u_y^{1f} dx} \tag{4.7}$$

Similarly, the second flapwise mode shapes are also computed by using the following orthogonality condition.

$$\int_0^R u_z^{1e} m u_z^{2f} dx + \int_0^R u_y^{1e} m u_y^{2f} dx = 0 \tag{4.8}$$

Hence, the second flapwise mode shapes are obtained as in the following equations.

$$
\begin{aligned}
u_z^{2f} &= u_z - const_2 u_z^{1e} \\
u_y^{2f} &= u_y - const_2 u_y^{1e}
\end{aligned}
\tag{4.9}
$$

where the constant, $const_2$ is given below.

$$const_2 = \frac{\int_0^R u_z^{1e} m u_z dx + \int_0^R u_y^{1e} m u_y dx}{\int_0^R u_z^{1e} m u_z^{1e} dx + \int_0^R u_y^{1e} m u_y^{1e} dx} \tag{4.10}$$

The computed mode shapes are given in the following figure.
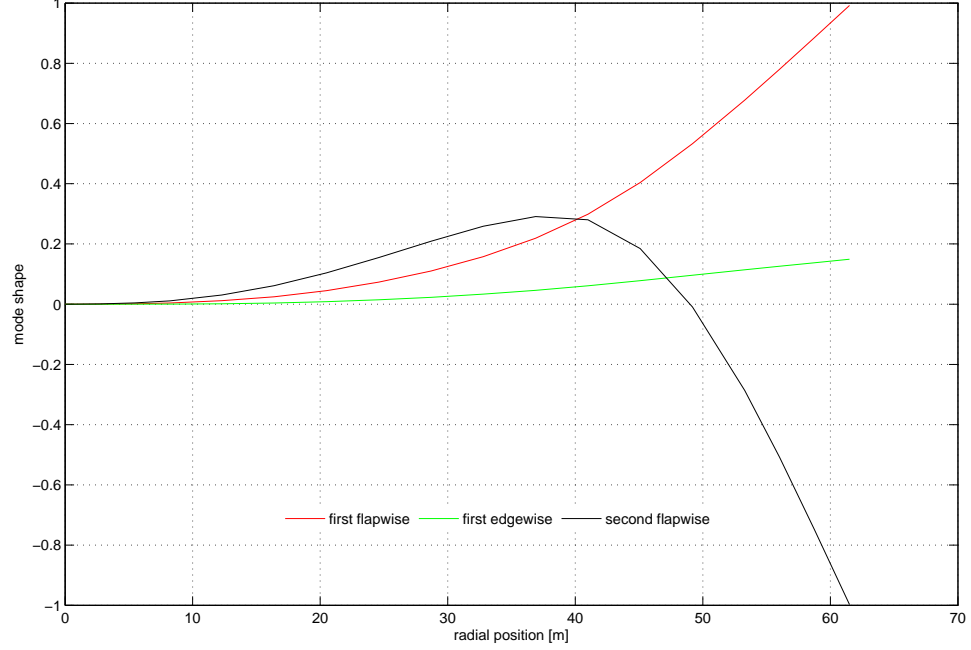
FIGURE 4.5: Blade mode shapes

These input data are used to generate an onshore wind turbine model. The unsteady BEM derived in the previous chapter is implemented for unsteady aerodynamic loads. The mean rotor thrust from the present implementation (877 kN) is comparable with that of literature (800 kN), Jonkman et al. (2009) and Joensen et al. (2007).

4.1.2 Platform model

The floater is modeled using the data given in Joensen et al. (2007), which has three degrees of freedom, viz. surge, heave and pitch in plane motion. The tendons are assumed to be linear elastic with negligible bending stiffness. As the tendon mass is small compared to the mass of the floater and wind turbine, the inertia and buoyancy forces from the tendons are further neglected in the equations of motion.

The static stability of the platform is illustrated in Figure 4.6. From the figure, to balance the excess buoyancy, a pretension T_0 is applied. The pretension is equally distributed to both of the tendons with a magnitude equal to $\frac{T_0}{2}$. At static equilibrium, x coordinates of centres of buoyancy, x_b, and gravity, x_G, are at zero position, as both buoyancy and gravity forces are assumed to be acting along the centre line of the tower, which coincides with the reference point.
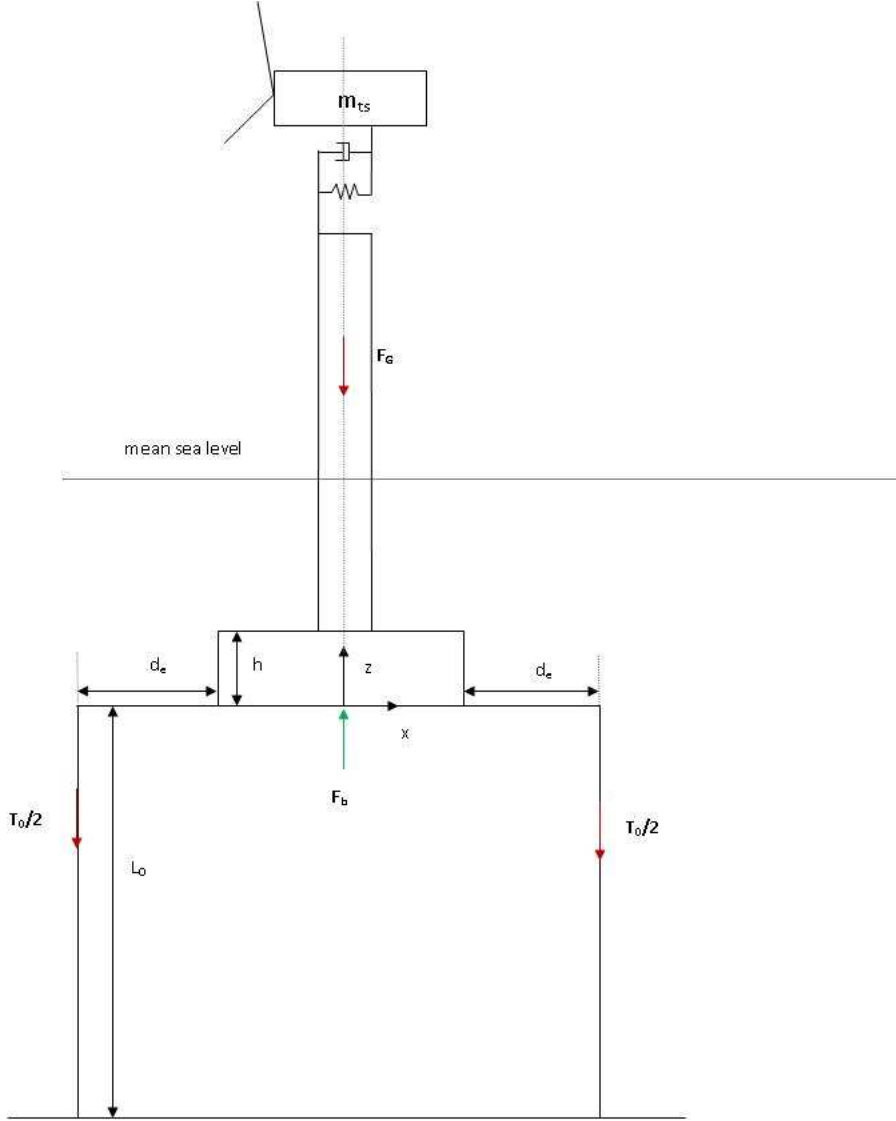
FIGURE 4.6: 2D - Static stability

Hence, the static stability of the complete system can be written as follows.

$$T_0 = F_b - F_G \tag{4.11}$$

where F_b is the total buoyancy force and F_G is the total gravity force, which are expressed in the following equations.

$$F_b = F_{b,f} + F_{b,t} = \frac{\pi}{4} D_f^2 h \rho g + \frac{\pi}{4} D_t^2 h_t \rho g \tag{4.12}$$

$$F_G = F_{G,f} + F_{G,t} = m_f g + m_t g + m_n g \tag{4.13}$$

where the quantities with subscripts f and t are contributions from floater and turbine, h is the floater height, h_t is the tower submergence, ρ is the sea water density, m_f, m_t and m_n

are mass of floater, tower and nacelle respectively. The diameters are represented using the letter D.

The dynamic stability of the platform in plane motion is described in Figure 4.7. The figure shows both un-displaced and displaced configurations. The displaced configuration is an exaggerated figure when the platform is subjected to a combined displacement of surge, η_{1f}, heave, η_3, and pitch, η_5.
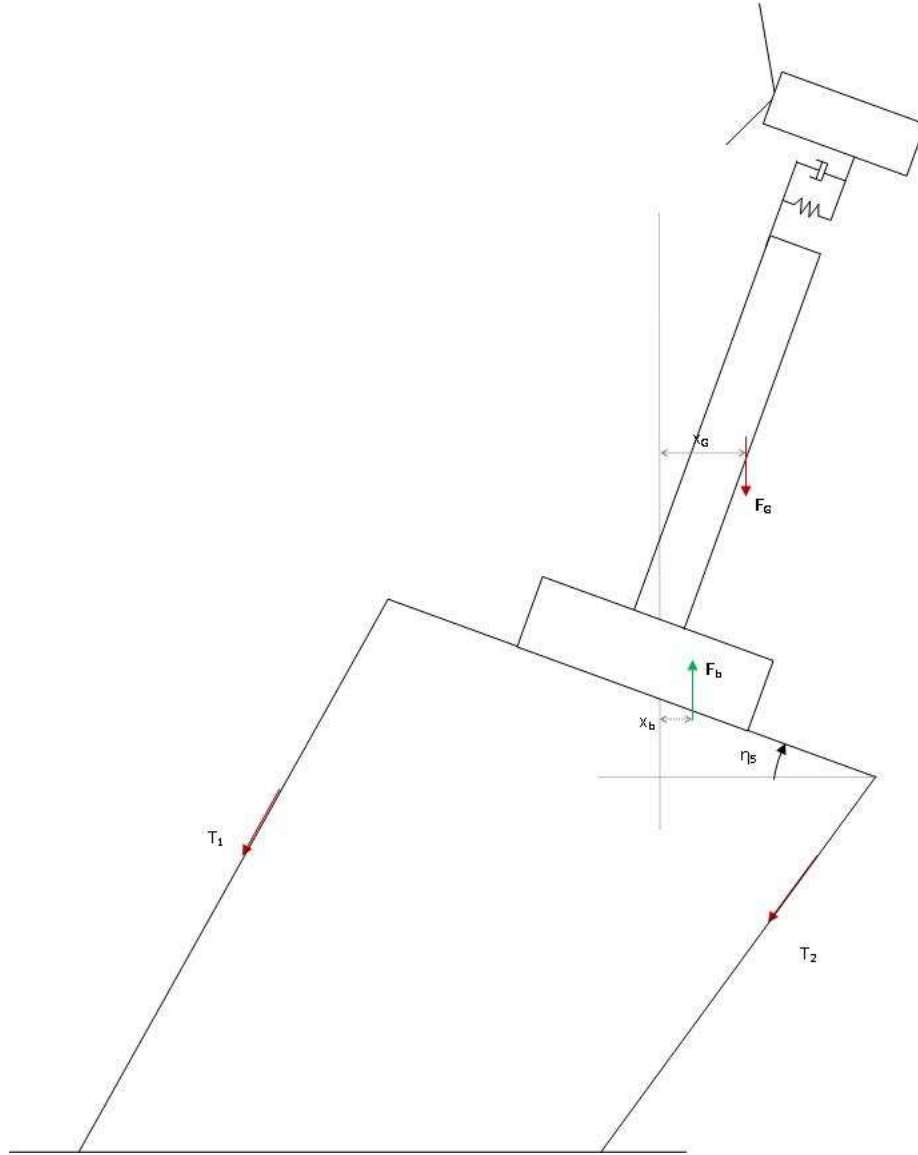
FIGURE 4.7: 2D - Dynamic stability

While the platform is subjected to pitch, the buoyancy and gravity positions change according to the following equations.

$$x_b = \frac{F_{b,f}x_{b,f} + F_{b,t}x_{b,t}}{F_b}$$

$$= \left(\frac{F_{b,f}0.5h + F_{b,t}\left(h + 0.5h_t + \left(\frac{D_t^2\left(2+\tan^2\eta_5\right)}{32h_t} \right) \right)}{F_b} \right) \sin\eta_5 \tag{4.14}$$

$$x_G = \frac{F_{G,f}x_{G,f} + F_{G,t}x_{G,t}}{F_G} = \left(\frac{F_{G,f}0.5h + F_{G,t}\left(H_t + 0.5h \right)}{F_G} \right) \sin\eta_5 \tag{4.15}$$

where H_t is the turbine hub height and other parameters are the same as explained earlier. As the tendons are extensible, a change in platform position causes a change in instantaneous tendon lengths and hence the instantaneous tensions of the tendons, as shown in Figure 4.7. Using the geometry, the instantaneous lengths, L_1 and L_2, are expressed in the following equations.

$$L_1 = \sqrt{\left(L_0 + \eta_3 + \tilde{d}\sin\eta_5 \right)^2 + \left(\eta_{1f} + \tilde{d}\left(1 - \cos\eta_5 \right) \right)^2} \tag{4.16}$$

$$L_2 = \sqrt{\left(L_0 + \eta_3 - \tilde{d}\sin\eta_5 \right)^2 + \left(\eta_{1f} - \tilde{d}\left(1 - \cos\eta_5 \right) \right)^2} \tag{4.17}$$

where L_0 is the initial length of the tendons, $\tilde{d} = 0.707\left(\frac{D_f}{2} + d_e \right)$ and d_e is the spoke length.

The change in tendon lengths, ΔL_1 and ΔL_2, are computed as a difference between the final and initial lengths. Hence, the instantaneous tensions, T_1 and T_2, of the tendons are computed as given in the following equations.

$$T_1 = \frac{T_0}{2} + \left(\frac{A_{tend}E_{tend}}{L_0} \right)\Delta L_1 \tag{4.18}$$

$$T_2 = \frac{T_0}{2} + \left(\frac{A_{tend}E_{tend}}{L_0} \right)\Delta L_2 \tag{4.19}$$

where the area of cross-section of tendon, $A_{tend} = \frac{\pi}{4}d_{tend}^2$, d_{tend} being the diameter of a tendon and the Young's modulus of tendon is, $E_{tend} = 2.1E11\ N/m^2$, assuming the material as steel. While the tendon diameter is 75.6 mm in the real configuration, in 2D to have the same tendon stiffness, the two dimensional tendon diameter is chosen as 107 mm.

4.1.3   Semi-coupling method

In principle, the platform and wind turbine models need to be combined along with aerodynamic and hydrodynamic loads and each of the models interact continuously. Formulation of aerodynamic and hydrodynamic loads are described in the previous chapters. As a first step, a simplified coupling of the aerodynamics, hydrodynamics and the platform dynamics is carried out. The time varying rotor thrust for a configuration with clamped tower base is obtained in section 4.1.1, is used for the semi-coupling. Next, the forces at the tower base are applied within the dynamic model for the platform, wherein the hydrodynamic forces are also external loads. The hydrodynamic loads interact with the platform dynamics instantaneously. The platform dynamics, including the rotor thrust and hydrodynamic loads, is modeled using the following equations of motion using Newton's second law.

The equation of motion in the surge direction is written as follows.

$$m_1\ddot{\eta}_{1f} = F_1 + k_t\eta_{1t} + c_t\dot{\eta}_{1t} - T_1\left(\frac{\eta_{1f} + \tilde{d}\left(1 - \cos\eta_5\right)}{L_1}\right) - T_2\left(\frac{\eta_{1f} - \tilde{d}\left(1 - \cos\eta_5\right)}{L_2}\right) \quad (4.20)$$

whereas in the heave direction, it is given by,

$$m_3\ddot{\eta}_3 = F_3 + F_b - F_G - \rho g\frac{\pi}{4}D_t^2\eta_3 - T_1\left(\frac{L_0 + \eta_3 + \tilde{d}\sin\eta_5}{L_1}\right) - T_2\left(\frac{L_0 + \eta_3 - \tilde{d}\sin\eta_5}{L_2}\right) \quad (4.21)$$

and in the pitch direction the equation of motion becomes:

$$J_5\ddot{\eta}_5 = F_5 + F_G x_G - F_b x_b + F_w\left(H_t + h\right)\cos\eta_5 + T_2\left(\frac{L_0 + \eta_3 - \tilde{d}\sin\eta_5}{L_2}\right)\tilde{d}\cos\eta_5$$

$$+ T_2\left(\frac{\eta_{1f} - \tilde{d}\left(1 - \cos\eta_5\right)}{L_2}\right)\tilde{d}\sin\eta_5 - T_1\left(\frac{L_0 + \eta_3 + \tilde{d}\sin\eta_5}{L_1}\right)\tilde{d}\cos\eta_5 \quad (4.22)$$

$$- T_1\left(\frac{\eta_{1f} + \tilde{d}\left(1 - \cos\eta_5\right)}{L_1}\right)\tilde{d}\sin\eta_5$$

while the relative deflection of the tower top is governed by the following equation.

$$m_{ts}\ddot{\eta}_{1t} = F_w - k_t\eta_{1t} - c_t\dot{\eta}_{1t} - m_{ts}\ddot{\eta}_{1f} \quad (4.23)$$

where η_{1t} is the longitudinal motion of the tower top, $\dot{()}$ and $\ddot{()}$ represent first and second derivatives of the variable with respect to time respectively. Further in the equations, F_w is the rotor thrust from the wind. The wave excitation forces F_1 (surge), F_3 (heave) and F_5 (pitch moment) are given in section 3.6 of Chapter 3.

The surge mass, m_1, heave mass, m_3 and mass moment of inertia in pitch direction, J_5, are the sum of structural mass and added mass in the corresponding directions. Equivalent tower top mass, $m_{ts} = m_n + 0.5m_t$, where m_n is nacelle mass and m_t is the tower mass. Tower stiffness and structural damping are represented through the spring stiffness coefficient k_t and damping coefficient c_t.

Hence, a response of the platform from simultaneous wind and wave loads is obtained, while the influence from the wave-induced rotor motion on the aerodynamic loads is missing.

4.1.4 Natural frequency analysis

Analytical expressions for surge, heave and pitch natural frequencies are given in the following equations.

$$\left(f_n\right)_{surge} = \frac{1}{2\pi}\sqrt{\frac{T_0}{L_0 m_1}} = 0.026 Hz \quad (4.24)$$

$$\left(f_n\right)_{heave} = \frac{1}{2\pi}\sqrt{\frac{\frac{2A_{tend}E_{tend}}{L_0} + \frac{\pi}{4}\rho g D_t^2}{m_3}} = 0.34 Hz \quad (4.25)$$

$$(f_n)_{pitch}$$

$$= \frac{1}{2\pi} \sqrt{\frac{1}{J_5} \left(-\left(W_t \left(H_t + 0.5h\right) + 0.5W_f h\right) + F_{bt} \left(h + 0.5h_t + \frac{D_t^2}{16h_t}\right) + 0.5F_{bf}h + \frac{2A_{tend}E_{tend}}{L_0}\tilde{d}2 \right)}$$

$$= 0.143 Hz$$

$$(4.26)$$

where all the parameters are explained in the previous section.

The semi-coupled model is validated by carrying out free decay numerical tests for surge, heave and pitch degrees of freedom. The free decay tests are conducted to obtain natural frequencies and the frequency domain responses are shown in Figures 4.8 to 4.10. The results in the figures and that in the equations are agreeing very well for all of the frequencies. Hence, further load cases can be computed using the present model.
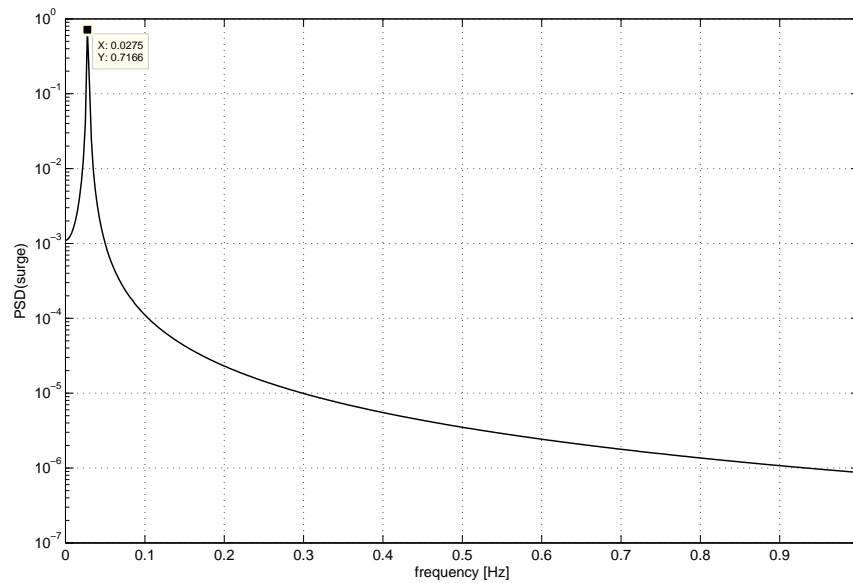
FIGURE 4.8: 2D - frequency response plot for surge
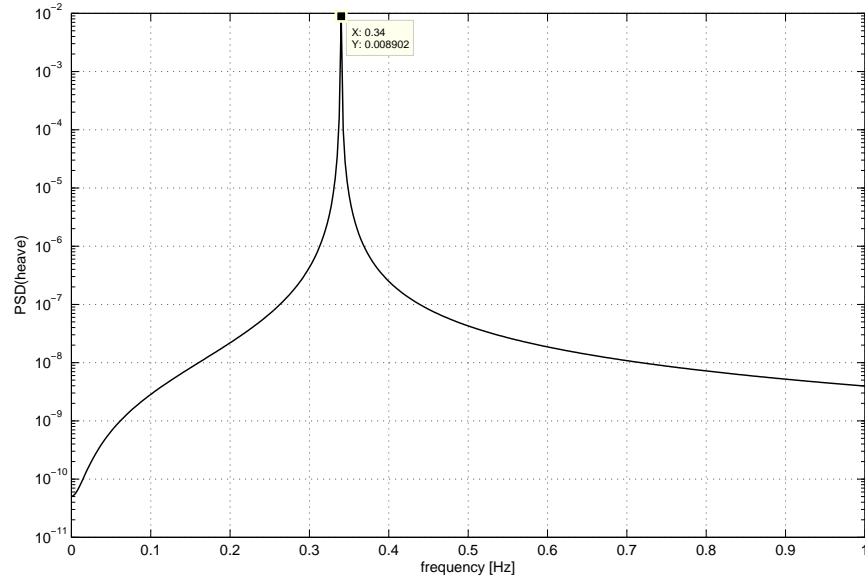
FIGURE 4.9: 2D - frequency response plot for heave
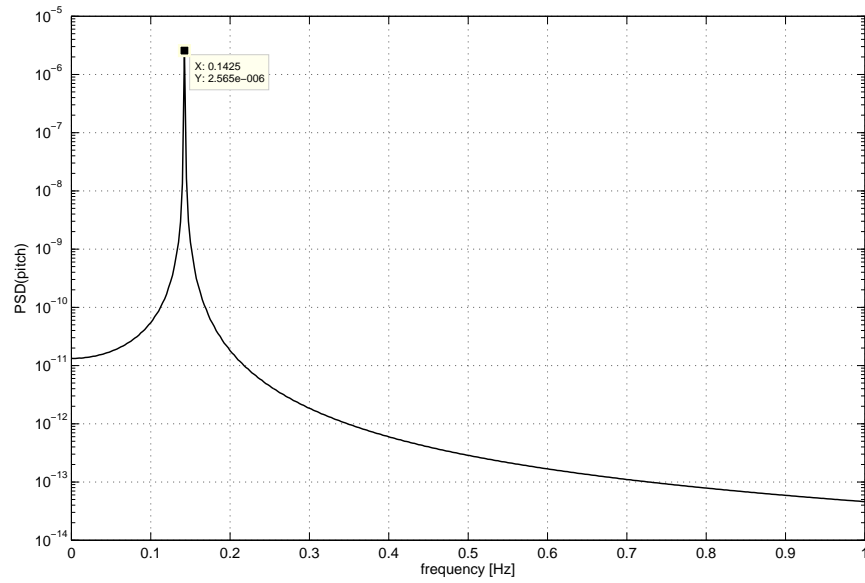
FIGURE 4.10: 2D - frequency response plot for pitch

4.1.5 Semi-coupled model - Load cases

As the semi-coupled model is achieved, the following four load cases are considered.

- LC1 - a simplified deterministic constant thrust force (877 kN), Joensen et al. (2007)

- LC2 - time series thrust from BEM with constant mean flow of 10 m/s wind speed,

- LC3 - time series thrust from BEM with a sheared wind flow of 10 m/s mean wind speed and

- LC4 - time series thrust from BEM with a sheared wind profile with mean 10 m/s wind speed and a spatially coherent turbulence on top of it.

The turbulent wind signals were produced from a wind spectrum of the Mann model, Mann (1994). The time series and frequency domain wind spectrum for spatially coherent turbulence are shown in Figure 4.11. In the figure, the frequency domain y-axis is chosen as semi-log axis for the quantity $fS(f)$. In all of the load cases, the rotor thrust is ramped to the real value within a time span of 50 s, to avoid unrealistic initial transient responses.
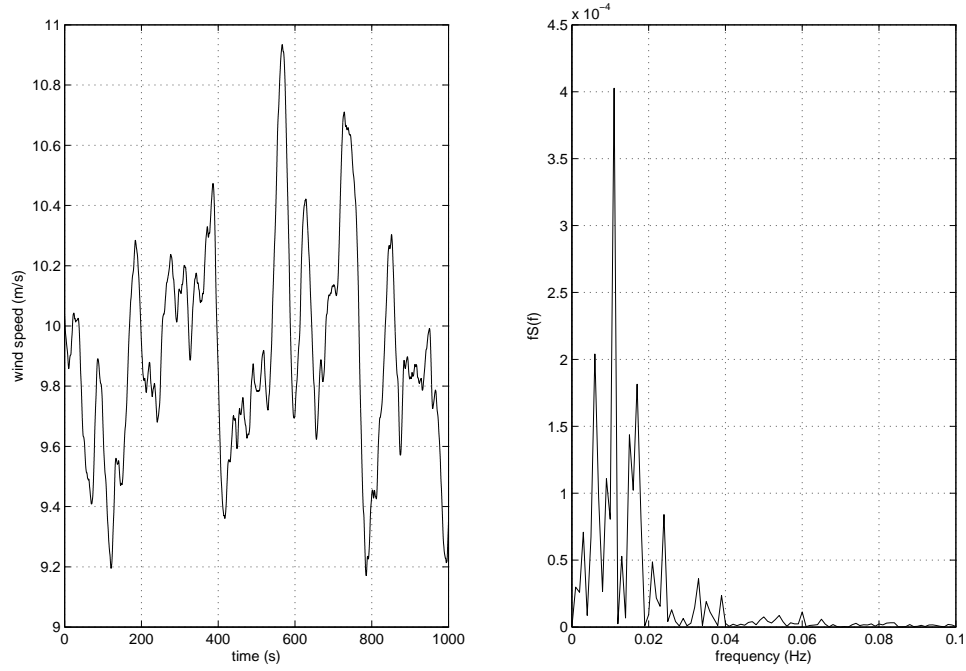
FIGURE 4.11: Wind input for Load Case 4

The equations of motion are solved using MATLAB's built in function *ode*15*s*, which is an implicit solver with adaptive time stepping. Because the system to be solved is stiff, the *ode*15*s* solver is preferred to *ode*45.

4.1.6   Semi-coupled model - Results and discussion

Responses are obtained for all the four load cases and are explained as follows.

The time and frequency domain response plots for irregular wave forcing for the four different cases of aerodynamic loading are shown in Figures 4.12, 4.13, 4.14 and 4.15 respectively. From 1000 s time series computation, 200 s steady state results are shown and for the frequency response, the structural natural frequencies are indicated in the plots.
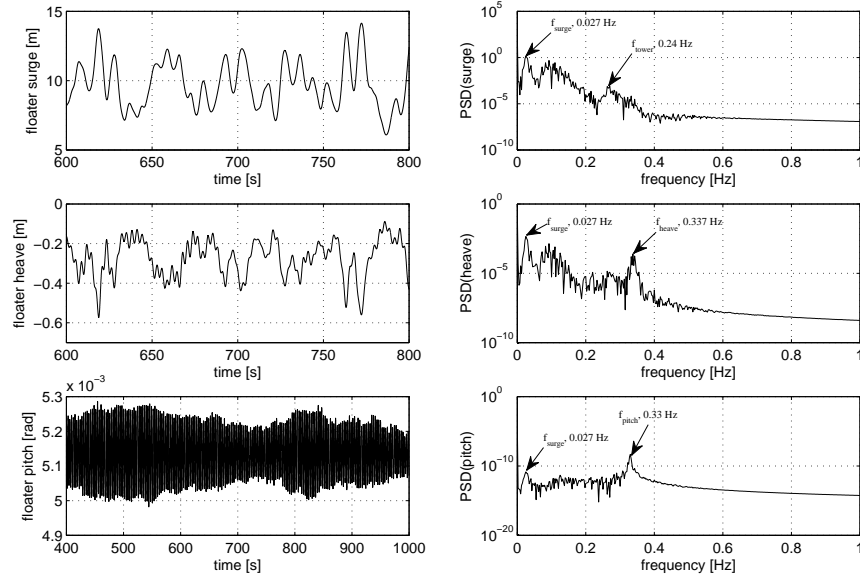
FIGURE 4.12: 2D semi-coupled responses - Load Case 1
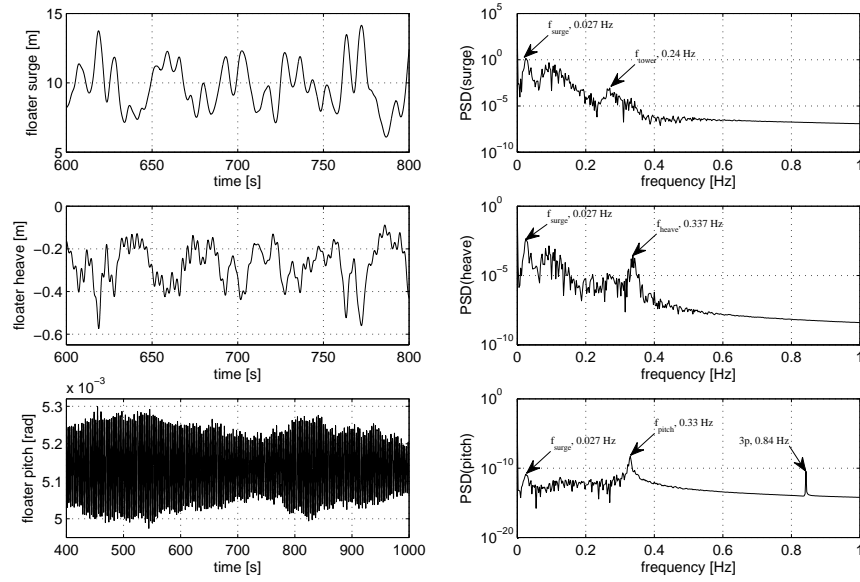
FIGURE 4.13: 2D semi-coupled responses - Load Case 2

Surge response (η_{1f})

The time series results show a positive mean surge response, which is expected because of the presence of rotor thrust. The surge response is very similar for the first and second load cases (Figures 4.12 and 4.13). Constant thrust of Load Case 1 is chosen as the same mean thrust of Load Case 2 (877 kN), which give rise to the similar responses. The mean surge
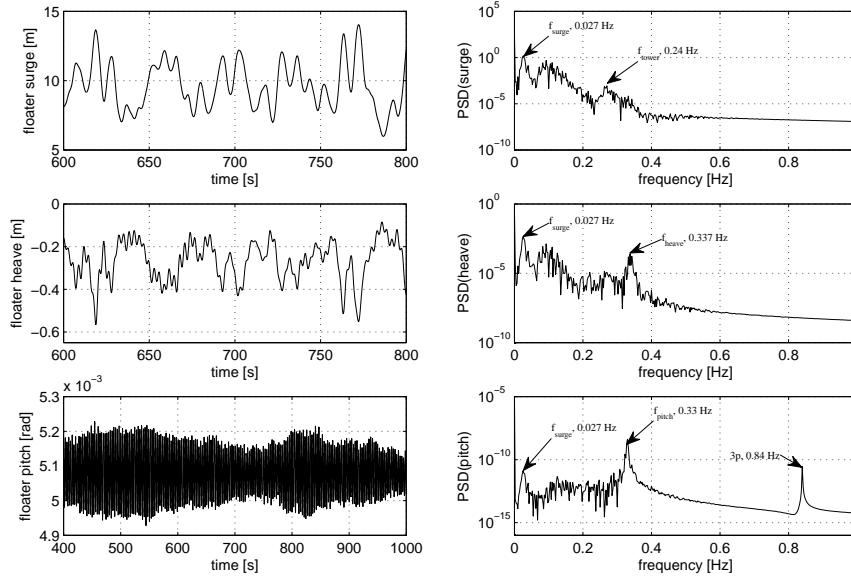
FIGURE 4.14: 2D semi-coupled responses - Load Case 3
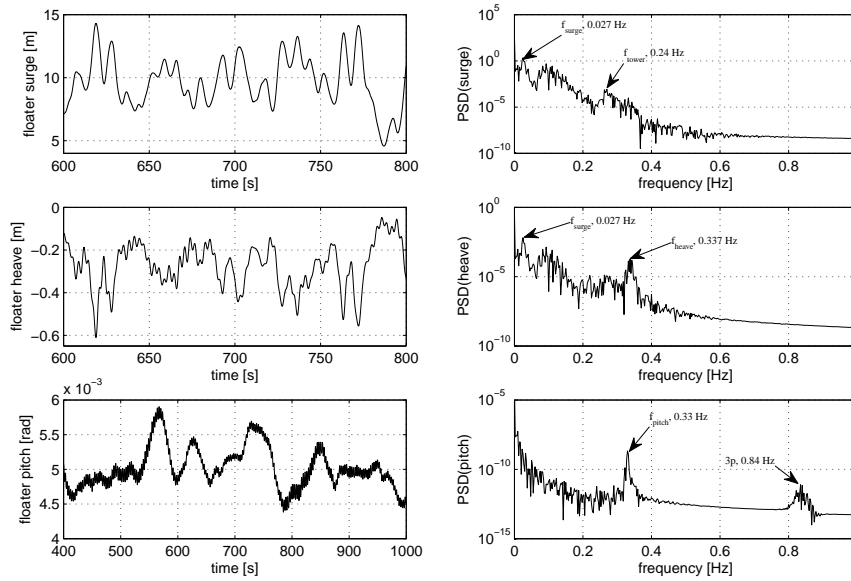
FIGURE 4.15: 2D semi-coupled responses - Load Case 4

response for the third Load Case is slightly lesser than that of the first and second cases. The reason for the smaller response is the reduced mean thrust at the lower part of the rotor, which is due to the wind shear. In the case of turbulent wind, the surge response is similar to that of Load Case 3 apart from a low frequency component associated with the low frequency part of the turbulent wind spectrum.

The predominant peak is at the peak wave frequency (0.1 Hz) and peaks corresponding to surge (0.027 Hz) and tower natural frequencies (0.24 Hz) are also seen.

Heave response (η_3)

The time series shows a negative mean, which is expected because of the set-down effect of the system. The predominant peak is at the peak wave frequency (0.1 Hz) and other peaks corresponding to surge (0.027 Hz), heave (0.34 Hz) and tower natural frequencies (0.24 Hz) are also seen. Presence of the surge frequency is a consequence of surge-heave coupling through set-down effect. Since the presence of rotor thrust moves the platform to a distance corresponding to a mean surge response and hence the platform is subjected to oscillatory motion around this mean value, the platform does not cross the mean equilibrium position. This condition leads to the excitation at coupled surge frequency, instead of a peak at the double surge frequency.

Pitch response (η_5)

The pitch response has a positive mean, which is due to the presence of rotor thrust. The mean pitch (0.3 degrees) and fluctuation are very small, which may be caused by using a longer spokes instead of the right dimension. When a real configuration is simplified to 2D, the fairlead position should have been at $\tilde{d} = 0.707 \left(\frac{D_f}{2} + d_e \right)$ instead of $\tilde{d} = \left(\frac{D_f}{2} + d_e \right)$. While the mismatch is only with numerical implementation, the right dimensions are shown in the derivation of equations of motion. However, this mistake in implementation re-affirms the understanding that longer spokes stabilize the rotational displacements. Using the longer spokes enhances the natural frequency in the pitch mode. As a result, the predominant frequency for all the load cases are found to be at around 0.33 Hz, which is the enhanced pitch frequency. In real, the pitch frequency should have been around 0.14 Hz, as given in the natural frequency equation (4.26). Having a pitch frequency at 0.33 Hz poses another problem because the pitch response has a coupling with heave response, which has a natural frequency around 0.34 Hz. The closely spaced two frequencies can lead to resonance conditions, which can be observed as a growing pitch response in the figures. In addition, the pitch response grows over time, dies out after some time and again grows with a time interval, corresponding to the difference in these frequencies. In order to show the complete pitch response, the x-axis for the time domain pitch response is chosen from 400 s to 1000 s. The mistake in using wrong spoke dimensions is rectified in the subsequent computations.

In addition to the peak at 0.33 Hz, the frequency domain response has peaks at surge (0.027 Hz), peak wave and a peak corresponding to three times the rotor frequency (3p = 0.84 Hz), which is a consequence of the coupling between rotor and platform. However, the 3p excitation could not be seen for the first load case, which was also not expected because the rotor thrust is a constant value. In Load Case 4, the low frequency (0.01 Hz) wind forcing is seen to induce a low frequency pitch response and unlike other cases, a peak corresponding to surge natural frequency is not present. This may be because the turbulence effect dominates as compared to the surge.

The semi-coupled model responses provide motivation for extending the model to a fully-coupled model, which is explained in the next section.

4.2   Fully coupled model

Based on the understanding of the semi-coupled responses, the model is extended by formulating the platform and wind turbine degrees of freedom together and implementing a solver to obtain fully-coupled responses. The assumptions and number of degrees of free-

dom remain the same as used for semi-coupled model. The wind and wave loading are fully coupled in time domain through the structural degrees of freedom. Hereby, the rotor loads become part of the floater generalized forces and the floater motion, contributes to the relative velocity seen by the blade and hence the rotor loads, which will eventually affect the tower top and blade displacements. This will give rise to a coupled rotor-floater dynamics, when subjected to simultaneous wind and wave loads. The equations of motion are derived using the principle of virtual work and are given in the following equation.

$$[\mathbf{M}]\{\ddot{\mathbf{x}}\} + [\mathbf{C}]\{\dot{\mathbf{x}}\} + [\mathbf{K}]\{\mathbf{x}\} = \{\mathbf{F_g}\} \tag{4.27}$$

where $\mathbf{M}$, $\mathbf{C}$ and $\mathbf{K}$ are 14×14 mass, damping and stiffness matrices respectively, $\mathbf{x}$ is the field vector consisting of the 14 degrees of freedom and $\mathbf{F_g}$ is the generalized force vector. The damping matrix contains diagonal element corresponding to the tower longitudinal degree of freedom. A Rayleigh damping model with 2% structural damping for the tower is considered. For a detailed description on principle of virtual work applied to wind turbines, the reader may consult Chapter 12 of Hansen (2008).

The generalized force vector, mass, stiffness and damping matrices are derived as follows:

Generalized force vector:

Each element of the generalized force vector is derived by giving a virtual displacement in the corresponding degree of freedom by keeping all other degrees of freedom to locked condition and writing the virtual work done. Hereby, the generalized force vector is obtained as given below.

$$\mathbf{F_g} = \begin{Bmatrix} F_1 + F_w + F_{moor1} \\ F_3 + F_b - F_G + F_{moor3} \\ F_5 + F_w Z_n - F_b x_b + F_G x_G + F_{moor5} \\ F_w \\ M_{aero} - M_{gen} \\ F_{g6} \\ F_{g7} \\ F_{g8} \\ F_{g6} \\ F_{g7} \\ F_{g8} \\ F_{g6} \\ F_{g7} \\ F_{g8} \end{Bmatrix} \tag{4.28}$$

where F_1, F_3 and F_5 are the hydrodynamic surge, heave forces and pitch moment respectively and F_b, F_G, x_b and x_G are the buoyancy and gravity forces, x coordinate of centres of buoyancy and gravity and F_{moor1}, F_{moor3} and F_{moor5} represent the mooring or the restoring forces in surge, heave and pitch directions respectively. The vertical distance from the platform bottom to the hub centre can be written as, $Z_n = h + H_t$. The subscripts $g6$ to $g8$ represent the generalized quantities for the blade degrees of freedom viz. first flapwise, first edgewise and second flapwise, respectively.

The rotor thrust from the aerodynamic loads, F_w is computed using unsteady BEM and is written as:

$$F_w = \int_0^R \left(p_n^{B1} dr + p_n^{B2} dr + p_n^{B3} dr \right) \tag{4.29}$$

whereas the rotor torque, M_{aero}, can be written as:

$$M_{aero} = \int_0^R \left(p_t^{B1} r + p_t^{B2} r + p_t^{B3} r \right) dr \tag{4.30}$$

where p_n and p_t represent the normal and tangential forces at a blade section of length dr, placed at a radial position r. Superscripts $B1$ to $B3$ represent blade numbers 1 to 3 respectively.

Further, the generator torque, M_{gen}, follows different equations based on the control method adopted. In the below rated power region, the control method is speed control, wherein the rotor speed is varying while the blade pitch angles are kept constant. As the rotor speed varies, the generator speed also varies proportional to gearbox ratio and hence the generator torque varies based on a linear relation. Just below rated, the rotor speed follows a steep variation to reach rated speed and power and subsequently the power control method switches to pitch control thereby varying the blade pitch angles to obtain rated power. The generator torque steep variation is given in the below equation, wherein, the proportional constant, A_{gen}, is arbitrary.

$$M_{gen} = A_{gen} \left(\omega - \omega_{ref} \right) \tag{4.31}$$

When the rpm, ω, reaches the reference rpm, ω_{ref}, the rotor speeds up thereby forcing the generator to generate the rated power so that the pitch control is activated immediately to control the rotor acceleration. The reference rpm is chosen just below the rated rpm, which is a typical characteristic for each generator design. An example of generator torque characteristic is given in Figure 4.16.
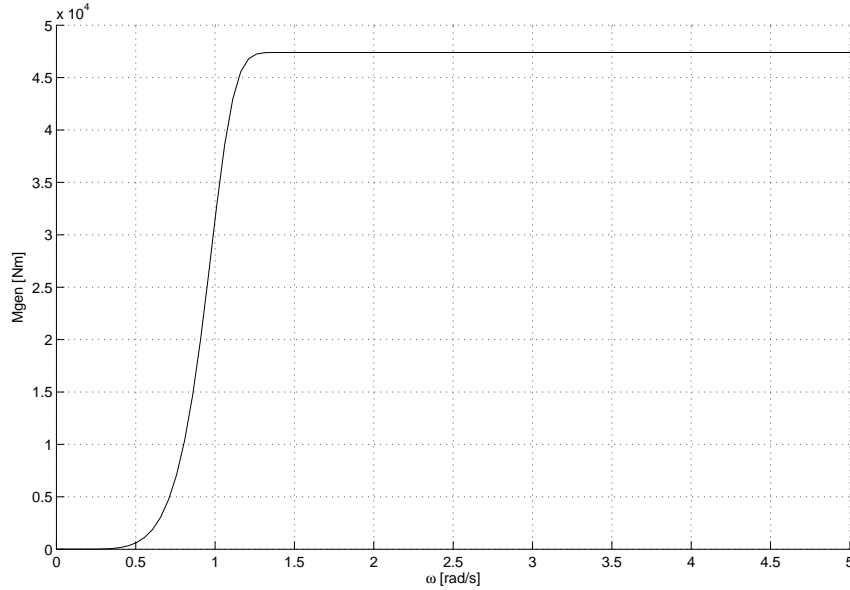
FIGURE 4.16: Generator torque variation

The generalized forces for the blade deflections are obtained as given in the following equations.

$$F_{g6} = \int_0^R \begin{pmatrix} 0 \\ p_t^{B1} \\ p_n^{B1} \end{pmatrix} \cdot \begin{pmatrix} 0 \\ \phi_{1,y}^{1f} \\ \phi_{1,z}^{1f} \end{pmatrix} dr$$

$$= \int_0^R \left(p_t^{B1} \left(\phi_{1f}^e \cos\theta_p + \phi_{1f}^f \sin\theta_p \right) + p_n^{B1} \left(-\phi_{1f}^e \sin\theta_p + \phi_{1f}^f \cos\theta_p \right) \right) dr$$

(4.32)

where $\phi_{1,y}^{1f}$ and $\phi_{1,z}^{1f}$ are the y and z components of the first mode shape of blade 1. If a blade pitch angle, θ_p, is present, the mode shapes derived based on the blade coordinate system shall be transformed to the rotor system and hence the transformation using the flapwise and edgewise components of first flapwise mode.

Similarly, generalized blade forces for first edge and second flapwise degrees of freedom are also derived as given below.

$$F_{g7} = \int_0^R \left(p_t^{B1} \left(\phi_{1e}^e \cos\theta_p + \phi_{1e}^f \sin\theta_p \right) + p_n^{B1} \left(-\phi_{1e}^e \sin\theta_p + \phi_{1e}^f \cos\theta_p \right) \right) dr \qquad (4.33)$$

$$F_{g8} = \int_0^R \left(p_t^{B1} \left(\phi_{2f}^e \cos\theta_p + \phi_{2f}^f \sin\theta_p \right) + p_n^{B1} \left(-\phi_{2f}^e \sin\theta_p + \phi_{2f}^f \cos\theta_p \right) \right) dr \qquad (4.34)$$

where F_{g6}, F_{g7} and F_{g8} represent the generalized forces for blade 1 in first flapwise, first edgewise and second flapwise degrees of freedom respectively. In the present computation, it is assumed that all the three blades are identical in all aspects of the structural and mass properties and hence the generalized forces derived for blade 1 is applicable for the other two blades as well. Thus, $F_{g6} = F_{g9} = F_{g12}$, $F_{g7} = F_{g10} = F_{g13}$ and $F_{g8} = F_{g11} = F_{g14}$. However, the normal and tangential forces in all the blades are not necessarily be equal since the platform is subjected to rotational displacement. This difference is not taken into account since the pitch displacement is assumed to be smaller. The superscript $B1$ represents blade 1 and the superscripts f and e represent flapwise and edgewise components of the mode shapes. Subscripts $1f$, $2f$ and $1e$ represent the first and second flapwise mode shapes and first edgewise mode shape respectively.

Generalized mass matrix:

The method for the derivation of mass matrix is briefly described. Mass elements for each of the columns are computed by first computing the inertia force corresponding to a unit acceleration in that degree of freedom, whereas all other accelerations are kept zero. Next, the virtual work done is computed by giving a virtual displacement to each of the degree of freedom and by taking the dot product of the inertia force and the virtual displacement. Each of the elements in the column under consideration is also computed following the same procedure. Hereby, the following mass matrix is obtained.

$$\mathbf{M_g} = \begin{pmatrix}
m_{1,1} & 0 & m_{1,3} & m_{ts} & 0 & a_{6,1} & a_{7,1} & a_{8,1} & a_{6,1} & a_{7,1} & a_{8,1} & a_{6,1} & a_{7,1} & a_{8,1} \\
0 & m_{2,2} & 0 & 0 & 0 & 0 & 0 & 0 & 0 & 0 & 0 & 0 & 0 & 0 \\
m_{3,1} & 0 & m_{3,3} & m_{3,4} & 0 & 0 & 0 & 0 & 0 & 0 & 0 & 0 & 0 & 0 \\
m_{ts} & 0 & m_{4,3} & m_{ts} & 0 & a_{6,1} & a_{7,1} & a_{8,1} & a_{6,1} & a_{7,1} & a_{8,1} & a_{6,1} & a_{7,1} & a_{8,1} \\
0 & 0 & 0 & 0 & J_z & a_{6,5} & a_{7,5} & a_{8,5} & a_{6,5} & a_{7,5} & a_{8,5} & a_{6,5} & a_{7,5} & a_{8,5} \\
a_{6,1} & 0 & 0 & a_{6,1} & a_{6,5} & m_6 & 0 & 0 & 0 & 0 & 0 & 0 & 0 & 0 \\
a_{7,1} & 0 & 0 & a_{7,1} & a_{7,5} & 0 & m_7 & 0 & 0 & 0 & 0 & 0 & 0 & 0 \\
a_{8,1} & 0 & 0 & a_{8,1} & a_{8,5} & 0 & 0 & m_8 & 0 & 0 & 0 & 0 & 0 & 0 \\
a_{6,1} & 0 & 0 & a_{6,1} & a_{6,5} & 0 & 0 & 0 & m_6 & 0 & 0 & 0 & 0 & 0 \\
a_{7,1} & 0 & 0 & a_{7,1} & a_{7,5} & 0 & 0 & 0 & 0 & m_7 & 0 & 0 & 0 & 0 \\
a_{8,1} & 0 & 0 & a_{8,1} & a_{8,5} & 0 & 0 & 0 & 0 & 0 & m_8 & 0 & 0 & 0 \\
a_{6,1} & 0 & 0 & a_{6,1} & a_{6,5} & 0 & 0 & 0 & 0 & 0 & 0 & m_6 & 0 & 0 \\
a_{7,1} & 0 & 0 & a_{7,1} & a_{7,5} & 0 & 0 & 0 & 0 & 0 & 0 & 0 & m_7 & 0 \\
a_{8,1} & 0 & 0 & a_{8,1} & a_{8,5} & 0 & 0 & 0 & 0 & 0 & 0 & 0 & 0 & m_8
\end{pmatrix} \tag{4.35}$$

The mass matrix is symmetric, the diagonal elements being the generalized masses for the corresponding degrees of freedom. First square section of 4×4 matrix corresponds to the platform and tower degrees of freedom. It is assumed that the blade cross-coupling terms are negligible for platform heave and pitch and hence these terms are not considered. However, the blade cross-coupling terms with platform surge, tower top displacement and rotor azimuthal degrees of freedom are considered, which is shown using the terms $a_{6,1}$ to $a_{8,1}$ and $a_{6,5}$ to $a_{8,5}$. From the mass matrix, it is clear that the platform surge motion induces a platform pitch and tower top surge.

The generalized mass elements are given below.

$$m_{1,1} = m_1 + m_{ts} \tag{4.36}$$

$$m_{2,2} = m_3 + m_{ts} \tag{4.37}$$

$$m_{3,3} = I_G + m_{ts}Z_n^2 \tag{4.38}$$

$$m_{1,3} = m_{3,1} = m_{3,4} = m_{4,3} = m_{ts}Z_n \tag{4.39}$$

where m_1, m_3 are the surge and heave mass, including the corresponding added mass terms and I_G is the pitch mass moment of inertia about the centre of gravity including the pitch added mass. The diagonal generalized mass elements, GM_1, GM_2 and GM_3, corresponding to each of the blade mode shapes are given below.

$$m_6 = GM_1 = \int_0^R \left(m \left(\left(\phi_{1f}^f \right)^2 + \left(\phi_{1f}^e \right)^2 \right) \right) dr \tag{4.40}$$

$$m_7 = GM_2 = \int_0^R \left(m \left(\left(\phi_{1e}^f \right)^2 + \left(\phi_{1e}^e \right)^2 \right) \right) dr \tag{4.41}$$

$$m_8 = GM_3 = \int_0^R \left(m \left(\left(\phi_{2f}^f \right)^2 + \left(\phi_{2f}^e \right)^2 \right) \right) dr \tag{4.42}$$

As assumed for the generalized forces, all the blades have the same generalized masses, which is shown in the mass matrix. The off-diagonal coupling elements corresponding to all

the modes for blade 1 are given below. The other two blades also have the same inertia-coupling coefficients as the blades are assumed to have the same properties and for small pitch approximation. This leads to $a_{6,1} = a_{9,1} = a_{12,1}$, $a_{7,1} = a_{10,1} = a_{13,1}$ and $a_{8,1} = a_{11,1} = a_{14,1}$. Hence, the cross-coupling terms for the surge displacement are given in the following equations.

$$a_{6,1} = \int_0^R \left(p_x.0 + p_y.\phi_{1,y}^{1f} + p_z.\phi_{1,z}^{1f} \right) dx$$

$$= \int_0^R \left(p_y \left(\phi_{1,e}^{1f} \cos\theta_p + \phi_{1,f}^{1f} \sin\theta_p \right) + p_z \left(-\phi_{1,e}^{1f} \sin\theta_p + \phi_{1,f}^{1f} \cos\theta_p \right) \right) dr \tag{4.43}$$

$$a_{7,1} = \int_0^R \left(p_x.0 + p_y.\phi_{1,y}^{1e} + p_z.\phi_{1,z}^{1e} \right) dx$$

$$= \int_0^R \left(p_y \left(\phi_{1,e}^{1e} \cos\theta_p + \phi_{1,f}^{1e} \sin\theta_p \right) + p_z \left(-\phi_{1,e}^{1e} \sin\theta_p + \phi_{1,f}^{1e} \cos\theta_p \right) \right) dr \tag{4.44}$$

$$a_{8,1} = \int_0^R \left(p_x.0 + p_y.\phi_{1,y}^{2f} + p_z.\phi_{1,z}^{2f} \right) dx$$

$$= \int_0^R \left(p_y \left(\phi_{1,e}^{2f} \cos\theta_p + \phi_{1,f}^{2f} \sin\theta_p \right) + p_z \left(-\phi_{1,e}^{2f} \sin\theta_p + \phi_{1,f}^{2f} \cos\theta_p \right) \right) dr \tag{4.45}$$

where the inertia forces, $\begin{pmatrix} p_x \\ p_y \\ p_z \end{pmatrix}_6 = m[T]_{26} \begin{pmatrix} 1 \\ 0 \\ 0 \end{pmatrix}$

wherein m is the mass per unit length of blade along the length, $[T]_{26}$ is the transformation matrix from system 2 to system 6 and 1 in the vector corresponds to a unit acceleration in the surge degree of freedom. In all the cross-coupling terms, p_x is multiplied with 0 because the blade extensional degree of freedom (axial displacement) is not considered.

Similarly, the cross-coupling terms for the azimuthal rotor position are given below.

$$a_{6,5} = \int_0^R \left(p_x.0 + p_y.\phi_{1,y}^{1f} + p_z.\phi_{1,z}^{1f} \right) dx$$

$$= \int_0^R \left(p_y \left(\phi_{1,e}^{1f} \cos\theta_p + \phi_{1,f}^{1f} \sin\theta_p \right) + p_z \left(-\phi_{1,e}^{1f} \sin\theta_p + \phi_{1,f}^{1f} \cos\theta_p \right) \right) dr \tag{4.46}$$

$$a_{7,5} = \int_0^R \left(p_x.0 + p_y.\phi_{1,y}^{1e} + p_z.\phi_{1,z}^{1e} \right) dx$$

$$= \int_0^R \left(p_y \left(\phi_{1,e}^{1e} \cos\theta_p + \phi_{1,f}^{1e} \sin\theta_p \right) + p_z \left(-\phi_{1,e}^{1e} \sin\theta_p + \phi_{1,f}^{1e} \cos\theta_p \right) \right) dr \tag{4.47}$$

$$a_{8,5} = \int_0^R \left(p_x.0 + p_y.\phi_{1,y}^{2f} + p_z.\phi_{1,z}^{2f} \right) dx$$

$$= \int_0^R \left(p_y \left(\phi_{1,e}^{2f} \cos\theta_p + \phi_{1,f}^{2f} \sin\theta_p \right) + p_z \left(-\phi_{1,e}^{2f} \sin\theta_p + \phi_{1,f}^{2f} \cos\theta_p \right) \right) dr \tag{4.48}$$

where the inertia force for the coupling term $a_{6,5}$ is $\begin{pmatrix} p_x \\ p_y \\ p_z \end{pmatrix}_6 = m[T]_{56} \begin{pmatrix} 0 \\ 0 \\ 1 \end{pmatrix} \times \begin{pmatrix} r \\ \phi_{1,y}^{1f} \\ \phi_{1,z}^{1f} \end{pmatrix}$.

The inertia force for coupling-terms $a_{7,5}$ and $a_{8,5}$ vary from $a_{6,5}$ since the y and z coordinates in the first edgewise and second flapwise degrees of freedom are different. Hence the corresponding coordinates for the mode shapes are used. The rotational acceleration vector about z axis needs to be transformed to the blade coordinate system using the transformation matrix $[T]_{56}$.

Since the inertia-coupling between the heave and pitch degrees of freedom with blade degrees of freedom are not considered, these coupling terms, M(6,2) to M(14,2) and M(6,3) to M(14,3) are set to zero. The inertia coupling terms for the tower top displacement with blade degrees of freedom are exactly identical to those of the contributions from surge displacement. The inertia-coupling terms between the blade degrees of freedom are zero since the blades are assumed as independent to each other.

Generalized stiffness matrix:

Similar to the mass matrix, the stiffness matrix is computed column-wise. For the first column, the first step is to compute the spring force corresponding to a unit displacement in the first degree of freedom. While the system is subjected to this spring force, a virtual displacement is given to the first degree of freedom, in order to compute the virtual work done, which will give the first element of stiffness matrix in the first column. Similarly all the elements in the first column are computed by giving virtual displacements to the corresponding degrees of freedom. This way, all the columns of the stiffness matrix are computed. The only non-zero elements in the stiffness matrix correspond to the tower stiffness and the diagonal elements for the blade mode shapes, which are listed below.

$$K(4,4) = \omega_t^2 m_{4,4} \tag{4.49}$$

$$K(6,6) = K(9,9) = K(12,12) = GK_1 = \omega_{1f}^2 m_{6,6} \tag{4.50}$$

$$K(7,7) = K(10,10) = K(13,13) = GK_2 = \omega_{1e}^2 m_{7,7} \tag{4.51}$$

$$K(8,8) = K(11,11) = K(14,14) = GK_3 = \omega_{2f}^2 m_{8,8} \tag{4.52}$$

While ω_t is the tower longitudinal natural frequency, ω_{1f}, ω_{1e} and ω_{2f} are the first flapwise, first edgewise and second flapwise blade circular natural frequencies respectively. The blade natural frequencies are obtained from the eigen value analysis. The generalized stiffness coefficients for all the blades are the same because the blades are assumed to be identical.

Generalized damping matrix:

As described for the stiffness matrix, the damping matrix is also computed column-wise. For the first column, the first step is to compute the damping force corresponding to a unit velocity in the first degree of freedom. While the system is subjected to this force, a virtual displacement in given to the first degree of freedom, in order to compute the virtual work done, which will give the first element of damping matrix in the first column. Similarly, all the elements in the first column are computed by giving virtual displacements to the corresponding degrees of freedom. This way, all the columns of the damping matrix are computed. The only non-zero element in the damping matrix correspond to the tower longitudinal degree of freedom, which is given below.

$$C(4,4) = \omega_{1t} m_{4,4} \frac{\delta}{\pi} = 2\zeta m_{4,4} \omega_{1t} \tag{4.53}$$

where δ is the logarithmic decrement corresponding to tower longitudinal structural damping and ζ is the critical damping ratio for tower structural damping corresponding to a Rayleigh damping model. The structural damping contribution from the blades are not considered. However, the hydrodynamic damping contribution from quadratic drag is included in the hydrodynamic loads and aerodynamic damping contribution is included using a dynamic stall model in BEM. Since no other damping is being considered, all other damping matrix elements are set to zero.

The centre-point at the bottom side of the floater is chosen as reference point for solving the equations of motion. The coupled equations of motion are solved using the Runge-Kutta-Nystrom algorithm, see Hansen (2008). The solver uses a fixed time step, which is governed by the highest natural frequency of the system. For the present case, the highest natural frequency does not go beyond 2.5 Hz, which give rise to a time step of $dt = 1/(20 \times 2.5) = 0.02s$.

4.2.1   Comparison of responses

The responses computed using the semi-coupled model, as described in section 4.1, are used for comparison. In the present computation, the semi-coupled model uses the correct spoke dimension. A similar computation is carried out using the fully-coupled model and the responses are compared and are shown in Figure 4.17. In the figure, both comparisons in the time and frequency domain are shown. The response statistics are provided in Table 4.2 and the observations are discussed as follows.
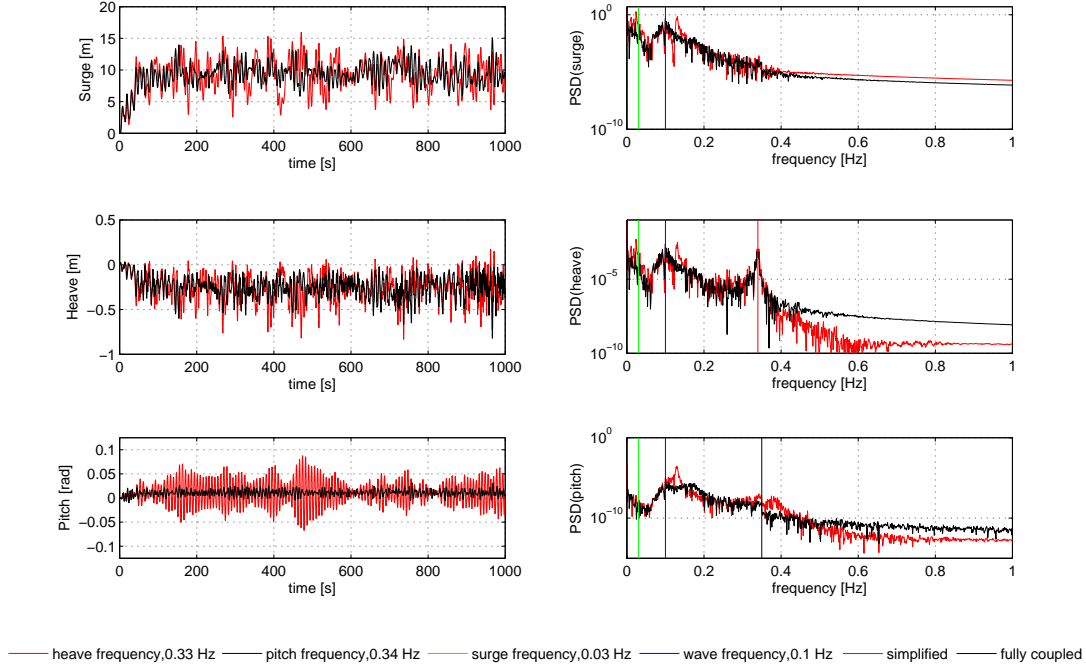
FIGURE 4.17: Comparison of semi and fully coupled responses

TABLE 4.2: 2D response statistics comparison

	Surge		Heave		Pitch	
	Semi-coupled (m)	Fully-coupled (m)	Semi-coupled (m)	Fully-coupled (m)	Semi-coupled (deg)	Fully-coupled (deg)
Min.	2.598	5.86	0.174	0.017	-3.86	-0.32
Max.	15.95	15.09	-0.831	-0.821	4.98	1.84
Mean	9.4	9.52	-0.27	-0.26	0.61	0.63
SD	2.44	1.55	0.15	0.11	1.46	0.35

Surge response (η_{1f})

The fully-coupled surge response is comparable with that of semi-coupled case. The comparison is more close with respect to the mean and maximum values. The fully-coupled standard deviation is about 36% lower than that of semi-coupled surge. However, the fully-coupled minimum value is about 55% higher than that of semi-coupled case. Looking at the difference in standard deviation, it is observed that the fully-coupled response has less fluctuation compared to that of semi-coupled response.

Predominant peaks are at the surge natural frequency and at the peak wave frequency. In addition, a small peak corresponding to the pitch frequency can also be seen only in the case of semi-coupled response. This peak in the fully-coupled response would have been damped out. The interesting part is that comparatively larger energy content is seen at surge natural frequency and near the peak wave frequency in the case of semi-coupled response. This might likely be due to larger damping in the fully-coupled model relative to that of the semi-coupled model. This is also true for higher frequencies. The higher damping can be attributed to the aerodynamic damping of the rotor, which was missing in the case of semi-coupled response.

Heave response (η_3)

The mean and maximum heave responses are comparable, however, the minimum fully-coupled response is about 90% lesser than that of semi-coupled heave and the fully-coupled standard deviation is about 27% lesser than that of semi-coupled case. Hence, similar to the surge response comparison, it is observed that the fully-coupled response has less fluctuation compared to that of simplified-coupling.

Predominant peaks are at the surge natural frequency, at the peak wave frequency and at the heave natural frequency. Here also, comparatively larger energy content is seen at surge and near the peak wave frequencies in the case of semi-coupled response. The reason for higher damping might be the same as explained for the surge response.

In addition, it is noticed that the difference in energy content is not seen at the heave natural frequency, which can be explained by the fact that the heave motion has no component perpendicular to the rotor plane. Hereby, no aerodynamic damping is induced for pure heave modes.

Pitch response (η_5)

The pitch response from fully-coupled computation has much smaller fluctuation compared to that of the semi-coupled response. However, the mean values of the responses remain comparable. Frequency responses are comparable, however with a difference in energy con-

tents at the predominant frequencies. The fully-coupled response has comparatively lesser energy content than that of the semi-coupled model. In the case of fully coupled response, the aerodynamic damping is present for the tower top motion, whereas this is not the case for the semi-coupled response. Aerodynamic damping takes out considerable energy content at the predominant frequencies, which may be the reason of smaller fluctuation of the pitch response.

4.2.2 Two-dimensional fully coupled load cases

Four load cases with same wind and wave conditions used for semi-coupled model are investigated. The Load Cases 1, 2 and 4 are identical to Load Cases 2, 3 and 4 of semi-coupled model. The load cases are listed below.

- Load Case 1 - no shear, no turbulence

- Load Case 2 - with shear, no turbulence

- Load Case 3 - no shear, with turbulence

- Load Case 4 - with shear, with turbulence

4.2.3 Fully-coupled model - Results and Discussion

Responses and loads are obtained for Load Case 1 to Load Case 4 and are shown in Figures 4.18 to 4.21. Each of the loads and responses are also shown as Power Spectral Densities (PSD) in the frequency domain including an identification of major eigen frequencies. All the responses are extracted with reference to the floater bottom point. The low frequency peak (0.01 Hz) in all the platform responses for Load Cases 3 and 4 is due to the turbulent wind excitation. Comparing the differences of responses for all the load cases leads to the following observations:

- Presence of wind shear reduces the mean response slightly due to the reduced mean thrust at the lower part of the rotor for a sheared wind profile leading to a smaller integrated force, as observed for the semi-coupled case.

- Presence of wind turbulence slightly increases the mean responses, due to the increase of mean thrust force associated with the addition of the fluctuating wind velocity component. As the instantaneous wind velocity, $V = \bar{V} + V'$, where $\bar{V}$ is the mean wind velocity and V' is the fluctuating velocity component due to turbulence. This was also observed in semi-coupled response.

- Presence of turbulence also slightly increases the fluctuation of responses. Though the difference is negligibly small, a higher turbulence may cause more difference. In addition, turbulence also induces low frequency (0.01 Hz) excitation in pitch response.

A comparison of the surge response from all the four load cases is shown in Figure 4.22. A positive mean surge is the consequence of rotor thrust. It is seen that, the surge response from all the load cases compares well implying that the shear and turbulence are of minor importance for the platform surge.

In the heave frequency response, the surge-heave coupling is noticed from the peak corresponding to the surge natural frequency as a consequence of set-down effect.

The pitch response is very small due to the geometric constraint of the tendons, which only allows pitch through elastic extension of the tendons. The positive mean pitch is due to the pitch moment from the rotor thrust.
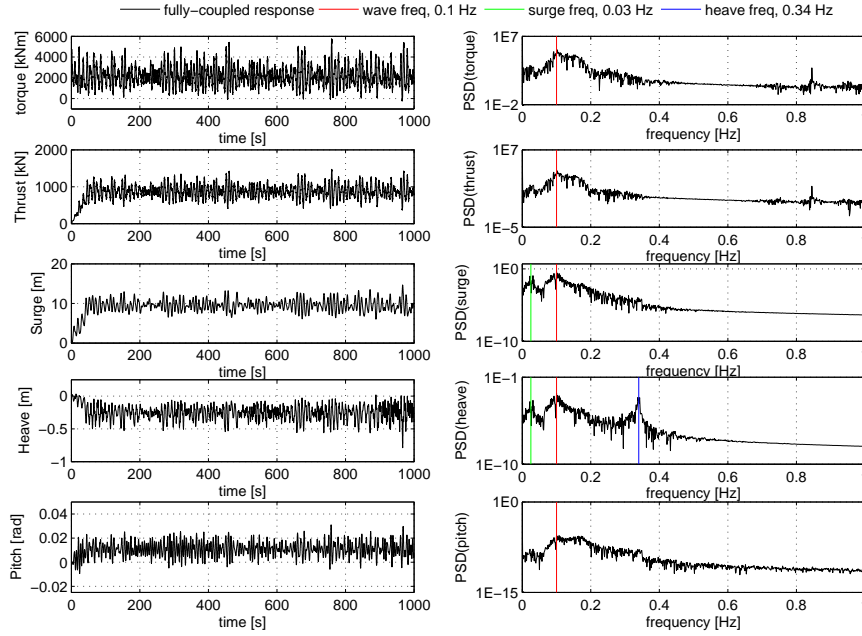
FIGURE 4.18: 2D fully coupled loads and responses - Load Case 1
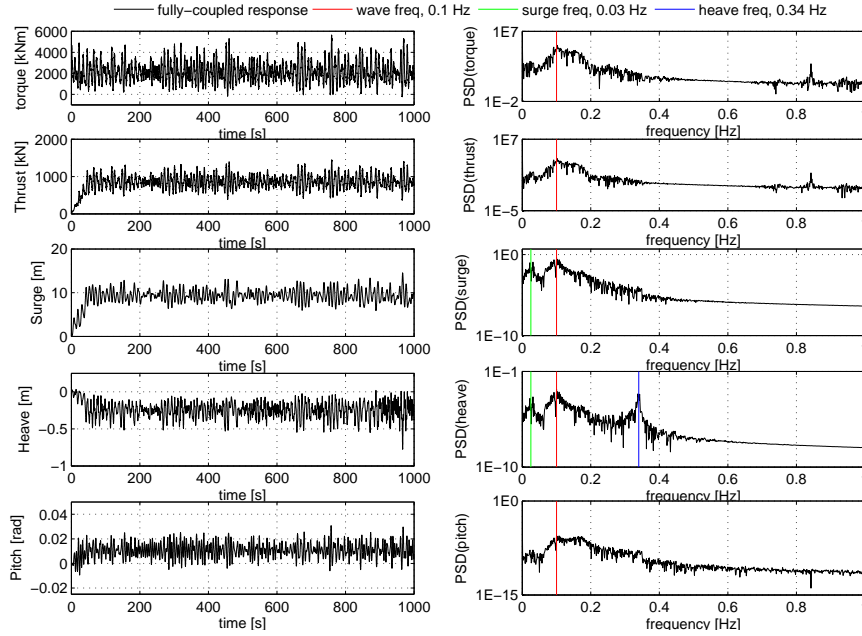
FIGURE 4.19: 2D fully coupled loads and responses - Load Case 2

The mean of the coupled rotor thrust is comparable with the mean thrust value of the wind turbine, 800 kN, given in Joensen et al. (2007). The rotor loads frequency responses have a minor energy peak around 0.84 Hz, corresponding to three times the rotor frequency (3p) of 0.28 Hz (1p). From the frequency plots, a predominant peak at the wave frequency is seen in the rotor loads, which shows a strong coupling with the wave forcing through platform-induced motion. Further, the rotor thrust from Load Case 4 is compared with that of an
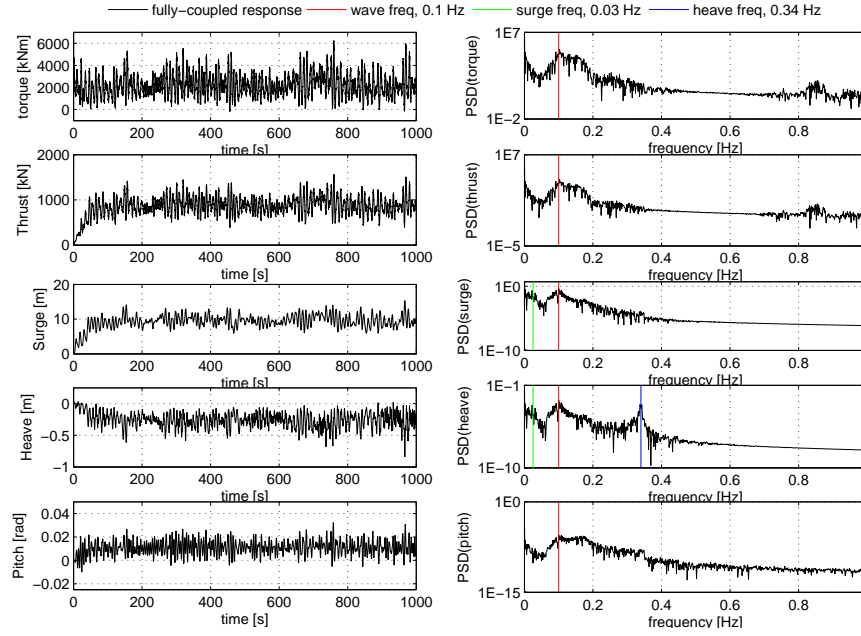
FIGURE 4.20: 2D fully coupled loads and responses - Load Case 3
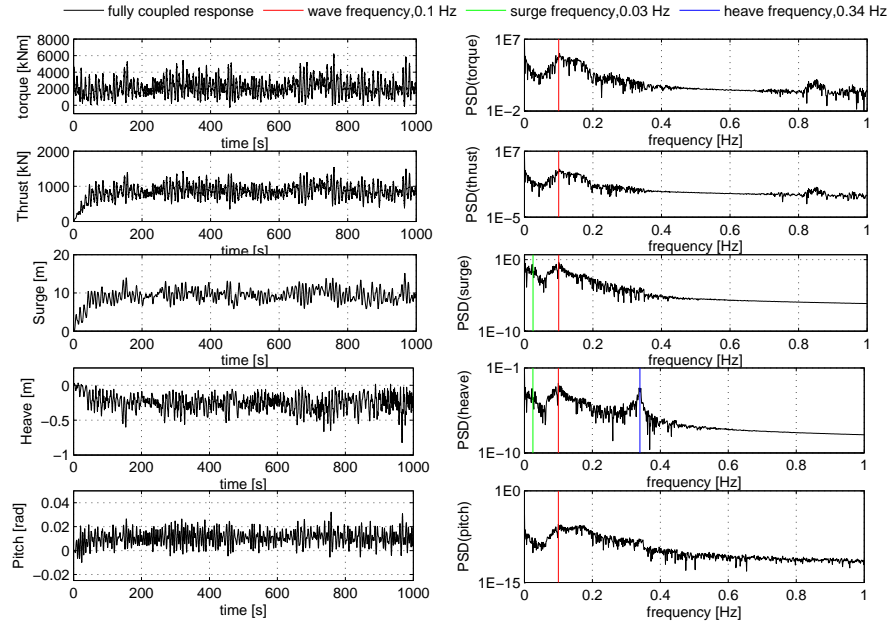
FIGURE 4.21: 2D fully coupled loads and responses - Load Case 4

onshore wind turbine thrust in Figure 4.23. The up-scaled tower top displacement is shown as well. It is seen that the mean thrust from the fully coupled computation is similar to the onshore wind turbine mean thrust (for the time duration shown in the figure, the mean values for the onshore and floating wind turbines are 856 kN and 862 kN respectively), however, with a large additional fluctuation. The fluctuation is a consequence of the platform motion and subsequently the tower top displacement.
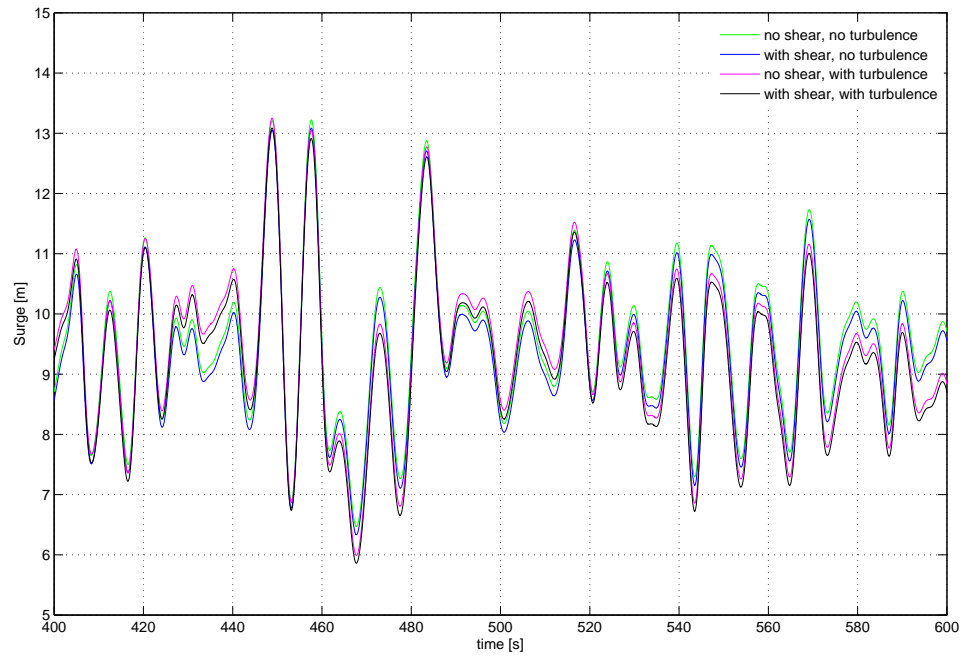
FIGURE 4.22: 2D fully coupled surge response comparison
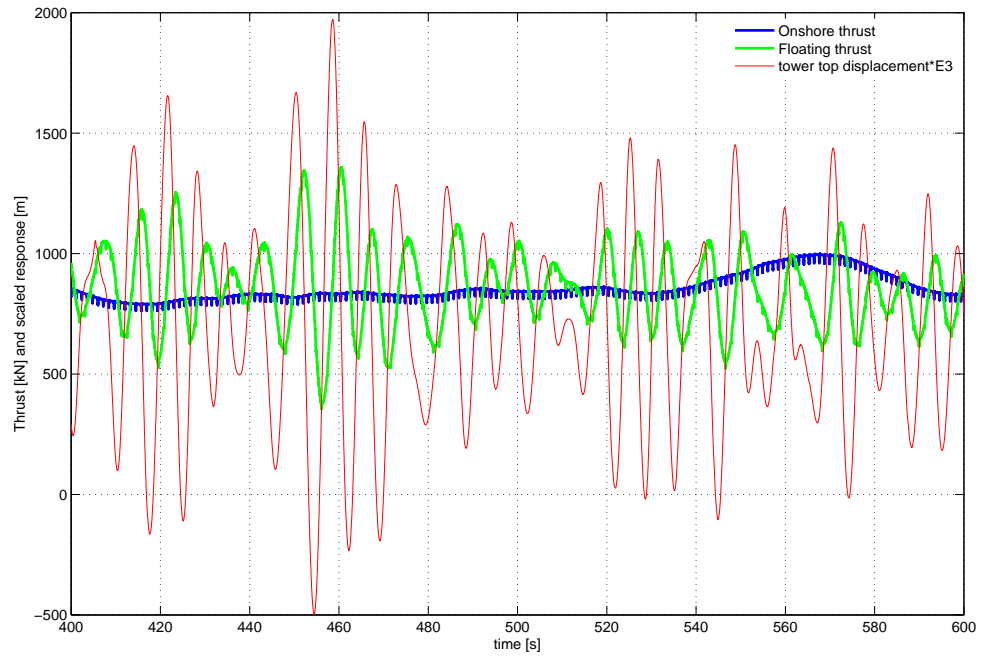
FIGURE 4.23: Comparison of fully coupled and onshore rotor thrust with scaled surge responses

4.3   Two-dimensional coupling - Conclusions

The conclusions of model development for two-dimensional coupling are detailed below.

4.3.1   Semi-coupled model

As a first step, the problem was formulated and implemented in a two-dimensional framework. While the platform equations of motion are derived based on a force equilibrium, the aerodynamic loads are derived using Runge-Kutta-Nystrom scheme. The aerodynamic and hydrodynamic loads and wind turbine and platform dynamics are coupled in a simplified manner resulting in a rotor load induced platform motion. However, the platform induced rotor dynamics was missing in the responses. The dynamics of TLP wind turbine was investigated in terms of four load cases. The model includes the surge-heave coupling through set-down effect. In addition, the presence of turbulence excites the low frequency response in pitch and the presence of tower shadow induces a 3p excitation in the pitch response.

4.3.2   Fully-coupled model

A fully coupled hydro-aero-elastic model is implemented for a floating TLP wind turbine in plane motion with fourteen degrees of freedom. Coupled loads and responses were predicted and compared to those of the semi-coupled model.

The effects of wind shear and turbulence were implemented in the aerodynamic loads using a power law and spatially coherent turbulence model respectively. Presence of wind shear slightly reduces the surge response, which is due to the reduced mean thrust at the lower part of the rotor, when wind shear is present compared to that of a constant mean flow. Presence of the turbulence excites the low frequency response in pitch.

The platform motion has a strong influence on the rotor loads, viz. thrust and torque. This is seen as a predominant peak at the peak wave frequency in the thrust and torque frequency responses. This is caused by the instantaneous relative velocity change seen by the blade, which also includes the platform velocity. The change in relative velocity in turn changes the angle of attack and the corresponding aerodynamic force coefficients.

It is observed that the rotor aerodynamics enhances the surge, heave and pitch response damping at surge and wave frequencies.

The above observations and conclusions provide motivation for extension of the model to include all the six platform degrees of freedom and the complete cross-coupling of blade inertia terms, which is the scope of a three-dimensional model. This is carried out in the next chapter.

4.4   Summary

In this chapter, a two-dimensional representation of the problem is formulated and implemented in two stages of coupling viz. semi-and fully-coupled models. Both of the coupled responses are compared for a set of load cases and significant conclusions are listed. The coupled responses provide motivation for extending the code to 3D, which will be explained in the next chapter.

CHAPTER 5

Three-Dimensional Coupling

In this chapter, the fully-coupled two-dimensional model implemented in the previous chapter is extended to three-dimensional space, considering all the platform degrees of freedom. Three-dimensional hydrodynamics derived in Chapter 3 is used for hydrodynamic loading. Aerodynamic and hydrodynamic loads and platform dynamics are fully coupled to each other giving rise to coupled loads and responses. The implementation is verified by comparing with that of the 2D results. In addition, the effect of wind-wave misalignment is investigated.

5.1 Three-dimensional problem formulation

The platform and wind turbine together are formulated using a seventeen degrees of freedom system in 3D. All the seventeen degrees of freedom are listed in Table 5.1. First six degrees of freedom corresponds to the motion of the platform, whereas the remaining eleven degrees of freedom relates to the wind turbine. The wind turbine degrees of freedom are the same as used for two-dimensional formulation. Since the same wind turbine is being used, all the mass and structural properties of the wind turbine remain the same. One difference is on the number of tendons used. In the case of 2D space, the number of tendons were two, whereas for 3D, four tendons are used, each attached to each of the spokes.

The equations of motion are derived using the principle of virtual work and can be written as follows.

$$[\mathbf{M}]\{\ddot{\mathbf{x}}\} + [\mathbf{C}]\{\dot{\mathbf{x}}\} + [\mathbf{K}]\{\mathbf{x}\} = \{\mathbf{F_g}\} \tag{5.1}$$

where $\mathbf{M}$, $\mathbf{C}$ and $\mathbf{K}$ are 17×17 generalized mass, damping and stiffness matrices, $\mathbf{x}$ is the field vector consisting of the 17 degrees of freedom, (˙) and (¨) represent first and second derivatives

TABLE 5.1: Degrees of freedom.

	Degrees of freedom	Number of DOF
Platform (translation)	surge, sway and heave	3
Platform (rotation)	roll, pitch and yaw	3
Tower	Longitudinal	1
Shaft	Azimuthal position	1
Blade	First and second flap for each blade	6
Blade	First edge for each blade	3
	Total	**17**

with respect to time and $\mathbf{F_g}$ is the generalized force vector. For a detailed description on principle of virtual work applied to wind turbines, the reader may consult Chapter 12 of Hansen (2008).

The generalized force vector, mass, stiffness and damping matrices are derived as follows.

Generalized force vector

Each element of the generalized force vector is derived by giving a virtual displacement in the corresponding degree of freedom by keeping all other degrees of freedom in the locked condition and writing the virtual work done. Hence, the generalized force vector obtained is given below.

$$
\mathbf{F_g} = \begin{Bmatrix}
F_1 + F_w + F_{moor1} \\
F_2 + F_{moor2} \\
F_3 + F_b - F_G + F_{moor3} \\
F_4 + M_w - F_b y_b + F_G y_G + F_{moor4} \\
F_5 + F_w Z_n - F_b x_b + F_G x_G + F_{moor5} \\
F_{moor6} \\
F_w \\
M_{aero} - M_{gen} \\
F_{g9} \\
F_{g10} \\
F_{g11} \\
F_{g12} \\
F_{g13} \\
F_{g14} \\
F_{g15} \\
F_{g16} \\
F_{g17}
\end{Bmatrix}
\tag{5.2}
$$

where F_1, F_2, F_3, F_4 and F_5 are the hydrodynamic surge, sway, heave forces, roll and pitch moments respectively. Hydrodynamic yaw moment, F_6 is considered to be zero. The hydrodynamic forces and moments are explained in section 3.6 of Chapter 3. The buoyancy and gravity forces are represented using F_b and F_G, the x and y coordinates of the centres of buoyancy and gravity are represented using x_b, y_b, x_G and y_G. The mooring forces, F_{moor1}, F_{moor2}, F_{moor3}, F_{moor4}, F_{moor5} and F_{moor6} in surge, sway, heave translational and roll, pitch and yaw rotational directions are derived in Appendix A. Vertical distance from the platform bottom to the hub centre, $Z_n = h + H_t$, M_w represents the effective rotor torque, which is a difference between the aerodynamic and generator torque.

One of the generalized force terms corresponding to the first flapwise degree of freedom of blade 1 is given below, whereas the complete derivation of the generalized force is given in Appendix B.

$$
\begin{aligned}
F_{g9} = \int_0^R \left(p_t^{B1} \phi_{1,y}^{1f} + p_n^{B1} \phi_{1,z}^{1f} \right) dr &= \int_0^R \left(p_t^{B1} \left(\phi_{1,e}^{1f} \cos\theta_p + \phi_{1,f}^{1f} \sin\theta_p \right) \right) dr \\
&+ \int_0^R \left(p_n^{B1} \left(-\phi_{1,e}^{1f} \sin\theta_p + \phi_{1,f}^{1f} \cos\theta_p \right) \right) dr
\end{aligned}
\tag{5.3}
$$

where p_n and p_t are the normal and tangential force per unit length for the blade 1, B1. The subscripts f and e represent flapwise and edgewise components of the mode shapes, whereas the superscripts $1f$, $2f$ and $1e$ represent the first and second flapwise mode shapes

and first edgewise mode shape respectively and ϕ is used for the mode shape. Blade pitch angle is represented using the symbol θ_p and R represents blade length. Presence of pitch angle requires the blade mode shapes to be transformed to the global coordinate system. The blade mode shapes are the same for three of the blades, as derived in Section 4.2 of Chapter 4.

Generalized mass matrix

The mass matrix is also derived using the method of virtual work. The mass elements for each of the columns are computed by first computing the inertia force corresponding to a unit acceleration in that degree of freedom, whereas all other accelerations are kept zero. Next, the virtual work done is computed by giving a virtual displacement to each of the degree of freedom and taking the dot product of the inertia force and the virtual displacement, which will lead to the corresponding mass element. Each of the element in the column under consideration is computed the similar way and then proceeding to the next column. The mass matrix is fully populated because of the interaction between the platform and blade degrees of freedom. Hence, the mass matrix can be written as follows.

$$\mathbf{M_g} =$$

$$
\begin{pmatrix}
m1 & 0 & 0 & 0 & p1 & 0 & m7 & 0 & a1 & a2 & a3 & a4 & a5 & a6 & a7 & a8 & a9 \\
0 & m2 & 0 & p2 & 0 & 0 & 0 & 0 & b1 & b2 & b3 & b4 & b5 & b6 & b7 & b8 & b9 \\
0 & 0 & m3 & 0 & 0 & 0 & 0 & 0 & c1 & c2 & c3 & c4 & c5 & c6 & c7 & c8 & c9 \\
0 & p2 & 0 & m4 & 0 & 0 & 0 & 0 & d1 & d2 & d3 & d4 & d5 & d6 & d7 & d8 & d9 \\
p1 & 0 & 0 & 0 & m5 & 0 & p1 & 0 & e1 & e2 & e3 & e4 & e5 & e6 & e7 & e8 & e9 \\
0 & 0 & 0 & 0 & 0 & m6 & 0 & 0 & f1 & f2 & f3 & f4 & f5 & f6 & f7 & f8 & f9 \\
m7 & 0 & 0 & 0 & p1 & 0 & m7 & 0 & g1 & g2 & g3 & g4 & g5 & g6 & g7 & g8 & g9 \\
0 & 0 & 0 & 0 & 0 & 0 & 0 & m8 & h1 & h2 & h3 & h4 & h5 & h6 & h7 & h8 & h9 \\
a1 & b1 & c1 & d1 & e1 & f1 & g1 & h1 & m9 & 0 & 0 & 0 & 0 & 0 & 0 & 0 & 0 \\
a2 & b2 & c2 & d2 & e2 & f2 & g2 & h2 & 0 & m10 & 0 & 0 & 0 & 0 & 0 & 0 & 0 \\
a3 & b3 & c3 & d3 & e3 & f3 & g3 & h3 & 0 & 0 & m11 & 0 & 0 & 0 & 0 & 0 & 0 \\
a4 & b4 & c4 & d4 & e4 & f4 & g4 & h4 & 0 & 0 & 0 & m9 & 0 & 0 & 0 & 0 & 0 \\
a5 & b5 & c5 & d5 & e5 & f5 & g5 & h5 & 0 & 0 & 0 & 0 & m10 & 0 & 0 & 0 & 0 \\
a6 & b6 & c6 & d6 & e6 & f6 & g6 & h6 & 0 & 0 & 0 & 0 & 0 & m11 & 0 & 0 & 0 \\
a7 & b7 & c7 & d7 & e7 & f7 & g7 & h7 & 0 & 0 & 0 & 0 & 0 & 0 & m9 & 0 & 0 \\
a8 & b8 & c8 & d8 & e8 & f8 & g8 & h8 & 0 & 0 & 0 & 0 & 0 & 0 & 0 & m10 & 0 \\
a9 & b9 & c9 & d9 & e9 & f9 & g9 & h9 & 0 & 0 & 0 & 0 & 0 & 0 & 0 & 0 & m11
\end{pmatrix}
\tag{5.4}
$$

The diagonal elements of the mass matrix are the generalized masses for corresponding degrees of freedom. The first square section of 7×7 matrix corresponds to the platform and tower degrees of freedom. One of the cross-coupling terms between the platform surge and first flapwise degree of freedom of blade 1 is given below, whereas the complete derivation is given in Appendix B.

$$
\begin{aligned}
M(9,1) = a1 &= \int_0^R \left(p_x 0 + p_y \phi_{1,y}^{1f} + p_z \phi_{1,z}^{1f} \right) dr \\
&= \int_0^R \left(p_y \left(\phi_{1,e}^{1f} \cos \theta_p + \phi_{1,f}^{1f} \sin \theta_p \right) \right) dr \\
&\quad + \int_0^R \left(p_z \left(-\phi_{1,e}^{1f} \sin \theta_p + \phi_{1,f}^{1f} \cos \theta_p \right) \right) dr
\end{aligned}
\tag{5.5}
$$

where $\phi_{1,f}^{1f}$ and $\phi_{1,e}^{1f}$ are flapwise and edgewise contributions of the first blade, first flapwise

degree of freedom. Expressions for normal and tangential force distributions p_z and p_y are given in the following equation.

$$\left\{ \begin{array}{c} p_x \\ p_y \\ p_z \end{array} \right\} = m(r)[T] \left\{ \begin{array}{c} 1 \\ 0 \\ 0 \end{array} \right\} \tag{5.6}$$

where $m(r)$ is the distributed mass per length along the blade and $[T]$ is the transformation matrix from platform coordinate system to the blade coordinate system.

Generalized stiffness matrix

Similar to the mass matrix, the stiffness matrix is also computed column-wise. For the first column, the first step is to compute the spring force corresponding to a unit displacement in the first degree of freedom. While the system is subjected to this spring force, a virtual displacement is given in the first degree of freedom. Dot product of the spring force with virtual displacement in the first degree of freedom will give the virtual work done and hence the first element of the stiffness matrix in the first column. Similarly all the elements in the first column are computed by giving virtual displacements to the corresponding degrees of freedom. This way, all the columns of the stiffness matrix are computed. The stiffness contributions from the wind turbine are formulated using mass proportional terms by means of the eigen frequencies. The only non-zero elements in the stiffness matrix correspond to the tower stiffness and the diagonal elements for the blade degrees of freedom, which are listed below.

$$K(7,7) = \omega_t^2 M(7,7) \tag{5.7}$$

$$K(9,9) = K(12,12) = K(15,15) = GK_1 = \omega_{1f}^2 M(9,9) \tag{5.8}$$

$$K(10,10) = K(13,13) = K(16,16) = GK_2 = \omega_{1e}^2 M(10,10) \tag{5.9}$$

$$K(11,11) = K(14,14) = K(17,17) = GK_3 = \omega_{2f}^2 M(11,11) \tag{5.10}$$

Here ω_t is the tower longitudinal natural frequency, ω_{1f}, ω_{1e} and ω_{2f} are the first flapwise, first edgewise and second flapwise blade circular natural frequencies respectively. The generalized stiffness for blade 1 are assumed to be the same for the other blades, since the blades are identical.

Generalized damping matrix

The damping matrix is also computed similar to mass and stiffness matrices using the method of virtual work. For the first column, the first step is to compute the damping force corresponding to a unit velocity in the first degree of freedom. While the system is subjected to this force, a virtual displacement is given in the first degree of freedom. Dot product of the damping force and the virtual displacement in the first degree of freedom provides the virtual work done and hence the first element of the damping matrix in the first column. Similarly, all the elements in the first column are computed by giving virtual displacements to the corresponding degrees of freedom. This way, all the columns of the damping matrix are computed.

The hydrodynamic damping is incorporated with the hydrodynamic forcing through quadratic drag contribution, whereas the aerodynamic damping is incorporated using a dynamic stall

model. Since these contributions are included in the force vector, the corresponding terms in the damping matrix are zeros. The only non-zero element in the damping matrix is the diagonal element corresponding to the tower longitudinal degree of freedom, which corresponds to 2% structural damping from the tower and is given below.

$$C(7,7) = \omega_t M(7,7) \frac{\delta}{\pi} = 2\zeta M(7,7)\omega_t \tag{5.11}$$

where δ is the logarithmic decrement corresponding to tower longitudinal structural damping and ζ is the critical damping ratio for tower structural damping.

For the floater motion, the centre-point at the bottom side of the floater is chosen as reference point for deriving the equations of motion. The coupled equations of motion are solved using the Runge-Kutta-Nystrom algorithm, see Hansen (2008).

5.1.1   Wave loading

Linear irregular three-dimensional wave forcing with directional spreading is considered for the wave climate mentioned in Table 2.2. The three-dimensional wave kinematics can be derived from a directional wave spectrum, consists of both frequency- and direction-dependent spectra. As the Joint North Sea Wave Project (JONSWAP) spectrum usually represents the measured frequency spectrum fairly well for the North Sea, the JONSWAP spectrum with a peak enhancement factor of 3.3 was used. The wave energy below 0.04 Hz and above 0.35 Hz was omitted as the JONSWAP spectrum had negligible energy here. A frequency resolution of 0.001 Hz is chosen. This corresponds to a maximum computation time duration of 1000 s before repetition. The direction-dependent spectrum takes the standard form of a cosine-power distribution with a degree of spreading, $s = 1$, Sumer and Fredsøe (2006). Wave amplitudes were computed from the power spectral density corresponding to each of these frequencies and directions from the wave spectrum. The wave kinematics are obtained using the relations derived in Section 3.3 of Chapter 3.

The wave kinematics are Delta stretched, ISO (2005), from 25 m below mean sea level. A Fast Fourier Transform (FFT) algorithm was implemented to achieve an efficient time domain computation of the wave kinematics, see e.g. Bredmose (2002). Further, to achieve computational efficiency, the wave kinematics are computed at the mean position. The pre-computed kinematics are Taylor expanded to obtain the corresponding values at the instantaneous positions. An example is shown in equation (5.12) for surface elevation. Kinematics at intermediate time steps are computed by linear interpolation.

$$\eta = \eta_0 + \eta_{1f}\frac{\partial \eta}{\partial x}|_0 + \eta_2 \frac{\partial \eta}{\partial y}|_0 \tag{5.12}$$

where η is the instantaneous surface elevation, obtained by Taylor expansion, η_0, $\frac{\partial \eta}{\partial x}|_0$ and $\frac{\partial \eta}{\partial y}|_0$ represent surface elevation at mean position and first derivatives of surface elevation with respect to x and y directions at mean position respectively and η_{1f} and η_2 represent instantaneous platform surge and sway displacements.

From the wave kinematics, the wave induced forces are computed by means of Morison's equation as described in Section 3.6 of Chapter 3.

5.1.2   Wind loading

The aerodynamic loading is computed by means of unsteady Blade Element Momentum theory, with inclusion of Prandtl's tip loss factor for finite number of blades, Glauert correction

for high values of the axial induction factor and corrections for the effects of tower shadow, dynamic stall, dynamic wake and dynamic yaw, Hansen (2008). The model is capable of handling wind shear and turbulence effects.

5.1.3 Coupling

The wind and wave loading are fully coupled in time domain through the structural degrees of freedom. Hereby, the rotor loads become part of the floater generalized forces and the floater motion, contributes to the relative velocity seen by the blade and hence the rotor loads, which will eventually affect the tower top and blade displacements. By this way, a coupled rotor-floater dynamics is achieved when subjected to simultaneous wind and wave loads.

5.2 Natural frequency analysis

The 3D model implementation is verified through a comparison of decay tests using 3D and 2D codes. The heave natural frequency depends on axial tendon stiffness, which is dependent on the tendon diameter. For the 3D configuration, each of the tendons has a diameter of 75.66 mm. While simplifying the 3D configuration to 2D, to have the same axial tendon stiffness, the tendon diameter is chosen as 107 mm for the 2D model. This is illustrated below.

In the case of 3D, the axial stiffness is equal to $\frac{4A_{tend}E_{tend}}{L_0}$, where 4 designate the number of tendons, the area of cross section of a tendon is, $A_{tend} = \frac{\pi}{4}d_{tend}^2$, $d_{tend} = 75.66\ mm$ is the diameter and E_{tend} represents Young's modulus of the tendon. Simplification to 2D gives rise to a tendon diameter of $(d_{tend})_{2D} = \sqrt{2}\,(d_{tend})_{3D}$ and hence the tendon diameter of 2D computation is equal to 107 mm.

Decay tests are conducted by using the correct tendon diameters and with the absence of external loading from wind and wave, which is given below.

Surge decay test

The surge decay test is conducted by constraining all the degrees of freedom except surge and applying an initial perturbation in the surge degree of freedom. Responses are obtained and the frequency response is shown in Figure 5.1. The analytical expression for surge natural frequency is shown in the following equation. From the equation and figure, the surge frequency is found to be the same, 0.026 Hz, which is matching with the 2D surge decay test result, as shown in Figure 4.8.

$$(f_n)_{surge} = \frac{1}{2\pi}\sqrt{\frac{T_0}{L_0 m_1}} = 0.026 Hz \tag{5.13}$$

Tests are also conducted by activating all the degrees of freedom and giving an initial perturbation in the surge degree of freedom. The surge-heave coupling is visible in the heave response with a peak corresponding to double the surge natural frequency, which is shown in the Figure 5.2.

Sway decay test

The sway decay test is conducted by constraining all the degrees of freedom except sway and applying an initial perturbation in the sway degree of freedom. Responses are obtained and the frequency response is shown in Figure 5.3. The analytical expression for sway
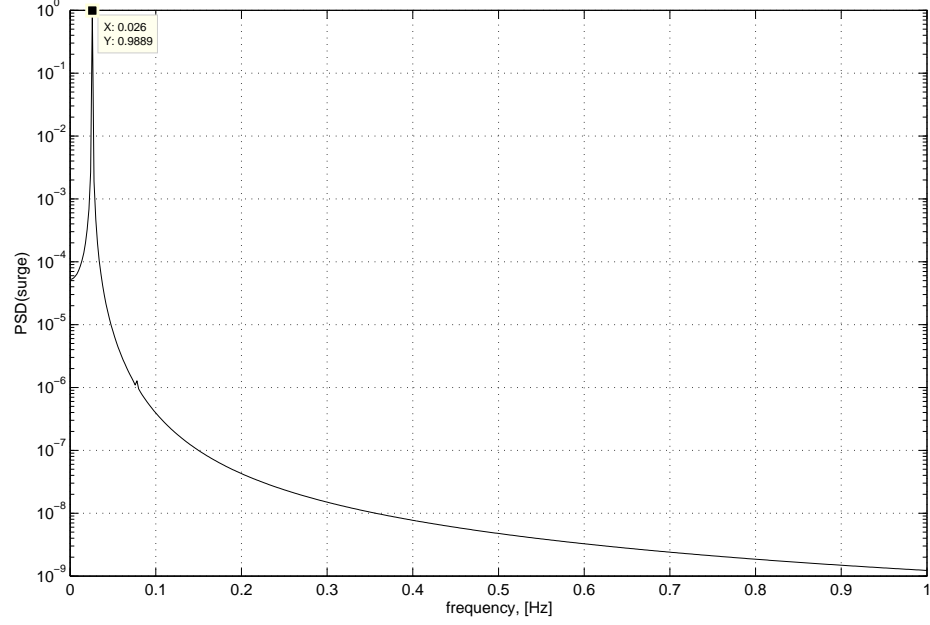
FIGURE 5.1: 3D - frequency response plot for surge natural frequency
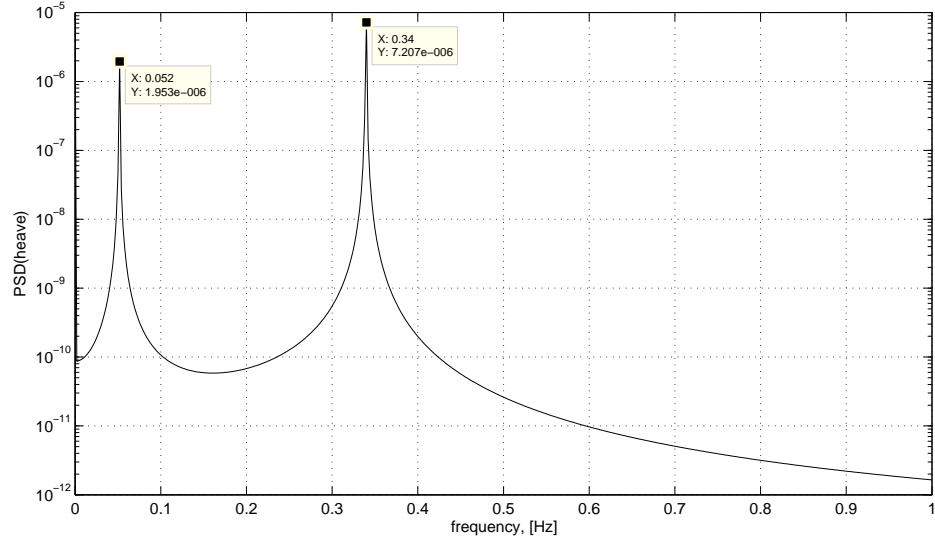
FIGURE 5.2: 3D - heave frequency response plot for surge decay test

natural frequency is shown in the following equation. From the equation and figure, the sway frequency is found to be the same, 0.026 Hz.

$$(f_n)_{sway} = \frac{1}{2\pi}\sqrt{\frac{T_0}{L_0 m_2}} = 0.026 Hz \tag{5.14}$$
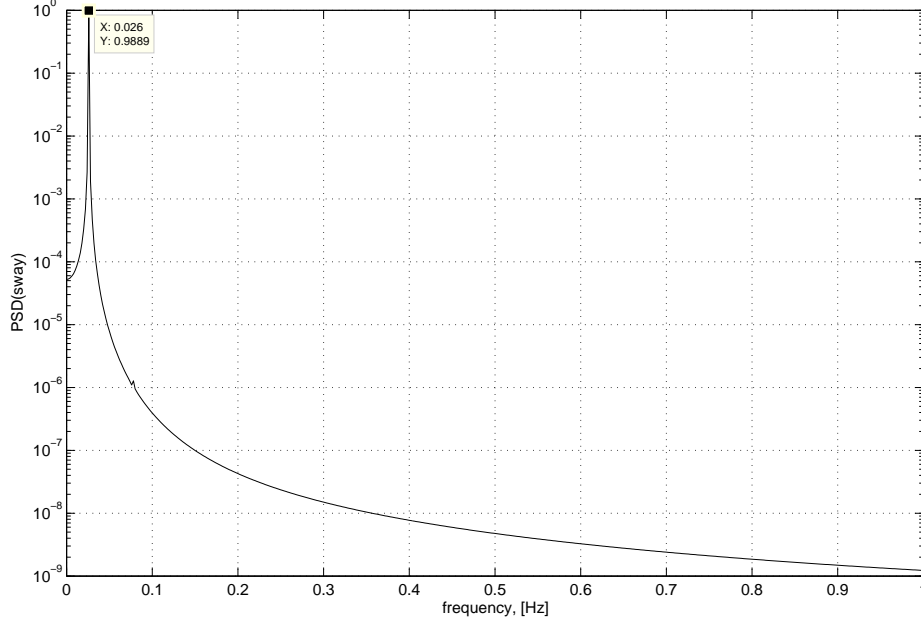
FIGURE 5.3: 3D - frequency response plot for sway natural frequency

Similar to the surge decay test, a test is also conducted by activating all the degrees of freedom and giving an initial perturbation in the sway degree of freedom. The sway-heave coupling is visible in the heave response with a peak corresponding to double the sway natural frequency, which is shown in the Figure 5.4.

Heave decay test

The heave decay test is conducted by constraining all the degrees of freedom except heave and applying an initial perturbation in the heave degree of freedom. Responses are obtained and the frequency response is shown in Figure 5.5. The analytical expression for heave natural frequency is shown in the following equation. From the equation and figure, the heave frequency is found to be the same, 0.34 Hz, which is matching with the 2D heave decay test result, as shown in Figure 4.9.

$$(f_n)_{heave} = \frac{1}{2\pi}\sqrt{\frac{\frac{4AE}{L_0} + \frac{\pi}{4}\rho g D_t^2}{m_3}} = 0.34 Hz \tag{5.15}$$

Roll decay test

The roll decay test is conducted by constraining all the degrees of freedom except roll and applying an initial perturbation in the roll degree of freedom. Responses are obtained and the frequency response is shown in Figure 5.6. The analytical expression for roll natural frequency is shown in the following equation. From the equation and figure, the roll frequency is found to be the same, 0.14 Hz.
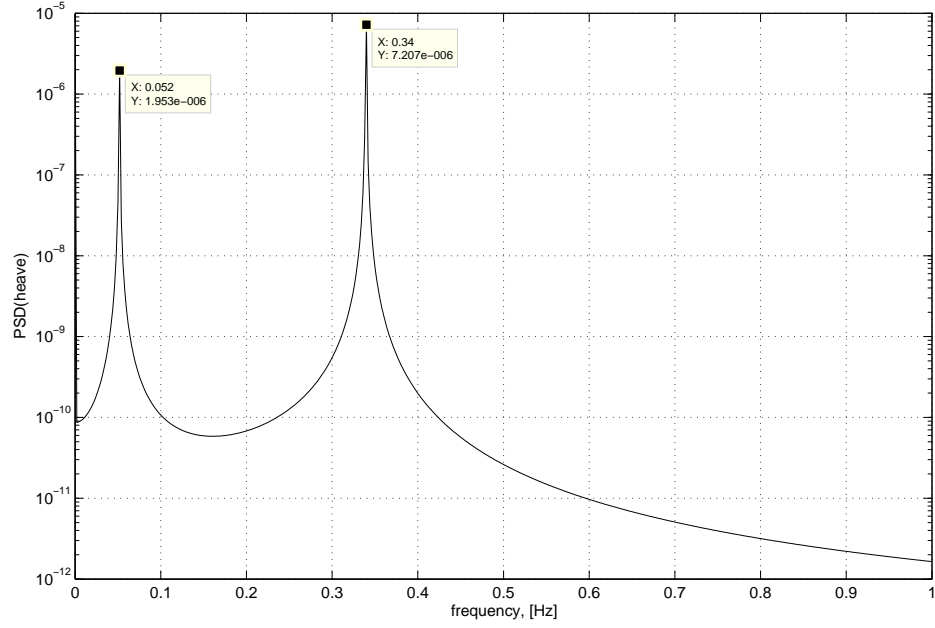
FIGURE 5.4: 3D - heave frequency response plot for sway decay test
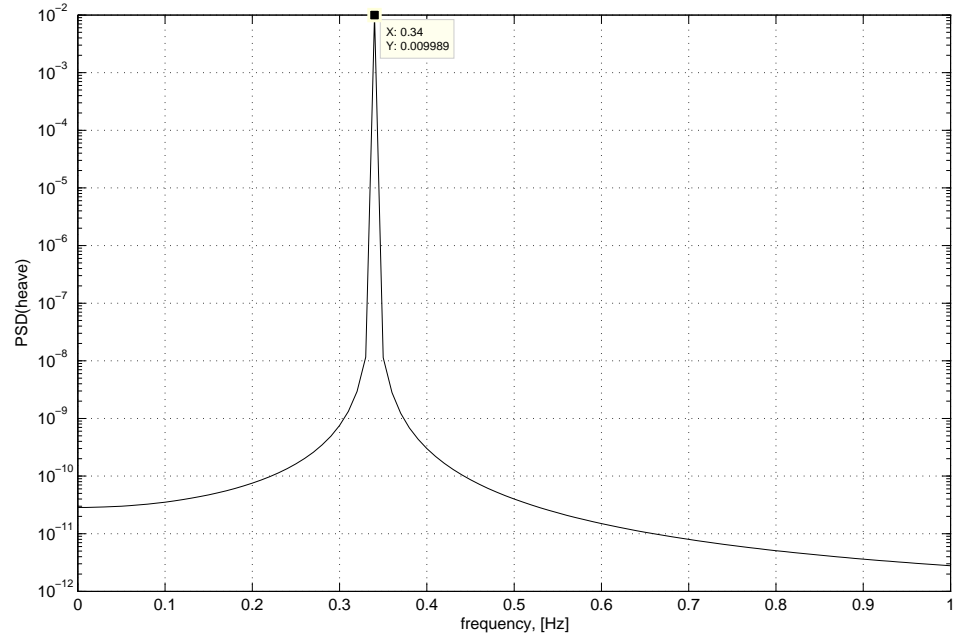
FIGURE 5.5: 3D - frequency response plot for heave natural frequency

$$(f_n)_{roll} =$$

$$\frac{1}{2\pi}\sqrt{\frac{\left(-W_t\left(H_t+h\right)-0.5W_fh+F_{bt}\left(0.5h_t+h+\frac{D_t^2}{16h_t}\right)+0.5F_{bf}h+\frac{4AE}{L_0}\tilde{d}^2\right)}{J_4}} \quad (5.16)$$

$$= 0.14Hz$$
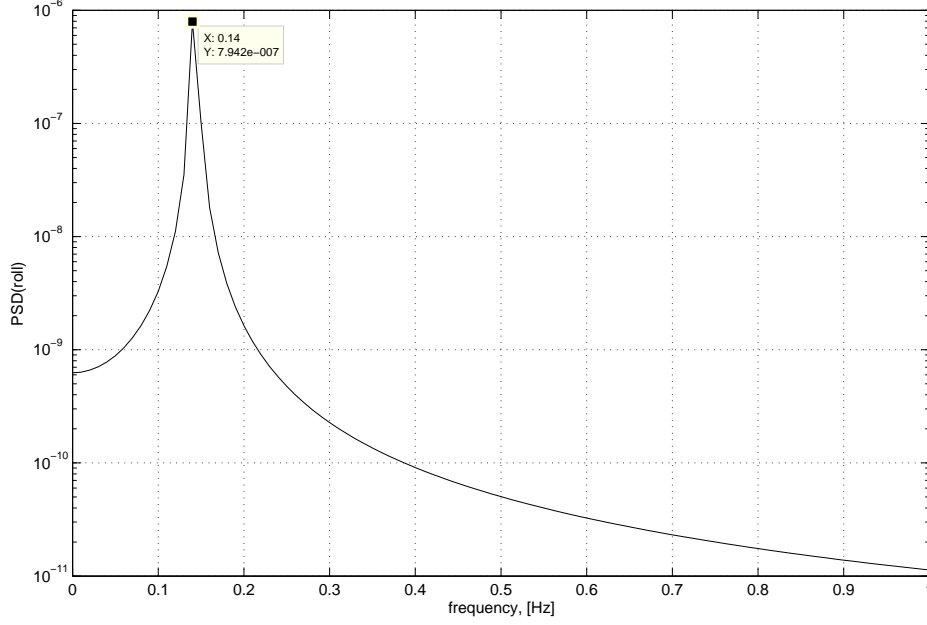
FIGURE 5.6: 3D - frequency response plot for roll natural frequency

Pitch decay test

The pitch decay test is conducted by constraining all the degrees of freedom except pitch and applying an initial perturbation in the pitch degree of freedom. Responses are obtained and the frequency response is shown in Figure 5.7. The analytical expression for pitch natural frequency is shown in the following equation. From the equation and figure, the pitch frequency is found to be the same, 0.14 Hz, which is matching with the 2D pitch decay test result, as shown in Figure 4.10.

$$(f_n)_{pitch} = \frac{1}{2\pi}\sqrt{\frac{\left(-W_t\left(H_t + h\right) - 0.5W_f h + F_{bt}\left(0.5h_t + h + \frac{D_t^2}{16h_t}\right) + 0.5F_{bf}h + \frac{4AE}{L_0}\tilde{d}^2\right)}{J_5}} = 0.14Hz \tag{5.17}$$

Yaw decay test

The yaw decay test is conducted by constraining all the degrees of freedom except yaw and applying an initial perturbation in the yaw degree of freedom. Responses are obtained and the frequency response is shown in Figure 5.8. The analytical expression for yaw natural frequency is shown in the following equation. From the equation and figure, the yaw frequency is found to be the same, 0.28 Hz.

$$(f_n)_{yaw} = \frac{1}{2\pi}\sqrt{\frac{T_0\tilde{d}^2}{L_0 J_6}} = 0.28Hz \tag{5.18}$$
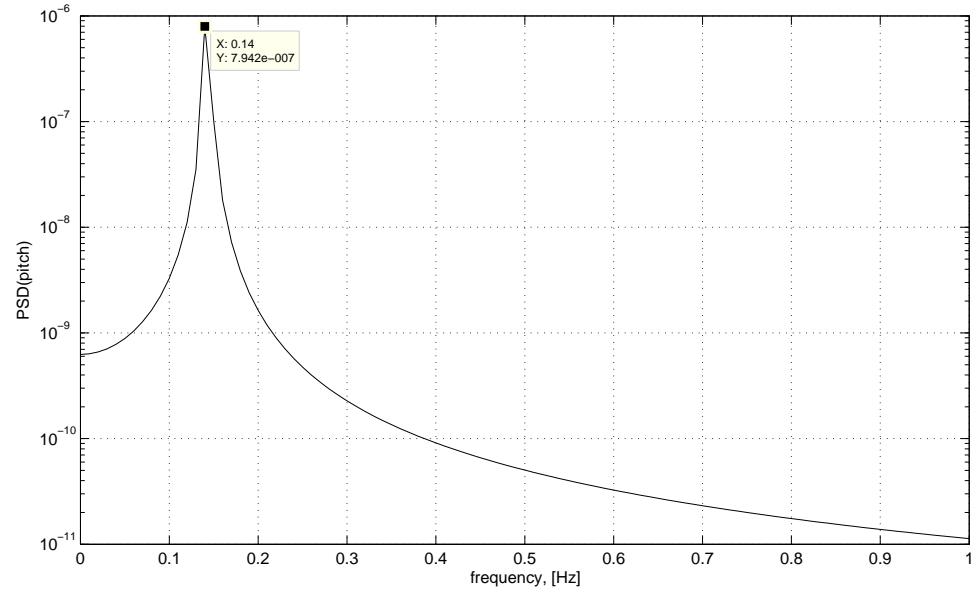
FIGURE 5.7: 3D - frequency response plot for pitch natural frequency
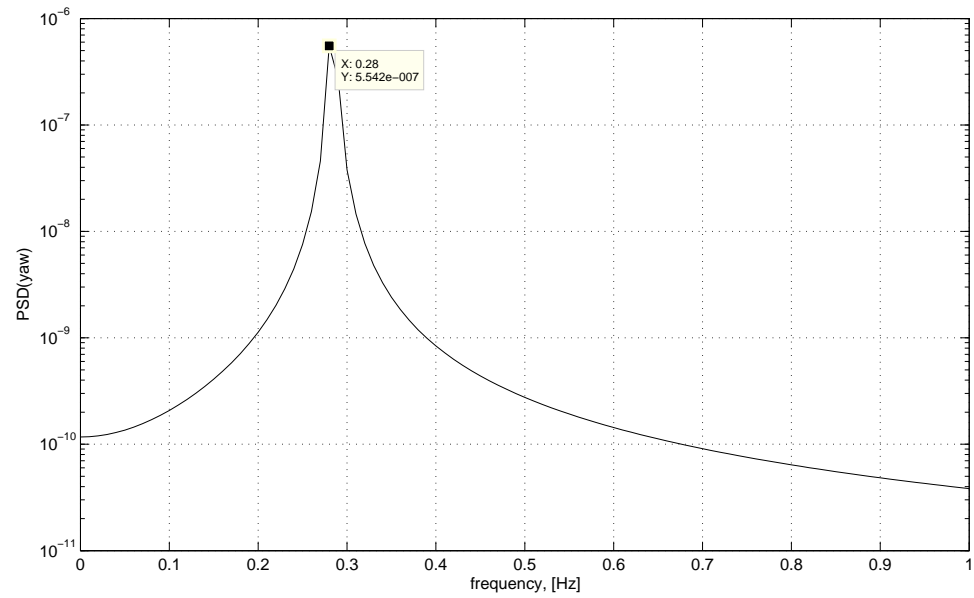
FIGURE 5.8: 3D - frequency response plot for yaw natural frequency

The parameters used in the equations are explained in the subsequent sections in detail.

5.3   Comparison of 3D responses with 2D responses

The 3D model implementation is verified through a comparison of responses from 3D and 2D codes. Hence, the 3D code is forced to perform like a 2D code by constraining the additional degrees of freedom. Loads and responses are computed for the Load Case 1 (mean wind speed of 10 m/s, no shear and no turbulence) of two-dimensional fully-coupled case using 2D and 3D codes. Results are obtained and the comparison of responses is shown in Figure 5.9. From the figure, it can be observed that a complete agreement for all the responses in both time- and frequency-domains are achieved. The 2D results (red curve) are completely on top of the 3D results (green curve). The predominant natural frequencies are marked. The response comparison provides confidence in the 3D implementation.
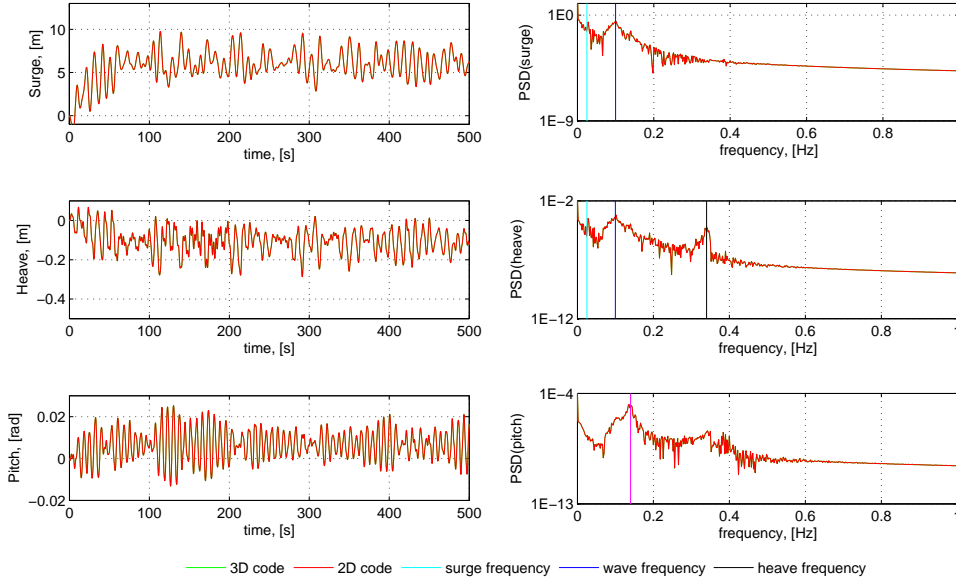
FIGURE 5.9: 2D and 3D responses comparison

5.4   Three-dimensional coupled responses

Validation of the 3D model implementation helps to carry out computations for multiple load cases using the 3D code.

5.4.1   Load cases

Two load cases for wind conditions and four load cases for wave headings are investigated. Combining wind and wave give rise to a total of eight load cases.

Load Case 1 - no shear, no turbulence with four predominant wave directions viz. 0, $\frac{\pi}{4}$, $\frac{\pi}{2}$ and π radians, where 0 radians corresponds to the wind direction.

Load Case 2 - with shear, with turbulence with four predominant wave directions viz. 0, $\frac{\pi}{4}$, $\frac{\pi}{2}$ and π radians.

Wind conditions

A mean wind speed of 10 m/s is considered. The Load Case 1 is with a constant mean wind velocity, while the Load Case 2 is using a sheared wind profile with the same mean wind speed and a spatially coherent turbulence on top of it. The spatial coherence for the turbulence was assumed for simplicity. Temporal variation is considered only for the main wind direction component, u, whereas the variation in other components, v and w are not considered. The fluctuating u component is produced from a wind spectrum of the Mann model, Mann (1998).

In all load cases, the rotor thrust was ramped to the real value within a time span of 50 s, to avoid an unrealistic initial transient response.

5.4.2 Three-dimensional coupling - Results and discussion

Rotor Loads

The rotor loads from a computation of Load Case 2 having wave direction aligned with wind (0°) is presented in Figure 5.10. The rotor torque and thrust are shown in the figure as time series and the Power Spectral Densities (PSD) in the frequency domain. The predominant frequency is marked. In addition to the peak wave frequency excitation, a smaller peak around 0.49 Hz, corresponding to three times the rotor frequency (3p) of 0.163 Hz (1p) is also visible. The 1p frequency corresponds to a rotor speed of 9.8 rpm, which is related to the rotor speed proportional to 10 m/s wind speed (below rated).

The time series shows a larger fluctuation of the rotor loads compared to that of onshore wind turbine rotor loads, as in figure 4.23, which is a consequence of the floater motion. The same is confirmed from the predominant peak at 0.1 Hz, corresponding to the peak wave frequency in the frequency domain.
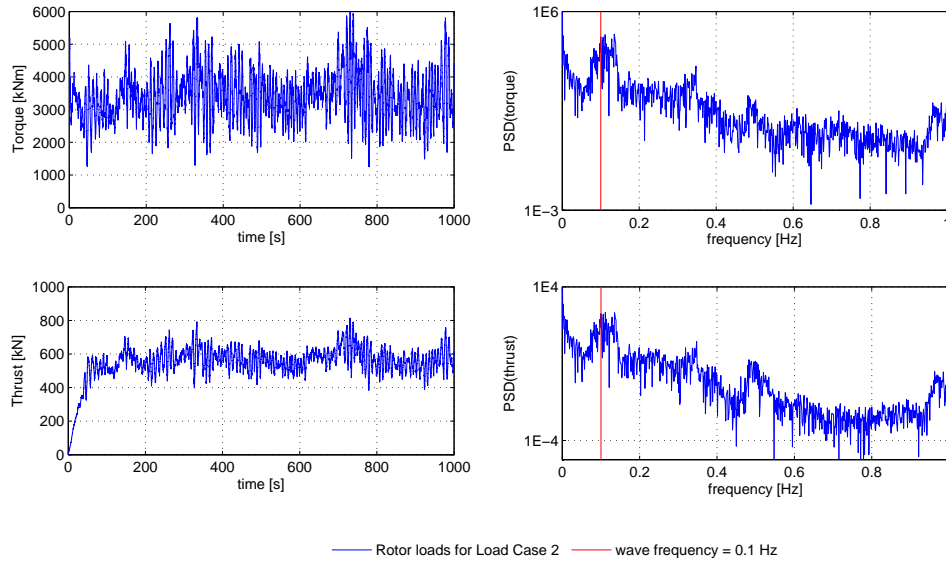
FIGURE 5.10: Rotor loads - Load Case 2 with a wave direction of 0 radian

Responses

Figure 5.11 shows the floater response, which is extracted with reference to the floater bottom point. The figure shows both time- and frequency-domain responses. Major frequency peaks are identified.
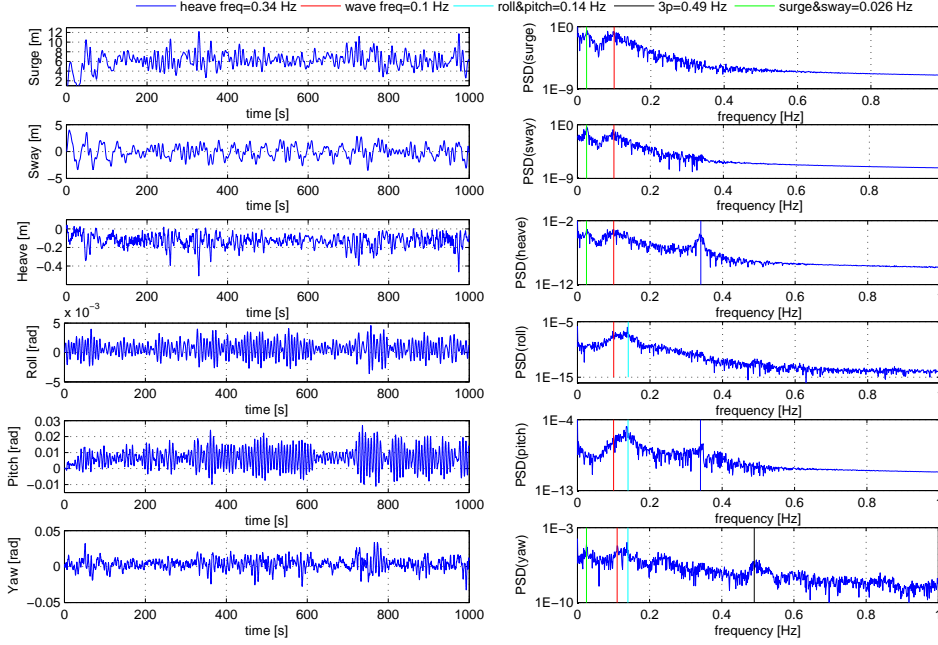
FIGURE 5.11: Floater response - Load Case 2 with a wave direction of 0 radian

- *Surge response*

  The surge response is fluctuating around a mean of 6.3 m. The mean response is attributed to the rotor thrust, whereas the fluctuating part is attributed to the wave forcing. The predominant peaks are at the surge natural frequency (0.026 Hz) and at the peak wave frequency (0.1 Hz). The low-frequency excitation of the response is caused by the turbulent fluctuations in the wind.

- *Sway response*

  The sway response standard deviation is 25% smaller than that of surge response, which is due to the predominant wave direction along the global x-axis. It may be because of the comparatively smaller sway force due to the smaller energy content in the sway direction in the wide banded directional wave spectrum. In addition, the rotor thrust from wind is not present in the sway direction, which makes the sway response fluctuate near to zero mean. In the frequency domain, the predominant peaks are at sway and peak wave frequencies. The sway natural frequency is identical to the surge natural frequency owing to the symmetry of the configuration.

- *Heave response*

  The heave response has a negative mean and the fluctuations are smaller. The frequency response shows peaks corresponding to surge (0.026 Hz), heave and peak wave frequencies. The heave frequency peak is at 0.34 Hz, corresponding to the heave natural frequency in equation (5.15). The energy content available in the surge frequency is due to the surge-heave coupling.

- *Roll response*

  The roll response is fluctuating about an almost zero mean. The fluctuations are growing and decaying intermittently. This could be caused by the proximity of roll natural frequency with peak wave frequency. The fluctuations were also triggered by the largely varying rotor torque, which is a part of roll excitation. The influence of rotor torque on roll response can be noticed by the presence of a smaller peak corresponding to 3p excitation in the frequency domain response. The maximum response is not very large (lesser than 0.3 degrees). The frequency response has peaks corresponding to peak wave frequency and roll natural frequency (0.14 Hz).

- *Pitch response*

  The pitch response is fluctuating about a positive mean as a consequence of the moment created by the rotor thrust. The pitch response also has growing tendency intermittently, caused by the low frequency fluctuations in amplitude because of the adjacent frequencies. The standard deviation of pitch is larger compared to roll response owing to the predominant wave direction. Peaks corresponding to peak wave frequency, pitch natural frequency (0.14 Hz) and a small peak at heave natural frequency are seen. The $3p$ excitation in the pitch response is broadened because of the presence of wind turbulence. In addition, the low frequency response (0.01 Hz) is driven by the turbulence.

- *Yaw response*

  The yaw response is a highly fluctuating DOF, though around an approximately zero mean. This is expected for a system similar to an inverted pendulum. The influence of other degrees of freedom on yaw can be noticed from the presence of smaller peaks corresponding to surge or sway and heave, roll and pitch DOFs. The surge/sway and roll/pitch peaks are equally stronger as the wave excitation peak. The yaw excitation can be seen at yaw natural frequency, 0.28 Hz. In addition, the presence of 3p excitation reveals the strong influence of rotor loads on platform yaw.

  The yaw rotations can be reduced by incorporating suitable floater damping in the equations of motion. This damping may be the hydrodynamic damping caused by the spokes, which is a physical phenomenon. While the floater is subjected to a yaw rotation, the spokes move laterally by interacting with the wave motion resulting in an added mass and a proportional damping. This added mass depends on the size and shape of the spokes, which may be quantified as given in the following equation, Withee (2004), valid for a square cross-sectioned spoke, having a width of w.

$$A_6 = 4.754 \left(\frac{w}{2}\right)^2 \rho \left(\left(d_e + \frac{D_f}{2}\right)^3 - \left(\frac{D_f}{2}\right)^3\right) \tag{5.19}$$

  where ρ is the sea water density, d_e is the spoke length and D_f is the floater diameter.

5.4.3   Comparison of different wave heading cases

The influence of different wave headings is investigated to understand the severity of wind-wave misalignment. For this purpose, four different directions, viz. 0 (wind-wave aligned), $\frac{\pi}{4}$, $\frac{\pi}{2}$ and π radians are chosen. Irrespective of the wave heading, the wind is assumed to be aligned with the rotor in all the cases. The floater responses from Load Case 2 for all different wave headings are compared in Figure 5.12. The frequency response comparison is given in Figure 5.13. From the frequency response, it is noticed that the sway, heave, roll

and yaw responses have higher energy contents at 90 degrees wave heading. At 180 degrees wave heading, all the responses have higher energy contents at higher frequencies except for sway and pitch responses. In the case of sway, the 90 degrees wave heading dominates throughout the spectrum, which was expected. This imply that the larger responses are also coinciding with response directions corresponding to lesser aerodynamic damping. For other cases, the 180 degrees wave heading imposes larger fluctuating forces opposite to the wind direction giving rise to much larger fluctuating responses based on whether the two fluctuating loadings are in or out of phase to each other and hence a repeating high frequency component.

The comparison shows that the wave heading at 90 and 180 degrees cases are more severe. It is observed that while 90 degrees wave heading is detrimental for sway, heave, roll and yaw responses, 180 degrees wave heading is severely affecting the surge and pitch responses.
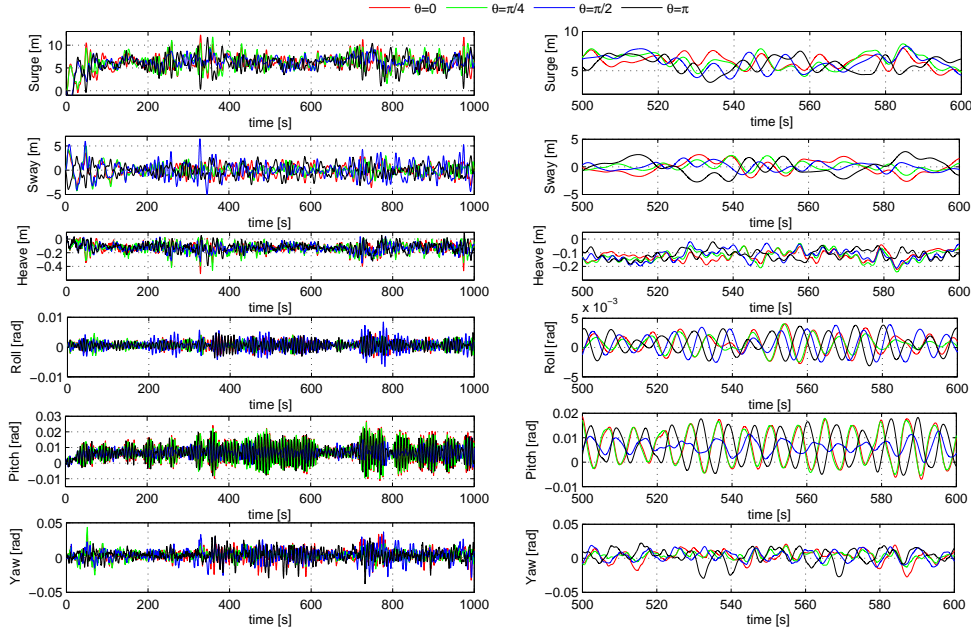
FIGURE 5.12: Response comparison - Load Case 2 for all wave heading

A statistical analysis is carried out between the Load Cases 1 and 2 for all the wave headings. Mean and standard deviation are used for the comparison. The comparison is shown in Figure 5.14. From the figure, it is noticed that the standard deviation of Load Case 2 has a slightly higher value compared to that of Load Case 1, which is explained by means of the higher fluctuation present in the turbulent wind compared to a constant mean flow. In the case of 90 degrees wave heading, the standard deviation for all the responses undergo a change, whereas for 180 degrees wave heading, only slight change is visible. The changes are explained as follows:

Considering the 0 degree wave heading responses as reference, in the case of 90 degrees wave heading, the surge force in 90 degrees is acting as a sway force in 0 degrees and vice versa. This is leading to a smaller standard deviation in surge and a higher standard deviation in sway compared to 0 degree wave heading responses. In the same manner, the increase in roll response (the cause being roll moment, which is a consequence of sway force) and the decrease in pitch response (the cause being pitch moment, which is a consequence of surge force) are also explained. Heave is not very much affected, however, yaw response undergo a similar change because of the resultant of roll and pitch moments causing the platform
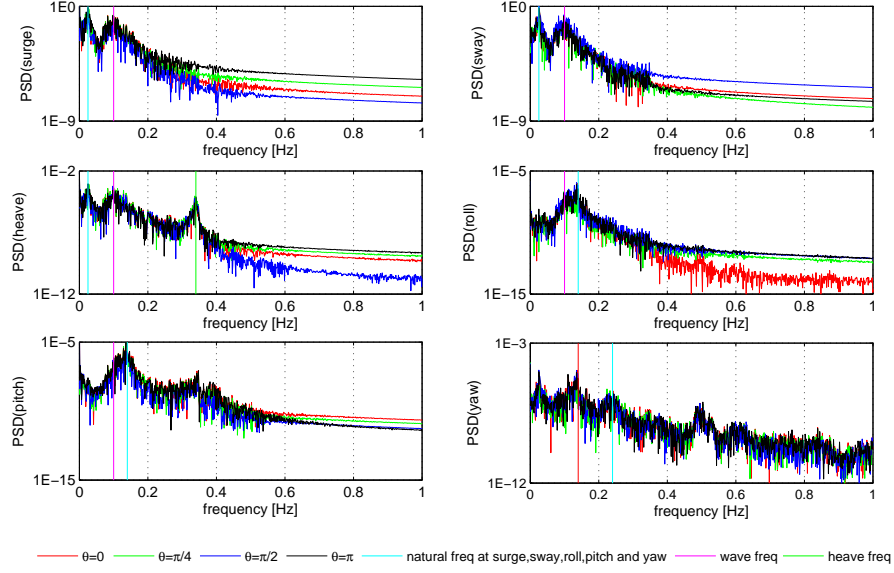
FIGURE 5.13: Frequency response comparison - Load Case 2 for all wave heading

yaw. The mean yaw response may be caused by the resultant of roll and pitch moments. The mean responses are unaffected because of the reason that the mean is dominated by the rotor loads.

FIGURE 5.14: Response statistics comparison - Load Cases 1 and 2 for all wave heading

5.5 3D coupling - conclusions

The following conclusions are made from the present chapter:

- A three dimensional fully coupled hydro-aero-elastic model was implemented for a floating TLP wind turbine with seventeen degrees of freedom. The aerodynamic loads were implemented using unsteady BEM, whereas the hydrodynamic loads were implemented using Morison's equation. 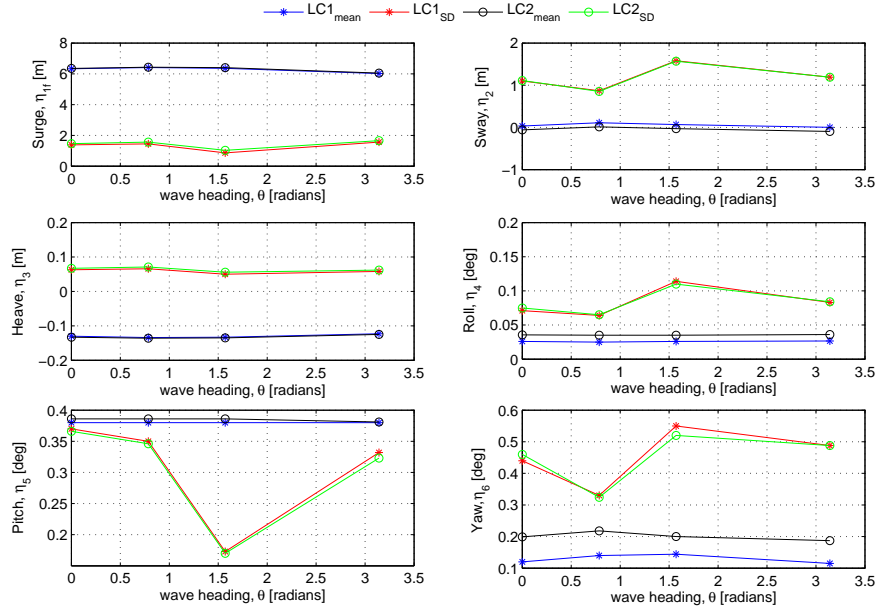The coupled loads and responses are predicted, which are compared to that of a two-dimensional response. The comparison confirms the three-dimensional implementation.

- Effects of wind shear and turbulence were implemented in the aerodynamic loads using a power law and spatially coherent turbulence model respectively. The presence of turbulence excites the low frequency responses and give rise to higher standard deviation for the responses.

- The effect of various wave headings have been implemented and responses were predicted. Comparison of the responses shows that the 90 and 180 degrees wave headings are critical load cases for the TLP configuration.

- Computations show that the fluctuating rotor torque is causing larger roll response, which needs specialized control algorithms or floater design optimization.

- From the results, the yaw response can be reduced by incorporating a damping and added mass contribution from the spokes by appropriately selecting the spokes dimensions through a parametric study.

- The above observations show that further implementing the model in an advanced aero-elastic code, Flex5, is necessary.

5.6 Summary

In this chapter, a three-dimensional representation of the problem is formulated and implemented. Test cases are conducted to validate the implementation with respect to 2D responses. Comparison of responses with 2D code provides excellent agreement. Different wave heading cases are studied and recommendations are made. Although the 3D code can represent the wind turbine reasonably well, the computation time is more. In addition, the absence of a comprehensive controller model limits the capability of the code to operate in broader operational conditions. These shortcomings can be overcome by implementing the concept in an advanced aero-elastic code, Flex5, which will be explained in the next chapter.

Flex5 Coupling

In this chapter, the three-dimensional hydrodynamics and platform dynamics are implemented in an advanced aero-elastic code Flex5. By default, the six degrees of freedom corresponding to the foundation are constrained, which represents an onshore wind turbine. In the present work, the constrained six foundation degrees of freedom are activated giving rise to a floating wind turbine model. The NREL 5MW reference wind turbine was implemented and verified for a set of test cases. Based on the analysis, recommendations / conclusions are made.

6.1 Flex5 description

Flex5 is a modal based code developed by Stig Øye at Technical University of Denmark, Øye (1996). Flex5 uses 28 degrees of freedom model for the wind turbine including six foundation degrees of freedom. Modeling of wind turbines using 28 degrees of freedom in Flex5 is carried out by reading in all the relevant input data of the wind turbine and environmental conditions through input files. The generalized equations of motion are formulated using the input data and are solved in Flex5 using the Runge-Kutta-Nystrom scheme as detailed in Hansen (2008).

6.1.1 Flex5 coordinate system

The coordinate system followed in Flex5 is illustrated in Figure 6.1. The sketch shows the coordinate system followed in Flex5 for a mono-pile wind turbine. The tower bottom has two coordinate systems, F and T, wherein F refers to a ground fixed system and T refers to a moving system, which can move along with the mono-pile deflection. The positive Z axis is pointing along the wind direction, X axis is pointing down and the Y axis is pointing into the plane. Compared to the coordinate system followed in the previous chapters for the Matlab code, the Flex5 coordinate system is somewhat different. This can be taken into account by a proper implementation of transformation matrices. The $K2$ system belongs to the tower top, which is a fixed coordinate system. From the $K2$ system, at the intersection of the tower centre line and main shaft, the K system is placed, which rotates along with the shaft. Moving from the K system towards the rotor centre, other coordinate systems such as $R1$ and R can be seen, which are rotating. However, the N system is a non-rotating system, which is located in the main bearing housing.
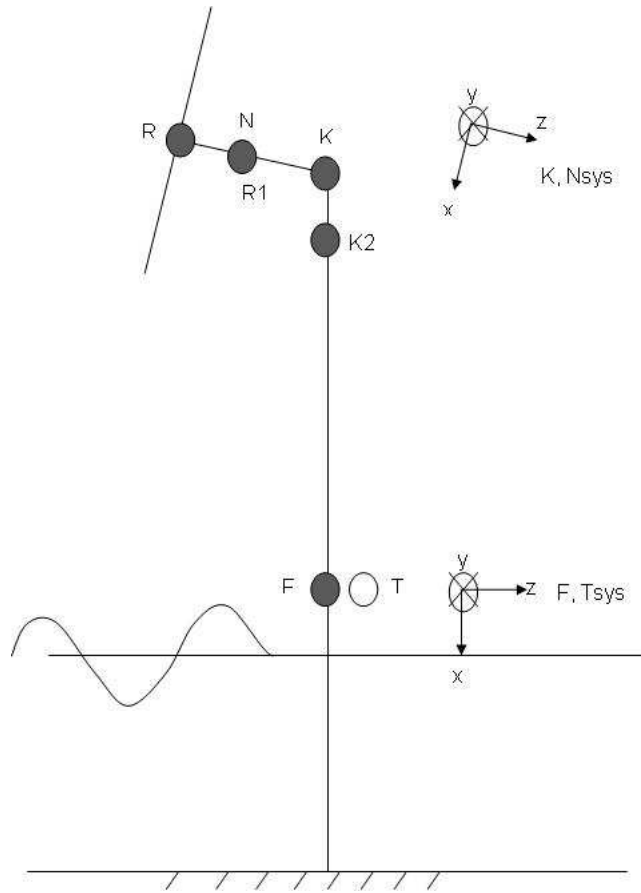
FIGURE 6.1: Flex5 coordinate system

6.1.2 Flex5 degrees of freedom

The degrees of freedom used in Flex5 aero-elastic code to represent a wind turbine are explained in Table 6.1.

TABLE 6.1: Flex5 - Degrees of freedom.

Flex5 Degrees of freedom	**Number of DOF**
Foundation top	1-6
Translation X (down) (heave)	1
Translation Z (horizontal downwind) (surge)	2
Rotation about Y (pitch)	3
Translation Y (sway)	4
Rotation about Z (roll)	5
Rotation about X (torsion in T_{sys})(yaw)	6
Tower top deflection (bending)	7-10
Longitudinal first mode	7
Longitudinal second mode	8
	Continued on next page

Table 6.1 – continued from previous page

Flex5 Degrees of freedom	Number of DOF
Transverse first mode	9
Transverse second mode	10
Nacelle	11-13
Rotation about X (yaw) (in K1 system)	11
Rotation about Y (tilt) (in K system to Nsys)	12
Shaft rigid body rotation about Z (in R1 system)	13
Shaft bending	14-15
Rotation about X (yaw mode)	14
Rotation about Y (tilt mode) (in R2 system to Rsys)	15
Deflection of Blade1 in V1sys	16-19
First flapwise mode (out of plane - Z)	16
Second flapwise mode (out of plane - Z)	17
First edgewise mode (in-plane - Y)	18
Second edgewise mode (in-plane - Y)	19
Deflection of Blade2 in V2sys	20-23
First flapwise mode (out of plane - Z)	20
Second flapwise mode (out of plane - Z)	21
First edgewise mode (in-plane - Y)	22
Second edgewise mode (in-plane - Y)	23
Deflection of Blade3 in V3sys	24-27
First flapwise mode (out of plane - Z)	24
Second flapwise mode (out of plane - Z)	25
First edgewise mode (in-plane - Y)	26
Second edgewise mode (in-plane - Y)	27
Shaft torsion in ZR1sys	28
Total	**28**

In the present formulation, the foundation module is modified to include the hydrodynamic loading, restoring forces from the mooring lines, time dependent mass matrix caused by the time dependent added mass term and the platform dynamics thereby making a floating foundation. The turbine can be made stiff by constraining the corresponding degrees of freedom. The hydrodynamic and mooring forces are treated as external loads apart from the gravity and buoyancy contributions, which are the static contributions to the loading.

6.1.3   Flex5 input data

Flex5 needs several input data related to the wind turbine, its control system, the environmental conditions such as wind, wave and current data, active and inactive degrees of freedom. The wind turbine data include various geometric, stiffness, mass, damping properties of the structural and mechanical components. The data for the structural components

are used to obtain the mode shapes such as the longitudinal and lateral modes for the tower and similarly the flapwise and edgewise modes for the blades. The second modes for these mode shapes are also calculated. Aerodynamic data such as lift, drag and moment coefficients for various angles of attack related to each of the airfoils used are provided through look up tables. Operational data such as wind speed, turbulence intensity, air density, rated speed are also provided. The control system, generator, mechanical brake, yaw system and the blade pitch controller can be modeled by providing corresponding parameters such as the controller gain, proportional and integral constants for a Proportional Integral (PI) controller, generator rpm, power and power loss, mechanical brake moment, time delay. The foundation data is provided through a separate data file, wherein the wave kinematics data are specified. The parent Flex5 version does not have the option for wave kinematics data, however, the idea is inspired by the offshore mono-pile version of Flex5. By this way, the surface elevation and wave kinematics data obtained externally are taken as input for wave load computations inside Flex5.

The present input data for the NREL 5-MW reference wind turbine was prepared based on Jonkman et al. (2009).

6.1.4 Flex5 wind data

The mean wind speed and turbulence intensity are provided in the input file along with the names of turbulence field files. The turbulence files are generated using a program, *vindsim*7. This program works based on the Mann turbulence model, Mann (1998), with rotational sampling. By rotational sampling, the wind fields are interpolated for the instantaneous azimuthal position of the blades so that a reasonable wind description for the location is obtained.

6.2 Flex5 development / modification

Modification of Flex5 to compute the floating wind turbine loads and responses is described in the following sections.

6.2.1 Flex5 coupling method

Coupling of the platform dynamics and wave loads with the basic Flex5 equations of motion is done using the following method. By default, Flex5 solves for the deflection, velocity and acceleration of the six degrees of freedom for the tower bottom point.

To have a rigid coupling between the tower bottom and foundation top points, the force balance needs to be maintained. Hence the equations of motion at the tower bottom point in Flex5 can be represented as given below.

$$[M]^F \{\ddot{\eta}\} + [C]^F \{\dot{\eta}\} + [K]^F \{\eta\} = \{F\}^F + \{F_c\} \tag{6.1}$$

Similarly, the equations of motion for the platform top may be expressed as:

$$[M]^H \{\ddot{\eta}\} + [C]^H \{\dot{\eta}\} + [K]^H \{\eta\} = \{F\}^H - \{F_c\} \tag{6.2}$$

where F_c represents the connection force, which ensures that the tower bottom is rigidly fixed to the platform top. The superscripts F and H represent *Flex*5 and *Hydrodynamics* respectively. Adding the above two equations gives rise to the following coupled equation, which is implemented in the coupled Flex5 model.

$$\left[M^F + M^H\right]\{\ddot{\eta}\} + \left[C^F + C^H\right]\{\dot{\eta}\} + \left[K^F + K^H\right]\{\eta\} = \{F\}^F + \{F\}^H \qquad (6.3)$$

The above equation illustrates that the coupling can be done by augmenting the mass, damping and stiffness matrices and the force vector with corresponding hydrodynamic contributions provided the coordinate transformations are carried out consistently. Thus by supplying $[M]^H$, $[C]^H$, $[K]^H$ and $\{F\}^H$ at each time step, Flex5 can include the motion of the substructure in the computations.

6.2.2 Flex5 modification

The foundation module of the basic Flex5 version is modified to accommodate the floating platform dynamics, which includes hydrodynamic loads and mooring forces. The wave kinematics data read from an external file is used to compute the hydrodynamic loads, which are computed at the instantaneous positions by Taylor expanding the wave kinematics data, in the space from the the mean position of the platform. The instantaneous wave kinematics at the specific time of integration are obtained by linear interpolation in the pre-computed data. It needs to be noted that the reference point for deriving the hydrodynamics forces using the wave kinematics is the centre point of floater bottom face, however, in Flex5, the reference point is at the intersection of the tower and foundation and the coordinate system is different than the one used for deriving platform dynamics. Hence a transformation is required from the floater bottom reference coordinate system to the Flex5 foundation coordinate system. This is carried out in two steps. The first step is the transformation from the floater coordinate system, *system O*, to the floater top coordinate system , *system T*. In the second step, a transformation is carried out on *system T* to obtain *system F*, which is the tower bottom Flex5 coordinate system. This is illustrated in Figures 6.2 to 6.3.
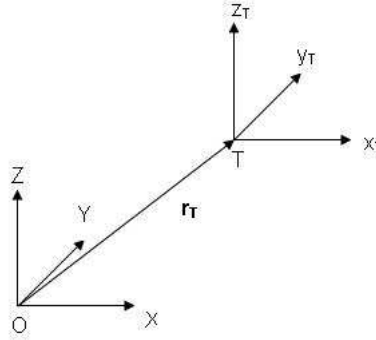
FIGURE 6.2: Coordinate system transformation from O to T

For the transformation from system O to T, the rotational displacements about T will be the same as that about O, whereas the translational displacements undergo a transformation, which is illustrated as follows:

$\eta_j^T = \eta_j^O$, for j = 4 to 6.

$$\left\{ \begin{array}{c} \eta_1 \\ \eta_2 \\ \eta_3 \end{array} \right\}^T = \left\{ \begin{array}{c} \eta_1 \\ \eta_2 \\ \eta_3 \end{array} \right\}^O + \left\{ \begin{array}{c} \eta_4 \\ \eta_5 \\ \eta_6 \end{array} \right\}^O \times \left\{ \begin{array}{c} r_T^1 \\ r_T^2 \\ r_T^3 \end{array} \right\} \qquad (6.4)$$

where the vector, connecting the reference points O and T, $\mathbf{r_T}$ is given by the following equation.
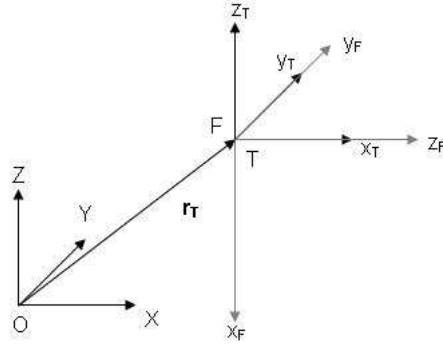
FIGURE 6.3: Coordinate system transformation from T to F

$$\mathbf{r_T} = \left\{ \begin{array}{c} 0 \\ 0 \\ h \end{array} \right\} \tag{6.5}$$

The transformation can be expressed in matrix form as follows:

$$\eta^T = [T_{OT}]\eta^O \tag{6.6}$$

$$\eta^O = [T_{TO}]\eta^T \tag{6.7}$$

where the transformation matrices are given by,

$$[T_{OT}] = \begin{pmatrix} 1 & 0 & 0 & 0 & r_T^3 & -r_T^2 \\ 0 & 1 & 0 & -r_T^3 & 0 & r_T^1 \\ 0 & 0 & 1 & r_T^2 & -r_T^1 & 0 \\ 0 & 0 & 0 & 1 & 0 & 0 \\ 0 & 0 & 0 & 0 & 1 & 0 \\ 0 & 0 & 0 & 0 & 0 & 1 \end{pmatrix} \tag{6.8}$$

$$[T_{TO}] = \begin{pmatrix} 1 & 0 & 0 & 0 & -r_T^3 & r_T^2 \\ 0 & 1 & 0 & r_T^3 & 0 & -r_T^1 \\ 0 & 0 & 1 & -r_T^2 & r_T^1 & 0 \\ 0 & 0 & 0 & 1 & 0 & 0 \\ 0 & 0 & 0 & 0 & 1 & 0 \\ 0 & 0 & 0 & 0 & 0 & 1 \end{pmatrix} \tag{6.9}$$

and

$$[T_{TO}] = [T_{OT}]^{-1} \tag{6.10}$$

Similar to the displacements, the forces in systems T and O can also be related through the transformation matrices. The forces in T are the same as those in O, ie, $F_{1..3}^T = F_{1..3}^O$, whereas the moments are different, which are given in the following equations.

$$F_{4..6}^T = F_{4..6}^O - \mathbf{r_T} \times F_{1..3}^O \tag{6.11}$$

The force transformation can be expressed in matrix form as follows:

$$F^T = [TF_{OT}]F^O \tag{6.12}$$

$$F^O = [TF_{TO}]F^T \tag{6.13}$$

where the transformation matrices, $[TF_{OT}]$ and $[TF_{TO}]$, are given by,

$$[TF_{OT}] = \begin{pmatrix} 1 & 0 & 0 & 0 & 0 & 0 \\ 0 & 1 & 0 & 0 & 0 & 0 \\ 0 & 0 & 1 & 0 & 0 & 0 \\ 0 & r_T^3 & -r_T^2 & 1 & 0 & 0 \\ -r_T^3 & 0 & r_T^1 & 0 & 1 & 0 \\ r_T^2 & -r_T^1 & 0 & 0 & 0 & 1 \end{pmatrix} \tag{6.14}$$

$$[TF_{TO}] = \begin{pmatrix} 1 & 0 & 0 & 0 & 0 & 0 \\ 0 & 1 & 0 & 0 & 0 & 0 \\ 0 & 0 & 1 & 0 & 0 & 0 \\ 0 & -r_T^3 & r_T^2 & 1 & 0 & 0 \\ r_T^3 & 0 & -r_T^1 & 0 & 1 & 0 \\ -r_T^2 & r_T^1 & 0 & 0 & 0 & 1 \end{pmatrix} \tag{6.15}$$

and

$$[TF_{TO}] = [TF_{OT}]^{-1} \tag{6.16}$$

In the second step, the displacements are transformed from system T to system F and vice versa, which are given below.

The displacement in system F is given by,

$$\eta^F = [T_{TF}]\eta^T \tag{6.17}$$

With the inverse transformation,

$$\eta^T = [T_{FT}]\eta^F \tag{6.18}$$

Similarly, the forces are also transformed from system T to F and vice versa using the following transformations.

$$F^F = [T_{TF}]F^T \tag{6.19}$$

$$F^T = [T_{FT}]F^F \tag{6.20}$$

where the transformation matrices $[T_{TF}]$ and $[T_{FT}]$ are given by,

$$[T_{TF}] = \begin{pmatrix} 0 & 0 & -1 & 0 & 0 & 0 \\ 0 & 1 & 0 & 0 & 0 & 0 \\ 1 & 0 & 0 & 0 & 0 & 0 \\ 0 & 0 & 0 & 0 & 0 & -1 \\ 0 & 0 & 0 & 0 & 1 & 0 \\ 0 & 0 & 0 & 1 & 0 & 0 \end{pmatrix} \tag{6.21}$$

$$[T_{FT}] = \begin{pmatrix} 0 & 0 & 1 & 0 & 0 & 0 \\ 0 & 1 & 0 & 0 & 0 & 0 \\ -1 & 0 & 0 & 0 & 0 & 0 \\ 0 & 0 & 0 & 0 & 0 & 1 \\ 0 & 0 & 0 & 0 & 1 & 0 \\ 0 & 0 & 0 & -1 & 0 & 0 \end{pmatrix} \tag{6.22}$$

and

$$[T_{FT}] = [T_{TF}]^{-1} \tag{6.23}$$

After obtaining the displacement and force transformations, the equations of motion are transformed from system T to system F.

The equations of motion in system O are represented as:

$$[\mathbf{M}]^O \{\ddot{\eta}\}^O + [\mathbf{C}]^O \{\dot{\eta}\}^O + [\mathbf{K}]^O \{\eta\}^O = \{F\}^O \tag{6.24}$$

The transformation of displacements in system O is given by:

$$\eta^O = [T_{TO}][T_{FT}]\eta^F \tag{6.25}$$

Inserting the above transformation in equation (6.24) implies the following equation of motion in system F.

$$[\mathbf{T}_{TF}][\mathbf{TF}_{OT}][\mathbf{M}]^O[\mathbf{T}_{TO}][\mathbf{T}_{FT}]\{\ddot{\eta}\}^F + [\mathbf{T}_{TF}][\mathbf{TF}_{OT}][\mathbf{C}]^O[\mathbf{T}_{TO}][\mathbf{T}_{FT}]\{\dot{\eta}\}^F +$$
$$[\mathbf{T}_{TF}][\mathbf{TF}_{OT}][\mathbf{K}]^O[\mathbf{T}_{TO}][\mathbf{T}_{FT}]\{\eta\}^F = \{F\}^F \tag{6.26}$$

The mass matrix in floater bottom coordinate system is given by the following equation.

$$[\mathbf{M}]^O = \begin{pmatrix} m_1 & 0 & 0 & 0 & m_{1,5} & 0 \\ 0 & m_2 & 0 & m_{2,4} & 0 & 0 \\ 0 & 0 & m_3 & 0 & 0 & 0 \\ 0 & m_{2,4} & 0 & m_4 & 0 & 0 \\ m_{1,5} & 0 & 0 & 0 & m_5 & 0 \\ 0 & 0 & 0 & 0 & 0 & m_6 \end{pmatrix} \tag{6.27}$$

where the non-zero mass elements in the mass matrix are the same as given in Appendix B for the 3D code implementation with only one difference. The difference is the absence of tower mass contribution in Flex5 implementation, whereas in the 3D code, the tower mass is divided into two parts by lumping it with sub-structure and with the tower top mass.

The mass matrix in the Flex5 coordinate system is given by the following equation.

$$[\mathbf{M}]^F = [\mathbf{T}_{TF}][\mathbf{TF}_{OT}][\mathbf{M}]^O[\mathbf{T}_{TO}][\mathbf{T}_{FT}] \tag{6.28}$$

In the above equation, all the transformation matrices and the mass matrix in floater bottom coordinate system, $[\mathbf{M}]^O$, were already given in the previous equations. The damping and stiffness contributions from the foundation are included in the mooring line terms. The hydrodynamic, restoring and static forces are transformed to the Flex5 system as given below.

$$[\mathbf{F_H}]^F = [\mathbf{T}_{TF}][\mathbf{TF}_{OT}][\mathbf{F_H}]^O \tag{6.29}$$

$$[\mathbf{F_R}]^F = [\mathbf{T}_{TF}][\mathbf{TF}_{OT}][\mathbf{F_R}]^O \tag{6.30}$$

$$[\mathbf{F_S}]^F = [\mathbf{T}_{TF}][\mathbf{TF}_{OT}][\mathbf{F_S}]^O \tag{6.31}$$

where $[\mathbf{F_H}]^O$ is the hydrodynamic force, $[\mathbf{F_R}]^O$ is the restoring force and $[\mathbf{F_S}]^O$ is the static force in the floater bottom coordinate system. All the transformations are linearly accurate as it assume small rotations. Computation of hydrodynamic force is detailed in section 3.6 of Chapter 3, whereas the restoring force calculation is explained in Appendix A. The static force is given in the following equation.

$$[\mathbf{F_S}]^O = \begin{Bmatrix} 0 \\ 0 \\ F_b - F_{G,f} \\ 0 \\ 0 \\ 0 \end{Bmatrix} \tag{6.32}$$

The only non zero term in the static force is the resultant of buoyancy force, F_b and floater gravity force, $F_{G,f}$.

6.2.3 Flex5 controller modification

The onshore wind turbine controller is modified to accommodate the floating foundation as described below. The NREL 5MW reference wind turbine has mainly three control regimes with two transition regimes. Control regime 1 corresponds to below cut-in wind speed, wherein the generator torque is zero, which will move to the second regime, in which the rpm is controlled for optimum tip speed ratio using the filtered generator rpm for a fixed pitch angle. In regime 3, which is above rated wind speed, the blade pitch is controlled to keep the power constant. The change over from one control regime to the other is obtained by a linear transition through the transition regimes.

In Flex5, the pitch controller uses three parameters for a Proportional-Integral-Derivative (PID) controller to represent the controller equations of motion, Hansen et al. (2005). For a linearized case, the Derivative terms is neglected giving rise to a PI controller with the following controller parameters Jonkman and Buhl (2005).

The proportional constant, K_P is given by,

$$K_P = \frac{2I_D\Omega_0\zeta_\varphi\omega_{\varphi n}}{N_{gear}\left(-\frac{\partial P}{\partial \theta}\right)} \tag{6.33}$$

Similarly, the integral constant, K_I is given by,

$$K_I = \frac{I_D\Omega_0\omega_{\varphi n}^2}{N_{gear}\left(-\frac{\partial P}{\partial \theta}\right)} \tag{6.34}$$

where I_D is the drive train inertia, $\Omega_0 = 12.1\ rpm$, the rated rotor speed, natural frequency and damping of the controller are $\omega_{\varphi n}$ and ζ_φ respectively. The gear box ratio is N_{gear} and $\left(-\frac{\partial P}{\partial \theta}\right)$ is the aerodynamic power sensitivity to the blade pitch angle.

Selection of a control frequency and damping will give rise to the K_P and K_I parameters. For an onshore turbine, the controller parameters are given by, $K_P = 0.08$ and $K_I = 0.028$. However, as reported by Larsen and Hansen (2007), the floating wind turbines may experience a pitch instability. For this reason, the influence of a range of control frequency parameters on the responses are investigated. Hence, four cases are considered, which are explained below.

Case 1 is the onshore control parameters, ie, $K_P = 0.08$ and $K_I = 0.028$, Case 2 corresponds to a control frequency of $2f_{surge}$, which gives rise to a $K_P = 0.0115$ and $K_I = 0.0027$. Case 3 is using a $K_P = 0.0033$ and $K_I = 1.67E-4$ corresponding to a control frequency of $0.5f_{surge}$ and finally, Case 4 corresponds to a control frequency of $3f_{surge}$, which gives rise to a $K_P = 0.0197$ and $K_I = 0.0006$.

Implementing these parameter, gives rise to the responses, which are compared in Figure 6.4. From the comparison, it can be observed that using the modified control parameters give rise to reduced responses. Except that the responses are slightly reduced, the pitch instability as referred by Larsen and Hansen (2007) could not be observed. The possibility is that the TLP configuration is not sensitive to the pitch instability. To confirm this conclusion, many test cases are carried out with different control frequencies and none of the results show any influence of platform pitch instability.
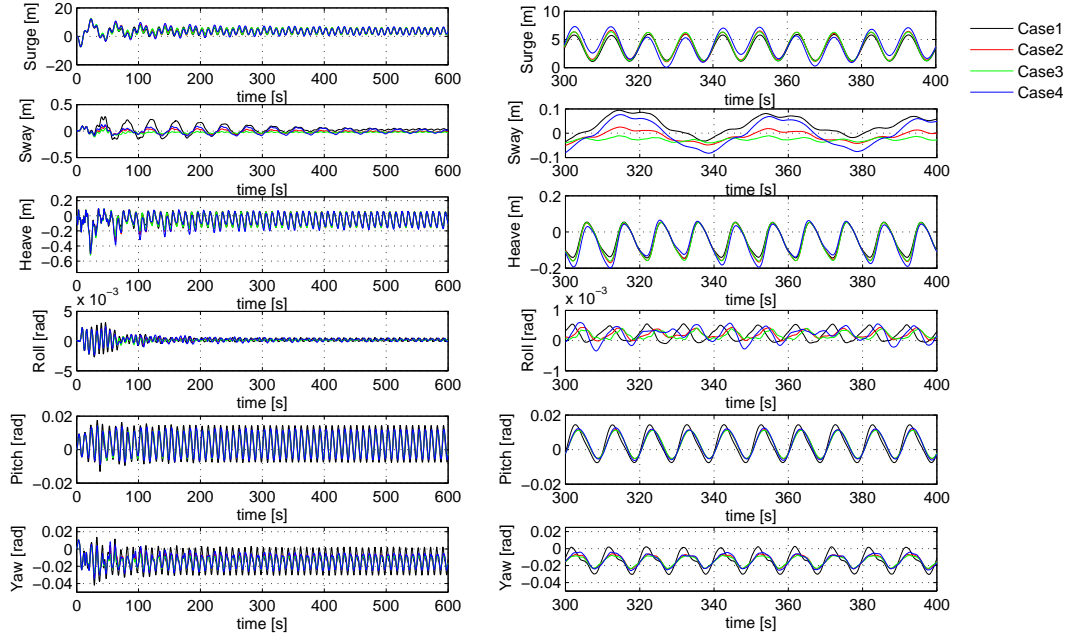
FIGURE 6.4: Controller influence on responses

6.3   Flex5 static stability test

The coupled model is tested to ensure the static stability. Hence the test was carried out by not applying wind or wave loading. Equilibrium in each of the degrees of freedom are computed by activating only one of the corresponding degrees of freedom and observing the response. If the system is in equilibrium, the response would be approximately zero.

The response statistics and the responses are provided in Table 6.2 and Figure 6.5 respectively. All the static stability responses are obtained by activating only the corresponding degree of freedom and constraining all the remaining foundation DOFs.

For the surge and sway static stability, the response is oscillating at the surge and sway natural frequencies with a very small magnitude. The heave response is zero to the machine accuracy level and hence it is not shown in the figure. The roll response is oscillating with very small magnitude. For the first 200 s, the response is influenced by the initial conditions and the steady state response has an abnormal behaviour. However, further investigation on this is not carried out because of the very small values of the response magnitude. The pitch and yaw responses are also oscillating at its natural frequencies with very small magnitudes.

The investigations show that the system is statically stable in its mean position.
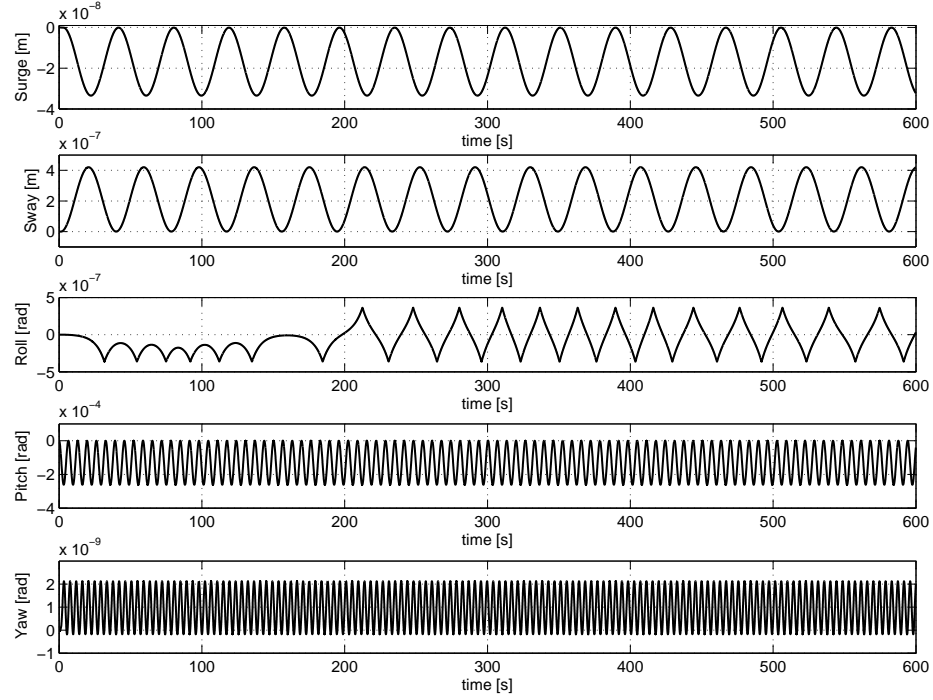
FIGURE 6.5: Static stability results

TABLE 6.2: Static stability results

	Mean	Std. deviation
Surge (m)	1.622E-8	1.181E-8
Sway (m)	2.096E-7	1.487E-7
Heave (m)	-3.481E-19	4.491E-20
Roll (rad)	-4.696E-8	1.821E-7
Pitch (rad)	-1.309E-4	9.245E-5
Yaw (rad)	9.684E-10	8.15E-10

6.4   Flex5 decay test

A decay test was conducted to test the response of the coupled system to an initial displacement in each of the degrees of freedom. While carrying out the tests, neither waves nor wind is present. The system is expected to oscillate in its natural frequencies. The oscillations would decay based on the amount of damping present. The presence of hydrodynamic damping is expected because of the motion of the platform in the still water. For all the tests, since a very low air density and wind speed are considered, the aerodynamic damping present in the system is negligible. The verification will also show the possible coupling effects present in the system when all the foundation degrees of freedom are active. Hence, all the tests consider two cases - Case 1 corresponds to the case where only one foundation DOF is active, whereas Case 2 deals with activating all the foundation DOFs. A summary of the decay test results with a comparison to that of the MATLAB code and analytical results is shown in the following table.

TABLE 6.3: Natural frequency comparison - Flex5, MATLAB and Analytical

	Flex5		MATLAB	Analytical
DOF	One DOF (Hz)	All DOF (Hz)	All DOF (Hz)	- (Hz)
Surge	0.026	0.026	0.026	0.026
Sway	0.026	0.026	0.026	0.026
Heave	0.34	0.34	0.34	0.34
Roll	0.15	0.15	0.15	0.15
Pitch	0.15	0.15	0.15	0.15
Yaw	0.23	0.23	0.23	0.23

6.4.1   Surge decay

The surge decay test is conducted by applying an initial displacement of 1 m in the surge degree of freedom. The system is expected to oscillate about its mean position.

Results are obtained for both Cases 1 and 2. Both of the cases provide identical surge response results and hence the result from Case 2 alone is shown in Figure 6.6, which shows the response is decaying, which is ascribed to the hydrodynamic damping present in the Morison's equation through the quadratic drag term.

The coupling effect can be observed from the heave response obtained for Case 2, as shown in Figure 6.7, which is due to the surge-heave coupling present in the system. The response is very small, which oscillates around the heave frequency and double the surge frequency, revealing the surge-heave coupling.
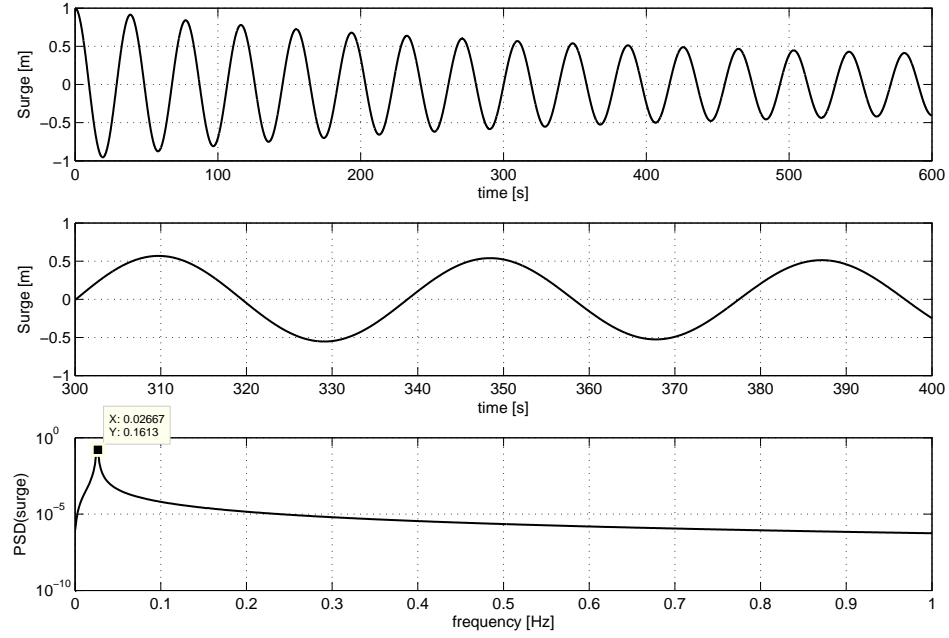
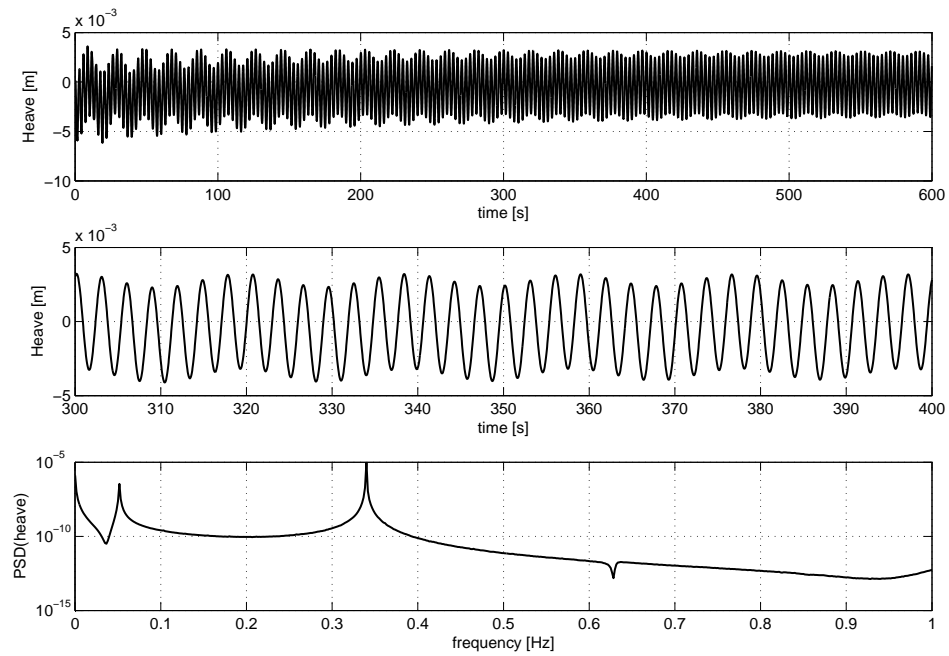FIGURE 6.6: Surge response for surge decay test - Case 2

FIGURE 6.7: Heave response for surge decay test

6.4.2 Sway decay

The sway decay test is also conducted for Cases 1 and 2 by applying an initial displacement of 1 m in the sway degree of freedom. The system is expected to oscillate at its natural frequency.

Similar to the surge, Case 2 result is only shown in Figure 6.8, which is oscillating at the sway natural frequency with the similar kind of damping. The sway - heave coupling can be observed from the Figure 6.9, wherein the response oscillates both at the heave and double the sway natural frequencies.
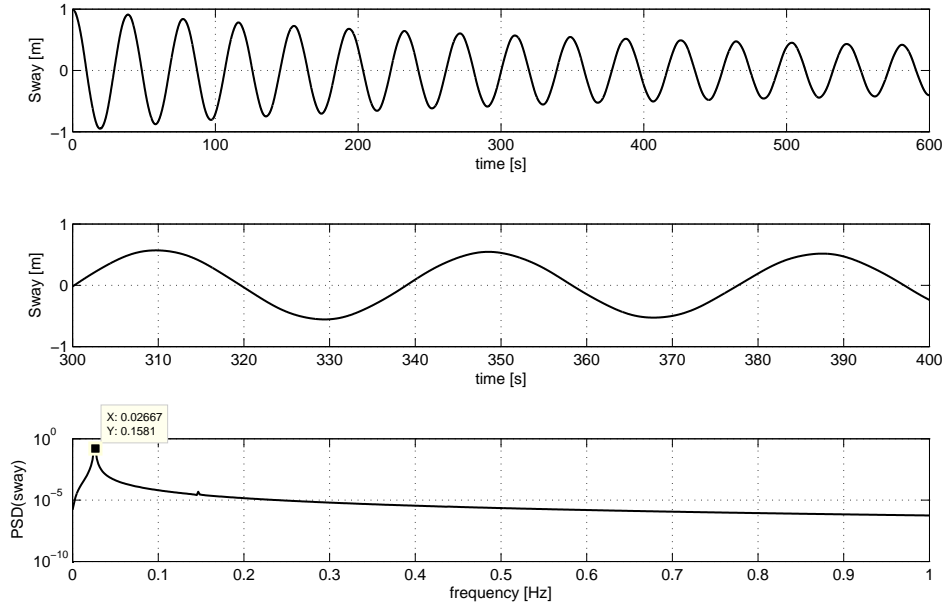
FIGURE 6.8: Sway response for sway decay test - Case 2
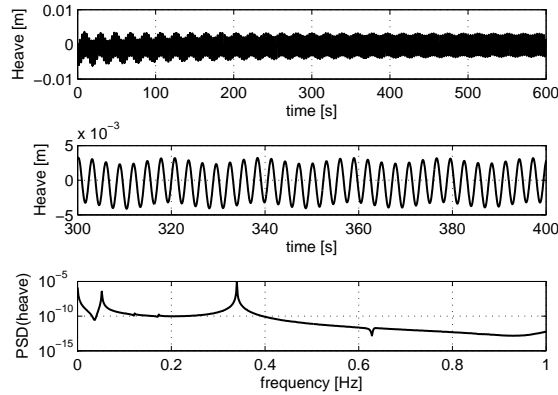
FIGURE 6.9: Heave response for sway decay test

6.4.3   Heave decay

The heave decay test is conducted for Cases 1 and 2 by applying an initial displacement of 0.1 m in the heave degree of freedom. Since there is no difference in the responses between the Cases 1 and 2, the results corresponding to the Case 2 is presented in Figure 6.10. Unlike other responses, the heave responses does not induce any coupled response because of the pure oscillations. The influence of hydrodynamic damping is also visible.
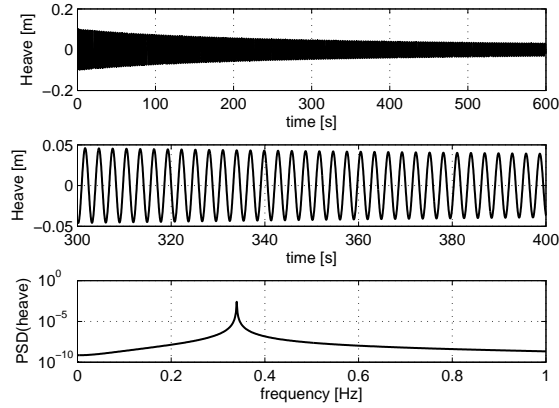
FIGURE 6.10: Heave response for heave decay test - Case 2

6.4.4   Roll decay

The roll decay test is carried out for both of the cases by applying an initial displacement of 1E-3 rad in the roll degree of freedom. The results for Case 2 are shown in Figure 6.11 because of the identical character of the results from both of the cases. The system is oscillating at its natural frequency (first peak) and at the tower sidewise frequency (second peak). This is because of the roll induced sidewise tower vibrations.

The results show that the response decay is very small compared to the other responses. This may be because the hydrodynamic damping in the roll degree of freedom is negligible compared to the translational degrees of freedom.
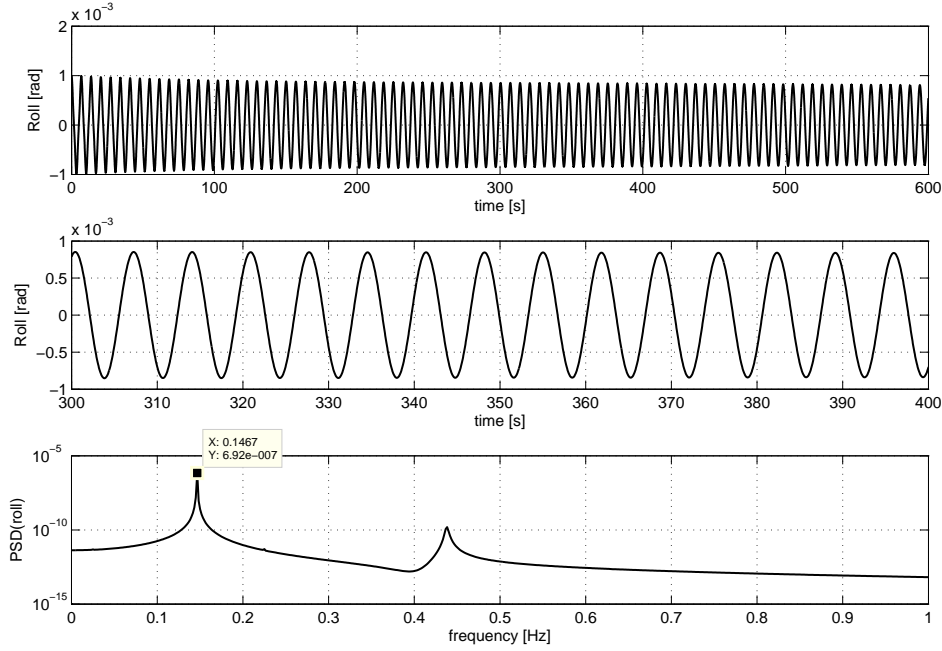
FIGURE 6.11: Roll response for roll decay test - Case 2

6.4.5   *Pitch decay*

The pitch decay test is also conducted for both of the cases by applying an initial displacement of 1E-3 rad in the pitch degree of freedom. The results for both Case 1 and Case 2 are given in Figures 6.12 and 6.13.

The results show that the response decay is very small for the Case 1 while a considerable amount of decay is present for the Case 2. The Case 1 response is identical to that of the roll response, whereas the decay present for the Case 2 is because of a combination of the hydrodynamic damping from the pitch and pitch induced surge motion and the structural damping from the tower flexibility.
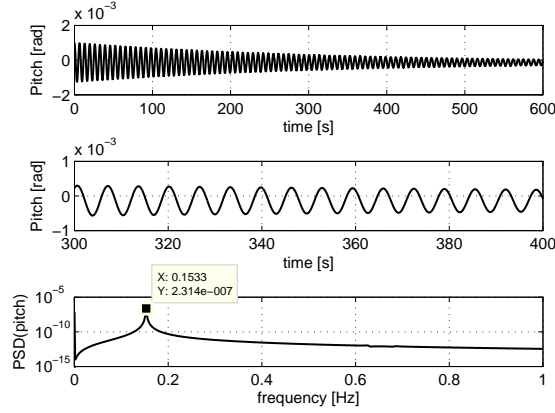
FIGURE 6.12: Pitch response for pitch decay test - Case 1
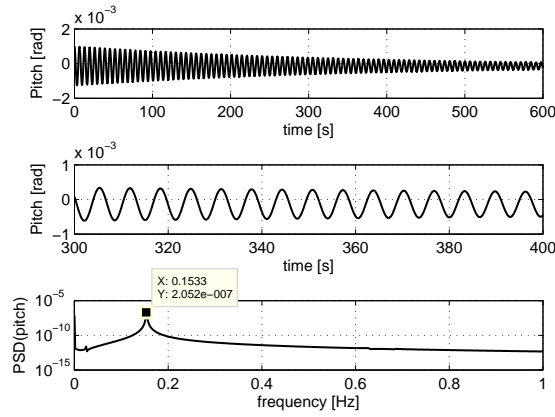
FIGURE 6.13: Pitch response for pitch decay test - Case 2

6.4.6   Yaw decay

The yaw decay test is carried out for Case 1 and 2 by applying an initial displacement of 1E-3 rad in the yaw degree of freedom. The results for Case 2 is given in Figure 6.14.

The results show that the response is oscillating with a constant amplitude and hence no response decay is present. The absence of response decay is because of the lack of hydrodynamic damping in the yaw degree of freedom as the hydrodynamic yaw moment is considered as zero. The second peak at around 0.83 Hz is due to the higher frequency from the tower.
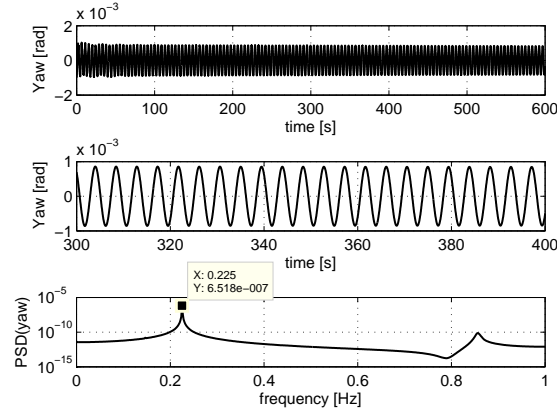
FIGURE 6.14: Yaw response for yaw decay test - Case 2

6.4.7   Combined roll and pitch decay

A decay test is carried out by applying an initial roll displacement of 1E-3 rad and a pitch displacement of 2E-3 rad. All the foundation degrees of freedom are active. Only relevant results are shown here.

The roll response is shown in Figure 6.15, which has a small decay. The response is oscillating at the roll natural frequency (0.15 Hz) and at the tower frequency (0.44 Hz).

The pitch response is shown in Figure 6.16, which has a considerable decay due to the damping contribution from the tower. The response is oscillating at the pitch natural frequency (0.15 Hz).

The yaw response is shown in Figure 6.17, which has no decay. The response is oscillating at the yaw natural frequency (0.23 Hz) and at the pitch (0.15 Hz) and tower (0.438 Hz) frequencies. From the yaw response, it is clear that on the absence of any of the yaw loading, the combined roll and pitch rotations induce yaw rotations and the yaw rotations are restored through the mooring system. Since the yaw natural period is less than all the other rotational natural periods, the system prefers to restore through the lowest period, which corresponds to the yaw natural frequency. This can also be confirmed from the frequency response plot in the figure.

FIGURE 6.15: Roll response for the combined decay test

FIGURE 6.16: Pitch response for the combined decay test
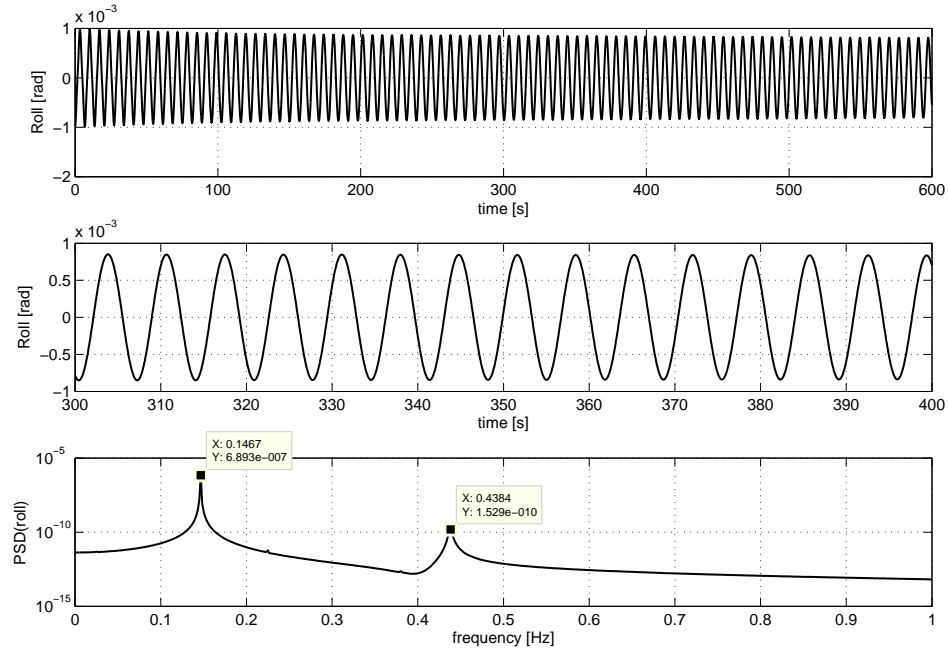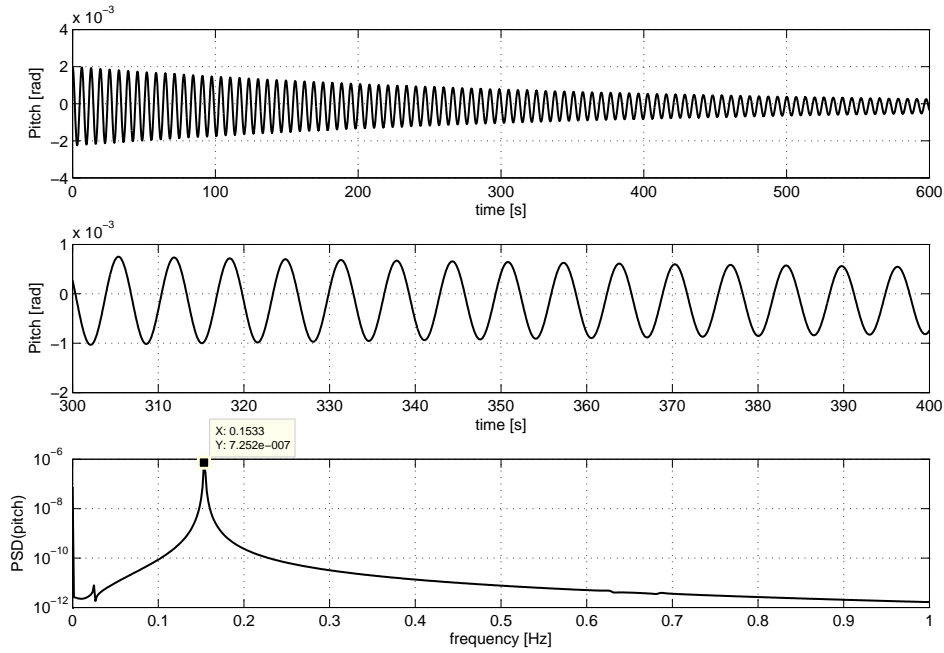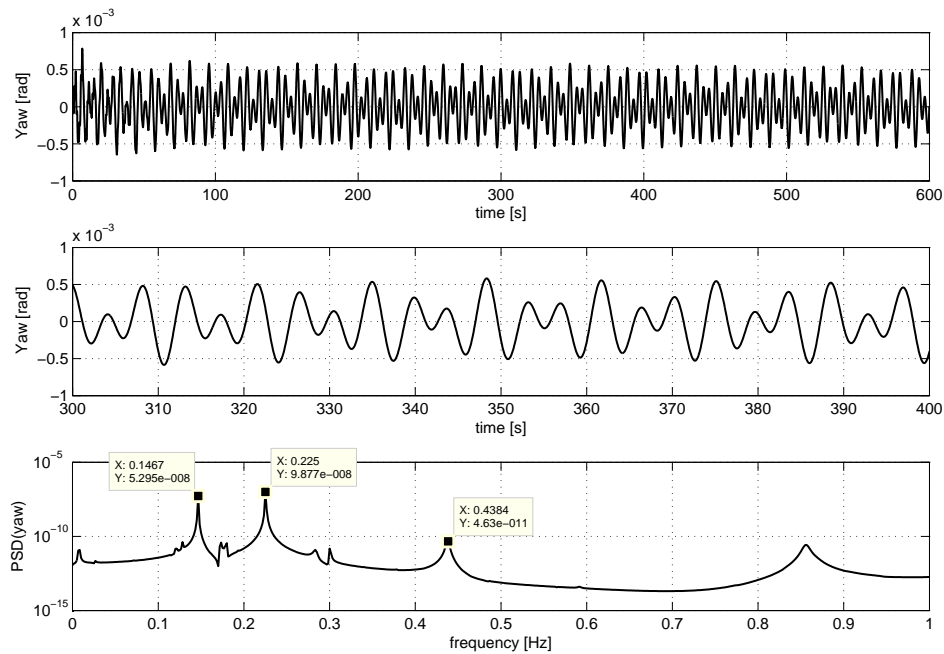

FIGURE 6.17: Yaw response for the combined decay test

6.5   Flex5 wave alone test cases

The Flex5 coupled code is tested for its capability to respond to wave alone situations. The following test cases are considered.

6.5.1   Two-dimensional regular wave with 0 degree wave heading

The TLP wind turbine model is subjected to two-dimensional regular waves with 0 degree wave heading. The generator is de-activated so that no power production is possible. The test results obtained are shown in the following figures.

The surge response obtained is given in Figure 6.18, which shows a regular variation of surge within the range of 5.7 m. Enlarged time series plot shows that the surge response is mainly caused by the waves with a frequency of 0.1 Hz. The frequency response shows the peaks corresponding to higher harmonics of the wave frequency and also a peak at the surge natural frequency (0.026 Hz) associated with the initial transient.
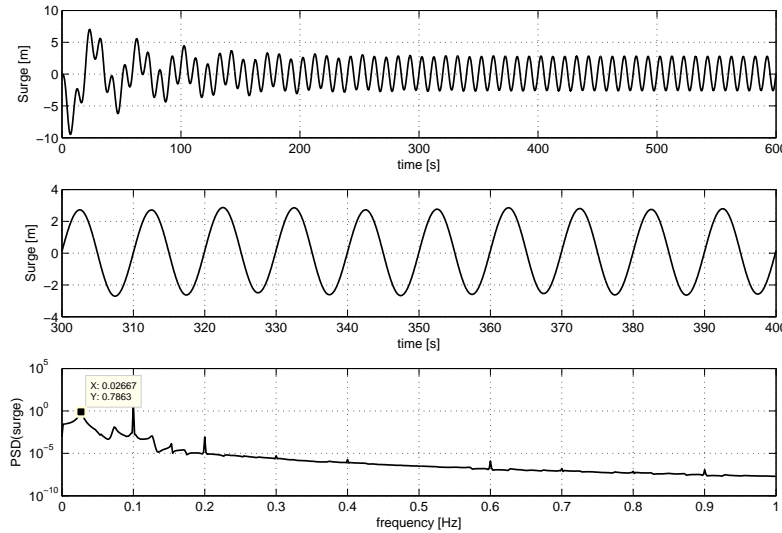
FIGURE 6.18: Surge response for 2D regular wave - 0 degree wave heading

Similar to the surge response, the sway response is shown in Figure 6.19. The sway response is smaller than the surge response as expected because of the predominant wave direction. The frequency response shows a major peak at the sway natural frequency of 0.026 Hz and at the roll natural frequency (0.15 Hz). The excitation at the roll frequency is caused by the roll induced sway response.

The heave response is shown in Figure 6.20, which shows a positive mean as expected. It needs to be noted that, in the previous chapters, the mean was negative because of the selection of the coordinate system. However, in Flex5, since the X axis is pointing down, mean response for the present case is positive. The negative part of the fluctuation is caused by the elastic deformation of the mooring system. In the frequency response, the major peaks are at the peak wave frequency and at the heave natural frequency (0.34 Hz). In addition, a peak at the double surge frequency is seen, revealing the surge-heave coupling. The double surge frequency is seen because of the absence of rotor thrust from wind, which is explained in section 4.1.6 of Chapter 4.
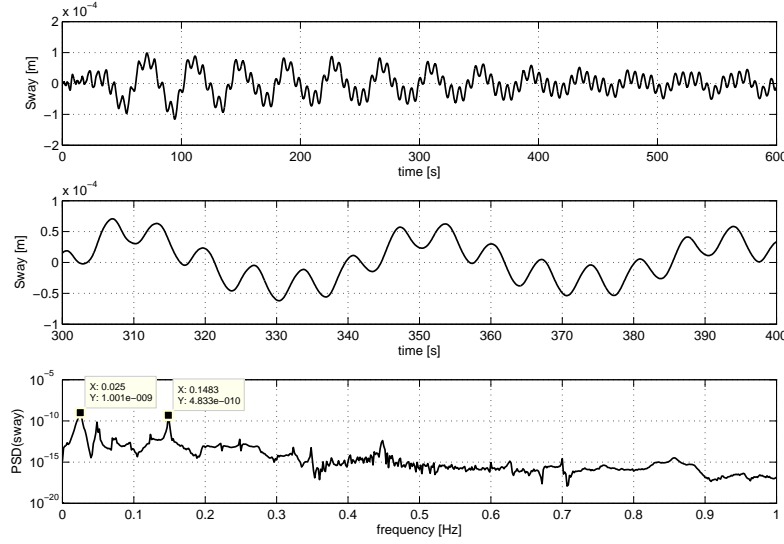
FIGURE 6.19: Sway response for 2D regular wave - 0 degree wave heading
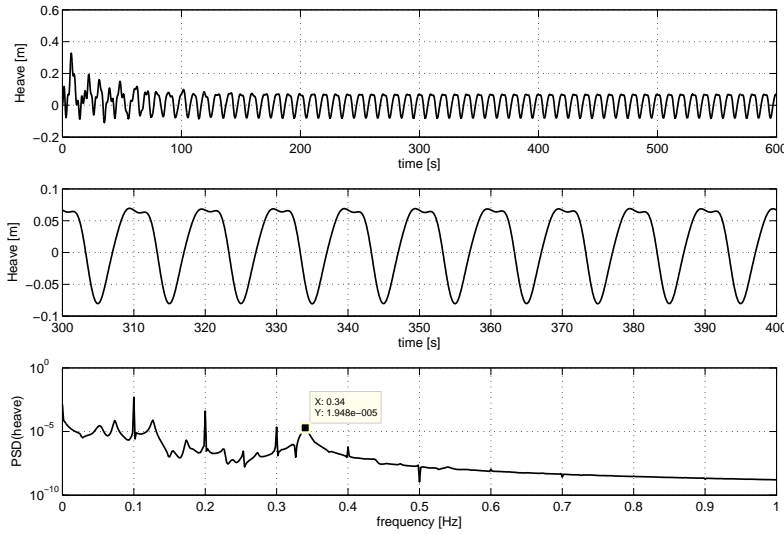
FIGURE 6.20: Heave response for 2D regular wave - 0 degree wave heading

The roll response is shown in Figure 6.21. The figure shows very small roll response, which is expected because of the predominant wave direction. A peak at the roll natural frequency (0.14 Hz) shows that the roll fluctuations are caused by a small excitation at the natural period.

The pitch response is given in Figure 6.22, which is fluctuating around zero mean with more or less constant range. The zero mean is because of the absence of rotor thrust from wind. The fluctuation is mainly caused by the wave excitation at its wave and higher wave harmonic frequencies. In addition, smaller excitations are visible at the surge (0.026 Hz)
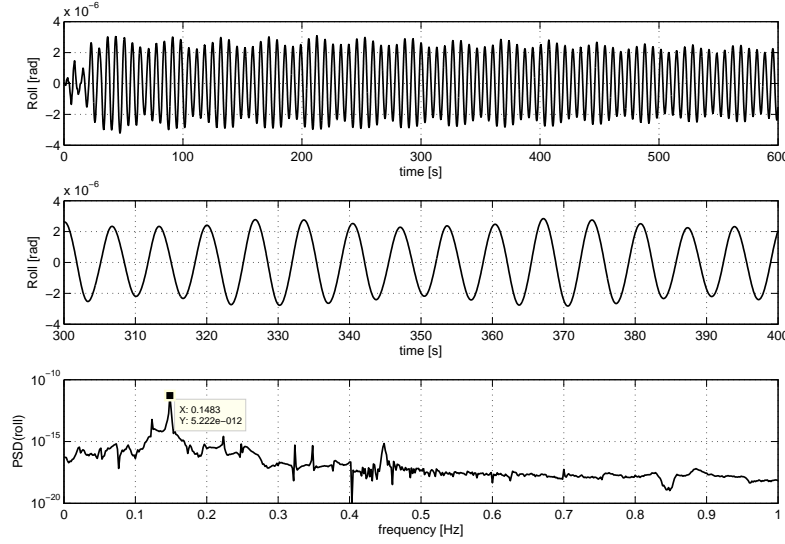
FIGURE 6.21: Roll response for 2D regular wave - 0 degree wave heading

and pitch natural frequencies (0.15 Hz). The surge natural frequency excitation is due to the surge-pitch coupling.
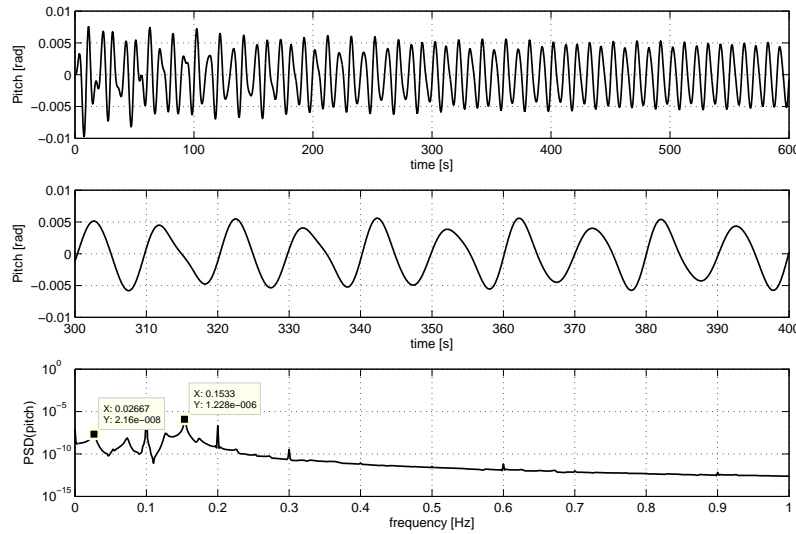
FIGURE 6.22: Pitch response for 2D regular wave - 0 degree wave heading

The yaw response is shown in Figure 6.23, which is fluctuating about almost zero mean. The modulation present in the response may be due to the closely spaced frequencies at 0.23 Hz and 0.2483 Hz, which can be seen in the frequency response. The difference between these closely spaced frequencies give rise to a frequency of 0.0253 Hz, which is corresponding to a time period of approximately 39 s, which is identical to the time period of the modulation. The two adjacent frequencies are corresponding to the yaw and lateral tower bending nat-

ural frequencies. The fluctuations are mainly caused by the natural frequency excitation, which can also be confirmed from the peaks at yaw (0.24 Hz) and heave (0.34 Hz) natural frequencies. In addition, a smaller peak at 0.85 Hz may be due to the tower excitation.
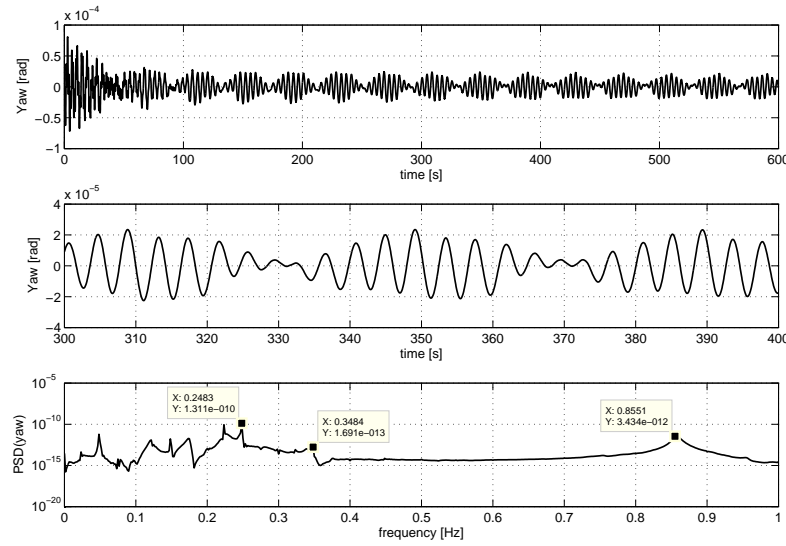
FIGURE 6.23: Yaw response for 2D regular wave - 0 degree wave heading

6.5.2   Two-dimensional regular wave with 45 degrees wave heading

The TLP wind turbine model is subjected to two-dimensional regular waves with 45 degrees wave heading. The test results are given below. All the responses are not shown here because either it has the similar characteristics of the previous case or it can be related to that of the previous case. However, the yaw response alone is shown here to demonstrates the differences in the response.

The surge response has a regular variation with a steady state range of 4 m. The range of 4 m can be related to the previous surge response by the simple relation of $5.7\cos(45)$. In other words, the amplitude can be related to the 0 degree case using the relation $a_{surge,0} = \sqrt{a_{surge,45}^2 + a_{sway,45}^2} = \sqrt{2^2 + 2^2} = 2.83$ and hence the response is verified. As in the previous case, the fluctuations are caused by the waves with a frequency of 0.1 Hz. The frequency response also has a smaller peak at surge natural frequency (0.026 Hz).

Unlike the 0 degree wave heading case, the sway response in the present case is equally significant as surge response corresponding to the range of $5.7\cos(45) \simeq 4m$. Similar to the surge response, the fluctuations are caused by the wave excitation corresponding to the peak wave frequency and a smaller natural frequency excitation at 0.026 Hz.

The heave response is fluctuating similar to the 0 degree case. The fluctuations are mainly caused by the waves; the peak wave frequency (0.1 Hz) and its higher harmonics and in addition the fluctuations around the natural period are also visible. Apart from these peaks, a smaller peak is also present at double the surge frequency (0.052 Hz), which is because of the surge-heave coupling.

The roll response has small roll fluctuations about zero mean mainly caused by the wave and natural period excitations, which can also be noticed from the peaks at 0.1 Hz, 0.2 Hz and 0.15 Hz. The roll fluctuation magnitude is much higher than that of 0 degree wave heading and comparable to that of the pitch fluctuation of the present case, which is expected because of the oblique wave heading.

The pitch response is fluctuating around a zero mean similar to the roll response. The fluctuation is mainly caused by the wave excitation (0.1 Hz and 0.2 Hz) and natural period excitation at 0.15 Hz. The pitch magnitude is comparable to that of the roll magnitude of the present case and that of the pitch magnitude of the 0 degree wave heading case, for which the maximum amplitude, 0.007 rad is equal to $\sqrt{2} \times 0.005$, wherein 0.005 rad is the maximum amplitude of the present case.

The yaw response is shown in Figure 6.24, which is fluctuating about a zero mean. The fluctuations are mainly caused by the natural frequency excitation, which can also be confirmed from the peaks at yaw (0.23 Hz) and heave (0.34 Hz) natural frequencies. A peak is also seen at the tower natural frequency.

The yaw response magnitude is much higher than that of the 0 degree wave heading. This may be a mooring-induced yaw because when the platform is subjected to a comparable magnitude of combined roll and pitch rotations, the restoring is achieved through the platform yaw degree of freedom by the moorings. The restoring is happening through the yaw degree of freedom because it has the lowest natural period compared to the other rotational degrees of freedom. This is also demonstrated in section 6.4.7.
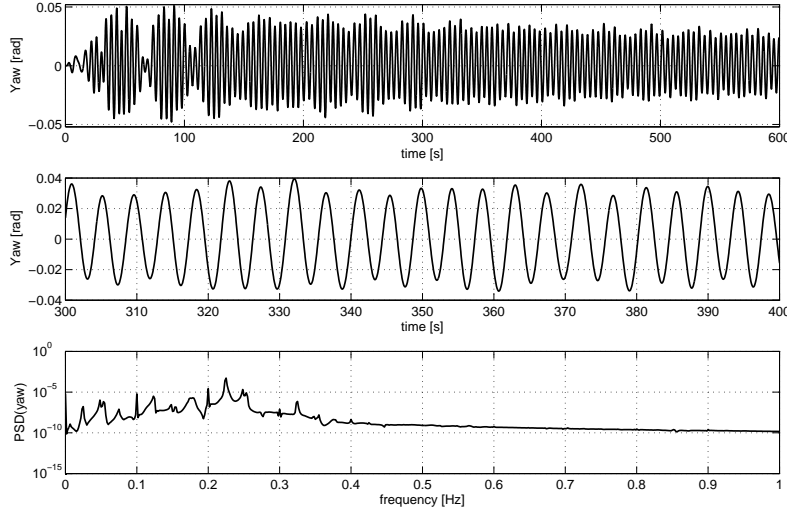
FIGURE 6.24: Yaw response for 2D regular wave - 45 degree wave heading

6.5.3 Response comparison for 2D regular waves with 0 and 90 degrees wave heading

A computation is carried out for a 90 degrees wave heading case and the responses are compared to that of the 0 degree wave heading case as described in section 6.5.1. Major differences are found when the 90 degrees wave heading roll response is compared to that of the 0 degree wave heading pitch response. This observation seems to be abnormal because both of these responses are expected to have similar characteristics. Investigations are carried out to identify the reasons for this difference and finally the root cause of this is identified as the influence of rotor orientation with respect to the wave direction. Hence, the rotor is yawed to 90 degrees and the responses are obtained for a 90 degrees wave heading, which give rise to identical responses with that of the 0 degree wave heading.

Perfect agreement is observed for the main two-dimensional responses viz. surge, heave and pitch considering 0 degree wave heading as reference. Because the 2D waves primarily induces the 2D responses, which will have a better comparison, whereas the additional degrees of freedom responses are due to the second order effects. Because of the presence of the second order effects, which could not be captured completely due to a certain linear accuracy of the problem formulation, the comparison of these responses may not produce perfect results. The comparisons are given in the following.

Surge and Sway responses comparison A comparison of the surge response from 0 degree wave heading and the sway response from 90 degrees wave heading is shown in Figure 6.25, which shows a very good agreement between the two responses. Since both of the responses are on top of each other, it can not be distinguished.

Similarly a comparison of the sway response from 0 degree wave heading and the surge response from 90 degrees wave heading is shown in Figure 6.26. The responses do not compare very well. Although the responses are different, both are smaller in magnitude.
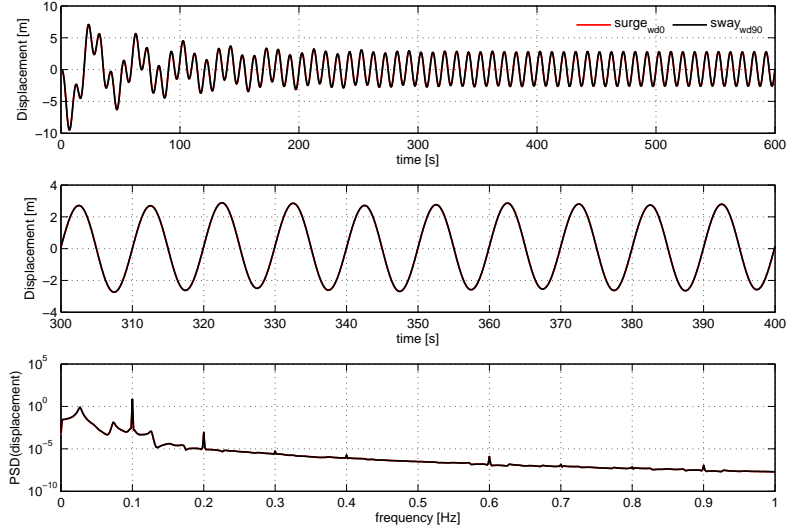
FIGURE 6.25: Surge and sway responses comparison for 2D regular wave - 0 and 90 degrees wave heading
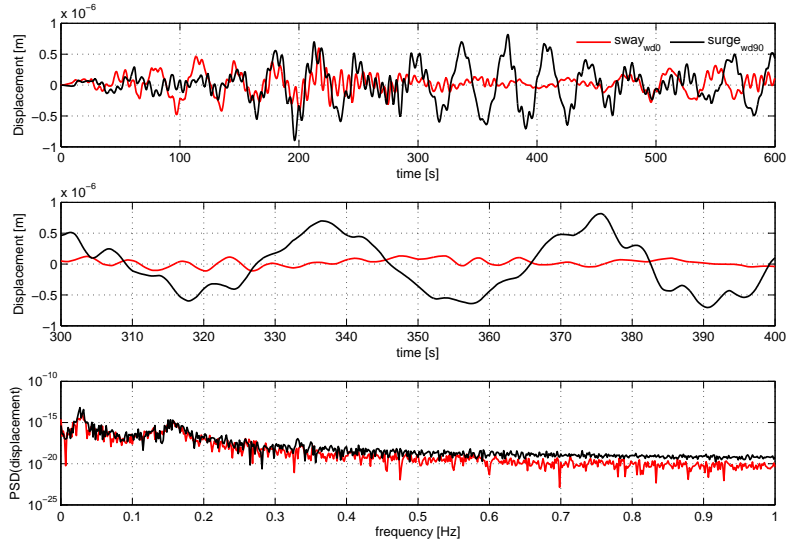
FIGURE 6.26: Sway and surge responses comparison for 2D regular wave - 0 and 90 degrees wave heading

Heave response   A comparison of the heave responses from 0 and 90 degrees wave heading is shown in Figure 6.27, which shows a very good agreement between the two responses.

Roll and Pitch responses comparison   A comparison of the pitch response from 0 degree wave heading and the roll response from 90 degrees wave heading is shown in Fig-
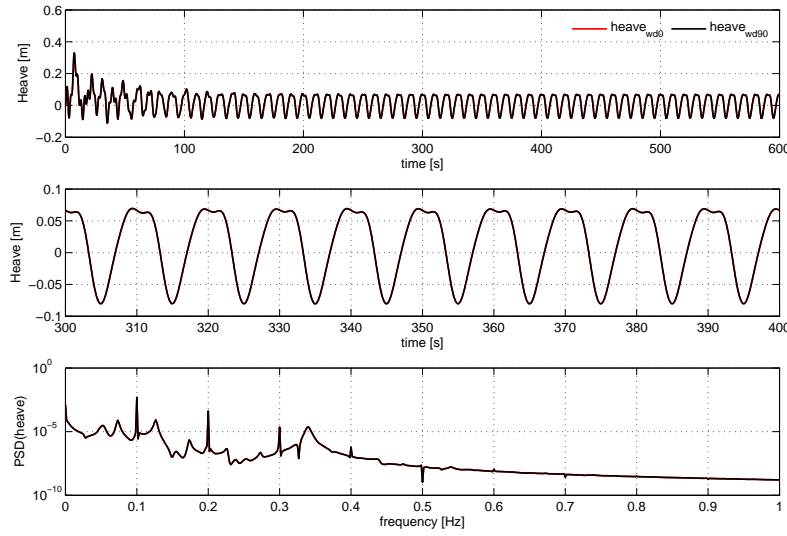
FIGURE 6.27: Heave response comparison for 2D regular wave - 0 and 90 degrees wave heading

ure 6.28. The responses show a good agreement in both amplitude and frequency, however with a difference in phase. The difference in phase is due to the negative roll moment produced by the waves heading in the positive y direction.
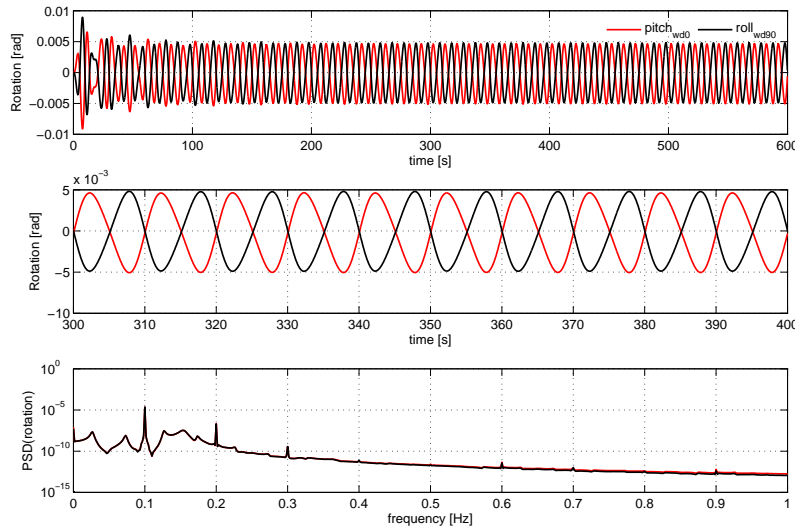
FIGURE 6.28: Pitch and roll responses comparison for 2D regular wave - 0 and 90 degrees wave heading

Similarly a comparison of the roll response from 0 degree wave heading and the pitch response from 90 degrees wave heading is shown in Figure 6.29, which are very small in magnitudes. The responses do not compare very well. This may be because these responses are the

consequence of the second order effects present in the system for a 2D forcing, however with a limited linear accuracy in the formulation.
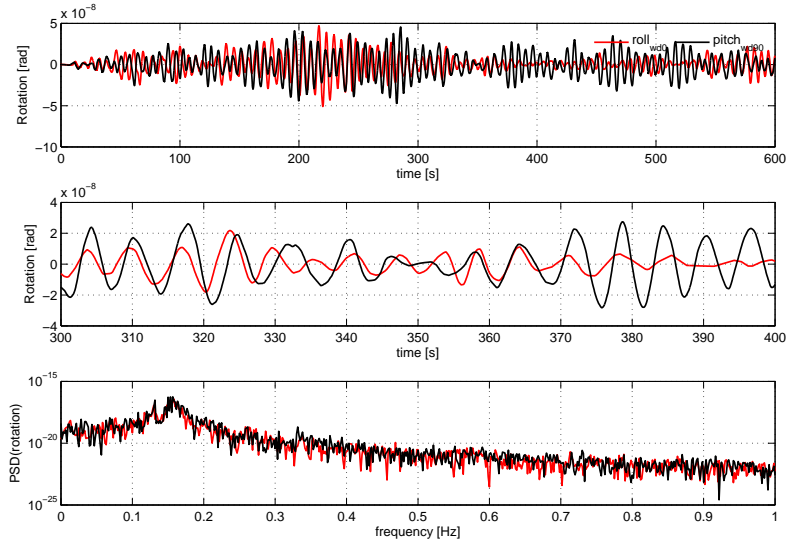
FIGURE 6.29: Roll and pitch responses comparison for 2D regular wave - 0 and 90 degrees wave heading

Yaw response   A comparison of the yaw responses from 0 and 90 degrees wave heading is shown in Figure 6.30. The yaw response is small as expected since excitation of the yaw degree of freedom is secondary for 2D regular waves. The responses do not compare very well because of the same reasons for the other response differences.
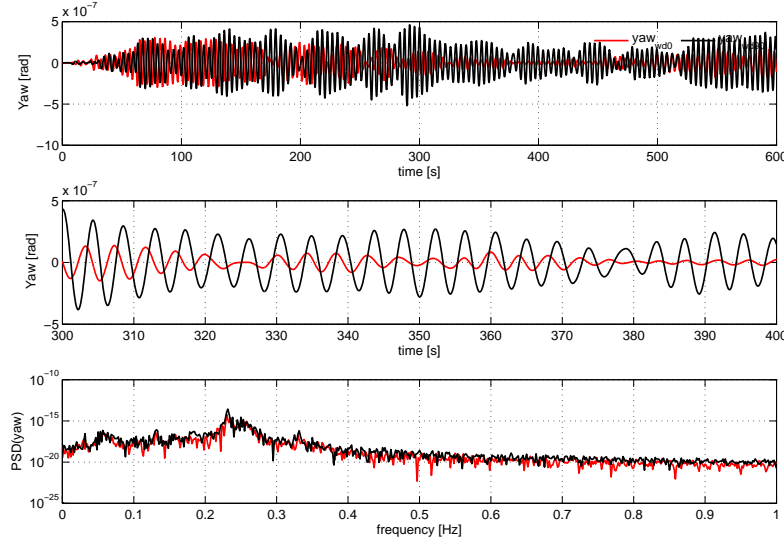
FIGURE 6.30: Yaw response comparison for 2D regular wave - 0 and 90 degrees wave heading

6.6 Response comparison for Flex5 and MATLAB coupled codes

Test cases are carried out to compare the response predicted by the MATLAB and modified Flex5 codes. In addition, the tests reveal some of the effects due to the influence of wind, tower flexibility, gyroscopic force, varying generator moment and roll and mooring induced yaw coupling. From each of the test cases, differences in the responses are identified along with a discussion of the root causes.

6.6.1 Case 1

Case 1 considers 2D regular waves with 10 m/s constant mean wind speed with the tower lateral flexibility constrained in the Flex5 code. The tower lateral flexibility is constrained because the MATLAB code is not equipped with this degree of freedom. In addition, the platform pitch degree of freedom is constrained in both of the codes so that the gyroscopic effect due to the platform motion is absent. The response comparison is shown in the following figures. The differences observed in the responses are mainly due to the comprehensive control action present in Flex5. Since the platform pitch degree of freedom is constrained, the pitch response is zero and hence the comparison is not shown.

The transient response phase of Flex5 is about 400 s due to the way the initial conditions are set up.

Comparing the yaw response with that of Case 3 would reveal the influence of the gyroscopic forces. In addition, comparing the yaw response with that of Case 2 would reveal the influence of the tower flexibility.

The surge responses compare well both in time and in frequency domains. However, Flex5 code slightly overestimates the mean response, which may be due to a slightly higher thrust caused by the instantaneous control action present in the Flex5 code. While the platform has a surge velocity, the effective velocity seen by the blade is slightly more when both the wind and the platform velocities are out of phase and vice versa. Based on the relative

velocity, the blade pitch angle is regulated in Flex5 by a built-in pitch-controller, which is not available in MATLAB code and hence a small difference in the response is present. In addition, since the wind speed is below rated, the rotor rpm is controlled by an rpm controller in Flex5, which is also not present in MATLAB code. The comparison is shown in Figure 6.31.
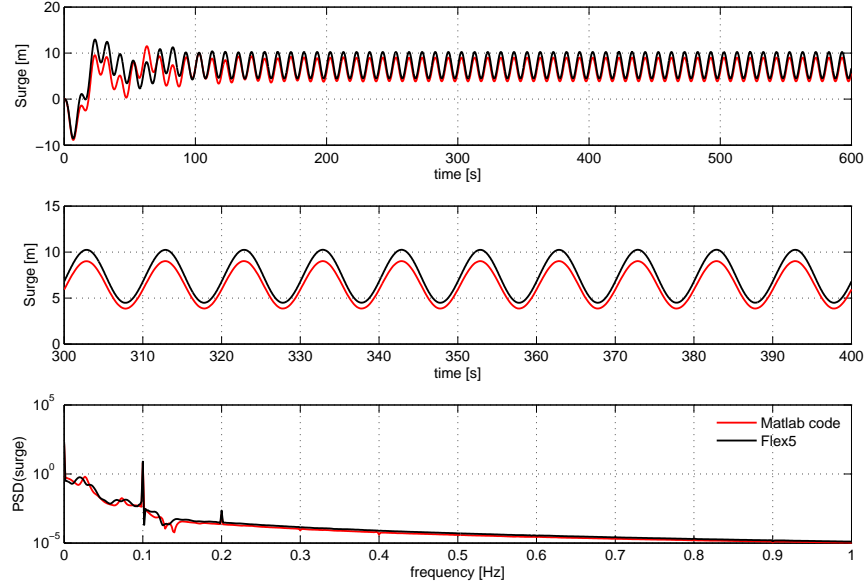
FIGURE 6.31: Case 1 - Surge response comparison (Flex5 and Matlab code)

The sway response is quite small compared to that of the surge response. The response predicted by Flex5 has large difference up to 400 s compared to that of MATLAB code, which is because of the influence of initial conditions in Flex5. However, above 400 s, both of the responses are in the same range with a small difference in mean, which may be caused by the roll moment (rotor torque) from the rotor, which is controlled proportional to the rpm in Flex5. The comparison is shown in Figure 6.32.

The heave response also compares well both in time and in frequency domains. Similar to surge response, Flex5 over-predicts heave response slightly, which is proportional to the influence of surge-heave coupling. This can also be confirmed from the slight frequency shift in the surge natural frequency. The comparison is shown in Figure 6.33.

Similar to the sway response, the roll response also has influence from the initial conditions, however, Flex5 over-predicts roll response, which may be mainly due to the rpm control in the Flex5 code. This can also be confirmed from the high frequency fluctuations present in Flex5. In addition, the roll-yaw coupling present in the restoring force also causes a difference in the response, which is observed from a peak in the frequency response at yaw natural frequency. The comparison is shown in Figure 6.34.

The yaw responses comparison is shown in Figure 6.35. The response is mostly of high frequency type, mainly due to the mooring induced roll-yaw coupling as described in section 6.4.7, which can be observed in the frequency response peak at the roll natural frequency. In addition, the rpm control in Flex5 also plays a role in the difference in responses.

FIGURE 6.32: Case 1 - Sway response comparison (Flex5 and Matlab code)

FIGURE 6.33: Case 1 - Heave response comparison (Flex5 and Matlab code)

FIGURE 6.34: Case 1 - Roll response comparison (Flex5 and Matlab code)

FIGURE 6.35: Case 1 - Yaw response comparison (Flex5 and Matlab code)

6.6.2   Case 2

Case 2 considers 2D regular waves with 10 m/s constant mean wind speed with the tower lateral flexibility constrained in the Flex5 code. Compared to Case 1, the pitch degree of freedom is not constrained in this case and hence the influence of gyroscopic effect can also be observed in the yaw response compared to that of Case 1. The response comparison is shown in the following figures. The differences observed in the responses are due to a combined effect of the control action and gyroscopic forces.

The surge responses compare well both in time and in frequency domains. The differences are similar to that of Case 1 and the comparison is shown in Figure 6.36.

FIGURE 6.36: Case 2 - Surge response comparison (Flex5 and Matlab code)

The sway response comparison is also similar to that of Case 1, however, the difference in steady state mean is larger compared to that of Case 1. This may be due to the larger energy content available at the roll natural frequency and an associated peak at the yaw natural frequency in the Flex5 response, which shows a stronger influence from the roll-yaw coupling. The comparison is shown in Figure 6.37.

The heave response comparison also has a similar character as that of Case 1, which is shown in Figure 6.38.

The roll response predicted by Flex5 has larger fluctuation compared to that of MATLAB code, which may be due to the strong influence of roll-yaw coupling and the control action of rotor rpm. The comparison is shown in Figure 6.39.

The pitch response also compares well with the Flex5 response having slightly higher fluctuation. The higher fluctuation may be due to the influence of rotor tilt moment acting on the platform. Since the rotor tilt degree of freedom is not available in the MATLAB code, this effect could not be captured in the pitch response. The comparison is shown in Figure 6.40.

Unlike Case 1, the yaw response predicted by Flex5 has larger fluctuation (both in terms of mean and standard deviation), which is mainly due to the influence of gyroscopic effect, which was absent in Case 1. The gyroscopic effect is an additional yaw moment produced

FIGURE 6.37: Case 2 - Sway response comparison (Flex5 and Matlab code)
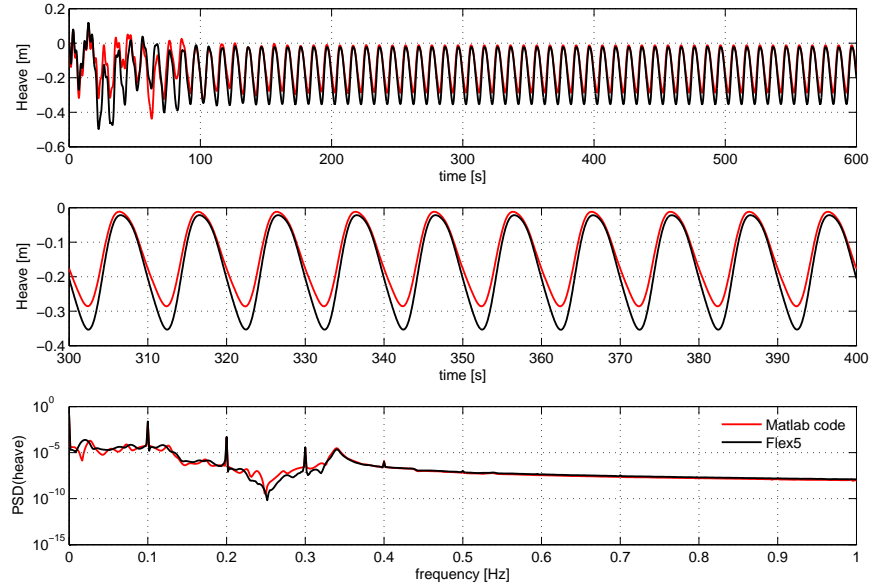
FIGURE 6.38: Case 2 - Heave response comparison (Flex5 and Matlab code)

when a spinning rotor is subjected to a rotor tilt or a platform pitch motion, which is not present in the MATLAB code. This can be observed in the Flex5 frequency response through the peaks at pitch and yaw natural frequencies. The comparison is shown in Figure 6.41.
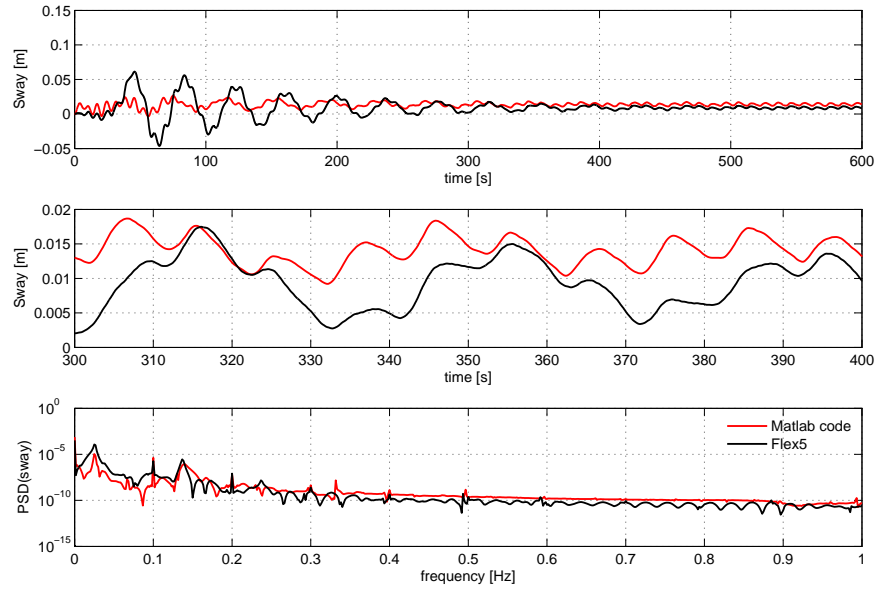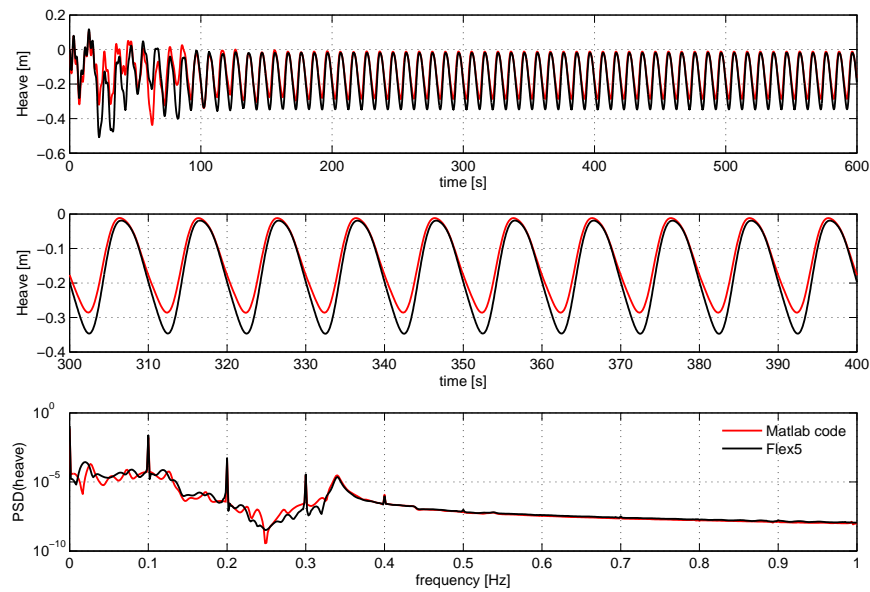
FIGURE 6.39: Case 2 - Roll response comparison (Flex5 and Matlab code)

FIGURE 6.40: Case 2 - Pitch response comparison (Flex5 and Matlab code)

FIGURE 6.41: Case 2 - Yaw response comparison (Flex5 and Matlab code)

6.6.3   Case 3

Case 3 considers 2D regular waves with 10 m/s constant mean wind speed. Compared to the Cases 1 and 2, none of the degrees of freedom are constrained in both of the codes. The response comparison is shown in the following figures. The differences observed in the responses are having a combined effect of the tower flexibility, control action and gyroscopic forces. Compared to Case 2, the tower flexibility induces more yaw responses through roll-yaw coupling.

The surge responses compare with a small difference in the mean, which may be due to a difference in rotor thrust predicted by Flex5 and MATLAB code. The comparison is shown in Figure 6.42.
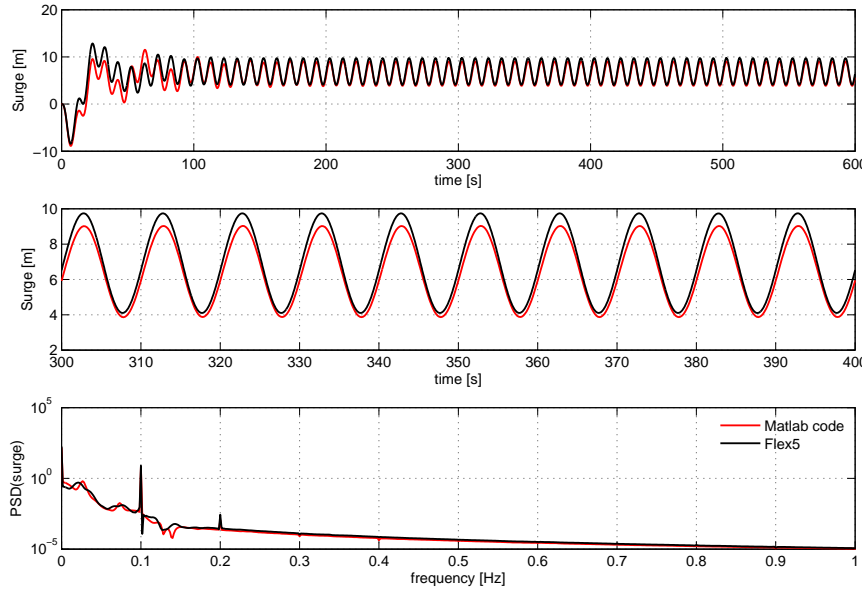
FIGURE 6.42: Case 3 - Surge response comparison (Flex5 and Matlab code)

The sway response comparison is similar to that of Case 2. The tower lateral flexibility present in Flex5 also influence the difference in the mean sway response. The comparison is shown in Figure 6.43.

The heave response comparison has a similar character as that of Cases 1 and 2, which is shown in Figure 6.44.

The roll response fluctuation in Flex5 is larger compared to that of MATLAB code, which may be due to the tower lateral flexibility present in Flex5 code and also the other reasons stated for cases 1 and 2. The comparison is shown in Figure 6.45.

The pitch response predicted by Flex5 has more fluctuation, which may be due to the influence of rotor tilt moment acting on the platform. Since the rotor tilt degree of freedom is not present in the MATLAB code, this effect could not be captured in the pitch response. The comparison is shown in Figure 6.46.

The yaw response predicted by Flex5 has much larger fluctuation, which is mainly due to the influence of the gyroscopic effect and the tower lateral flexibility. The tower lateral flexibility induces higher yaw moment which in turn produces higher yaw response. The comparison is shown in Figure 6.47.

FIGURE 6.43: Case 3 - Sway response comparison (Flex5 and Matlab code)

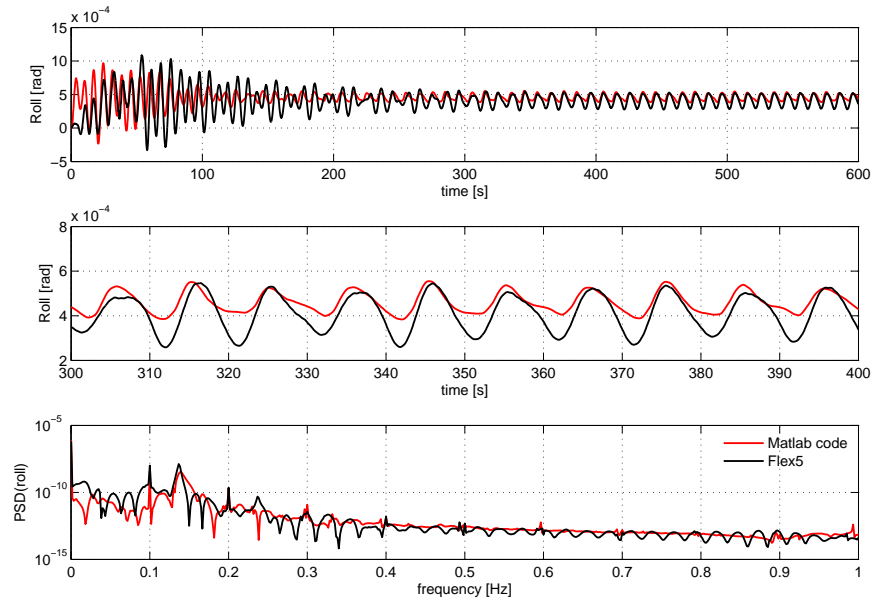FIGURE 6.44: Case 3 - Heave response comparison (Flex5 and Matlab code)
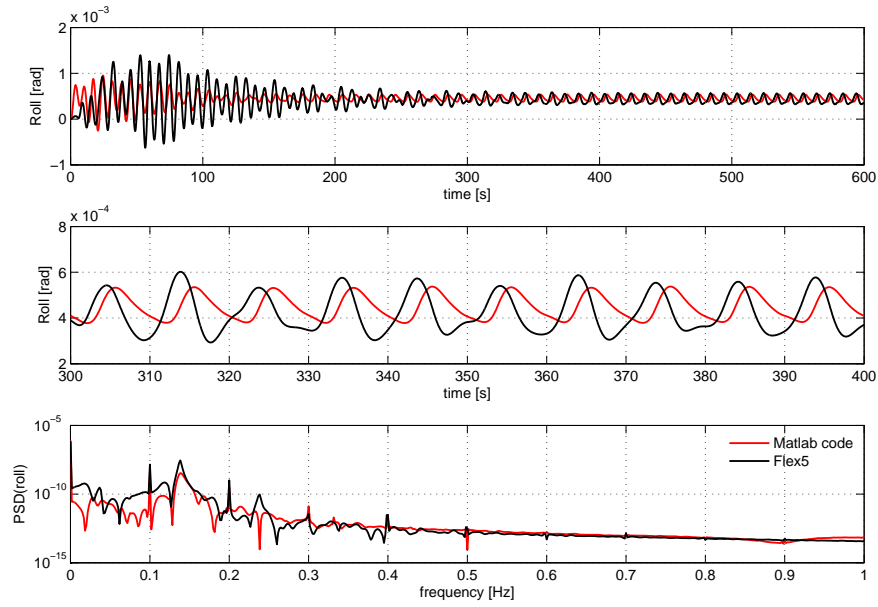
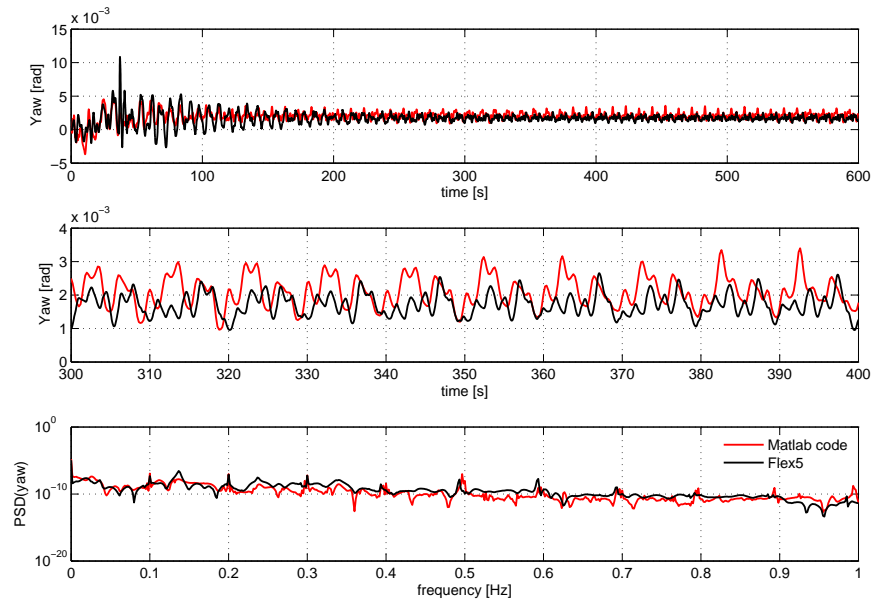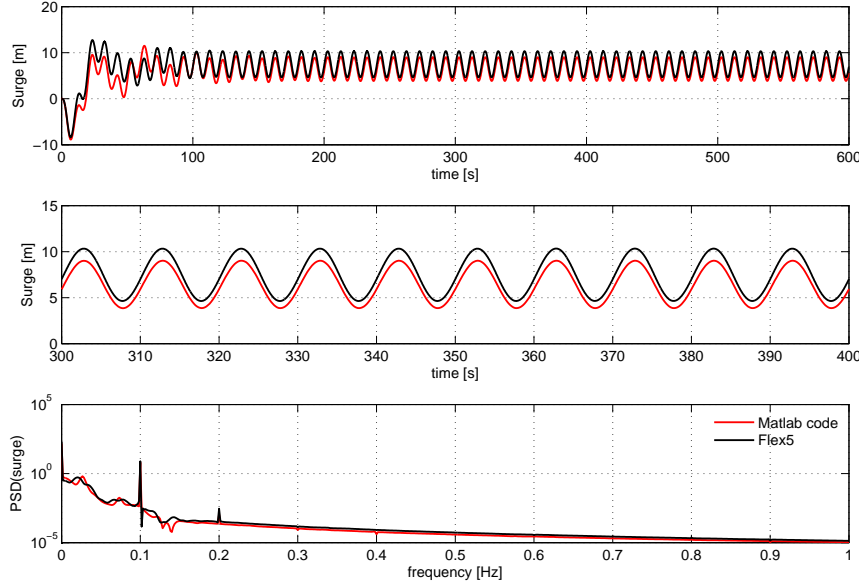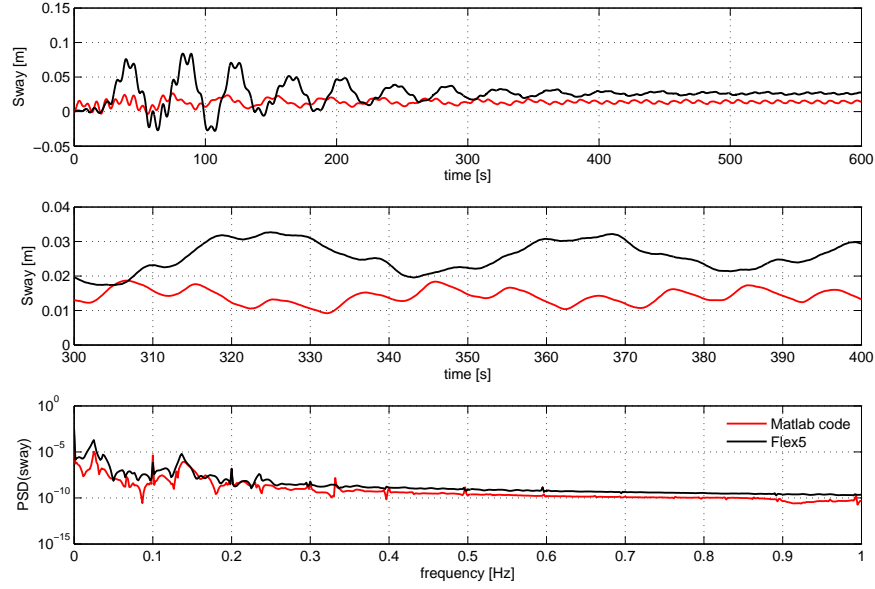FIGURE 6.45: Case 3 - Roll response comparison (Flex5 and Matlab code)
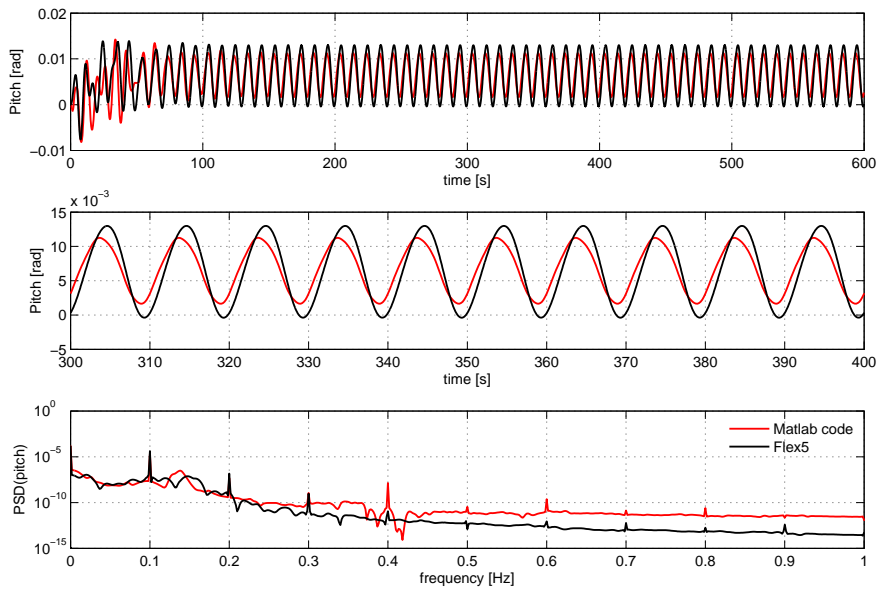
FIGURE 6.46: Case 3 - Pitch response comparison (Flex5 and Matlab code)
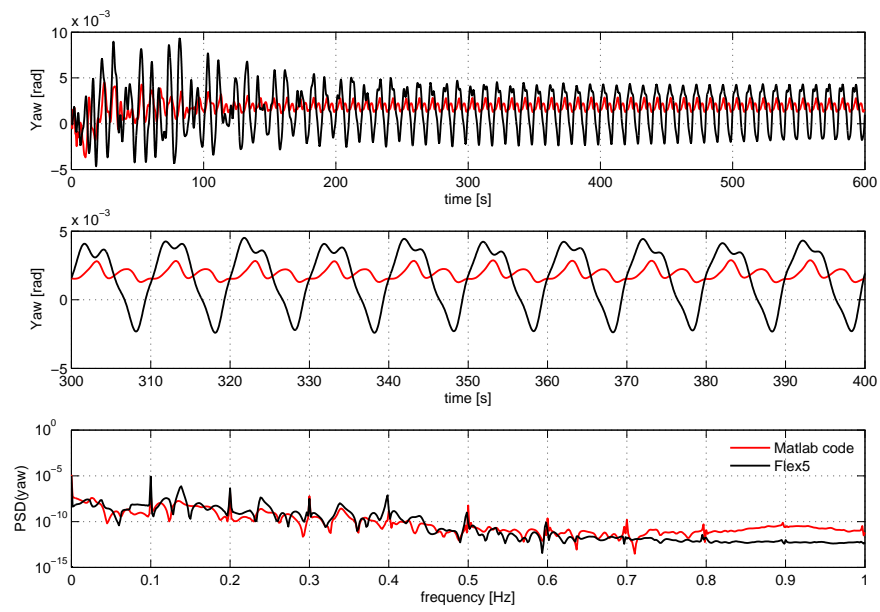
FIGURE 6.47: Case 3 - Yaw response comparison (Flex5 and Matlab code)

6.6.4   Case 4

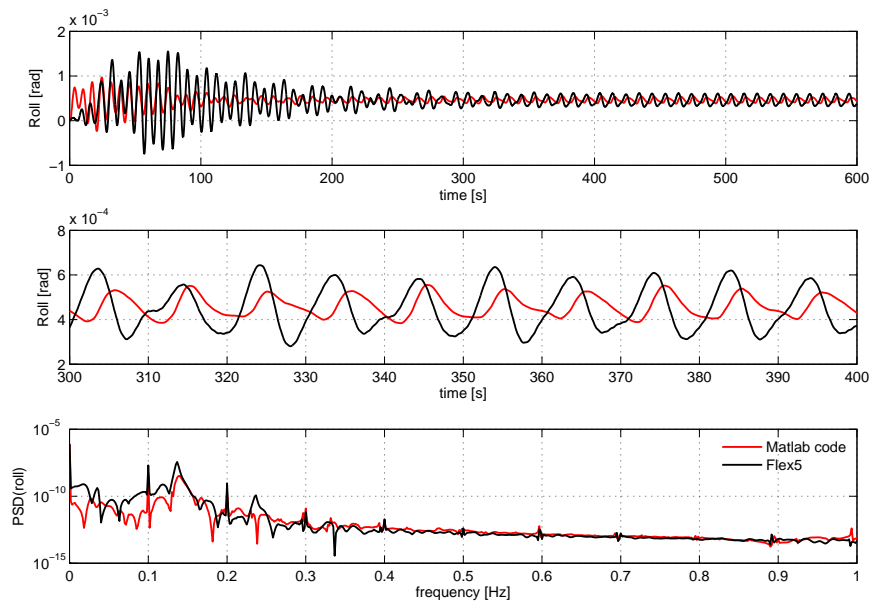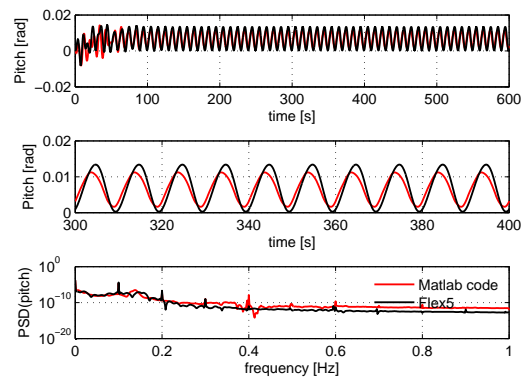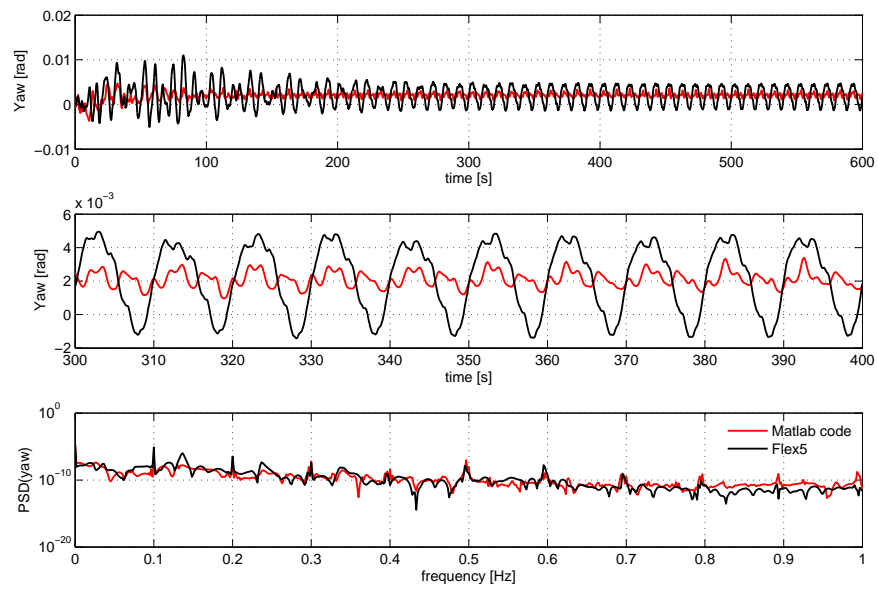Case 4 considers 2D regular wave alone case. The response comparison is shown in the following figures. The comparison works fine mainly for the 2D responses and the differences observed in the responses are identified and discussed.

In addition, Case 4 responses uncover influence of many of the effects. Comparing the Case 4 responses with that of Case 3 can demonstrate the influence of wind on roll and roll induced yaw, gyroscopic and control effects and the varying generator torque.

The surge responses compare very well both in time and in frequency domains. The comparison is shown in Figure 6.48.
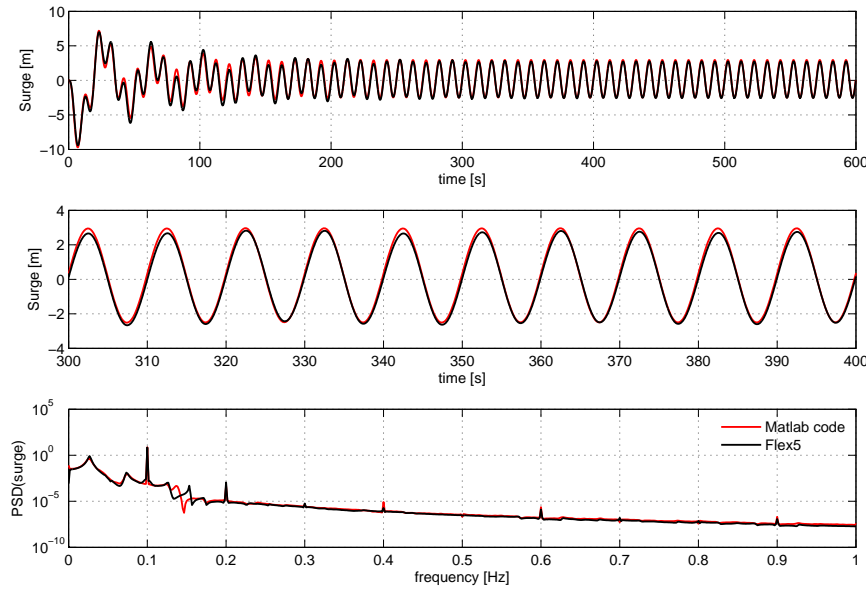
FIGURE 6.48: Case 4 - Surge response comparison (Flex5 and Matlab code)

The sway response, which is very small, as predicted by MATLAB code is fluctuating more compared to that of the Flex5 response, which was also expected based on the previous analysis. The comparison is shown in Figure 6.49.

The heave response compares very well with only a slight difference in the mean. The comparison is shown in Figure 6.50.

The roll response is very small and the fluctuation in MATLAB code is larger compared to that of Flex5, which may be because the roll degree of freedom is a secondary response to the 2D waves, as explained earlier. The response comparison is shown in Figure 6.51.

Compared to the Case 3 roll, the present response is one order lower, which is due to the higher roll caused by the wind and the varying generator moment in Case 3. Similarly, compared to the Case 2 roll, the present response is one order smaller, which is due to the influence of tower flexibility and varying generator moment. Compared to Case 1, because of the absence of varying generator moment, the present roll response is much smaller.

The pitch response compares well with only a slight difference. The comparison is shown in Figure 6.52.

Between Cases 2 and 3, the pitch response in Case 3 is slightly more because of the presence
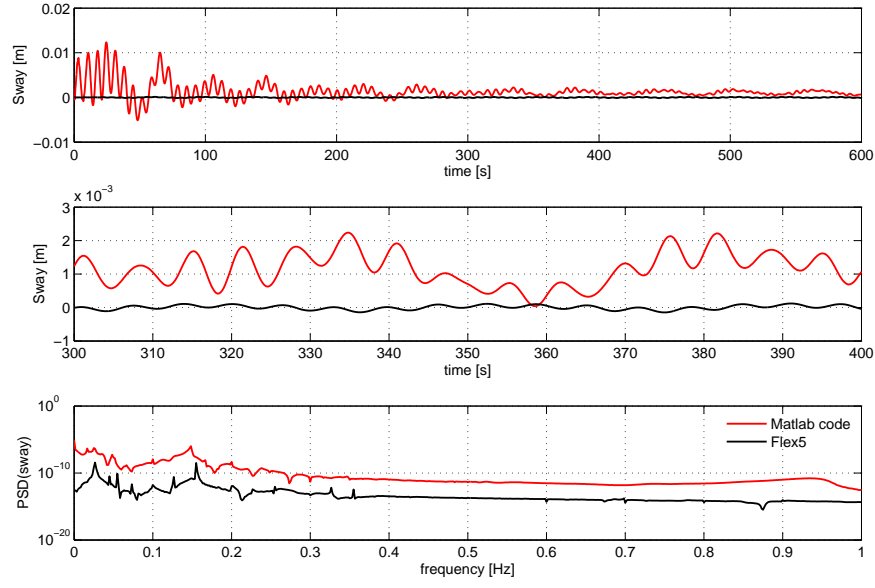
FIGURE 6.49: Case 4 - Sway response comparison (Flex5 and Matlab code)
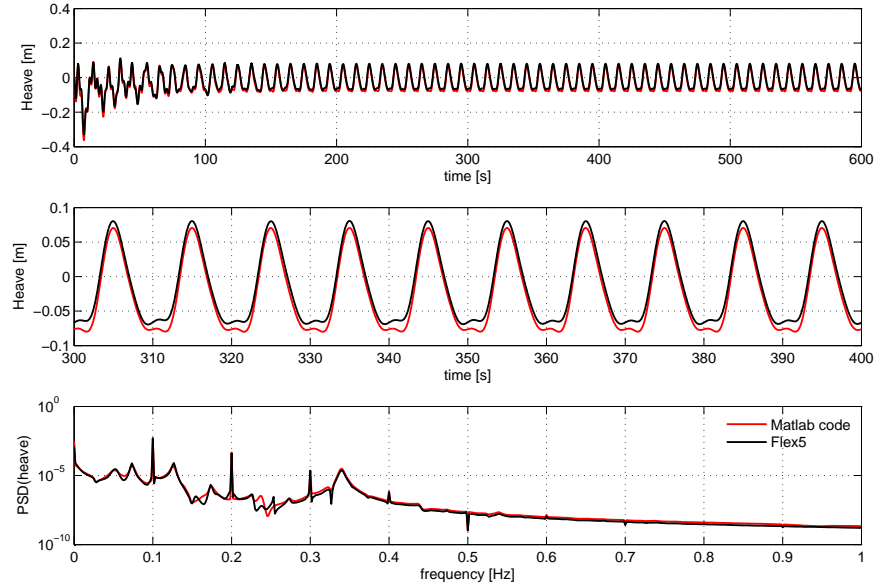
FIGURE 6.50: Case 4 - Heave response comparison (Flex5 and Matlab code)

of tower flexibility. Between 3 and 4, the variation is more or less the same, however, the Case 4 has zero mean compared to a positive mean in Case 3. This is because of the absence of rotor thrust in the present case.

The yaw response is very small and the response from MATLAB code has much larger
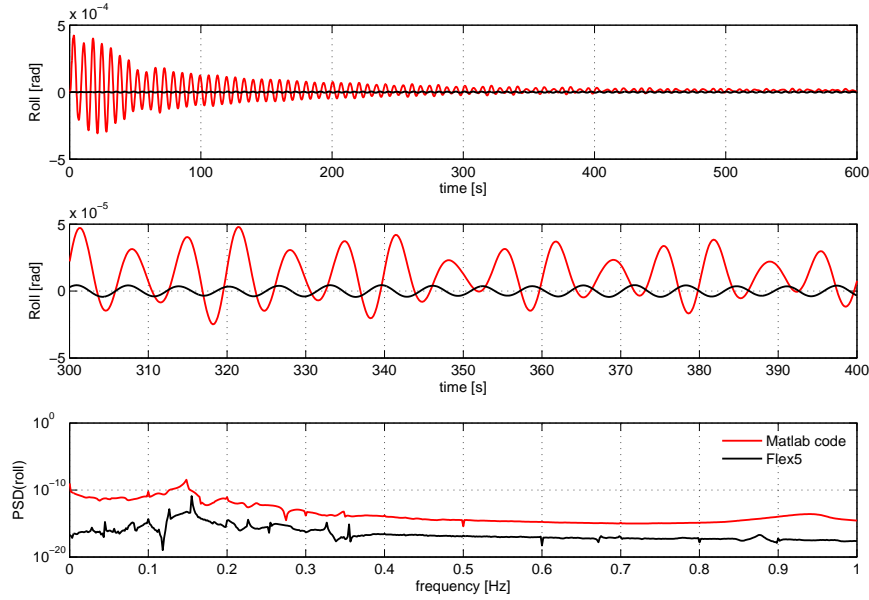
FIGURE 6.51: Case 4 - Roll response comparison (Flex5 and Matlab code)
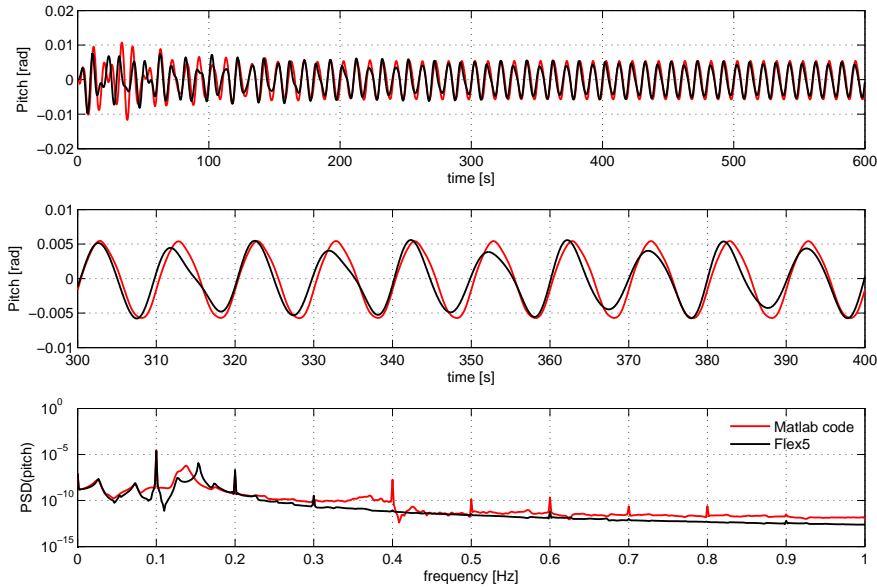
FIGURE 6.52: Case 4 - Pitch response comparison (Flex5 and Matlab code)

fluctuation, which has the same explanation as that of the roll response comparison. The comparison is shown in Figure 6.53.

The yaw response predicted by Flex5 is one order smaller than that of all other cases, which is an interesting observation because the presence of wind induces most of the coupling

effects. Comparing with that of Case 1 reveals that the varying torque induces roll, which in turn induces yaw through roll-yaw coupling. Case 2 comparison shows that in addition to the above effect, the gyroscopic effect enhances the yaw response.
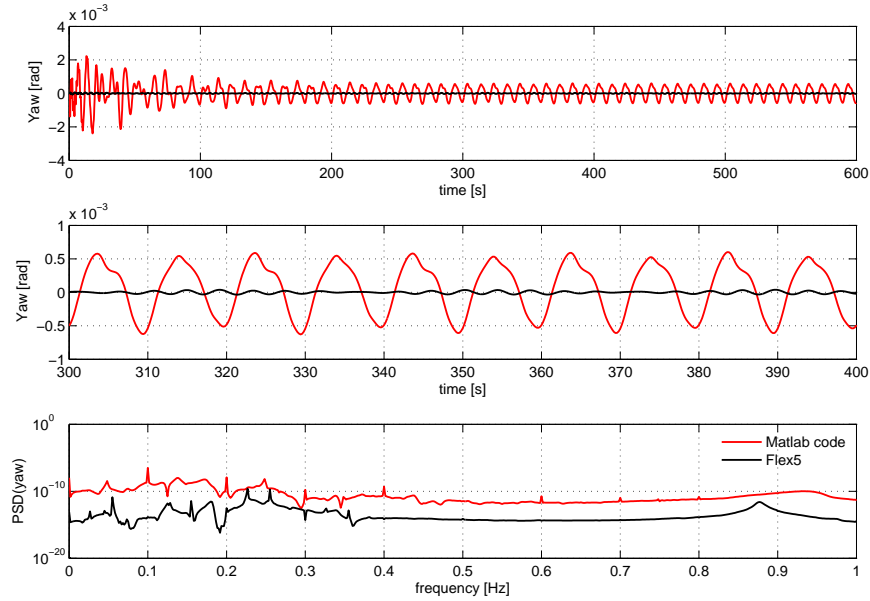
FIGURE 6.53: Case 4 - Yaw response comparison (Flex5 and Matlab code)

6.6.5 Case 5 - 3D irregular waves with 10 m/s constant wind

The responses from coupled Flex5 code is compared against that from the MATLAB code from the previous chapter. For this, the TLP configuration is subjected to combined wind and wave loads. A 3D wave with 0 degree wave heading and a constant mean wind speed of 10 m/s are considered. The responses are obtained using the coupled Flex5 and MATLAB codes. As the MATLAB code is a simplified code with limited degrees of freedom, obtaining a complete agreement on response comparison is not expected. The translational degrees of freedom are having better agreement, whereas the rotational degrees of freedom differ.

The surge responses compare well both in time and in frequency domains. The comparison is shown in Figure 6.54. Slight differences occur at times, however, the differences are very small. From the frequency response, it can be observed that the Matlab response has slightly higher energy content at the surge natural frequency, which may be due to the lesser aerodynamic damping in Matlab.

The sway responses are also comparable, however a complete agreement could not be obtained, which was also expected. The differences may be because of the less comprehensive wind turbine model in MATLAB code wherein the tower lateral (sidewise) degree of freedom and the forces in that direction are not included. The responses are within the same range and the comparison is shown in Figure 6.55.

A comparison of the heave responses from MATLAB and Flex5 code is shown in Figure 6.56, which shows a good agreement between the two responses. The heave comparison also shows that at the surge natural frequency, the energy content is more for the Matlab results, which indicates a lesser aerodynamic damping. The presence of surge natural frequency in the
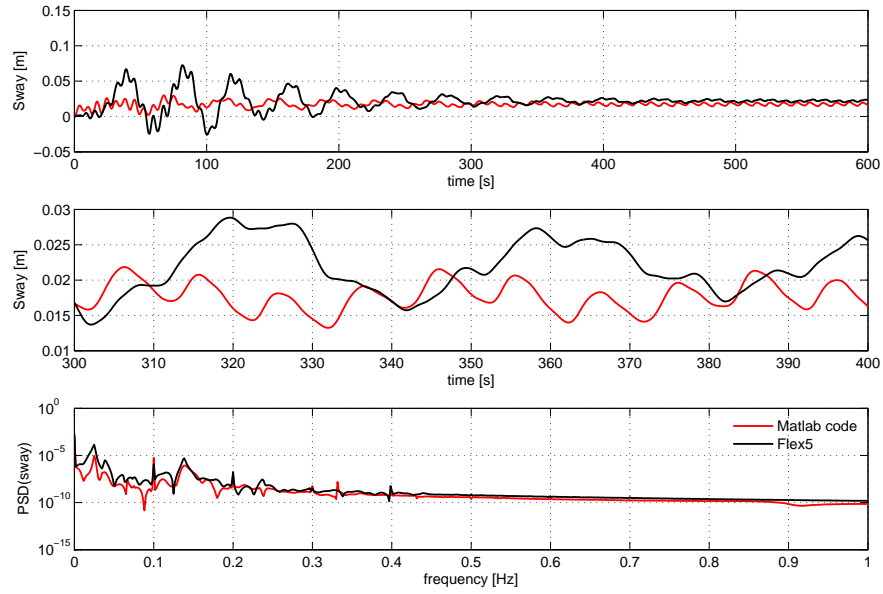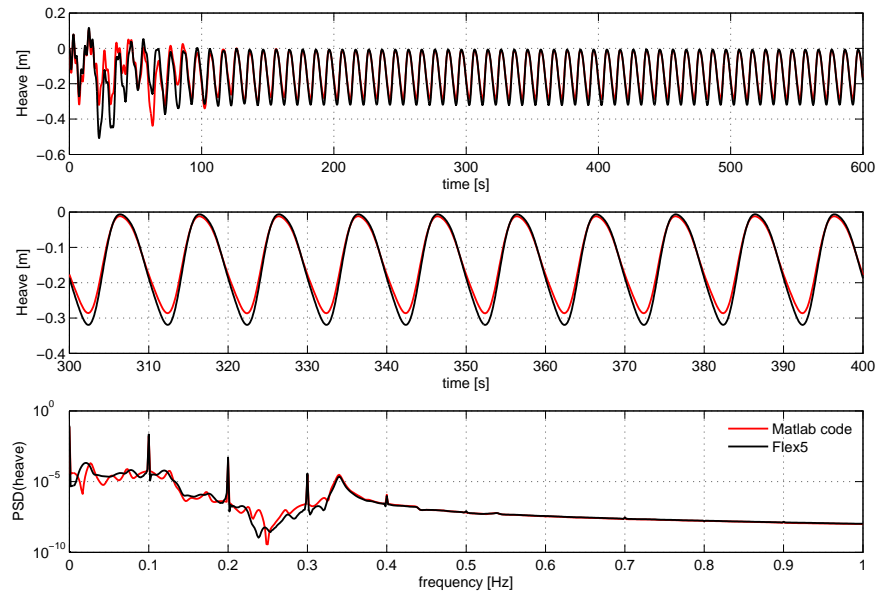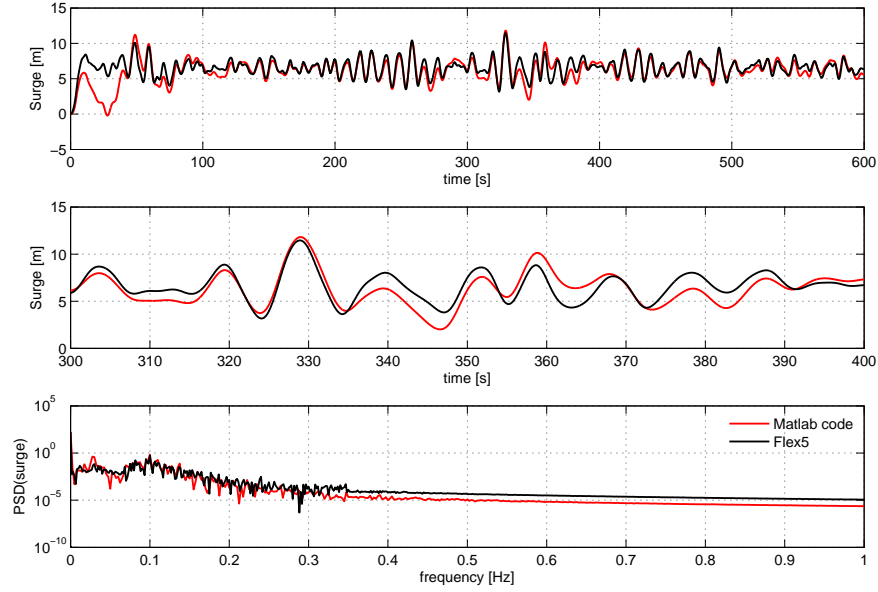
FIGURE 6.54: Case 5 - Surge response comparison (Flex5 and Matlab code)
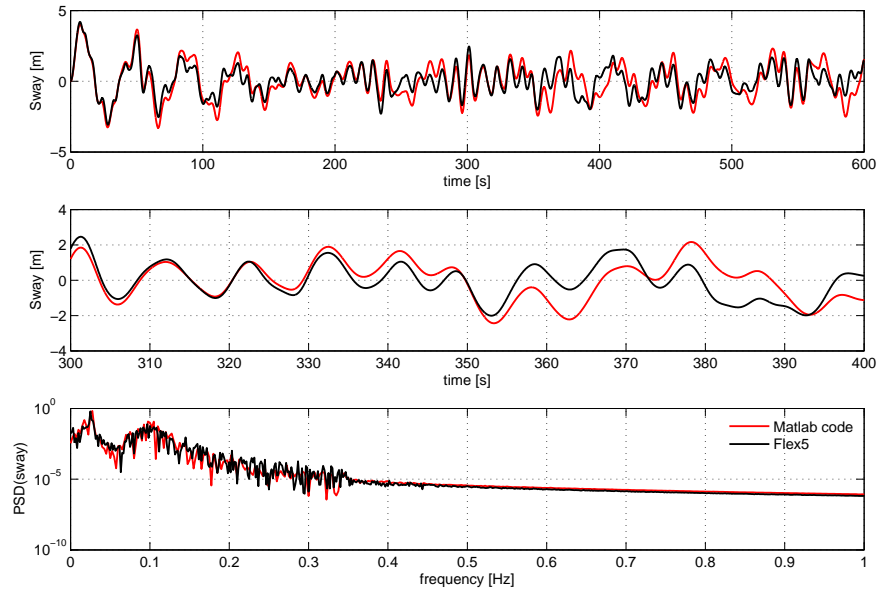
FIGURE 6.55: Case 5 - Sway response comparison (Flex5 and Matlab code)

heave response is due to the surge-heave coupling.

The roll responses are not fully comparable. The comparison is shown in Figure 6.57. The much higher roll response predicted by Flex5 is likely to be explained by a strong roll - yaw coupling through tower lateral flexibility, which was not captured by the Matlab code.
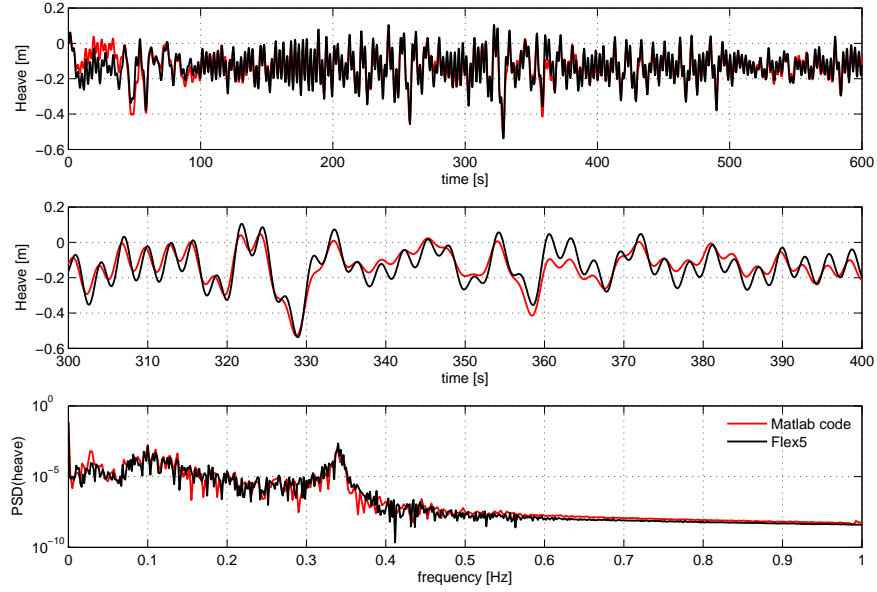
FIGURE 6.56: Case 5 - Heave response comparison (Flex5 and Matlab code)
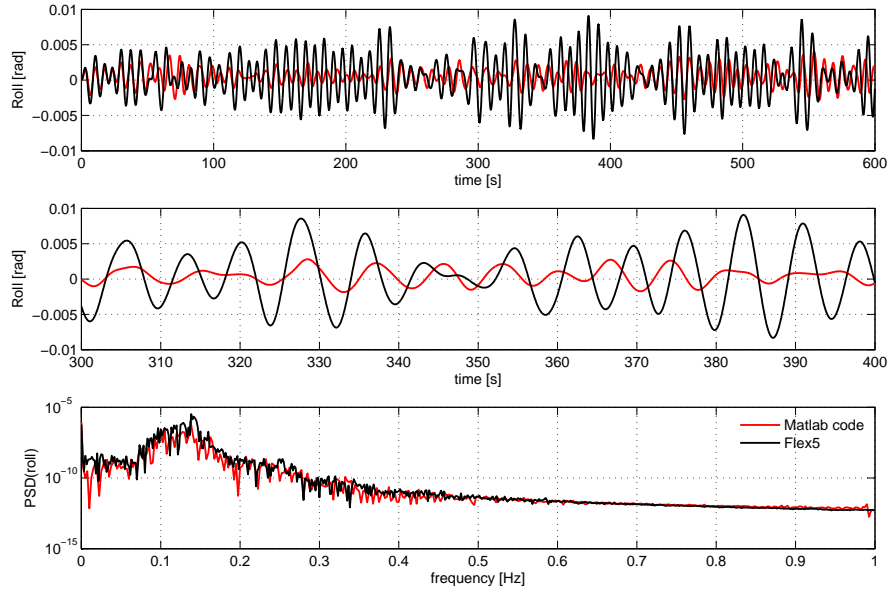
FIGURE 6.57: Case 5 - Roll response comparison (Flex5 and Matlab code)

A comparison of the pitch responses are shown in Figure 6.58. From the figure, the pitch responses are comparable, however some differences are also observed. Similar to the surge, the response from Matlab code has lower damping and hence larger fluctuations. The lower damping in Matlab code is due to the less comprehensive modeling of the wind turbine, espe-

cially the tower. In the case of Flex5, all the tower degrees of freedom are also contributing to the damping, whereas this effect is not present in the Matlab code.
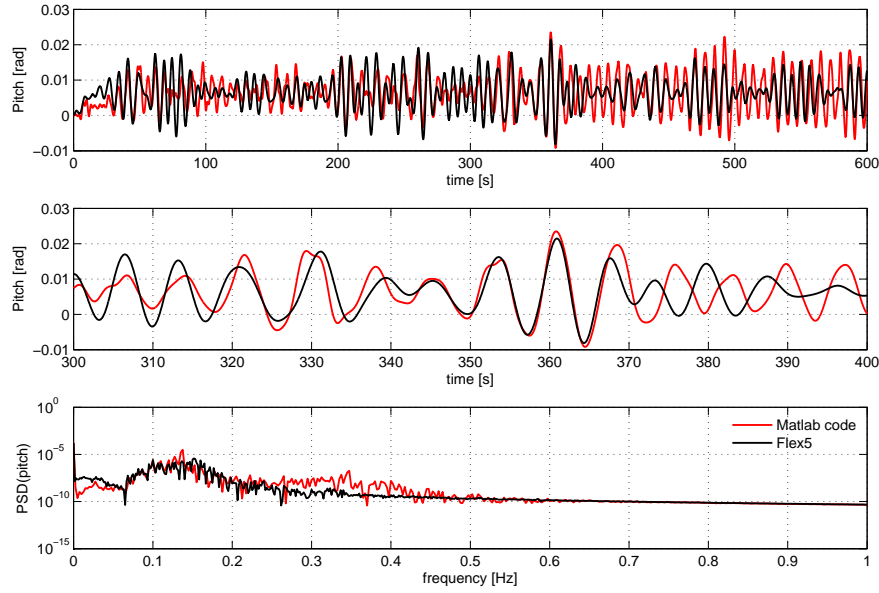
FIGURE 6.58: Case 5 - Pitch response comparison (Flex5 and Matlab code)

The yaw responses comparison is shown in Figure 6.59, which are not comparable. The reason for much higher yaw response predicted by Flex5 is because of the strong roll - yaw coupling induced by the tower lateral flexibility and gyroscopic effects, which could not be captured by the MATLAB code.
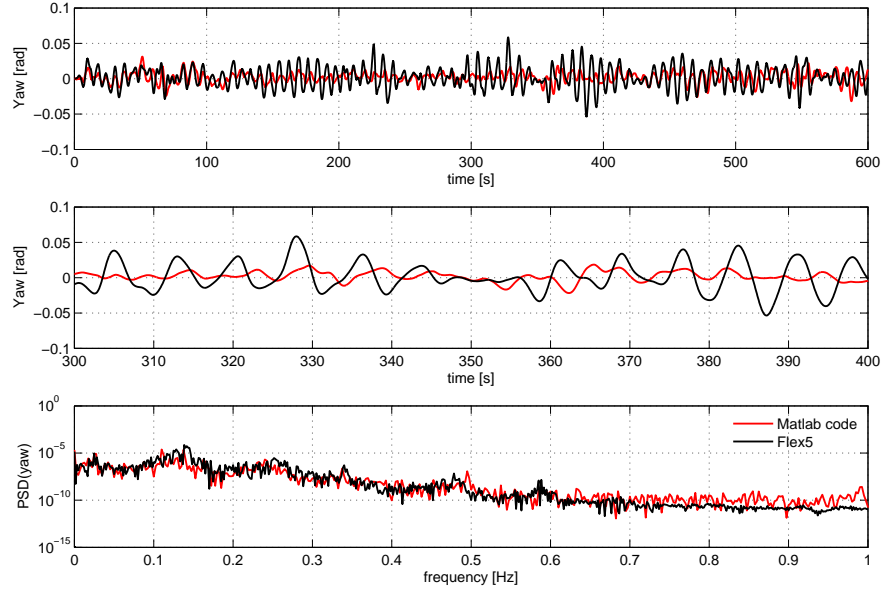
FIGURE 6.59: Case 5 - Yaw response comparison (Flex5 and Matlab code)

6.7   Summary

In this chapter, the advanced aero-elastic code Flex5 is extended to capture the dynamics of a TLP floating offshore wind turbine by including the platform dynamics and different wave forcing models by reading the wave kinematics through a data file. The coupled code is tested for various test cases along with a response comparison with the MATLAB code derived in the previous chapters. The models agree well for the wave alone excitation. Differences in sway, roll and yaw responses are observed, however, all these responses are small and hence not a significant difference. The investigations demonstrate the sensitiveness of rotor orientation when subjected to waves. In addition, the influence of wind, tower flexibility, gyroscopic effect, varying generator moment, control action and roll-yaw coupling on the responses are investigated. The extended Flex5 code may be used to carry out a parametric study, which is dealt in the next chapter.

Parametric Study

In this chapter, the modified Flex5 code is used to carry out a parametric study on the floating TLP wind turbine. Initially, the system is subjected to five sea states, for which the responses are computed. The computations showed larger yaw response, which needs to be controlled. As an alternative, different configurations are investigated and the responses are computed. Further, the better configuration is subjected to more severe sea states and recommendations are made.

7.1 TLP wind turbine subjected to various sea states

The baseline configuration of the TLP wind turbine is subjected to five different sea states, which are described in the following section. For these parameters, 3D irregular waves with different spreading parameters and turbulent wind conditions are applied. The wind turbine is under operational conditions while subjected to the above environmental loading.

7.1.1 Wind and wave climate

The five sea states considered for the investigation are listed in Table 7.1, Schløer et al. (2012). The wave climate is based on the North Sea wind and wave occurrences as detailed in Johannessen et al. (2002).

TABLE 7.1: Wind and wave climate

	H_s (m)	T_p (s)	V (m/s)	TI (%)
sea state1	2.3	6.8	6.7	22
sea state2	3.1	7.9	8.5	20
sea state3	5.1	10.5	13.4	16
sea state4	7.0	12.3	18.1	15
sea state5	9.4	14.2	23.5	14

As the wind speed (V) increases, the peak wave period (T_p) and significant wave height (H_s) also increases, however, the turbulence intensity (TI) decreases. The wind shear profile is considered with a power law index of 0.14. This range of wind and wave climate give rise to a realistic sea states so that the loads and responses can be studied.

7.1.2 Responses for the five sea states

Responses are computed for the five sea states with zero degree wave heading. The wave kinematics are corresponding to the spreading parameter $s = 1$. The responses are obtained

144

at the tower bottom point, which are transformed to the floater bottom point with the conventional coordinate system. The positive and negative peaks in the responses are identified, sorted and accumulated probability curves are drawn for each of the responses.

The surge response comparison is shown in Figure 7.1. In the figure, the responses corresponding to the first and second sea states behave alike and the remaining responses have slightly different characteristics because of the transition from the below rated control regime to the above rated, as described in section 6.2.3 of Chapter 6. The turbine control method changes the rotor thrust and hence affects the floater responses. The largest response happens for the sea state 5, as expected.

The sway response is shown in Figure 7.2, which has the similar characteristics of the surge response, however, with a smaller magnitude compared to the surge. The smaller response is due to the smaller rotor side-wise force and the smaller sway force caused by the 0 degree wave heading. Hence the mean is almost zero as influenced by the wind and the fluctuation is smaller as affected by the waves.

The heave responses as shown in Figure 7.3 are also behaving as expected. The stronger waves induce stronger heave. In addition, as the sea state is higher, stronger is the wind, which induces higher surge. A higher surge in turn induces a higher heave through the surge-heave coupling. These two effects constitute the cause for a varying heave against sea states. The positive peaks are mainly due to the tendon elasticity.

The roll response, which is shown in Figure 7.4, has a small positive mean due to the influence of rotor torque. An interesting observation is that the responses corresponding to the first and second sea states are more than that of the remaining three sea states. This is because the first and second wave frequencies (0.147 and 0.13 Hz) are very close to the roll and pitch natural frequencies, which induces resonance and hence larger response. It can be noted that though the resonant responses are larger than that of other responses, the responses are not growing over a period of time or affecting the structural integrity of the system. However, it is recommended to avoid the resonance regime.

Figure 7.5 shows the pitch response as expected, which has a positive mean due to the influence of rotor thrust. This response does not seem to have the same effect of resonance as in the case of roll. This may be because the aerodynamic damping available in the pitch direction plays an important role to attenuate the responses.

The yaw responses, as shown in Figure 7.6, are very large compared to the roll and pitch responses. The yaw responses corresponding to the first and second sea states are larger compared to the others, which is due to a strong roll-yaw coupling of the system. The maximum yaw response, which is more than 10 degrees, may affect some of the small angle approximation of the governing equations and hence may have higher impact on the results.

The yaw response is mainly caused by the combined effect of the aerodynamic forces, tower flexibility, control action and the platform motion. Minimization of yaw response requires each of these causes to be addressed. One of the easiest methods is to avoid the resonance influence thereby reducing the roll-yaw coupling or to increase the yaw stiffness. Both of these methods will increase the natural frequencies of rotational DOF. This requires an investigation of various configurations.
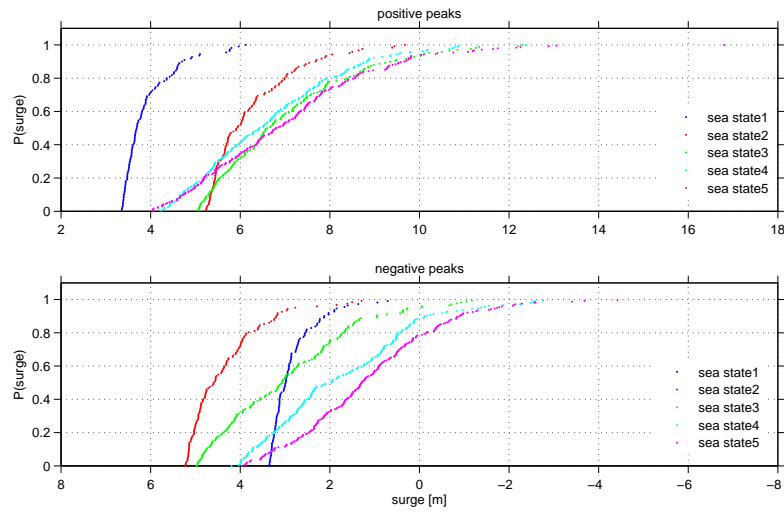
FIGURE 7.1: Surge response probability comparison - 0 degree wave heading
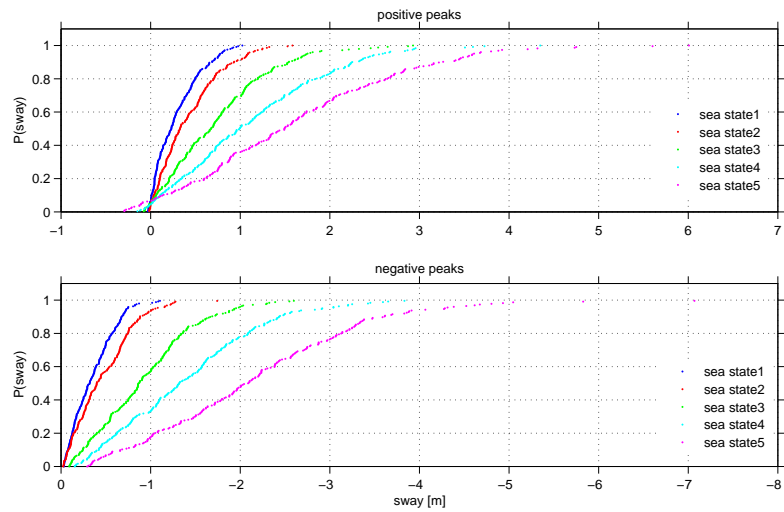
FIGURE 7.2: Sway response probability comparison - 0 degree wave heading
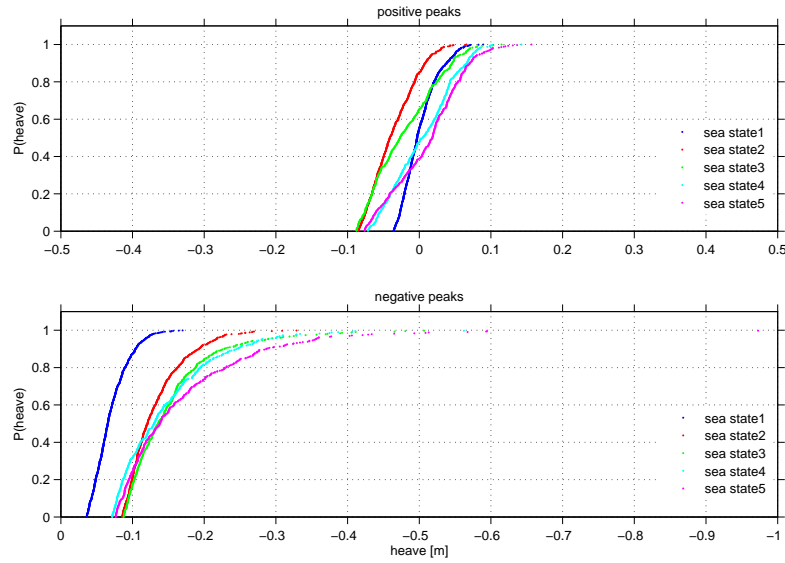
FIGURE 7.3: Heave response probability comparison - 0 degree wave heading
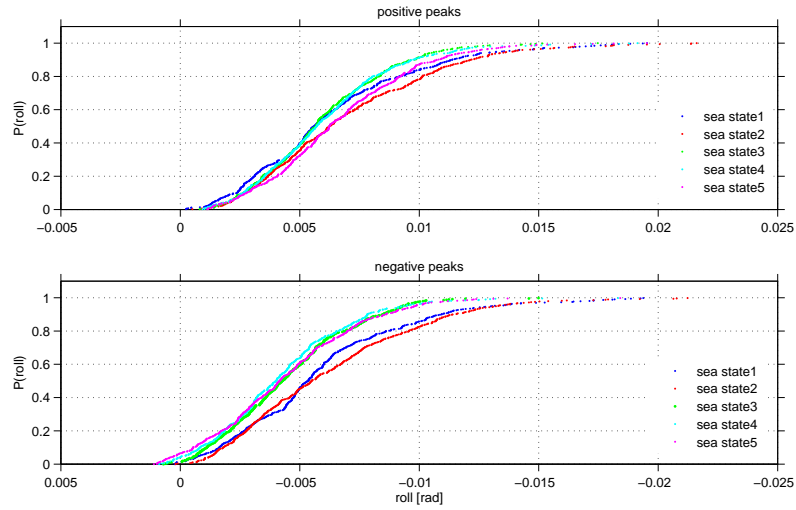
FIGURE 7.4: Roll response probability comparison - 0 degree wave heading
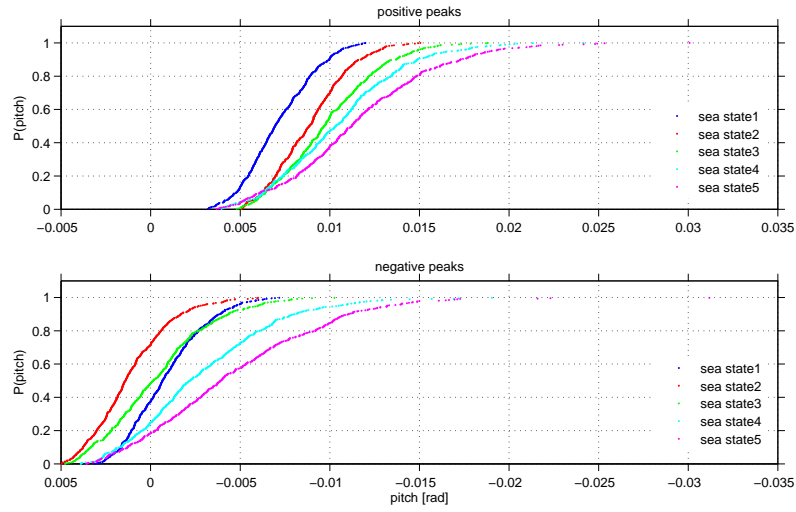
FIGURE 7.5: Pitch response probability comparison - 0 degree wave heading
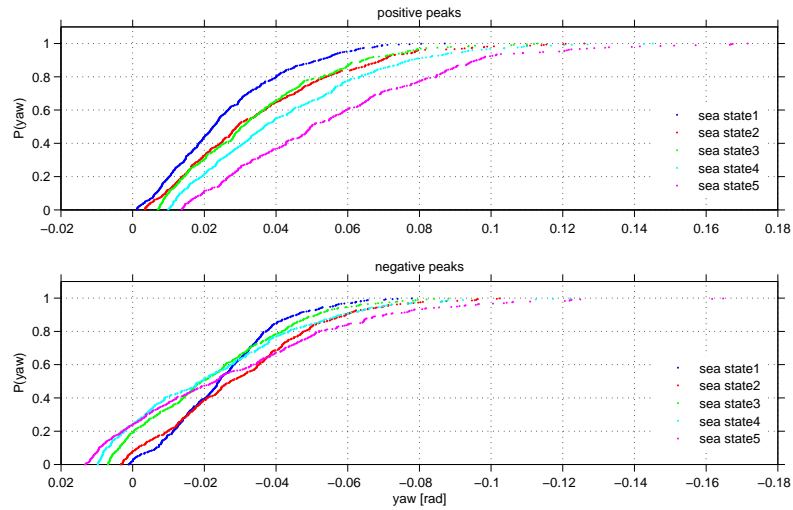
FIGURE 7.6: Yaw response probability comparison - 0 degree wave heading

7.2   Investigation of various configurations

Based on the results from the previous analysis, the yaw responses are larger and hence some of the probable configurations are investigated. The following three configurations are considered. Treating the baseline model as Configuration 1, the other models are listed below.

- Configuration 1 - Baseline model (C1)

- Configuration 2 - Diameter of the floater is increased from 16 m to 18 m (C2)

- Configuration 3 - Lengths of the spokes are increased from 22 m to 32 m (C3)

- Configuration 4 - Instead of straight tendons, inclined tendons with an angle of about 3° (C4)

A natural frequency sensitivity analysis is carried out for all of the configurations, for which the results are shown in Table 7.2.

TABLE 7.2: Natural frequencies (Hz)

	C1	C2	C3	C4
surge	0.026	0.036	0.026	0.038
sway	0.026	0.036	0.026	0.038
heave	0.34	0.317	0.347	0.344
roll	0.15	0.165	0.212	0.154
pitch	0.15	0.165	0.212	0.154
yaw	0.23	0.268	0.317	0.238

When the floater diameter is increased by keeping the floater mass constant, the buoyancy force and added mass in all the degrees of freedom increase. An increase in the buoyancy force increases the pretension. As described in section 5.2 of Chapter 5, the surge, sway and yaw natural frequencies are directly dependent on the pretension, whereas the roll and pitch natural frequencies are dependent on the buoyancy force. The heave natural frequency is independent of the pretension and the buoyancy force. In addition, all the natural frequencies are inversely proportional to the added mass. Hence, an increase in floater diameter increases all the natural frequencies except the heave natural frequency, which can also be observed in the above table. The heave natural frequency reduces slightly due to the marginal increase in the heave added mass, whereas for all the other natural frequencies, the increase in stiffness dominates the effect of the increased added mass.

An increase in the spokes lengths give rise to an increased rotational natural frequencies due to an increased stiffness, whereas the translational frequencies remain unchanged, as expected. Adopting inclined tendons give rise to slightly increased natural frequencies in all the DOFs, however, the increase in surge and sway natural frequencies are considerable, due to an increased stiffness from the tendons. The horizontal component of the tendon tension enhances the surge and sway stiffness.

7.2.1   Modified configuration responses

The modified configurations are subjected to the same five sea states and the responses are obtained. Similar to the baseline case, the cumulative probabilities are computed for each of the responses and a detailed discussion is given below.

Figures for only surge, pitch and yaw responses are given, whereas the results of all the DOFs are given and discussed in the statistical analysis. The surge and pitch responses demonstrate the in-plane motion, whereas the yaw response demonstrates the out-of-plane motion. The remaining three responses can be related to these three responses and hence those responses are not shown here.

The surge response is compared between the four configurations for each of the sea states, which is given in Figure 7.7. For all the sea states, the Configurations 2 and 4 have lesser response for a given probability compared to the other two configurations. This is mainly due to the increased surge stiffness for Configurations 2 and 4. The surge responses for sea states 2 and 3 have marginally higher mean compared to that of the sea states 4 and 5, which may be due to the controller regime change taking place between these sea states. It can also be confirmed because the mean response is mainly influenced by the rotor thrust, which is directly influenced by the wind turbine control.

The platform pitch response comparison is given in Figure 7.8. Configuration 4 has a clear advantage over other configurations for having smaller response for a given probability. The advantage is mainly due to a negative mean, which is introduced by the negative moment due to an additional mooring force in the surge direction. Otherwise, the Configuration 3 has smaller responses compared to the other configurations. Similar characteristics of the pitch response with the sea states is noticed as that of the surge response. Approximately 70% reduction in pitch response is noticed for the Configuration 3 compared to that of the baseline configuration.

Figure 7.9 shows the yaw response comparison, for which the response is smaller for configurations 3 and 4 for the smaller sea states, whereas a clear smaller response is observed only for Configuration 3 for the higher sea states. This is because of the higher yaw stiffness in Configuration 3 due to the longer spokes. Approximately 45% reduction in yaw response is noticed for the Configuration 3 compared to that of the baseline configuration. The second configuration has a comparable yaw response with that of the third due to a marginally higher yaw stiffness in Configuration 2, introduced by the increased effective length of the spoke (thereby the fairlead point) because of the increase of floater diameter. The yaw response is more or less consistently increasing with the sea states, both in terms of mean and maximum, mainly due to a higher wind and widely spread stronger waves. Stronger wind induces higher aerodynamic forcing, which induces higher yaw with an exemption of changes in controller action. Wider and stronger waves introduce higher roll, which in turn causes higher yaw through roll-yaw coupling.

The sway, heave and roll responses are also having the similar characteristics. However, the roll resonance effect for the first sea state in the case of second configuration is more dominant, which can be noticed in Figure 7.13. Both the maximum and standard deviation are higher than that of other responses, which is caused by the resonance effect. Similar to the pitch and yaw responses, approximately 50% reduction in maximum roll response is observed for Configuration 3.

With reference to the baseline configuration, approximately 25% of roll and pitch responses reduction is observed for Configuration 4, whereas approximately 20% yaw response reduction is observed at an 80% probability level. A statistical analysis is carried out in the next section to identify a feasible configuration.

FIGURE 7.7: Platform surge response probability comparison for configurations

FIGURE 7.8: Platform pitch response probability comparison for configurations
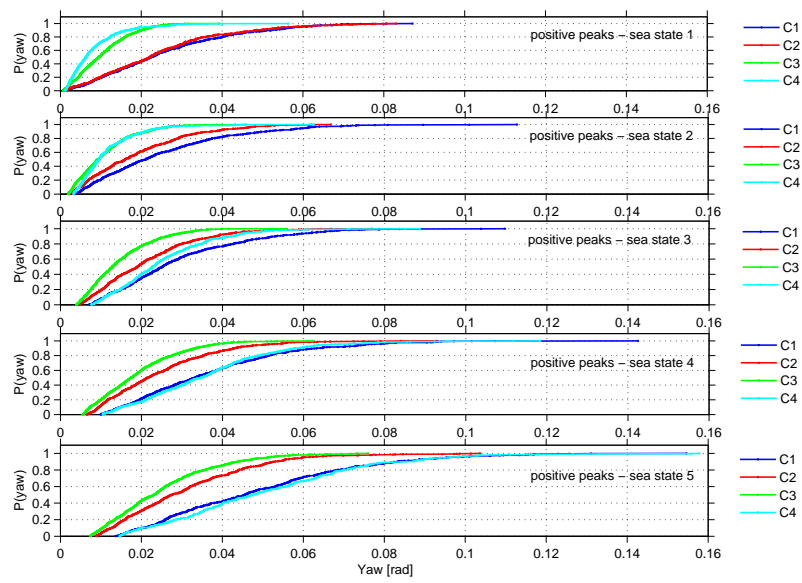
FIGURE 7.9: Platform yaw response probability comparison for configurations

7.2.2   Statistical analysis of various configurations

A statistical analysis is carried out to obtain an overview of the overall behaviour of the proposed configurations against the baseline configuration for different sea states. The results are given in the following figures from 7.10 to 7.15.

The surge response of Configurations 2 and 4 are marginally smaller upto the sea state 4, whereas it is almost the same for all the configurations for the sea state 5, which means all the configurations behave alike to the severe sea state. It may be because of a mixed influence of waves, wind turbulence and control actions. In the case of sea state 5, the wind speed is very close to the cut-out wind speed and hence the blade pitch regulation would be much greater due to an effective increase and decrease of relative wind speed below and above cut-out wind speed. This might cause additional response changes apart from the large wave at sea state 5.

All the configurations have almost the same sway response though the response of configuration 4 is slightly higher. Since the sway response is mainly caused by the spread waves in the sway direction, and hence it was expected to be smaller. However, the considerable amount of sway may be due to a combined effect of roll induced sway and the influence of the turbulent wind. Further, the lack of aerodynamic damping in this direction may accelerate this response.

In terms of the maximum and standard deviations, the Configuration 4 heave response is smaller than that of the other configurations up to the sea state 4 and beyond this, all the maximum responses are more or less the same. However, the heave standard deviation for Configuration 4 at sea state 5 is still smaller than that of the other responses. The difference in the maximum response may be mainly induced by the surge-heave coupling effect.

The Configuration 3 roll response is smaller than that of the other configurations and also more or less un-influenced by the sea states because of its higher stiffness from the longer spokes. Compared to the other two configurations, Configuration 4 has smaller responses both in terms of maximum and standard deviation.

The pitch and yaw responses are also smaller in the case of Configuration 3 because of the higher stiffness.

Based on the analysis, Configuration 3 has smaller responses, however, the modification may be expensive because of the material cost involved in making four 10 m larger spokes compared to the baseline configuration. This motivates to investigate the fourth configuration with inclined tendons further.

FIGURE 7.10: Surge response statistics comparison

FIGURE 7.11: Sway response statistics comparison

FIGURE 7.12: Heave response statistics comparison

FIGURE 7.13: Roll response statistics comparison

FIGURE 7.14: Pitch response statistics comparison

FIGURE 7.15: Yaw response statistics comparison

7.2.3   Detailed analysis of selected configuration

The Configuration 4 is subjected to severe sea states corresponding to narrow banded directional spectrum and oblique waves. Computations are carried out for these cases for the baseline configuration as well to compare the results. In addition to these sea states, a load case corresponding to a combined action of a main wave and a swell is also investigated. The responses are discussed below.

Zero degree wave heading   In this case, collinear wave kinematics corresponding to a spreading parameter of $s = 4$ is considered for all the sea states. Responses are obtained for the baseline and the fourth configurations and the comparison is discussed.

For all the sea states, the surge response for Configuration 4 is smaller than that of the baseline configuration, as shown in Figure 7.16. For the last sea state, the response difference is minimal beyond the 80% probability level. The reason for the smaller response for Configuration 4 is due to the additional restoring forces from the inclined tendons, as explained in the previous section.

The sway response is expected to be smaller than that of the previous case ($s = 1$) because of the narrow banded direction spectrum and which is the case as seen in the statistical analysis figure 7.26. However, the reduction in response is not dramatic because the wave spectrum still has energy in this direction.

The heave and roll responses have the similar characteristic as in the previous case.

The pitch response for the case of Configuration 4 is smaller for a given probability compared to that of the baseline configuration mainly because of the negative pitch moment caused by the inclined tendons. The pitch response comparison is shown in Figure 7.17. In addition, the maximum response for Configuration 4 is also lower.

The yaw response for the fourth configuration is smaller than the baseline configuration only for the smaller sea states. Both of the responses become identical as the sea state goes high, which can be noticed from the Figure 7.18. This may be due to the special condition of the mean wind speed being very close to the cut-out wind speed thereby the control action is quite extensive which might be dominating the basic character of the configuration.
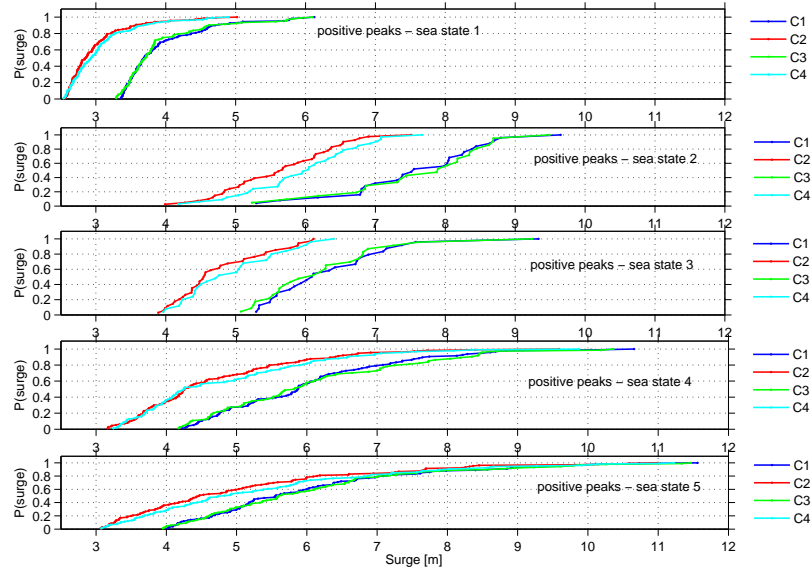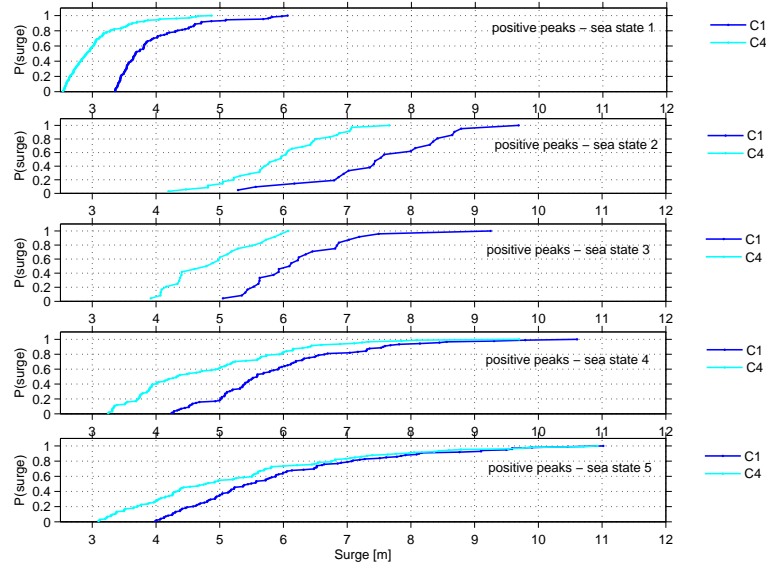
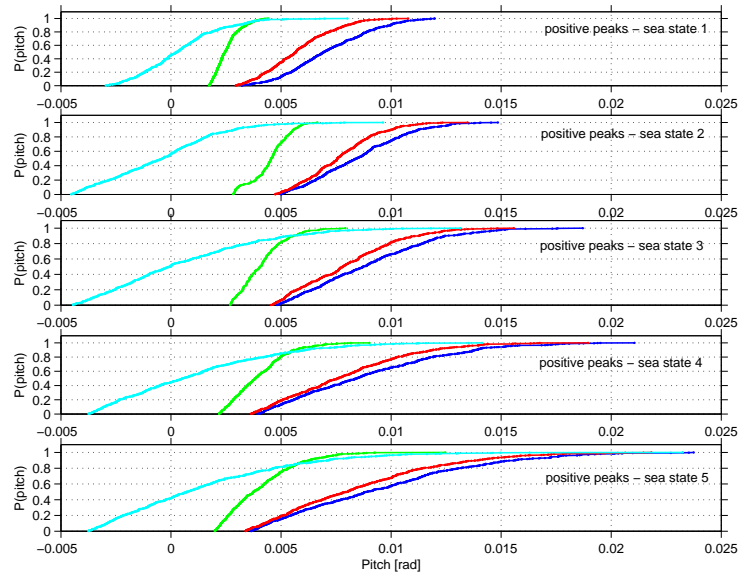FIGURE 7.16: Platform surge response probability comparison for 0 degree wave heading
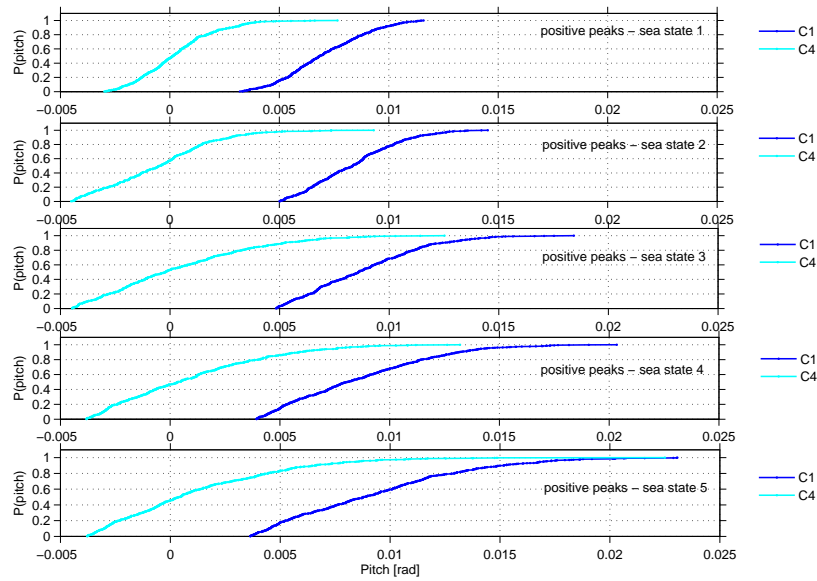
FIGURE 7.17: Platform pitch response probability comparison for 0 degree wave heading
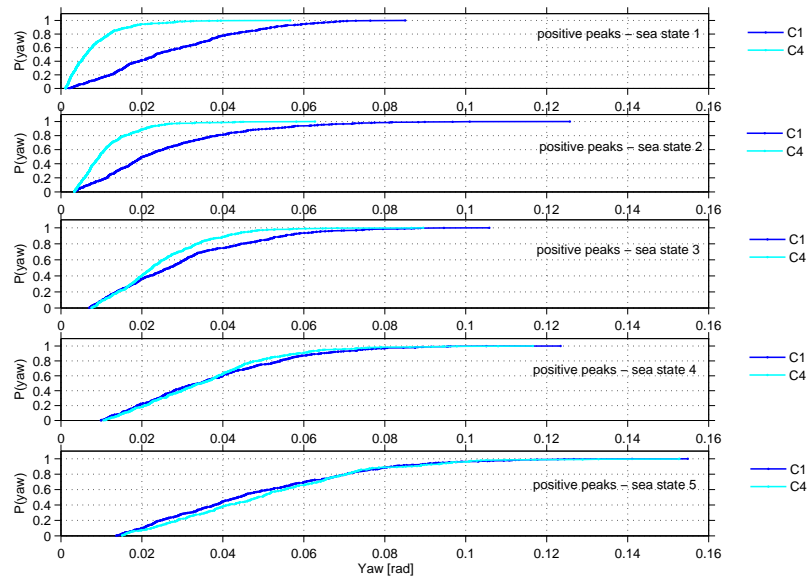
FIGURE 7.18: Platform yaw response probability comparison for 0 degree wave heading

45 degree wave heading   Oblique wave heading with 45 degree is considered for both the baseline and the Configuration 4. As in the previous case, the wave kinematics corresponding to a spreading parameter of $s = 4$ is considered. Responses are obtained for all the sea states and a response comparison is given below.

The surge, pitch and yaw responses are shown in Figures 7.19 to 7.21. From the figures, it can be noted that in general, the oblique wave heading does not affect the responses severely. In addition, the influence of oblique wave heading is very minimal in the case of Configuration 4 compared to the baseline configuration mainly due to additional stiffness and the inclined tendons. However, for the sea state 5, a very small difference in response is observed for the Configuration 4 between the collinear and oblique wave heading due to the dominating influence of the controller. In the case of sway, heave and roll responses, a small difference in responses is noted mainly because of the lack of aerodynamic damping in these degrees of freedom.

The frequency domain responses for the oblique wave heading case of Configuration 4 is given in Figure 7.22, which has peaks corresponding to the natural frequencies and peak wave frequency. The wind and wave spectra are also shown in the figure, wherein the wind spectrum is influenced by the turbulence. Two shorter time series of the extreme events, which occur for Configuration 4, subjected to 45 degree wave heading, are shown in Figures 7.23 and 7.24. The extreme waves occur at 1054 s and 2225 s and hence the maximum acceleration is obtained with a time delay corresponding to the phase shift which in turn produces the surge force. The maximum surge force has a phase shift proportional to the acceleration and hence the maximum surge response occurs with a time delay. Similarly, the maximum pitch and yaw responses are also observed with a time delay. The wave is acting like a focused wave during these time periods thereby triggering the maximum responses.
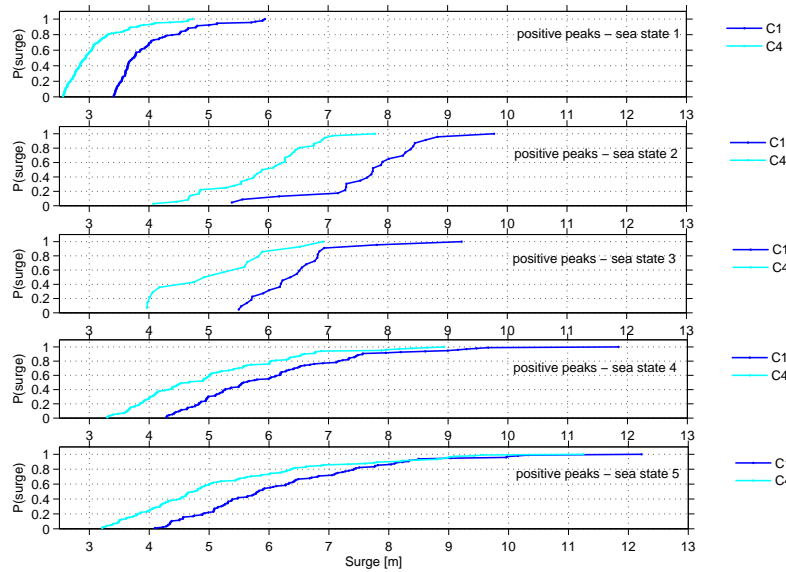
FIGURE 7.19: Platform surge response probability comparison for 45 degree wave heading
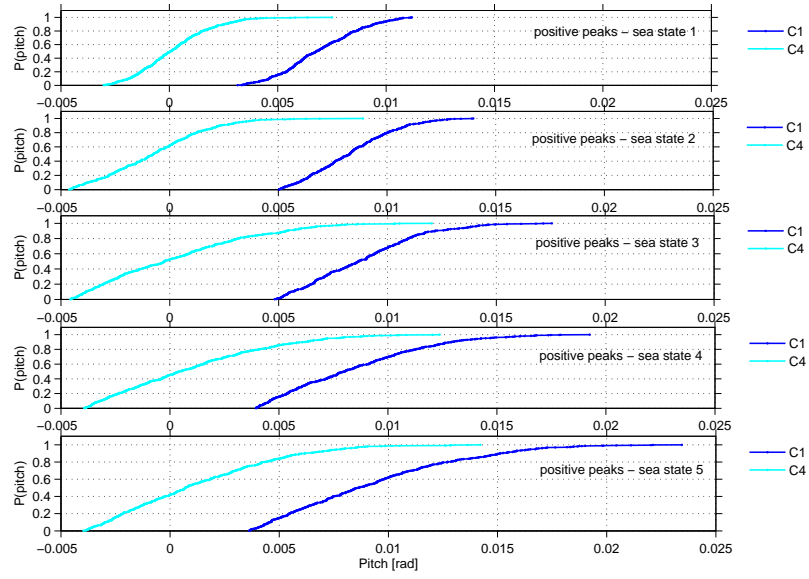
FIGURE 7.20: Platform pitch response probability comparison for 45 degree wave heading
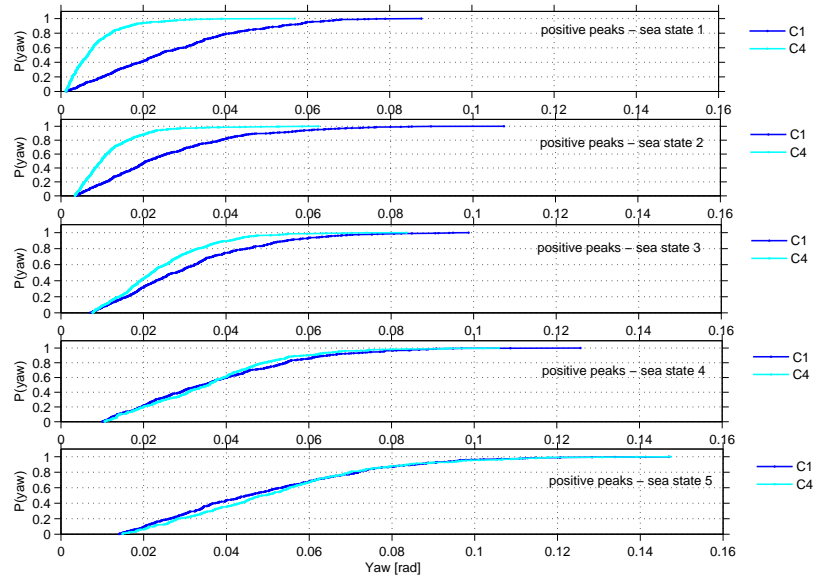
FIGURE 7.21: Platform yaw response probability comparison for 45 degree wave heading
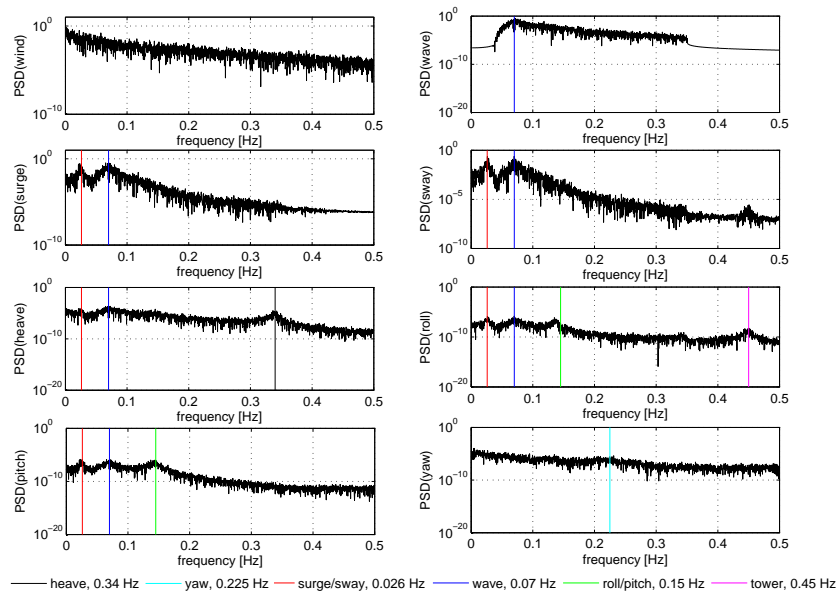
FIGURE 7.22: Platform frequency response of Configuration 4 with 45 degree wave heading
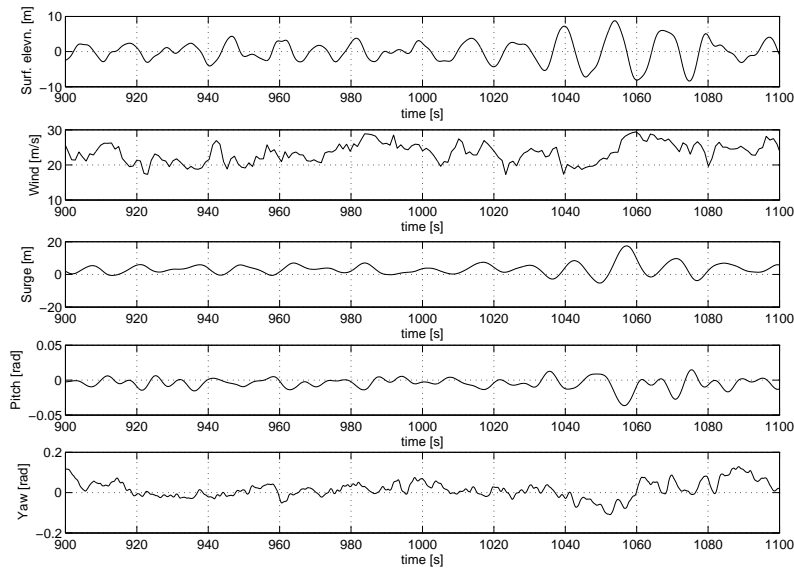
FIGURE 7.23: First extreme event in the platform response of Configuration 4 with 45 degree wave heading
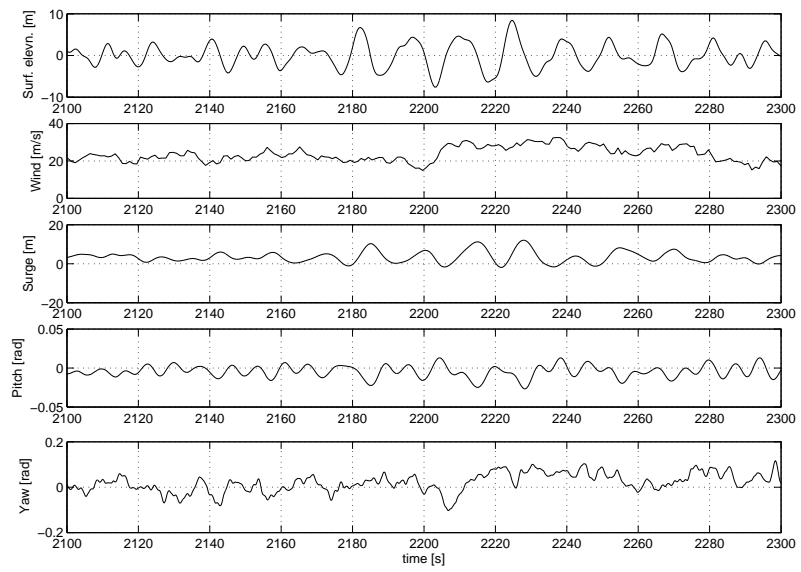
FIGURE 7.24: Second extreme event in the platform response of Configuration 4 with 45 degree wave heading

Statistical analysis of selected configuration subjected to severe sea states   A statistical analysis is carried out to demonstrate the overall characteristics of the fourth configuration compared to that of the baseline configuration against all the sea states including a swell.

A swell is a left over wave from a previous storm, which may reach the structure days after the storm. The swell is usually longer and more focused than the main wave, approaching the structure from an oblique direction. In the present case, the swell is generated using the standard JONSWAP spectrum with a spreading parameter of s=10 and a wave heading of 30 degrees. The wave kinematics are generated using both of the spectra with $S = S_1 + S_2$, where S_1 stands for the main wave and S_2 is that of the swell spectra. The sea states used for both the main wave and that of the swell are that of sea states 4 and 5 respectively. The maximum and standard deviation values are plotted in the statistical analysis plots.

The results are given in the following figures from 7.25 to 7.30. As far as the maximum response is concerned, the Configuration 4 responses are smaller than that of the baseline configuration. Between the collinear and inclined waves, not much of a difference is observed as explained in the previous section. The difference is marginal for the degrees of freedom, where the aerodynamic damping is smaller, which shows a strong influence of the rotor on floater responses. This observation is also applicable for the swell case, wherein the responses from the Configuration 4 and baseline configuration are more or less the same for the surge and pitch responses, whereas the difference in higher in the case of sway, heave, roll and yaw responses, which do not have enough aerodynamic damping in the swell direction.
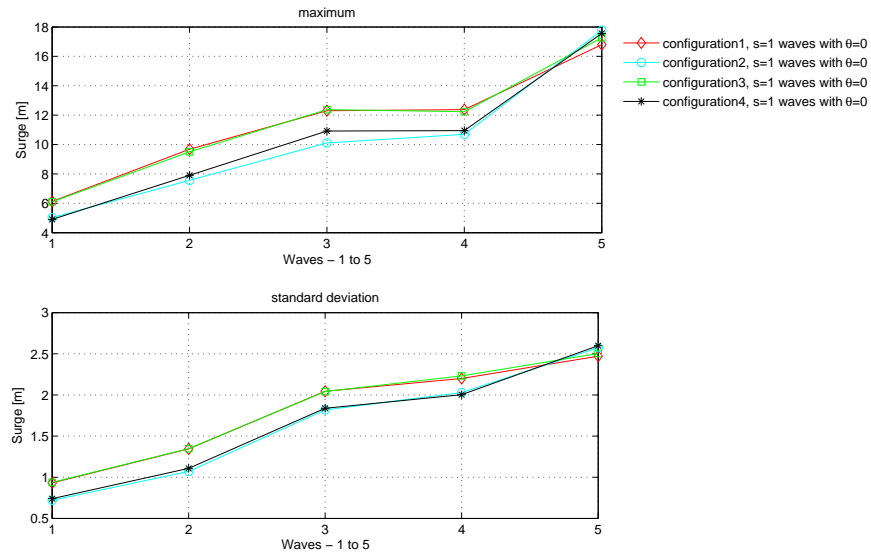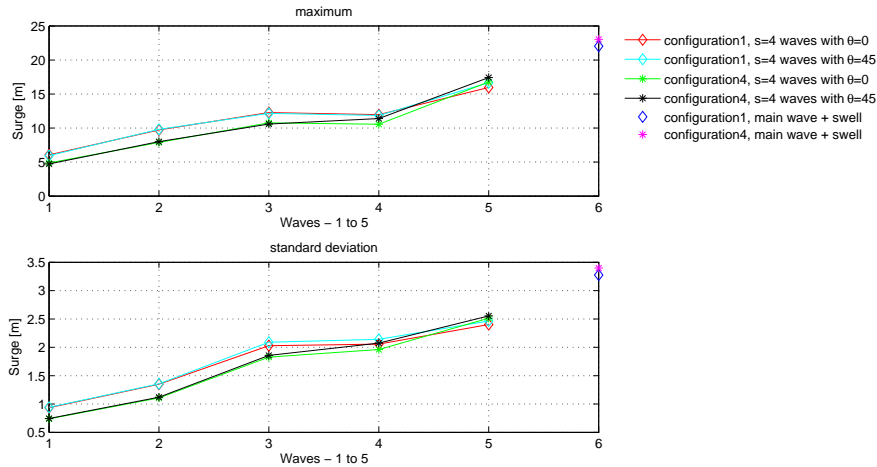

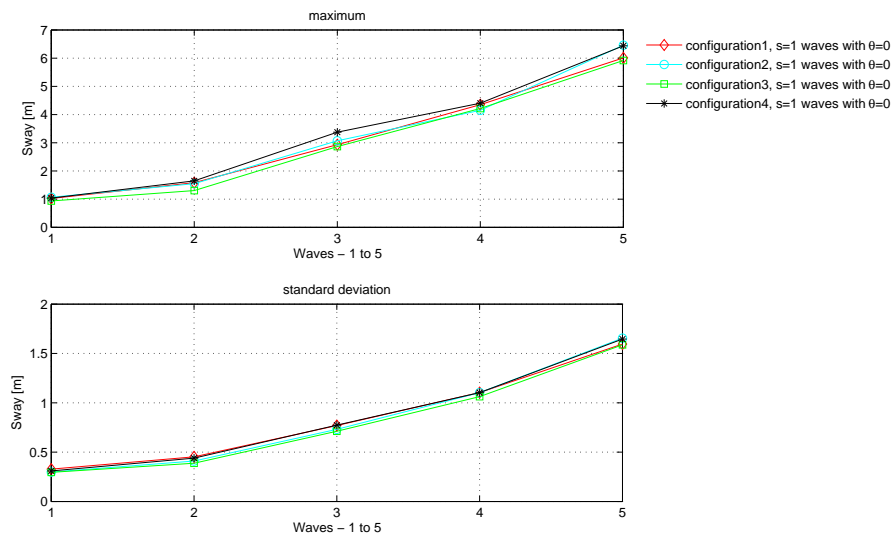FIGURE 7.25: Surge response statistics comparison
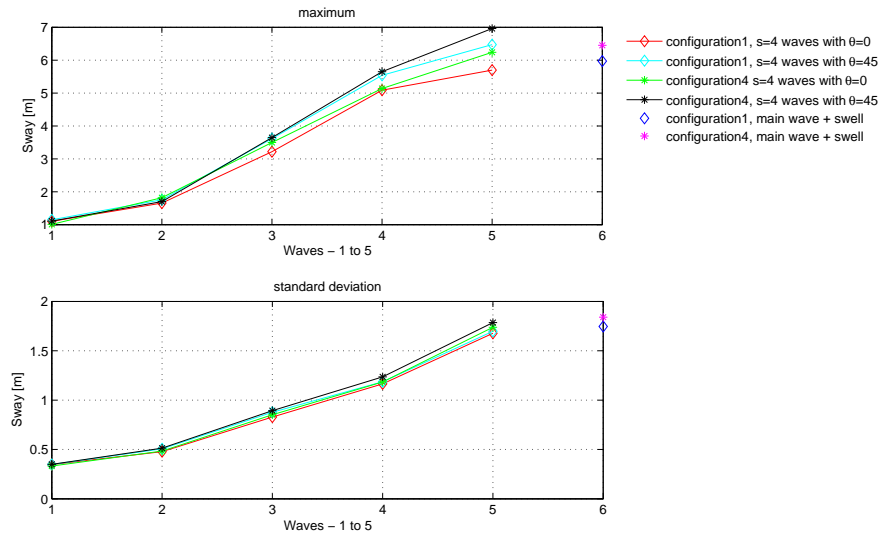
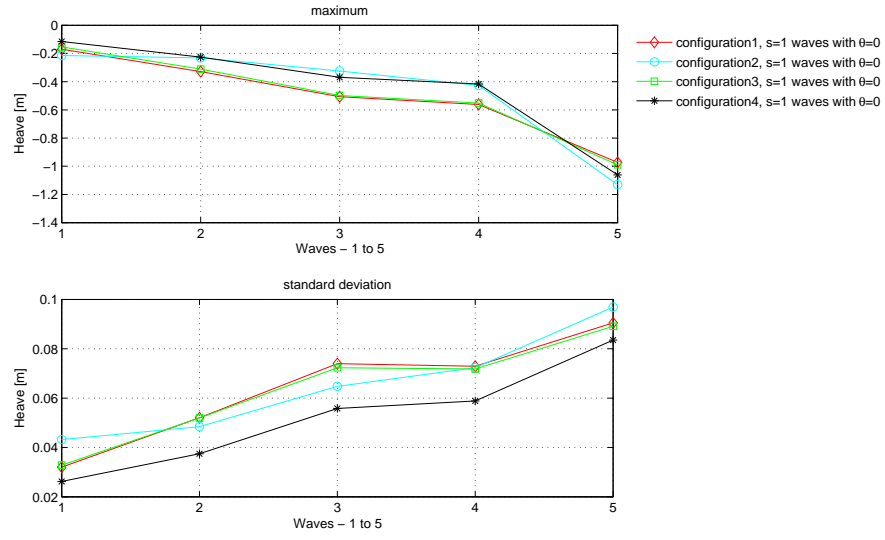FIGURE 7.26: Sway response statistics comparison
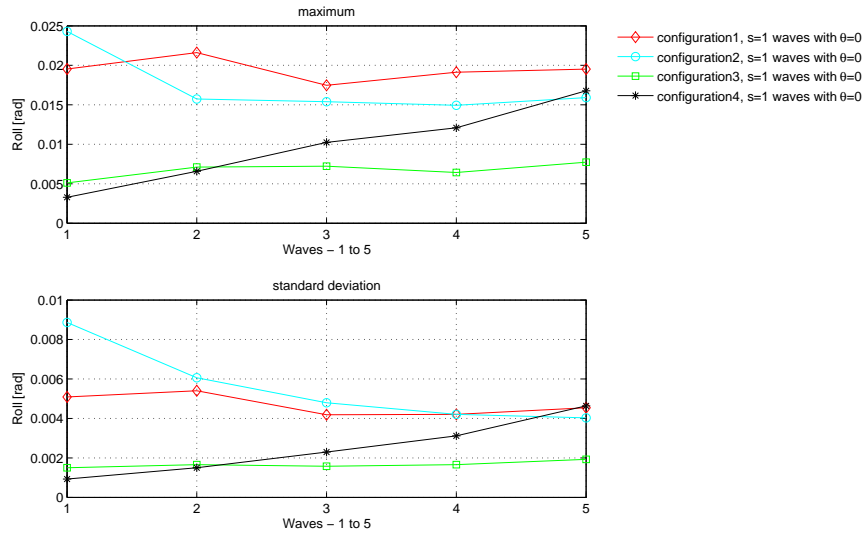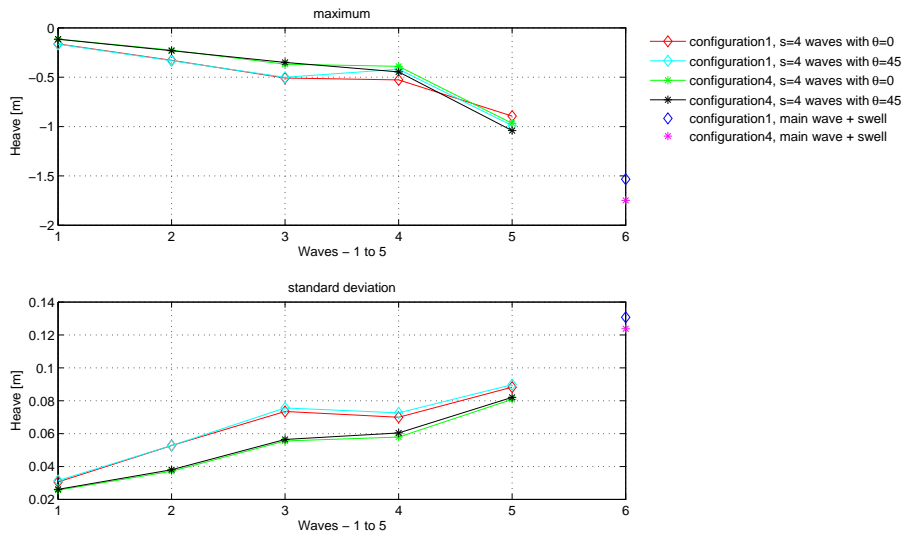

FIGURE 7.27: Heave response statistics comparison
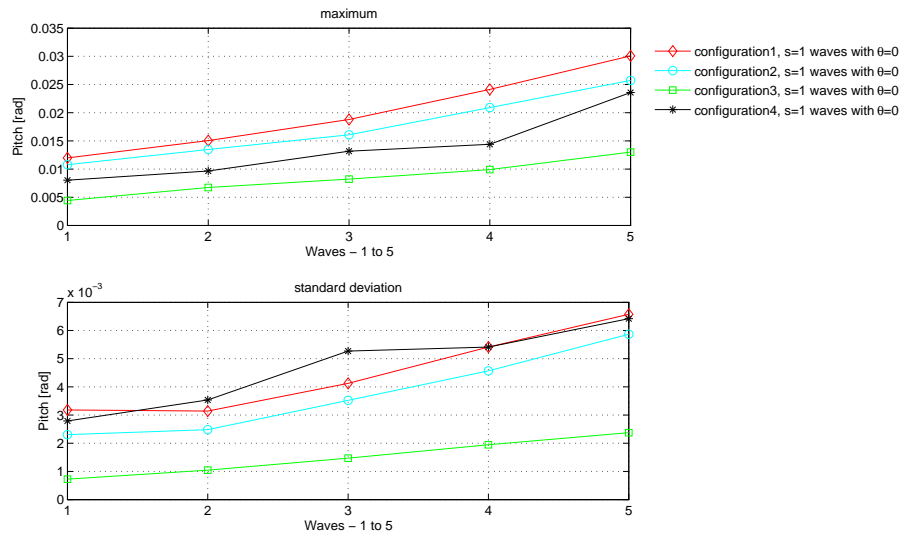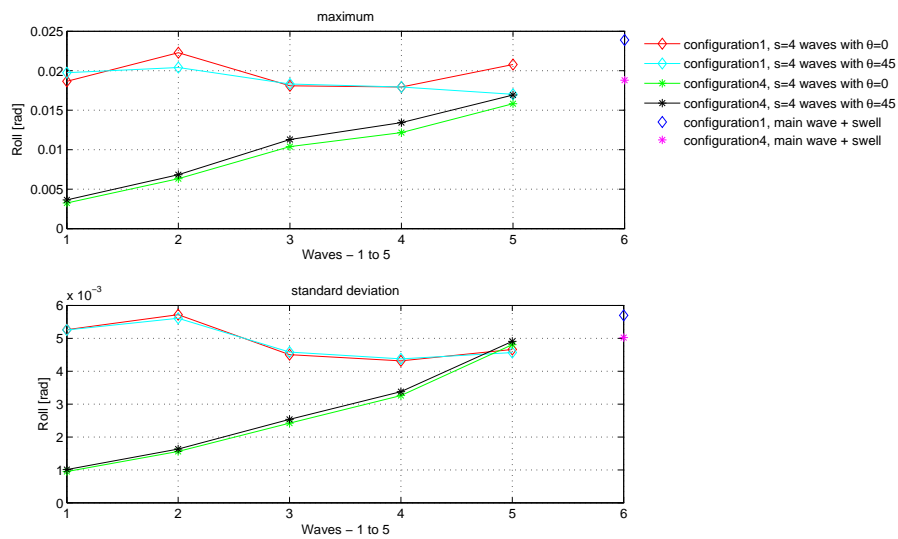
FIGURE 7.28: Roll response statistics comparison
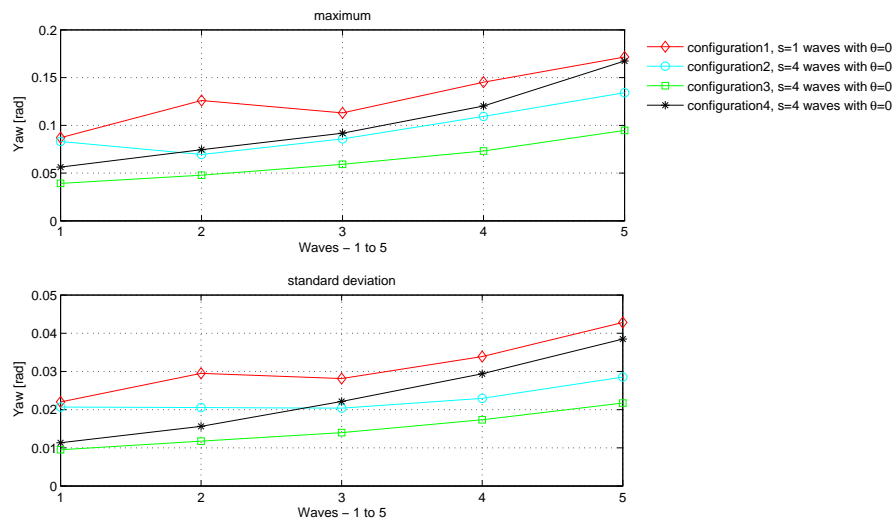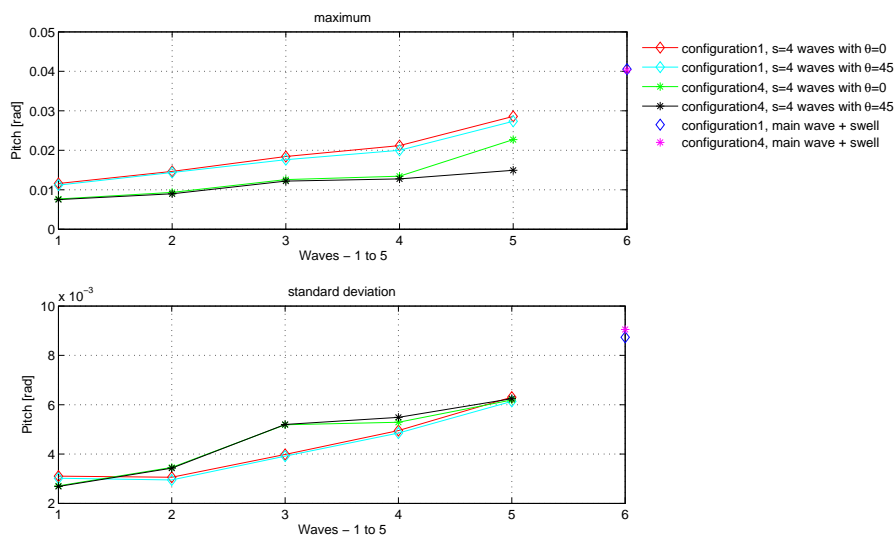

FIGURE 7.29: Pitch response statistics comparison
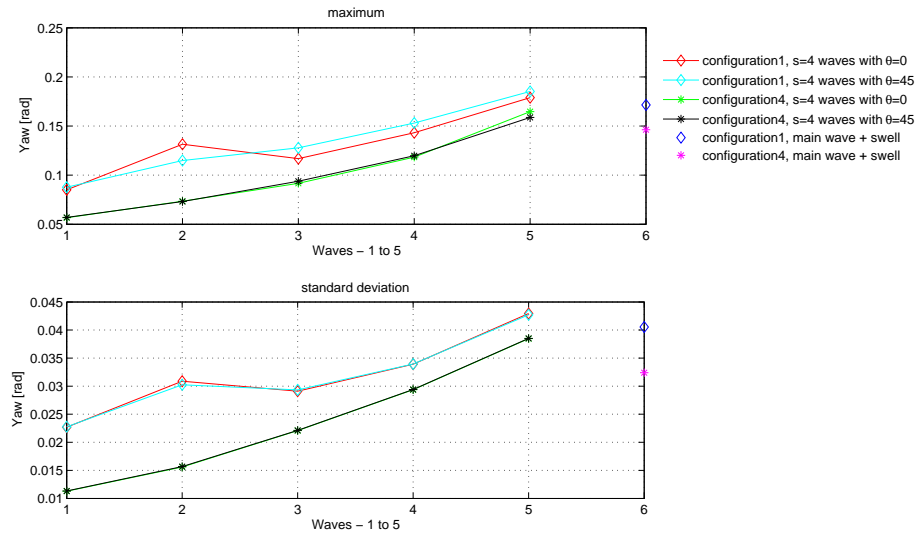
FIGURE 7.30: Yaw response statistics comparison

7.3   Statistical comparison of results using onshore and TLP controller parameters

The present model uses the control gain parameters, which are derived for the TLP wind turbine, as described in section 6.2.3 of Chapter 6. An investigation is carried out to understand the impact of the selection of control frequency and thereby the proportional and integral constants of the PI controller with respect to the onshore controller parameters when the wind turbine is subjected to a 3D wave and turbulent wind. The objective is to confirm the observations made in the section 6.2.3, when various configurations are subjected to severe sea states. Hence, computations are carried out for the fifth sea state for all the configurations using the onshore controller parameters. A statistical comparison is carried out between the responses with the onshore and floating turbine control parameters and the comparison is given in the following figures.

There is not an advantage observed for configuration 1 by using the floating control parameters, because of slightly increased rotor thrust. The fluctuation of sway response is lesser in the case of TLP control parameters, which is clearly due to a less fluctuating rotor torque, which is also influencing the platform roll standard deviation as seen in the figure. The heave response has an influence of the surge through the surge-heave coupling. The yaw response does not have a considerable difference between the response.

The main advantage of using the control parameters for floating turbines is on the floater pitch response, which can be clearly seen in the figure for all the configurations. This is achieved by obtaining a less fluctuating blade pitch angle and hence less fluctuating rotor moments.

Even in the severe sea states, the TLP configuration does not show any instabilities due to the control action. Hence the well known pitch instabilities as reported by Larsen and Hansen (2007) and Jonkman and Buhl (2005) for the floating wind turbines (mainly for spar) may not be applicable for the TLP wind turbines because of its stiff mooring configuration.
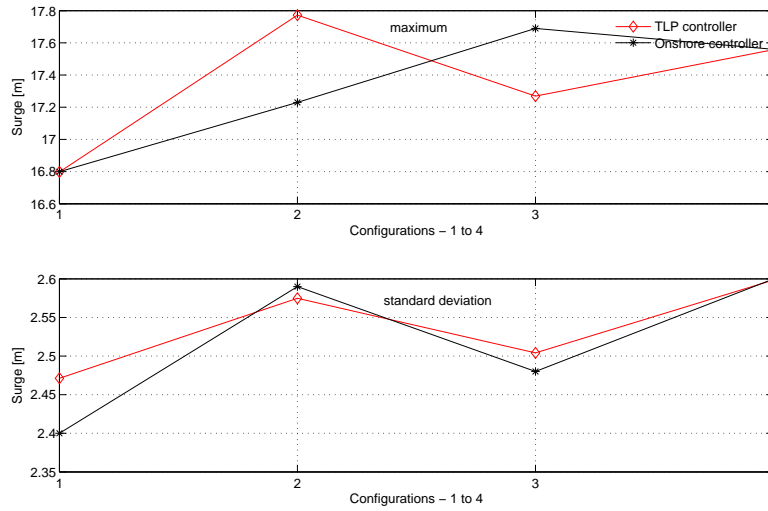
FIGURE 7.31: Surge response - statistical comparison with onshore controller
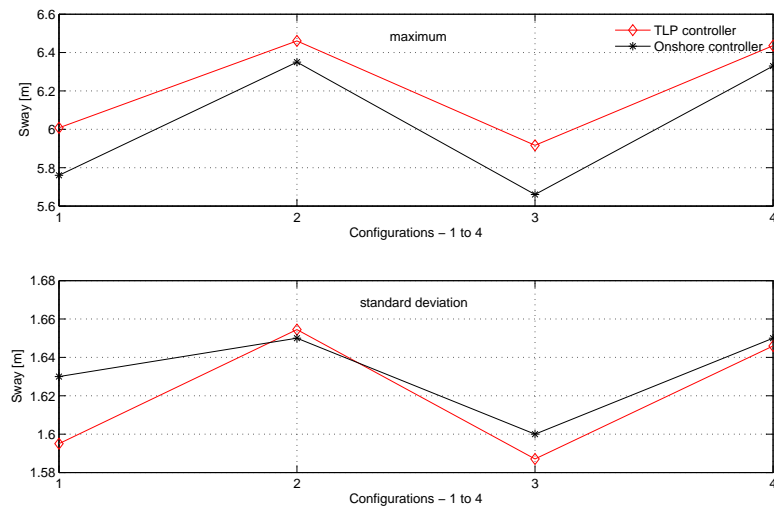
FIGURE 7.32: Sway response - statistical comparison with onshore controller
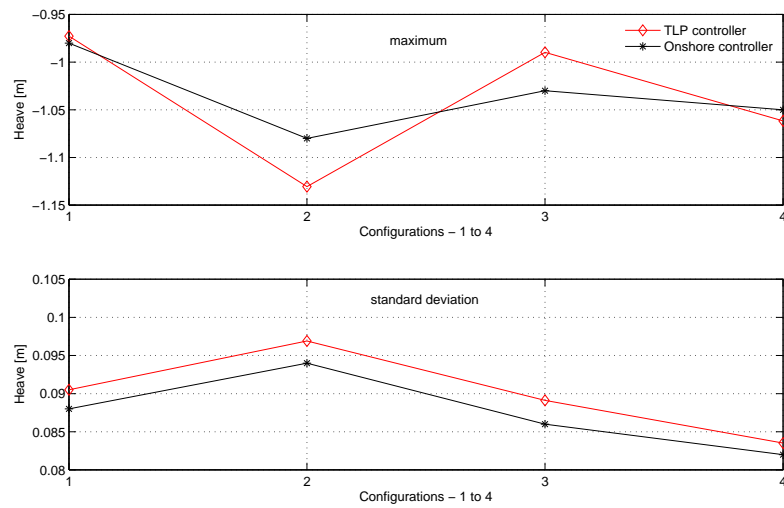
FIGURE 7.33: Heave response - statistical comparison with onshore controller
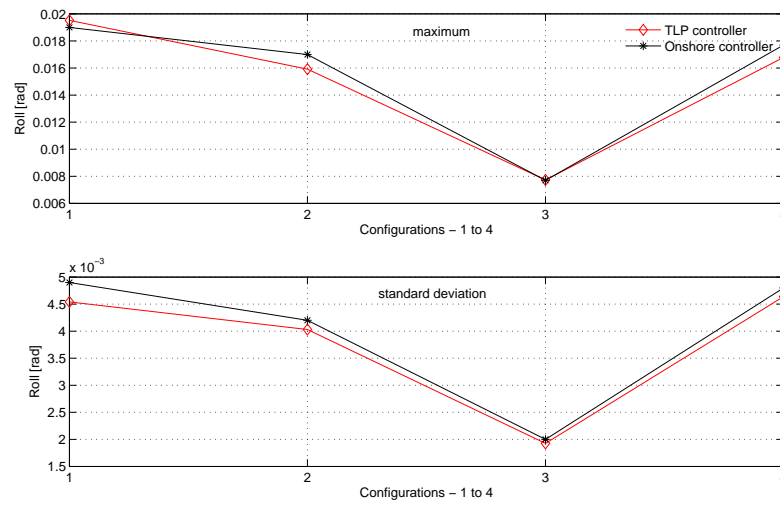
FIGURE 7.34: Roll response - statistical comparison with onshore controller
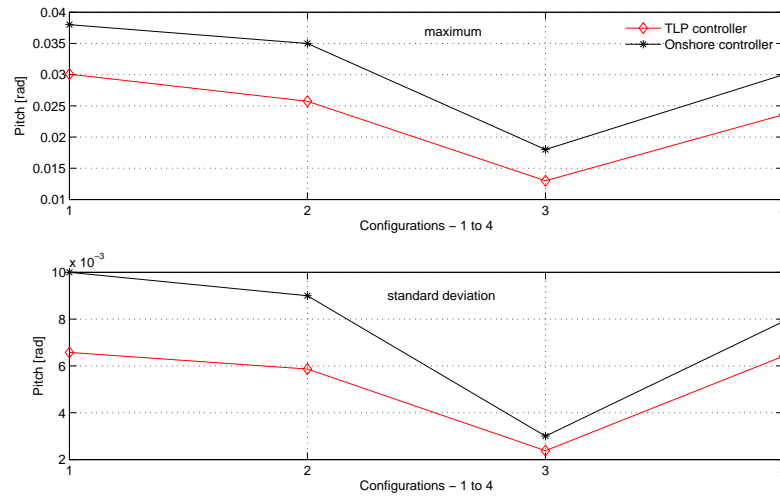
FIGURE 7.35: Pitch response - statistical comparison with onshore controller
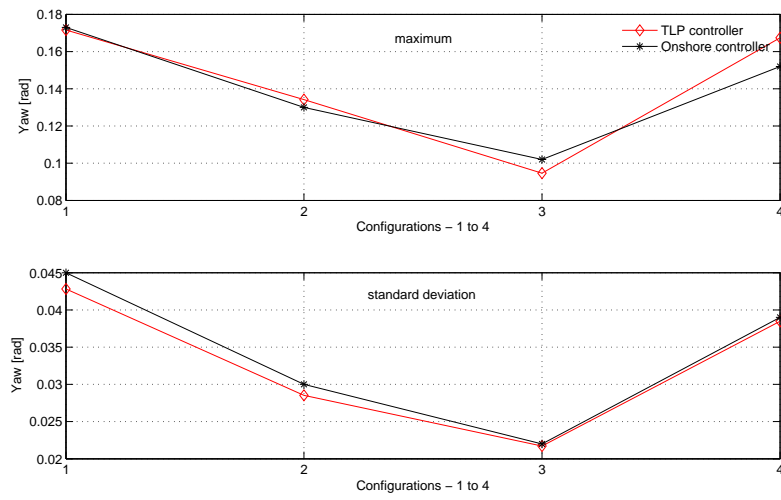
FIGURE 7.36: Yaw response - statistical comparison with onshore controller

7.4 Summary

A parametric study was carried out to investigate the responses of the TLP wind turbine subjected to various sea states. The influence of varying sea states was studied. Next, three alternative configurations were suggested and it was investigated on how the alternatives affect the responses. The responses were compared to that of the baseline configuration. Based on the response comparison, Configuration 4 was selected. As a further investigation, the selected configuration was subjected to the sea states with narrow banded wave spectrum, oblique wave heading and a swell. In addition, the impact of using the control parameters for floating wind turbines when the wind turbine was subjected to 3D irregular waves was studied in relation to the onshore control parameters. The responses were compared with that of the baseline configuration and the following conclusions are made.

The configuration with inclined tendons has smaller responses compared to the other configurations. Although the rotational responses are much smaller in the case of Configuration 3, the cost might prohibit this option, which is also the case for the Configuration 2. Based on the analysis, the Configuration 4 may be subjected to a more comprehensive loads and load cases analysis to quantify the extreme and fatigue loads, which is not considered in the present study.

The oblique and swell waves seem to induce larger responses than the collinear waves due to a lack of aerodynamic damping.

For the calculations carried out, the TLP configuration is not affected by the known pitch instability due to the control action because of its stiff configuration.

CHAPTER 8

Conclusions and Future Work

8.1 Conclusions

An independent fourteen degrees of freedom code coupled with two-dimensional irregular wave forcing for a tension leg platform wind turbine was derived and implemented. The code is based on Blade Element Momentum theory for computing aerodynamic loads. The wave kinematics were computed using linear Airy wave theory and the hydrodynamic forcing was formulated using Morison's equation. The 2D code was used to investigate the influence of platform dynamics on the rotor loads and similarly the influence of rotor loads on platform responses. It was found that an integral approach is needed to model floating offshore wind turbines. In addition, semi-coupled approach showed that the responses lack the influence of aerodynamic damping from the rotor. The surge-heave coupling present in the TLP foundation through the set-down effect was observed. The influence of wind shear showed a small reduction in the mean platform response because of a small reduction in rotor thrust. Presence of the turbulent wind was found to excite low frequency response of platform pitch.

The two-dimensional code was extended to include the three-dimensional platform dynamics and coupled to a three-dimensional hydrodynamic forcing module. The 3D hydrodynamic forcing was computed using the 3D wave kinematics with directional spreading. The three-dimensional implementation was verified by obtaining a perfect agreement of results with the 2D code. The 3D code was further applied to compute the loads and responses for wind-wave misalignment cases, which highlighted the direction sensitiveness of waves with respect to wind. The computations also showed that instabilities might occur near to the rated wind speed regime mainly due to the absence of a controller. A complete description of turbulent wind was not implemented in the 3D code. Further, the computational time used by the 3D code was quite large because of the implementation in Matlab.

The limitations of the 3D code were overcome by implementing the 3D sub-model for platform dynamics and hydrodynamic forcing into an advanced aero-elastic code, Flex5. This gave rise to a more complete hydro-aero-servo-elastic code for TLP wind turbines. The implementation was verified through a set of test cases, which gave a good agreement of responses with that of the initial 3D code. The test cases also enlightened the sensitiveness of rotor yaw to the wave heading. The investigations showed that following.

- Mooring-induced coupling enhanced the yaw response.

- The longitudinal tower flexibility increased the platform pitch and the lateral tower flexibility induced platform roll.

- A platform pitch increased platform yaw through the pitch-induced gyroscopic effects.

- A combined platform roll and pitch forced platform yaw through roll-yaw coupling.

- The varying generator moment induced larger roll.

The extended Flex5 code was used to carry out a parametric study to evaluate the performance of the TLP configuration subjected to five different sea states during operational conditions. The responses showed that the baseline configuration has more yaw response and hence alternative configurations were investigated. Based on the analysis, a configuration with inclined tendons was selected for further investigations. The further investigations were done using more narrow banded waves (both collinear and oblique) and a combination of main wave with a swell. The oblique and swell waves induced larger responses than the collinear waves because of the lack of aerodynamic damping in the transverse direction. A comparison of the responses with that of the baseline configuration showed that the configuration with inclined tendons has smaller response and hence a further comprehensive loads and load cases analysis is needed to finalize the selection.

The influence of controller parameters on the platform responses was investigated to observe if the well known pitch instability or any other controller related instability occur for the TLP configurations considered. Adapting the onshore control parameters based on the lowest natural frequency of the system helped to reduce the platform pitch response, however, the platform pitch response did not show any influence of the instability. This may be due to the reason that the TLP configuration is relatively stiff in pitch compared to a Spar buoy configuration. Hence, the TLP configuration may not be sensitive to a pitch instability because of its stiff configuration.

8.2   Future Work

A comprehensive loads and load cases analysis may be carried out to quantify the extreme and fatigue loads out to finalize a potential TLP configuration. The analysis would also helps to study the differences in loads and responses with respect to an onshore wind turbine thereby the feasibility of a TLP configuration may be assessed.

The loads and responses from the extended Flex5 may be compared with that of other codes for certain identified load cases, which will be a first step towards an extensive validation. By doing so, the strengths and weaknesses of the new implementation can be identified.

In the next step, the code may be validated using measurements from model study or field study, which will make the code more robust. This will enhance the confidence in floating wind turbine modeling.

The influence of diffraction and radiation may be investigated to validate the present assumptions. It will also help to investigate larger diameter floater concepts, which may be sensitive to diffraction and radiation.

A sophisticated controller algorithm module may be derived and implemented, which takes into account the platform responses. This will provide more physical representation of the concept and hence the loads and responses. In addition, stability aspects related to the control actions, if any, can be understood.

Bibliography

Bredmose, H. (2002). Deterministic modelling of water waves in the frequency domain. *PhD Thesis, Technical University of Denmark*, 174–179.

Bredmose, H. and N. G. Jacobsen (2010). Breaking wave impacts on offshore wind turbine foundations: Focused wave groups and cfd. In *Proceedings of the ASME 29th 2010 International conference on ocean, offshore and arctic engineering OMAE2010*, Shanghai (China).

Butterfield, S. (2005). Dynamic stall simulated as time lag of separation. In *Proceedings of the 4th IEA symposium on the aerodynamics of wind turbines*, Rome (Italy).

Chen, Z. (2005). Deepwater floater for wind turbines. *M.Sc. Thesis, Technical University of Denmark*.

Chen, Z., N. Tarp-Johansen, and J. Jensen (2006). Mechanical characteristics of some deepwater floater designs for offshore wind turbines. *Wind Engineering 30*, 417–430.

Cordle, A. and J. Jonkman (2011). State of the art in floating wind turbine design tools. In *Proceedings of the 21st (2011) International Offshore and Polar Engineering Conference (ISOPE)*, Hawaii (USA), pp. 367 – 374.

DNV (2011). Design of offshore wind turbine structures. *Offshore standard DNV-OS-J101*.

FINO (2011). *http ://www.fino3.de. downloaded on 05.10.2011.*

Forristall, G. Z. (1981). Kinematics of directionally spread waves. In *Proceedings of Conference on directional wave spectra applications*, California (USA), pp. 129–146.

Garrad and Hassan (2010). Bladed theory manual version 4.0. *October 2010.*

GL (2007). Guideline for the certification of offshore wind turbines. *Edition 2005.*

Gudmestad, O. T. (1993). Measured and predicted deep water wave kinematics in regular and irregular seas. *Marine Structures 6*, 1–73.

Halfpenny (1991). Dynamic stall simulated as time lag of separation. In *Proceedings of the 4th IEA symposium on the aerodynamics of wind turbines*, Rome (Italy).

Hansen, M. H., A. Hansen, T. Larsen, S. Øye, P. Sørensen, and P. Fuglsang (2005). Control design for a pitch-regulated, variable speed wind turbine. *Risø-R-1500(EN)*.

Hansen, M. O. L. (2008). Aerodynamics of wind turbines. *Second edition, Earthscan.*

Henderson, A. and M. Patel (1998). Floating offshore wind energy. In *Proceedings of the 20th BWEA annual conference.*

Henderson, A. R., B. Bulder, R. Huijsmans, J. Peeringa, J. Pierik, E. Snijders, M. van Hees, G. H. Wijnants, and M. J. Wolf (2003). Floating windfarms for shallow offshore sites. In *Offshore wind energy in mediterranean and other european seas conference*, Naples (Italy).

Henderson, A. R., R. Leutz, and T. Fujii (2002). Potential for floating offshore wind energy in japanese waters. In *Proceedings of the twelfth international offshore and polar engineering conference*, Kitakyushu (Japan).

Henderson, A. R. and M. H. Patel (2003). On the modelling of a floating offshore wind turbine. *Wind Energy 6*, 53–86.

Henderson, A. R., M. H. Patel, J. Halliday, and G. Watson (1999). Multiple turbine floating offshore windfarms. In *European Wind Energy Conference*, Nice (France).

Henderson, A. R., G. M. Watson, M. H. Patel, and J. A. Halliday (2000). Floating offshore windfarms - an option? In *Offshore wind energy in mediterranean and other european seas conference*, Sicilia (Italy).

Henderson, A. R. and D. Witcher (2010). Floating offshore wind energy - a review of the current status and an assessment of the prospects. *Wind Engineering 34*, 01–16.

Henderson, H. R. and J. H. Vugts (2001). Prospects for floating offshore wind energy. In *European Wind Energy Conference*, Copenhagen (Denmark).

IEC (2009). Wind turbines - part 3: Design requirements for offshore wind turbines, iec 61400-3.

ISO (2005). Petroleum and natural gas industries - specific requirements for offshore structures - part 1: Metocean design and operating considerations. *International Standard ISO-19901-1*.

Joensen, S., J. J. Jensen, and A. E. Mansour (2007). Extreme value predictions for wave and wind-induced loads on floating offshore wind turbines using form. In *10th Int. Symposium PRADS2007*, Pennsylvania (USA).

Johannessen, K., T. Meling, and S. Haver (2002). Joint distribution for wind and waves in the northern north sea. *International Journal of Offshore and Polar Engineering 12(1)*(18).

Jonkman, J. (2008). Influence of control on the pitch damping of a floating wind turbine. In *ASME Wind Energy symposium,NREL/CP-500-42589*, Reno (USA).

Jonkman, J. and M. Buhl (2005). Fast user's guide. *Technical report NREL/EL-500-38230 August 2005*.

Jonkman, J. and M. Buhl (2007a). Development and verification of a fully coupled simulator for offshore wind turbines. In *45th AIAA Aerospace sciences meeting and exhibition,AIAA-2007-212,NREL/CP-500-40979*, Reno (USA).

Jonkman, J. and M. Buhl (2007b). Loads analysis of a floating offshore wind turbine using fully coupled simulation. In *WINDPOWER 2007 conference and exhibition,NREL/CP-500-41714*, Los Angeles (USA).

Jonkman, J., S. Butterfield, W. Musial, and G. Scott (2009). Definition of a 5-mw reference wind turbine for offshore system development. *NREL/TP-500-38060*.

Jonkman, J., T. Larsen, A. Hansen, T. Nygaard, K. Maus, M. Karimirad, Z. Gao, T. Moan, I. Fylling, J. Nichols, M. Kohlmeier, J. P. Vergara, D. Merino, W. Shi, and H. Park (2010). Offshore code comparison collaboration within iea wind task 23: Phase iv results regarding floating wind turbine modeling. In *Proceedings of European wind energy conference, EWEC*, Warsaw (Poland).

Jonkman, J. and P. Sclavounos (2006). Development of fully coupled aeroelastic and hydrodynamic models for offshore wind turbines. In *44th AIAA Aerospace sciences meeting and exhibition,AIAA-2006-995,NREL/CP-500-39066*, Reno (USA).

Jonkman, J. M. (2007). Dynamics modeling and loads analysis of an offshore floating wind turbine. *PhD Thesis, NREL/TP-500-41958*.

Karimirad, M. (2011). Dynamic stall simulated as time lag of separation. In *Proceedings of the 4th IEA symposium on the aerodynamics of wind turbines*, Rome (Italy).

Karimirad, M., Z. Gao, and T. Moan (2009). Dynamic motion analysis of catenary moored spar wind turbine in extreme environmental condition. In *Proceedings of European offshore wind conference*, Stockholm (Sweden).

Karimirad, M. and T. Moan (2010). Effect of aerodynamic and hydrodynamic damping on dynamic response of spar-type floating wind turbine. In *Proceedings of European wind energy conference, EWEC*, Warsaw (Poland).

Karimirad, M. and T. Moan (2011a). Extreme dynamic structural response analysis of catenary moored spar wind turbine in harsh environmental conditions. *Journal of offshore mechanics and arctic engineering 133*.

Karimirad, M. and T. Moan (2011b). Wave and wind induced dynamic response of a spar-type offshore wind turbine. *Journal of waterway, port, coastal and ocean engineering*.

Knauer, A. (2006). Dynamic stall simulated as time lag of separation. In *Proceedings of the 4th IEA symposium on the aerodynamics of wind turbines*, Rome (Italy).

Kogaki, T., H. Matsumiya, and M. Nagai (2003). Technical and economic aspects of offshore wind energy development in japan. In *Proceedings of the International offshore and polar engineering conference*, Kitakyushu (Japan).

Kosugi, A., O. Ryu, K. Hiroshi, A. Yoshiaki, and K. Tsuguki (2002). A feasibility study on a floating wind farm off japan coast. In *Proceedings of the International offshore and polar engineering conference*.

Laino, D. and A. Hansen (2002). User's guide to the wind turbine aerodynamics computer software aerodyn.

Larsen, T. and A. Hansen (2007). How 2 hawc2, the user's manual. *December 2007*.

Larsen, T. J. and T. D. Hanson (2007). A method to avoid negative damped low frequent tower vibrations for a floating, pitch controlled wind turbine. *Journal of Physics: Conference series 75*.

Lee, K., P. Sclavounos, and E. Wayman (2005). Floating wind turbines. In *Proceedings of 20th International workshop on water waves and floating bodies*, Spitsbergen (Norway).

Lindenburg, C. (2005). Phatas release 'nov-2003' and 'apr-2005' user's manual - program for horizontal axis wind turbine analysis and simulation. *ECN-I–05-005 May 2005*.

Luxcey, N., H. Ormberg, and E. Passano (2011). Global analysis of a floating wind turbine using an aero-hydro-elastic model. part2: Benchmark study. In *Proceedings of 30th International conference on offshore mechanics and arctic engineering, OMAE2011*, Rotterdam (The Netherlands).

Mann, J. (1994). The spatial structure of neutral atmospheric surface-layer turbulence. *J. Fluid Mech. 273*, 141–168.

Mann, J. (1998). Wind field simulation. *Prob. Engng. Mech. 13*, 269–282.

Manwell, J. F., A. L. Rogers, and J. G. McGowan (2001). Status of offshore wind energy in the united states. In *Proceedings of power engineering society summer meeting*.

Morison, J. R., M. P. OBrien, J. W. Johnson, and S. A. Schaaf (1950). The forces exerted by surface waves on monopiles. *J. Petrol Techn. 189*, 149–154.

Musial, W. and S. Butterfield (2004). Future of offshore wind energy in the united states. In *Proceedings of EnergyOcean 2004*, Palm Beach (USA).

Nielsen, F. G., T. D. Hanson, and B. Skaare (2006a). Integrated dynamic analysis of floating offshore wind turbines. In *Proceedings of 25th International conference on offshore mechanics and arctic engineering, OMAE2006*, Hamburg (Germany).

Nielsen, F. G., T. D. Hanson, and B. Skaare (2006b). Integrated dynamic analysis of floating offshore wind turbines. In *Proceedings of European wind energy conference, EWEC*, Athens (Greece).

Ormberg, H., E. Passano, and N. Luxcey (2011). Global analysis of a floating wind turbine using an aero-hydro-elastic model. part1: Code development and case study. In *Proceedings of 30th International conference on offshore mechanics and arctic engineering, OMAE2011*, Rotterdam (The Netherlands).

Øye, S. (1991). Dynamic stall simulated as time lag of separation. In *Proceedings of the 4th IEA symposium on the aerodynamics of wind turbines*, Rome (Italy).

Øye, S. (1996). Flex4 simulation of wind turbine dynamics. In *28th IEA Meeting of Experts Concerning State of the Art of Aeroelastic Codes for Wind Turbine Calculationsn (available through International Energy Agency)*.

Roddier, D., C. Cermelli, and A. Weinstein (2001). Windfloat: A floating foundation for offshore wind turbines-part i: Design basis and qualification process. In *Proceedings of the 28th international conference on offshore mechanics and arctic engineering, OMAE2009*, Hawaii (USA).

Rodenbusch, G. and G. Z. Forristall (1986). An emperical model for random directional wave kinematics near the free surface. In *Proceedings of 18th Offshore technology conference*, Houston (USA), pp. 137–146.

Schløer, S., H. Bredmose, H. Bingham, and T. Larsen (2012). Effects from fully nonlinear irregular wave force on the fatigue life of an offshore wind turbine and its monopile foundation. In *Proceedings of the ASME 31st 2012 International Conferene on Ocean, Offshore and Arctic Engineering*, Rio de Janeiro (Brazil).

Sclavounos, P., C. Tracy, and S. Lee (2008). Floating offshore wind turbines: Responses in a seastate pareto optimal designs and economic assessment. In *Proceedings of 27th International conference on offshore mechanics and arctic engineering, OMAE2008*, Estoril (Portugal).

Sclavounos, P. D., S. Lee, J. DiPietro, G. Potenza, P. Caramuscio, and G. D. Michele (2010). Floating offshore wind turbines: Tension leg platform taught leg buoy concepts supporting 3-5 mw wind turbines. In *Proceedings of European wind energy conference, EWEC*, Warsaw (Poland).

Skaare, B., T. D. Hanson, F. G. Nielsen, R. Yttervik, A. M. Hansen, and K. Thomsen (2007a). Integrated dynamic analysis of floating offshore wind turbines. In *Proceedings of 26th International conference on offshore mechanics and arctic engineering, OMAE2007*, California (USA).

Skaare, B., T. D. Hanson, F. G. Nielsen, R. Yttervik, A. M. Hansen, and K. Thomsen (2007b). Integrated dynamic analysis of floating offshore wind turbines. In *Proceedings of European wind energy conference, EWEC*, Milan (Italy).

Sumer, B. M. and J. Fredsøe (2006). Hydrodynamics around cylindrical structures. *Revised edition, World Scientific*.

Suzuki, J. (1994). The spatial structure of neutral atmospheric surface-layer turbulence. *J. Fluid Mech. 273*, 141–168.

Vita, L., U. Paulsen, and T. Pedersen (2010). A novel floating offshore wind turbine concept:new developments. In *Proceedings of the European wind energy conference*, Warsaw (Poland).

Wayman, E., P. Sclavounos, S. Butterfield, J. Jonkman, and W. Musial (2006). Coupled dynamic modeling of floating wind turbine systems. In *Proceedings of the Offshore Technology Conference 2006,OTC-18287*, Houston (USA).

Wheeler, J. D. (1970). Method for calculating forces produced by irregular waves. *J. Petrol Techn.*, 119–137.

Withee, J. E. (2004). Fully coupled dynamic analysis of a floating wind turbine system. *PhD Thesis, Department of Ocean Engineering, Massachusetts Institute of Technology*.

Xü, H. (1995). Error analysis of popular wave models for long-crested seas. In *Proceedings of 27th Offshore technology conference*, Houston (USA), pp. 425–438.

Derivation of mooring force

A.1   Mooring force

The restoring forces offered by the mooring lines are formulated. A schematic sketch of the un-displaced system is shown in Figure A.1.
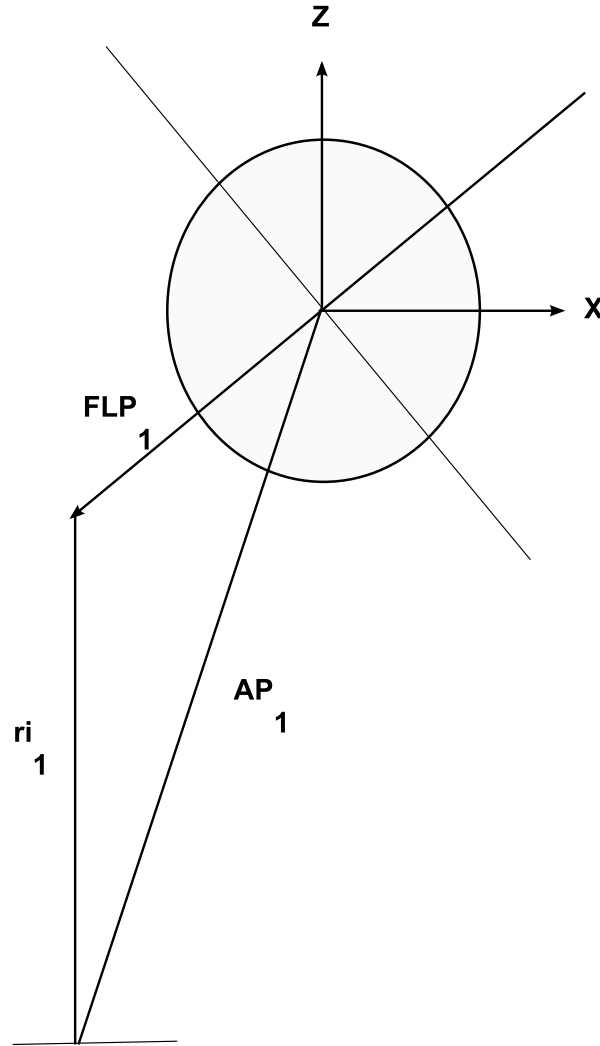
FIGURE A.1: Schematic sketch of mooring lines

In the figure, only the first mooring line is shown. The geometric position of the fairlead points, derived in system 2 (platform) is given below.

The fairlead positions of the tendons 1 to 4 are,

$$\mathbf{FLP_1} = \left\{ \begin{array}{c} -\tilde{d} \\ -\tilde{d} \\ 0 \end{array} \right\} \tag{A.1}$$

$$\mathbf{FLP_2} = \left\{ \begin{array}{c} \tilde{d} \\ -\tilde{d} \\ 0 \end{array} \right\} \tag{A.2}$$

$$\mathbf{FLP_3} = \left\{ \begin{array}{c} \tilde{d} \\ \tilde{d} \\ 0 \end{array} \right\} \tag{A.3}$$

$$\mathbf{FLP_4} = \left\{ \begin{array}{c} -\tilde{d} \\ \tilde{d} \\ 0 \end{array} \right\} \tag{A.4}$$

The anchor point positions with respect to the platform bottom centre point are written as follows.

$$\mathbf{AP_1} = \left\{ \begin{array}{c} -\tilde{d} \\ -\tilde{d} \\ -L_0 \end{array} \right\} \tag{A.5}$$

$$\mathbf{AP_2} = \left\{ \begin{array}{c} \tilde{d} \\ -\tilde{d} \\ -L_0 \end{array} \right\} \tag{A.6}$$

$$\mathbf{AP_3} = \left\{ \begin{array}{c} \tilde{d} \\ \tilde{d} \\ -L_0 \end{array} \right\} \tag{A.7}$$

$$\mathbf{AP_4} = \left\{ \begin{array}{c} -\tilde{d} \\ \tilde{d} \\ -L_0 \end{array} \right\} \tag{A.8}$$

The initial coordinates of the tendons are computed using the geometric relations as given below.

$$\mathbf{ri_1} = \mathbf{AP_1} - \mathbf{FLP_1} \tag{A.9}$$

$$\mathbf{ri_2} = \mathbf{AP_2} - \mathbf{FLP_2} \tag{A.10}$$

$$\mathbf{ri_3} = \mathbf{AP_3} - \mathbf{FLP_3} \tag{A.11}$$

$$\mathbf{ri_4} = \mathbf{AP_4} - \mathbf{FLP_4} \tag{A.12}$$

Hence, the initial tendon lengths can be computed by taking the modulus of the length vector, such as, $Li_1 = \|\mathbf{ri_1}\|$. Similarly, the initial lengths for other three tendons, Li_2, Li_3 and Li_4 can also be computed.

Let the platform is subjected to the following translational and rotational displacements.

$$\mathbf{s_{pc}} = \left\{ \begin{array}{c} \eta_1 \\ \eta_2 \\ \eta_3 \end{array} \right\} \tag{A.13}$$

$$\mathbf{r_{pc}} = \left\{ \begin{array}{c} \eta_4 \\ \eta_5 \\ \eta_6 \end{array} \right\} \tag{A.14}$$

where $\mathbf{s_{pc}}$ and $\mathbf{r_{pc}}$ are the translational and rotational displacements of the platform centre point, η_1, η_2, η_3, η_4, η_5 and η_6 are the platform surge, sway, heave, roll, pitch and yaw displacements respectively.

While the platform is subjected to the above displacements, the final tendon coordinates can be found out using the following equations.

$$\mathbf{rf_1} = \mathbf{ri_1} - \mathbf{s_{pc}} - \mathbf{r_{pc}} \times \mathbf{FLP_1} \tag{A.15}$$

$$\mathbf{rf_2} = \mathbf{ri_2} - \mathbf{s_{pc}} - \mathbf{r_{pc}} \times \mathbf{FLP_2} \tag{A.16}$$

$$\mathbf{rf_3} = \mathbf{ri_3} - \mathbf{s_{pc}} - \mathbf{r_{pc}} \times \mathbf{FLP_3} \tag{A.17}$$

$$\mathbf{rf_4} = \mathbf{ri_4} - \mathbf{s_{pc}} - \mathbf{r_{pc}} \times \mathbf{FLP_4} \tag{A.18}$$

Hence, the final tendon lengths are computed by taking the modulus of the length vector, such as Lf_1, which is given below.

$$Lf_1 = \|\mathbf{rf_1}\| \tag{A.19}$$

Similarly, the final lengths for other three tendons, Lf_2, Lf_3 and Lf_4 are also calculated. The change in lengths of the tendons are obtained by subtracting the initial length from the final tendon length as, $dL1 = Lf_1 - Li_1$ and similarly $dL2$, $dL3$ and $dL4$ are also computed.

The instantaneous tendon tensions when the platform is subjected to displacements are computed as given below.

$$T1 = \frac{T0}{4} + dT1 \tag{A.20}$$

where $T0$ is the initial tension and $dT1$ is the change in tension of first tendon, which is given below.

$$dT1 = \frac{A_{tend} E_{tend}}{Li_1} dL1 \tag{A.21}$$

where A_{tend} and E_{tend} are the area of cross-section and Young's modulus of the tendon. Similarly, the change in tension and instantaneous tendon tensions are computed for the other three tendons as well.

The instantaneous tendon tensions generate a moment about the platform bottom centre point, for which the moment arms are the same as the fair lead point vectors.

Hence the restoring force and moment vectors are computed as given below.

Restoring force from the first tendon is given by,

$$\mathbf{TF1} = T1\frac{\mathbf{rf_1}}{Lf_1} \tag{A.22}$$

where the ratio, $\mathbf{rf_1}/Lf_1$ represents the unit vector along the first tendon and similarly the restoring forces from the other tendons **TF2**, **TF3** and **TF4** are also computed.

The moment arm for computing the restoring moments are given below.

$$\mathbf{r1Moment} = \mathbf{FLP_1} + \mathbf{r_{pc}} \times \mathbf{FLP_1} \tag{A.23}$$

Similarly, the moment arms for other tendons, **r2Moment**, **r3Moment** and **r4Moment** can also be computed.

The restoring moments are computed using the following equation.

$$\mathbf{RM1} = \mathbf{r1Moment} \times \mathbf{TF1} \tag{A.24}$$

Similarly **RM2**, **RM3** and **RM4** can also be computed.

Hence, the total restoring forces and moments are calculated as given below.

$$\mathbf{TF} = \mathbf{TF1} + \mathbf{TF2} + \mathbf{TF3} + \mathbf{TF4} \tag{A.25}$$

$$\mathbf{RM} = \mathbf{RM1} + \mathbf{RM2} + \mathbf{RM3} + \mathbf{RM4} \tag{A.26}$$

where TF is the restoring force (surge, sway and heave) and RM is the restoring moment (roll, pitch and yaw).

Derivation of generalized force and mass

B.1 Generalized force

The generalized force is derived as given below.

First element:

A unit virtual displacement in the first degree of freedom gives rise to a virtual work of δW, which is the first element of the generalized force, as given below.

$$F_{g1} = F_1 \cdot 1 + F_w \cdot 1 + F_{moor1} \cdot 1 \tag{B.1}$$

where F_1 is the hydrodynamic surge force, F_{moor1} is the mooring force in the surge degree of freedom and F_w is the rotor thrust, given by the following equation.

$$F_w = \int_0^R \left(p_n^{B1} dr + p_n^{B2} dr + p_n^{B3} dr \right) \tag{B.2}$$

Second element:

A unit virtual displacement in the second degree of freedom gives rise to a virtual work of δW, which is the second element of the generalized force, as given below.

$$F_{g2} = F_2 \cdot 1 + F_{g2}^b \cdot 1 + F_{moor2} \cdot 1 \tag{B.3}$$

where F_2 is the hydrodynamic sway force, F_{moor2} is the mooring force in sway degree of freedom and F_{g2}^b is the force contribution from blades due to the platform sway virtual displacement, given by the following equation.

$$F_{g2}^b = \int_0^R \left\{ \begin{array}{c} 0 \\ p_t^{B1} \\ p_n^{B1} \end{array} \right\} \cdot [T]_{26}^{B1} \left\{ \begin{array}{c} 0 \\ 1 \\ 0 \end{array} \right\} dr + \int_0^R \left\{ \begin{array}{c} 0 \\ p_t^{B2} \\ p_n^{B2} \end{array} \right\} \cdot [T]_{26}^{B2} \left\{ \begin{array}{c} 0 \\ 1 \\ 0 \end{array} \right\} dr$$
$$+ \int_0^R \left\{ \begin{array}{c} 0 \\ p_t^{B3} \\ p_n^{B3} \end{array} \right\} \cdot [T]_{26}^{B3} \left\{ \begin{array}{c} 0 \\ 1 \\ 0 \end{array} \right\} dr \tag{B.4}$$

where $[T]_{26}^{B1}$, $[T]_{26}^{B2}$ and $[T]_{26}^{B3}$ represent the transformation matrices from platform (system 2) to blade 1, blade 2 and blade 3 (system 6) respectively and the vector $\left\{ \begin{array}{c} 0 \\ 1 \\ 0 \end{array} \right\}$ represents the platform displacement, wherein only sway is present.

Third element:

A unit virtual displacement in the third degree of freedom gives rise to a virtual work of δW, which is the third element of the generalized force, as given below.

$$F_{g3} = F_3 \cdot 1 + F_{g3}^b \cdot 1 + F_b \cdot 1 - F_G \cdot 1 + F_{moor3} \cdot 1 \tag{B.5}$$

where F_3 is the hydrodynamic heave force, F_b and F_G are the buoyancy and gravity force, F_{moor3} is the mooring force in heave degree of freedom and F_{g3}^b is the force contribution from blades due to the platform heave virtual displacement, which is given by the following equation.

$$
\begin{aligned}
F_{g3}^b = \int_0^R \left\{ \begin{array}{c} 0 \\ p_t^{B1} \\ p_n^{B1} \end{array} \right\} \cdot [T]_{26}^{B1} \left\{ \begin{array}{c} 0 \\ 0 \\ 1 \end{array} \right\} dr + \int_0^R \left\{ \begin{array}{c} 0 \\ p_t^{B2} \\ p_n^{B2} \end{array} \right\} \cdot [T]_{26}^{B2} \left\{ \begin{array}{c} 0 \\ 0 \\ 1 \end{array} \right\} dr \\
+ \int_0^R \left\{ \begin{array}{c} 0 \\ p_t^{B3} \\ p_n^{B3} \end{array} \right\} \cdot [T]_{26}^{B3} \left\{ \begin{array}{c} 0 \\ 0 \\ 1 \end{array} \right\} dr
\end{aligned}
\tag{B.6}
$$

where the vector $\left\{ \begin{array}{c} 0 \\ 0 \\ 1 \end{array} \right\}$ represents the platform displacement, wherein only heave is present.

Fourth element:

A unit virtual displacement in the fourth degree of freedom gives rise to a virtual work of δW, which is the fourth element of the generalized force, as given below.

$$F_{g4} = F_4 \cdot 1 + F_{g4}^b + F_b y_b - F_G y_G + F_{moor4} \cdot 1 \tag{B.7}$$

where F_4 is the hydrodynamic roll moment, y_b and y_G are the y coordinates of centres of buoyancy and gravity, F_{moor4} is the restoring moment in roll degree of freedom and F_{g4}^b is the moment contribution from blades due to the platform roll virtual displacement, which is given by the following equation.

$$
\begin{aligned}
F_{g4}^b = \int_0^R \left\{ \begin{array}{c} 0 \\ p_t^{B1} \\ p_n^{B1} \end{array} \right\} \cdot [T]_{26}^{B1} \left(\left\{ \begin{array}{c} 1 \\ 0 \\ 0 \end{array} \right\} \times \left\{ \begin{array}{c} r_x \\ r_y \\ r_z \end{array} \right\} \right) dr \\
+ \int_0^R \left\{ \begin{array}{c} 0 \\ p_t^{B2} \\ p_n^{B2} \end{array} \right\} \cdot [T]_{26}^{B2} \left(\left\{ \begin{array}{c} 1 \\ 0 \\ 0 \end{array} \right\} \times \left\{ \begin{array}{c} r_x \\ r_y \\ r_z \end{array} \right\} \right) dr \\
+ \int_0^R \left\{ \begin{array}{c} 0 \\ p_t^{B3} \\ p_n^{B3} \end{array} \right\} \cdot [T]_{26}^{B3} \left(\left\{ \begin{array}{c} 1 \\ 0 \\ 0 \end{array} \right\} \times \left\{ \begin{array}{c} r_x \\ r_y \\ r_z \end{array} \right\} \right) dr
\end{aligned}
\tag{B.8}
$$

where the vector $\left\{ \begin{array}{c} 1 \\ 0 \\ 0 \end{array} \right\}$ represents the platform displacement (only roll is present) and

the vector $\left\{ \begin{array}{c} r_x \\ r_y \\ r_z \end{array} \right\}$ represents the coordinates of the blade section under consideration with respect to the platform.

Fifth element:

A unit virtual displacement in the fifth degree of freedom gives rise to a virtual work of δW, which is the fifth element of the generalized force, as given below.

$$F_{g5} = F_5 \cdot 1 + F_{g5}^b + F_b x_b - F_G x_G + F_{moor5} \cdot 1 \tag{B.9}$$

where F_5 is the hydrodynamic pitch moment, x_b and x_G are the x coordinates of centres of buoyancy and gravity, F_{moor5} is the restoring moment in pitch degree of freedom and F_{g5}^b is the moment contribution from blades due to the platform pitch virtual displacement, which is given by the following equation.

$$
\begin{aligned}
F_{g5}^b = & \int_0^R \left\{ \begin{array}{c} 0 \\ p_t^{B1} \\ p_n^{B1} \end{array} \right\} \cdot [T]_{26}^{B1} \left(\left\{ \begin{array}{c} 0 \\ 1 \\ 0 \end{array} \right\} \times \left\{ \begin{array}{c} r_x \\ r_y \\ r_z \end{array} \right\} \right) dr \\
& + \int_0^R \left\{ \begin{array}{c} 0 \\ p_t^{B2} \\ p_n^{B2} \end{array} \right\} \cdot [T]_{26}^{B2} \left(\left\{ \begin{array}{c} 0 \\ 1 \\ 0 \end{array} \right\} \times \left\{ \begin{array}{c} r_x \\ r_y \\ r_z \end{array} \right\} \right) dr \\
& + \int_0^R \left\{ \begin{array}{c} 0 \\ p_t^{B3} \\ p_n^{B3} \end{array} \right\} \cdot [T]_{26}^{B3} \left(\left\{ \begin{array}{c} 0 \\ 1 \\ 0 \end{array} \right\} \times \left\{ \begin{array}{c} r_x \\ r_y \\ r_z \end{array} \right\} \right) dr
\end{aligned} \tag{B.10}
$$

where the vector $\left\{ \begin{array}{c} 0 \\ 1 \\ 0 \end{array} \right\}$ represents the platform displacement (only pitch is present).

Sixth element:

A unit virtual displacement in the sixth degree of freedom gives rise to a virtual work of δW, which is the sixth element of the generalized force, as given below.

$$F_{g6} = F_6 \cdot 1 + F_{g6}^b + F_{moor6} \cdot 1 \tag{B.11}$$

where F_6 is the hydrodynamic yaw moment, F_{moor6} is the restoring moment in yaw degree of freedom and F_{g6}^b is the moment contribution from blades due to the platform yaw virtual displacement, which is given by the following equation.

$$
\begin{aligned}
F_{g6}^b = & \int_0^R \left\{ \begin{array}{c} 0 \\ p_t^{B1} \\ p_n^{B1} \end{array} \right\} \cdot [T]_{26}^{B1} \left(\left\{ \begin{array}{c} 0 \\ 0 \\ 1 \end{array} \right\} \times \left\{ \begin{array}{c} r_x \\ r_y \\ r_z \end{array} \right\} \right) dr \\
& + \int_0^R \left\{ \begin{array}{c} 0 \\ p_t^{B2} \\ p_n^{B2} \end{array} \right\} \cdot [T]_{26}^{B2} \left(\left\{ \begin{array}{c} 0 \\ 0 \\ 1 \end{array} \right\} \times \left\{ \begin{array}{c} r_x \\ r_y \\ r_z \end{array} \right\} \right) dr \\
& + \int_0^R \left\{ \begin{array}{c} 0 \\ p_t^{B3} \\ p_n^{B3} \end{array} \right\} \cdot [T]_{26}^{B3} \left(\left\{ \begin{array}{c} 0 \\ 0 \\ 1 \end{array} \right\} \times \left\{ \begin{array}{c} r_x \\ r_y \\ r_z \end{array} \right\} \right) dr
\end{aligned} \tag{B.12}
$$

where the vector $\left\{ \begin{array}{c} 0 \\ 0 \\ 1 \end{array} \right\}$ represents the platform displacement (only yaw is present).

Seventh element:

The generalized force corresponding to a unit virtual displacement in the seventh degree of freedom is the rotor thrust and hence, $F_{g7} = F_w$.

Eighth element:

The generalized force corresponding to a unit virtual displacement in the eighth degree of freedom is the torque, which is given by, $F_{g8} = M_{aero} - M_{gen}$.

where M_{aero} is the rotor torque, which can be written as,

$$M_{aero} = \int_0^R \left(p_t^{B1} r + p_t^{B2} r + p_t^{B3} r \right) dr \tag{B.13}$$

and the generator torque, M_{gen}, is the same as given in section 4.2 of Chapter 4.

Ninth element:

The generalized force corresponding to a unit virtual displacement in the ninth degree of freedom (first flapwise deflection in blade 1) is given below. The contribution is only from blade 1 since the unit virtual displacement in blade 1 does not affect other blades.

$$F_{g9} = \int_0^R \begin{pmatrix} 0 \\ p_t^{B1} \\ p_n^{B1} \end{pmatrix} \cdot \begin{pmatrix} 0 \\ \phi_{1,y}^{1f} \\ \phi_{1,z}^{1f} \end{pmatrix} dr$$

$$= \int_0^R \left(p_t^{B1} \left(\phi_{1f}^e \cos\theta_p + \phi_{1f}^f \sin\theta_p \right) + p_n^{B1} \left(-\phi_{1f}^e \sin\theta_p + \phi_{1f}^f \cos\theta_p \right) \right) dr \tag{B.14}$$

where the blade displacements in the global coordinate system, $\phi_{1,y}^{1f} = \left(\phi_{1f}^e \cos\theta_p + \phi_{1f}^f \sin\theta_p \right)$ and $\phi_{1,z}^{1f} = \left(-\phi_{1f}^e \sin\theta_p + \phi_{1f}^f \cos\theta_p \right)$, wherein ϕ_{1f}^f and ϕ_{1f}^e are the flapwise and edgewise contributions of the first flapwise mode shape and θ_p is the pitch angle.

Tenth element:

The generalized force corresponding to a unit virtual displacement in the tenth degree of freedom (first edgewise deflection in blade 1) is given below.

$$F_{g10} = \int_0^R \begin{pmatrix} 0 \\ p_t^{B1} \\ p_n^{B1} \end{pmatrix} \cdot \begin{pmatrix} 0 \\ \phi_{1,y}^{1e} \\ \phi_{1,z}^{1e} \end{pmatrix} dr$$

$$= \int_0^R \left(p_t^{B1} \left(\phi_{1e}^e \cos\theta_p + \phi_{1e}^f \sin\theta_p \right) + p_n^{B1} \left(-\phi_{1e}^e \sin\theta_p + \phi_{1e}^f \cos\theta_p \right) \right) dr \tag{B.15}$$

where the blade displacements in the global coordinate system, $\phi_{1,y}^{1e} = \left(\phi_{1e}^e \cos\theta_p + \phi_{1e}^f \sin\theta_p \right)$ and $\phi_{1,z}^{1e} = \left(-\phi_{1e}^e \sin\theta_p + \phi_{1e}^f \cos\theta_p \right)$, wherein ϕ_{1e}^f and ϕ_{1e}^e are the flapwise and edgewise contributions of the first edgewise mode shape.

Eleventh element:

The generalized force corresponding to a unit virtual displacement in the eleventh degree of freedom (second flapwise deflection in blade 1) is given below.

$$F_{g11} = \int_0^R \begin{pmatrix} 0 \\ p_t^{B1} \\ p_n^{B1} \end{pmatrix} \cdot \begin{pmatrix} 0 \\ \phi_{1,y}^{2f} \\ \phi_{1,z}^{2f} \end{pmatrix} dr$$

$$= \int_0^R \left(p_t^{B1} \left(\phi_{2f}^e \cos\theta_p + \phi_{2f}^f \sin\theta_p \right) + p_n^{B1} \left(-\phi_{2f}^e \sin\theta_p + \phi_{2f}^f \cos\theta_p \right) \right) dr$$

(B.16)

where the blade displacements in the global coordinate system, $\phi_{1,y}^{2f} = \left(\phi_{2f}^e \cos\theta_p + \phi_{2f}^f \sin\theta_p \right)$ and $\phi_{1,z}^{2f} = \left(-\phi_{2f}^e \sin\theta_p + \phi_{2f}^f \cos\theta_p \right)$, wherein ϕ_{2f}^f and ϕ_{2f}^e are the flapwise and edgewise contributions of the second flapwise mode shape.

Twelfth element:

The generalized force corresponding to a unit virtual displacement in the twelfth degree of freedom (first flapwise deflection in blade 2) is given below.

$$F_{g12} = \int_0^R \begin{pmatrix} 0 \\ p_t^{B2} \\ p_n^{B2} \end{pmatrix} \cdot \begin{pmatrix} 0 \\ \phi_{2,y}^{1f} \\ \phi_{2,z}^{1f} \end{pmatrix} dr$$

$$= \int_0^R \left(p_t^{B2} \left(\phi_{1f}^e \cos\theta_p + \phi_{1f}^f \sin\theta_p \right) + p_n^{B2} \left(-\phi_{1f}^e \sin\theta_p + \phi_{1f}^f \cos\theta_p \right) \right) dr$$

(B.17)

Thirteenth element:

The generalized force corresponding to a unit virtual displacement in the thirteenth degree of freedom (first edgewise deflection in blade 2) is given below.

$$F_{g13} = \int_0^R \begin{pmatrix} 0 \\ p_t^{B2} \\ p_n^{B2} \end{pmatrix} \cdot \begin{pmatrix} 0 \\ \phi_{2,y}^{1e} \\ \phi_{2,z}^{1e} \end{pmatrix} dr$$

$$= \int_0^R \left(p_t^{B2} \left(\phi_{1e}^e \cos\theta_p + \phi_{1e}^f \sin\theta_p \right) + p_n^{B2} \left(-\phi_{1e}^e \sin\theta_p + \phi_{1e}^f \cos\theta_p \right) \right) dr$$

(B.18)

Fourteenth element:

The generalized force corresponding to a unit virtual displacement in the fourteenth degree of freedom (second flapwise deflection in blade 2) is given below.

$$F_{g14} = \int_0^R \begin{pmatrix} 0 \\ p_t^{B2} \\ p_n^{B2} \end{pmatrix} \cdot \begin{pmatrix} 0 \\ \phi_{2,y}^{2f} \\ \phi_{2,z}^{2f} \end{pmatrix} dr$$

$$= \int_0^R \left(p_t^{B2} \left(\phi_{2f}^e \cos\theta_p + \phi_{2f}^f \sin\theta_p \right) + p_n^{B2} \left(-\phi_{2f}^e \sin\theta_p + \phi_{2f}^f \cos\theta_p \right) \right) dr$$

(B.19)

Fifteenth element:

The generalized force corresponding to a unit virtual displacement in the fifteenth degree of freedom (first flapwise deflection in blade 3) is given below.

$$F_{g15} = \int_0^R \begin{pmatrix} 0 \\ p_t^{B3} \\ p_n^{B3} \end{pmatrix} \cdot \begin{pmatrix} 0 \\ \phi_{3,y}^{1f} \\ \phi_{3,z}^{1f} \end{pmatrix} dr$$

$$= \int_0^R \left(p_t^{B3} \left(\phi_{1f}^e \cos \theta_p + \phi_{1f}^f \sin \theta_p \right) + p_n^{B3} \left(-\phi_{1f}^e \sin \theta_p + \phi_{1f}^f \cos \theta_p \right) \right) dr$$

(B.20)

Sixteenth element:

The generalized force corresponding to a unit virtual displacement in the sixteenth degree of freedom (first edgewise deflection in blade 3) is given below.

$$F_{g16} = \int_0^R \begin{pmatrix} 0 \\ p_t^{B3} \\ p_n^{B3} \end{pmatrix} \cdot \begin{pmatrix} 0 \\ \phi_{3,y}^{1e} \\ \phi_{3,z}^{1e} \end{pmatrix} dr$$

$$= \int_0^R \left(p_t^{B3} \left(\phi_{1e}^e \cos \theta_p + \phi_{1e}^f \sin \theta_p \right) + p_n^{B3} \left(-\phi_{1e}^e \sin \theta_p + \phi_{1e}^f \cos \theta_p \right) \right) dr$$

(B.21)

Seventeenth element:

The generalized force corresponding to a unit virtual displacement in the seventeenth degree of freedom (second flapwise deflection in blade 3) is given below.

$$F_{g17} = \int_0^R \begin{pmatrix} 0 \\ p_t^{B3} \\ p_n^{B3} \end{pmatrix} \cdot \begin{pmatrix} 0 \\ \phi_{3,y}^{2f} \\ \phi_{3,z}^{2f} \end{pmatrix} dr$$

$$= \int_0^R \left(p_t^{B3} \left(\phi_{2f}^e \cos \theta_p + \phi_{2f}^f \sin \theta_p \right) + p_n^{B3} \left(-\phi_{2f}^e \sin \theta_p + \phi_{2f}^f \cos \theta_p \right) \right) dr$$

(B.22)

B.2   Generalized mass

The generalized mass is derived column-wise by giving a unit acceleration in the corresponding degree of freedom, which is detailed below.

First column:

A unit acceleration is given in the first degree of freedom and corresponding inertia loads are calculated.

First element in the first column is the virtual work by giving a virtual displacement in the first degree of freedom, which implies the following equation.

$$M(1,1) = m_1 + m_{ts}$$

(B.23)

where m_1 is the sum of the structural mass of the platform, half of the tower and the added mass in surge direction and m_{ts} is the sum of nacelle and half of the tower structural masses.

The second, third, fourth, sixth and eighth elements in the first column are zero since a unit acceleration in the first degree of freedom does not produce any inertia forces in these degrees of freedom.

The fifth element is obtained by computing the virtual work corresponding to a virtual displacement in the fifth degree of freedom, which is given below.

$$M(5,1) = m_{ts}Z_n \tag{B.24}$$

where Z_n is the vertical distance from floater bottom to the nacelle.

The seventh element is obtained by computing the virtual work corresponding to a virtual displacement in the seventh degree of freedom, which is given below.

$$M(7,1) = m_{ts} \tag{B.25}$$

The ninth element is obtained by computing the virtual work corresponding to a virtual displacement in the ninth degree of freedom, which is given below.

$$M(9,1) = \int_0^R \left(m(r)[T]_{26}^{B1} \left\{ \begin{array}{c} 1 \\ 0 \\ 0 \end{array} \right\} \right) \cdot \left\{ \begin{array}{c} 0 \\ \phi_{1,y}^{1f} \\ \phi_{1,z}^{1f} \end{array} \right\} dr \tag{B.26}$$

The tenth element is obtained by computing the virtual work corresponding to a virtual displacement in the tenth degree of freedom, which is given below.

$$M(10,1) = \int_0^R \left(m(r)[T]_{26}^{B1} \left\{ \begin{array}{c} 1 \\ 0 \\ 0 \end{array} \right\} \right) \cdot \left\{ \begin{array}{c} 0 \\ \phi_{1,y}^{1e} \\ \phi_{1,z}^{1e} \end{array} \right\} dr \tag{B.27}$$

The eleventh element is obtained by computing the virtual work corresponding to a virtual displacement in the eleventh degree of freedom, which is given below.

$$M(11,1) = \int_0^R \left(m(r)[T]_{26}^{B1} \left\{ \begin{array}{c} 1 \\ 0 \\ 0 \end{array} \right\} \right) \cdot \left\{ \begin{array}{c} 0 \\ \phi_{1,y}^{2f} \\ \phi_{1,z}^{2f} \end{array} \right\} dr \tag{B.28}$$

The twelfth element is obtained by computing the virtual work corresponding to a virtual displacement in the twelfth degree of freedom, which is given below.

$$M(12,1) = \int_0^R \left(m(r)[T]_{26}^{B2} \left\{ \begin{array}{c} 1 \\ 0 \\ 0 \end{array} \right\} \right) \cdot \left\{ \begin{array}{c} 0 \\ \phi_{2,y}^{1f} \\ \phi_{2,z}^{1f} \end{array} \right\} dr \tag{B.29}$$

The thirteenth element is obtained by computing the virtual work corresponding to a virtual displacement in the thirteenth degree of freedom, which is given below.

$$M(13,1) = \int_0^R \left(m(r)[T]_{26}^{B2} \left\{ \begin{array}{c} 1 \\ 0 \\ 0 \end{array} \right\} \right) \cdot \left\{ \begin{array}{c} 0 \\ \phi_{2,y}^{1e} \\ \phi_{2,z}^{1e} \end{array} \right\} dr \tag{B.30}$$

The fourteenth element is obtained by computing the virtual work corresponding to a virtual displacement in the fourteenth degree of freedom, which is given below.

$$M(14,1) = \int_0^R \left(m(r)[T]_{26}^{B2} \left\{ \begin{array}{c} 1 \\ 0 \\ 0 \end{array} \right\} \right) \cdot \left\{ \begin{array}{c} 0 \\ \phi_{2,y}^{2f} \\ \phi_{2,z}^{2f} \end{array} \right\} dr \tag{B.31}$$

The fifteenth element is obtained by computing the virtual work corresponding to a virtual displacement in the fifteenth degree of freedom, which is given below.

$$M(15,1) = \int_0^R \left(m(r)[T]_{26}^{B3} \left\{ \begin{array}{c} 1 \\ 0 \\ 0 \end{array} \right\} \right) \cdot \left\{ \begin{array}{c} 0 \\ \phi_{3,y}^{1f} \\ \phi_{3,z}^{1f} \end{array} \right\} dr \tag{B.32}$$

The sixteenth element is obtained by computing the virtual work corresponding to a virtual displacement in the sixteenth degree of freedom, which is given below.

$$M(16,1) = \int_0^R \left(m(r)[T]_{26}^{B3} \left\{ \begin{array}{c} 1 \\ 0 \\ 0 \end{array} \right\} \right) \cdot \left\{ \begin{array}{c} 0 \\ \phi_{3,y}^{1e} \\ \phi_{3,z}^{1e} \end{array} \right\} dr \tag{B.33}$$

The seventeenth element is obtained by computing the virtual work corresponding to a virtual displacement in the seventeenth degree of freedom, which is given below.

$$M(17,1) = \int_0^R \left(m(r)[T]_{26}^{B3} \left\{ \begin{array}{c} 1 \\ 0 \\ 0 \end{array} \right\} \right) \cdot \left\{ \begin{array}{c} 0 \\ \phi_{3,y}^{2f} \\ \phi_{3,z}^{2f} \end{array} \right\} dr \tag{B.34}$$

Second column:

A unit acceleration is given in the second degree of freedom and corresponding inertia loads are calculated.

The first, third, fifth, sixth, seventh and eighth elements in the second column are zero since a unit acceleration in the second degree of freedom does not produce any inertia forces in these degrees of freedom.

Second element in the second column is the virtual work by giving a virtual displacement in the second degree of freedom, which implies the following equation.

$$M(2,2) = m_2 + m_{ts} \tag{B.35}$$

where m_2 is the sum of the structural mass of the platform, half of the tower and the added mass in sway direction.

The fourth element is obtained by computing the virtual work corresponding to a virtual displacement in the fourth degree of freedom, which is given below.

$$M(4,2) = m_{ts} Z_n \tag{B.36}$$

The ninth element is obtained by computing the virtual work corresponding to a virtual displacement in the ninth degree of freedom, which is given below.

$$M(9,2) = \int_0^R \left(m(r)[T]_{26}^{B1} \left\{ \begin{array}{c} 0 \\ 1 \\ 0 \end{array} \right\} \right) \cdot \left\{ \begin{array}{c} 0 \\ \phi_{1,y}^{1f} \\ \phi_{1,z}^{1f} \end{array} \right\} dr \tag{B.37}$$

The tenth element is obtained by computing the virtual work corresponding to a virtual displacement in the tenth degree of freedom, which is given below.

$$M(10,2) = \int_0^R \left(m(r)[T]_{26}^{B1} \left\{ \begin{array}{c} 0 \\ 1 \\ 0 \end{array} \right\} \right) \cdot \left\{ \begin{array}{c} 0 \\ \phi_{1,y}^{1e} \\ \phi_{1,z}^{1e} \end{array} \right\} dr \qquad (B.38)$$

The eleventh element is obtained by computing the virtual work corresponding to a virtual displacement in the eleventh degree of freedom, which is given below.

$$M(11,2) = \int_0^R \left(m(r)[T]_{26}^{B1} \left\{ \begin{array}{c} 0 \\ 1 \\ 0 \end{array} \right\} \right) \cdot \left\{ \begin{array}{c} 0 \\ \phi_{1,y}^{2f} \\ \phi_{1,z}^{2f} \end{array} \right\} dr \qquad (B.39)$$

The twelfth element is obtained by computing the virtual work corresponding to a virtual displacement in the twelfth degree of freedom, which is given below.

$$M(12,2) = \int_0^R \left(m(r)[T]_{26}^{B2} \left\{ \begin{array}{c} 0 \\ 1 \\ 0 \end{array} \right\} \right) \cdot \left\{ \begin{array}{c} 0 \\ \phi_{2,y}^{1f} \\ \phi_{2,z}^{1f} \end{array} \right\} dr \qquad (B.40)$$

The thirteenth element is obtained by computing the virtual work corresponding to a virtual displacement in the thirteenth degree of freedom, which is given below.

$$M(13,2) = \int_0^R \left(m(r)[T]_{26}^{B2} \left\{ \begin{array}{c} 0 \\ 1 \\ 0 \end{array} \right\} \right) \cdot \left\{ \begin{array}{c} 0 \\ \phi_{2,y}^{1e} \\ \phi_{2,z}^{1e} \end{array} \right\} dr \qquad (B.41)$$

The fourteenth element is obtained by computing the virtual work corresponding to a virtual displacement in the fourteenth degree of freedom, which is given below.

$$M(14,2) = \int_0^R \left(m(r)[T]_{26}^{B2} \left\{ \begin{array}{c} 0 \\ 1 \\ 0 \end{array} \right\} \right) \cdot \left\{ \begin{array}{c} 0 \\ \phi_{2,y}^{2f} \\ \phi_{2,z}^{2f} \end{array} \right\} dr \qquad (B.42)$$

The fifteenth element is obtained by computing the virtual work corresponding to a virtual displacement in the fifteenth degree of freedom, which is given below.

$$M(15,2) = \int_0^R \left(m(r)[T]_{26}^{B3} \left\{ \begin{array}{c} 0 \\ 1 \\ 0 \end{array} \right\} \right) \cdot \left\{ \begin{array}{c} 0 \\ \phi_{3,y}^{1f} \\ \phi_{3,z}^{1f} \end{array} \right\} dr \qquad (B.43)$$

The sixteenth element is obtained by computing the virtual work corresponding to a virtual displacement in the sixteenth degree of freedom, which is given below.

$$M(16,2) = \int_0^R \left(m(r)[T]_{26}^{B3} \left\{ \begin{array}{c} 0 \\ 1 \\ 0 \end{array} \right\} \right) \cdot \left\{ \begin{array}{c} 0 \\ \phi_{3,y}^{1e} \\ \phi_{3,z}^{1e} \end{array} \right\} dr \qquad (B.44)$$

The seventeenth element is obtained by computing the virtual work corresponding to a virtual displacement in the seventeenth degree of freedom, which is given below.

$$M(17,2) = \int_0^R \left(m(r)[T]_{26}^{B3} \left\{ \begin{array}{c} 0 \\ 1 \\ 0 \end{array} \right\} \right) \cdot \left\{ \begin{array}{c} 0 \\ \phi_{3,y}^{2f} \\ \phi_{3,z}^{2f} \end{array} \right\} dr \tag{B.45}$$

Third column:

A unit acceleration is given in the third degree of freedom and corresponding inertia loads are calculated.

The first, second, fourth, fifth, sixth, seventh and eighth elements in the third column are zero since a unit acceleration in the third degree of freedom does not produce any inertia forces in these degrees of freedom.

Third element in the third column is the virtual work by giving a virtual displacement in the third degree of freedom, which implies the following equation.

$$M(3,3) = m_3 + m_{ts} \tag{B.46}$$

where m_3 is the sum of the structural mass of the platform, half of the tower and the added mass in heave direction.

The ninth element is obtained by computing the virtual work corresponding to a virtual displacement in the ninth degree of freedom, which is given below.

$$M(9,3) = \int_0^R \left(m(r)[T]_{26}^{B1} \left\{ \begin{array}{c} 0 \\ 0 \\ 1 \end{array} \right\} \right) \cdot \left\{ \begin{array}{c} 0 \\ \phi_{1,y}^{1f} \\ \phi_{1,z}^{1f} \end{array} \right\} dr \tag{B.47}$$

The tenth element is obtained by computing the virtual work corresponding to a virtual displacement in the tenth degree of freedom, which is given below.

$$M(10,3) = \int_0^R \left(m(r)[T]_{26}^{B1} \left\{ \begin{array}{c} 0 \\ 0 \\ 1 \end{array} \right\} \right) \cdot \left\{ \begin{array}{c} 0 \\ \phi_{1,y}^{1e} \\ \phi_{1,z}^{1e} \end{array} \right\} dr \tag{B.48}$$

The eleventh element is obtained by computing the virtual work corresponding to a virtual displacement in the eleventh degree of freedom, which is given below.

$$M(11,3) = \int_0^R \left(m(r)[T]_{26}^{B1} \left\{ \begin{array}{c} 0 \\ 0 \\ 1 \end{array} \right\} \right) \cdot \left\{ \begin{array}{c} 0 \\ \phi_{1,y}^{2f} \\ \phi_{1,z}^{2f} \end{array} \right\} dr \tag{B.49}$$

The twelfth element is obtained by computing the virtual work corresponding to a virtual displacement in the twelfth degree of freedom, which is given below.

$$M(12,3) = \int_0^R \left(m(r)[T]_{26}^{B2} \left\{ \begin{array}{c} 0 \\ 0 \\ 1 \end{array} \right\} \right) \cdot \left\{ \begin{array}{c} 0 \\ \phi_{2,y}^{1f} \\ \phi_{2,z}^{1f} \end{array} \right\} dr \tag{B.50}$$

The thirteenth element is obtained by computing the virtual work corresponding to a virtual displacement in the thirteenth degree of freedom, which is given below.

$$M(13,3) = \int_0^R \left(m(r)[T]_{26}^{B2} \begin{Bmatrix} 0 \\ 0 \\ 1 \end{Bmatrix} \right) \cdot \begin{Bmatrix} 0 \\ \phi_{2,y}^{1e} \\ \phi_{2,z}^{1e} \end{Bmatrix} dr \tag{B.51}$$

The fourteenth element is obtained by computing the virtual work corresponding to a virtual displacement in the fourteenth degree of freedom, which is given below.

$$M(14,3) = \int_0^R \left(m(r)[T]_{26}^{B2} \begin{Bmatrix} 0 \\ 0 \\ 1 \end{Bmatrix} \right) \cdot \begin{Bmatrix} 0 \\ \phi_{2,y}^{2f} \\ \phi_{2,z}^{2f} \end{Bmatrix} dr \tag{B.52}$$

The fifteenth element is obtained by computing the virtual work corresponding to a virtual displacement in the fifteenth degree of freedom, which is given below.

$$M(15,3) = \int_0^R \left(m(r)[T]_{26}^{B3} \begin{Bmatrix} 0 \\ 0 \\ 1 \end{Bmatrix} \right) \cdot \begin{Bmatrix} 0 \\ \phi_{3,y}^{1f} \\ \phi_{3,z}^{1f} \end{Bmatrix} dr \tag{B.53}$$

The sixteenth element is obtained by computing the virtual work corresponding to a virtual displacement in the sixteenth degree of freedom, which is given below.

$$M(16,3) = \int_0^R \left(m(r)[T]_{26}^{B3} \begin{Bmatrix} 0 \\ 0 \\ 1 \end{Bmatrix} \right) \cdot \begin{Bmatrix} 0 \\ \phi_{3,y}^{1e} \\ \phi_{3,z}^{1e} \end{Bmatrix} dr \tag{B.54}$$

The seventeenth element is obtained by computing the virtual work corresponding to a virtual displacement in the seventeenth degree of freedom, which is given below.

$$M(17,3) = \int_0^R \left(m(r)[T]_{26}^{B3} \begin{Bmatrix} 0 \\ 0 \\ 1 \end{Bmatrix} \right) \cdot \begin{Bmatrix} 0 \\ \phi_{3,y}^{2f} \\ \phi_{3,z}^{2f} \end{Bmatrix} dr \tag{B.55}$$

Fourth column:

A unit acceleration is given in the fourth degree of freedom and corresponding inertia loads are calculated.

The first, third, fifth, sixth, seventh and eighth elements in the fourth column are zero since a unit acceleration in the fourth degree of freedom does not produce any inertia forces in these degrees of freedom.

The second element is the same as that of fourth element in the second column because of symmetry, ie, $M(2,4) = M(4,2)$.

Fourth element in the fourth column is the virtual work by giving a virtual displacement in the fourth degree of freedom, which implies the following equation.

$$M(4,4) = J_{4G} + m_{ts} Z_n^2 \tag{B.56}$$

where J_{4G} is the sum of roll moment of inertia and the added mass in roll degree of freedom.

The ninth element is obtained by computing the virtual work corresponding to a virtual displacement in the ninth degree of freedom, which is given below.

$$M(9,4) = \int_0^R \left(m(r)[T]_{26}^{B1} \left(\left\{ \begin{array}{c} 1 \\ 0 \\ 0 \end{array} \right\} \times \left\{ \begin{array}{c} r_x \\ r_y \\ r_z \end{array} \right\} \right) \right) \cdot \left\{ \begin{array}{c} 0 \\ \phi_{1,y}^{1f} \\ \phi_{1,z}^{1f} \end{array} \right\} dr \tag{B.57}$$

The tenth element is obtained by computing the virtual work corresponding to a virtual displacement in the tenth degree of freedom, which is given below.

$$M(10,4) = \int_0^R \left(m(r)[T]_{26}^{B1} \left(\left\{ \begin{array}{c} 1 \\ 0 \\ 0 \end{array} \right\} \times \left\{ \begin{array}{c} r_x \\ r_y \\ r_z \end{array} \right\} \right) \right) \cdot \left\{ \begin{array}{c} 0 \\ \phi_{1,y}^{1e} \\ \phi_{1,z}^{1e} \end{array} \right\} dr \tag{B.58}$$

The eleventh element is obtained by computing the virtual work corresponding to a virtual displacement in the eleventh degree of freedom, which is given below.

$$M(11,4) = \int_0^R \left(m(r)[T]_{26}^{B1} \left(\left\{ \begin{array}{c} 1 \\ 0 \\ 0 \end{array} \right\} \times \left\{ \begin{array}{c} r_x \\ r_y \\ r_z \end{array} \right\} \right) \right) \cdot \left\{ \begin{array}{c} 0 \\ \phi_{1,y}^{2f} \\ \phi_{1,z}^{2f} \end{array} \right\} dr \tag{B.59}$$

The twelfth element is obtained by computing the virtual work corresponding to a virtual displacement in the twelfth degree of freedom, which is given below.

$$M(12,4) = \int_0^R \left(m(r)[T]_{26}^{B2} \left(\left\{ \begin{array}{c} 1 \\ 0 \\ 0 \end{array} \right\} \times \left\{ \begin{array}{c} r_x \\ r_y \\ r_z \end{array} \right\} \right) \right) \cdot \left\{ \begin{array}{c} 0 \\ \phi_{2,y}^{1f} \\ \phi_{2,z}^{1f} \end{array} \right\} dr \tag{B.60}$$

The thirteenth element is obtained by computing the virtual work corresponding to a virtual displacement in the thirteenth degree of freedom, which is given below.

$$M(13,4) = \int_0^R \left(m(r)[T]_{26}^{B2} \left(\left\{ \begin{array}{c} 1 \\ 0 \\ 0 \end{array} \right\} \times \left\{ \begin{array}{c} r_x \\ r_y \\ r_z \end{array} \right\} \right) \right) \cdot \left\{ \begin{array}{c} 0 \\ \phi_{2,y}^{1e} \\ \phi_{2,z}^{1e} \end{array} \right\} dr \tag{B.61}$$

The fourteenth element is obtained by computing the virtual work corresponding to a virtual displacement in the fourteenth degree of freedom, which is given below.

$$M(14,4) = \int_0^R \left(m(r)[T]_{26}^{B2} \left(\left\{ \begin{array}{c} 1 \\ 0 \\ 0 \end{array} \right\} \times \left\{ \begin{array}{c} r_x \\ r_y \\ r_z \end{array} \right\} \right) \right) \cdot \left\{ \begin{array}{c} 0 \\ \phi_{2,y}^{2f} \\ \phi_{2,z}^{2f} \end{array} \right\} dr \tag{B.62}$$

The fifteenth element is obtained by computing the virtual work corresponding to a virtual displacement in the fifteenth degree of freedom, which is given below.

$$M(15,4) = \int_0^R \left(m(r)[T]_{26}^{B3} \left(\left\{ \begin{array}{c} 1 \\ 0 \\ 0 \end{array} \right\} \times \left\{ \begin{array}{c} r_x \\ r_y \\ r_z \end{array} \right\} \right) \right) \cdot \left\{ \begin{array}{c} 0 \\ \phi_{3,y}^{1f} \\ \phi_{3,z}^{1f} \end{array} \right\} dr \tag{B.63}$$

The sixteenth element is obtained by computing the virtual work corresponding to a virtual displacement in the sixteenth degree of freedom, which is given below.

$$M(16,4) = \int_0^R \left(m(r)[T]_{26}^{B3} \left(\left\{ \begin{array}{c} 1 \\ 0 \\ 0 \end{array} \right\} \times \left\{ \begin{array}{c} r_x \\ r_y \\ r_z \end{array} \right\} \right) \right) \cdot \left\{ \begin{array}{c} 0 \\ \phi_{3,y}^{1e} \\ \phi_{3,z}^{1e} \end{array} \right\} dr \tag{B.64}$$

The seventeenth element is obtained by computing the virtual work corresponding to a virtual displacement in the seventeenth degree of freedom, which is given below.

$$M(17,4) = \int_0^R \left(m(r)[T]_{26}^{B3} \left(\left\{ \begin{matrix} 1 \\ 0 \\ 0 \end{matrix} \right\} \times \left\{ \begin{matrix} r_x \\ r_y \\ r_z \end{matrix} \right\} \right) \right) \cdot \left\{ \begin{matrix} 0 \\ \phi_{3,y}^{2f} \\ \phi_{3,z}^{2f} \end{matrix} \right\} dr \tag{B.65}$$

Fifth column:

A unit acceleration is given in the fifth degree of freedom and corresponding inertia loads are calculated.

The first element is the same as that of the fifth element in the first column because of symmetry, ie, $M(1,5) = M(5,1)$.

The second, third, fourth, sixth and eighth elements in the fifth column are zero since a unit acceleration in the fifth degree of freedom does not produce any inertia forces in these degrees of freedom.

Fifth element in the fifth column is the virtual work by giving a virtual displacement in the fifth degree of freedom, which implies the following equation.

$$M(5,5) = J_{5G} + m_{ts} Z_n^2 \tag{B.66}$$

where J_{5G} is the sum of pitch moment of inertia and the added mass in the pitch degree of freedom.

The seventh element is obtained by computing the virtual work corresponding to a virtual displacement in the seventh degree of freedom, which is given below.

$$M(7,5) = m_{ts} Z_n \tag{B.67}$$

The ninth element is obtained by computing the virtual work corresponding to a virtual displacement in the ninth degree of freedom, which is given below.

$$M(9,5) = \int_0^R \left(m(r)[T]_{26}^{B1} \left(\left\{ \begin{matrix} 0 \\ 1 \\ 0 \end{matrix} \right\} \times \left\{ \begin{matrix} r_x \\ r_y \\ r_z \end{matrix} \right\} \right) \right) \cdot \left\{ \begin{matrix} 0 \\ \phi_{1,y}^{1f} \\ \phi_{1,z}^{1f} \end{matrix} \right\} dr \tag{B.68}$$

The tenth element is obtained by computing the virtual work corresponding to a virtual displacement in the tenth degree of freedom, which is given below.

$$M(10,5) = \int_0^R \left(m(r)[T]_{26}^{B1} \left(\left\{ \begin{matrix} 0 \\ 1 \\ 0 \end{matrix} \right\} \times \left\{ \begin{matrix} r_x \\ r_y \\ r_z \end{matrix} \right\} \right) \right) \cdot \left\{ \begin{matrix} 0 \\ \phi_{1,y}^{1e} \\ \phi_{1,z}^{1e} \end{matrix} \right\} dr \tag{B.69}$$

The eleventh element is obtained by computing the virtual work corresponding to a virtual displacement in the eleventh degree of freedom, which is given below.

$$M(11,5) = \int_0^R \left(m(r)[T]_{26}^{B1} \left(\left\{ \begin{matrix} 0 \\ 1 \\ 0 \end{matrix} \right\} \times \left\{ \begin{matrix} r_x \\ r_y \\ r_z \end{matrix} \right\} \right) \right) \cdot \left\{ \begin{matrix} 0 \\ \phi_{1,y}^{2f} \\ \phi_{1,z}^{2f} \end{matrix} \right\} dr \tag{B.70}$$

The twelfth element is obtained by computing the virtual work corresponding to a virtual displacement in the twelfth degree of freedom, which is given below.

$$M(12,5) = \int_0^R \left(m(r)[T]_{26}^{B2} \left(\left\{ \begin{array}{c} 0 \\ 1 \\ 0 \end{array} \right\} \times \left\{ \begin{array}{c} r_x \\ r_y \\ r_z \end{array} \right\} \right) \right) \cdot \left\{ \begin{array}{c} 0 \\ \phi_{2,y}^{1f} \\ \phi_{2,z}^{1f} \end{array} \right\} dr \qquad (B.71)$$

The thirteenth element is obtained by computing the virtual work corresponding to a virtual displacement in the thirteenth degree of freedom, which is given below.

$$M(13,5) = \int_0^R \left(m(r)[T]_{26}^{B2} \left(\left\{ \begin{array}{c} 0 \\ 1 \\ 0 \end{array} \right\} \times \left\{ \begin{array}{c} r_x \\ r_y \\ r_z \end{array} \right\} \right) \right) \cdot \left\{ \begin{array}{c} 0 \\ \phi_{2,y}^{1e} \\ \phi_{2,z}^{1e} \end{array} \right\} dr \qquad (B.72)$$

The fourteenth element is obtained by computing the virtual work corresponding to a virtual displacement in the fourteenth degree of freedom, which is given below.

$$M(14,5) = \int_0^R \left(m(r)[T]_{26}^{B2} \left(\left\{ \begin{array}{c} 0 \\ 1 \\ 0 \end{array} \right\} \times \left\{ \begin{array}{c} r_x \\ r_y \\ r_z \end{array} \right\} \right) \right) \cdot \left\{ \begin{array}{c} 0 \\ \phi_{2,y}^{2f} \\ \phi_{2,z}^{2f} \end{array} \right\} dr \qquad (B.73)$$

The fifteenth element is obtained by computing the virtual work corresponding to a virtual displacement in the fifteenth degree of freedom, which is given below.

$$M(15,5) = \int_0^R \left(m(r)[T]_{26}^{B3} \left(\left\{ \begin{array}{c} 0 \\ 1 \\ 0 \end{array} \right\} \times \left\{ \begin{array}{c} r_x \\ r_y \\ r_z \end{array} \right\} \right) \right) \cdot \left\{ \begin{array}{c} 0 \\ \phi_{3,y}^{1f} \\ \phi_{3,z}^{1f} \end{array} \right\} dr \qquad (B.74)$$

The sixteenth element is obtained by computing the virtual work corresponding to a virtual displacement in the sixteenth degree of freedom, which is given below.

$$M(16,5) = \int_0^R \left(m(r)[T]_{26}^{B3} \left(\left\{ \begin{array}{c} 0 \\ 1 \\ 0 \end{array} \right\} \times \left\{ \begin{array}{c} r_x \\ r_y \\ r_z \end{array} \right\} \right) \right) \cdot \left\{ \begin{array}{c} 0 \\ \phi_{3,y}^{1e} \\ \phi_{3,z}^{1e} \end{array} \right\} dr \qquad (B.75)$$

The seventeenth element is obtained by computing the virtual work corresponding to a virtual displacement in the seventeenth degree of freedom, which is given below.

$$M(17,5) = \int_0^R \left(m(r)[T]_{26}^{B3} \left(\left\{ \begin{array}{c} 0 \\ 1 \\ 0 \end{array} \right\} \times \left\{ \begin{array}{c} r_x \\ r_y \\ r_z \end{array} \right\} \right) \right) \cdot \left\{ \begin{array}{c} 0 \\ \phi_{3,y}^{2f} \\ \phi_{3,z}^{2f} \end{array} \right\} dr \qquad (B.76)$$

Sixth column:

A unit acceleration is given in the sixth degree of freedom and the corresponding inertia loads are calculated.

The first, second, third, fourth, fifth, sixth, seventh and eighth elements in the sixth column are zero since a unit acceleration in the sixth degree of freedom does not produce any inertia forces in these degrees of freedom.

Sixth element in the sixth column is the virtual work by giving a virtual displacement in the sixth degree of freedom, which implies the following equation.

$$M(6,6) = J_{6G} \qquad (B.77)$$

where J_{6G} is the yaw moment of inertia.

The ninth element is obtained by computing the virtual work corresponding to a virtual displacement in the ninth degree of freedom, which is given below.

$$M(9,6) = \int_0^R \left(m(r)[T]_{26}^{B1} \left(\left\{ \begin{array}{c} 0 \\ 0 \\ 1 \end{array} \right\} \times \left\{ \begin{array}{c} r_x \\ r_y \\ r_z \end{array} \right\} \right) \right) \cdot \left\{ \begin{array}{c} 0 \\ \phi_{1,y}^{1f} \\ \phi_{1,z}^{1f} \end{array} \right\} dr \tag{B.78}$$

The tenth element is obtained by computing the virtual work corresponding to a virtual displacement in the tenth degree of freedom, which is given below.

$$M(10,6) = \int_0^R \left(m(r)[T]_{26}^{B1} \left(\left\{ \begin{array}{c} 0 \\ 0 \\ 1 \end{array} \right\} \times \left\{ \begin{array}{c} r_x \\ r_y \\ r_z \end{array} \right\} \right) \right) \cdot \left\{ \begin{array}{c} 0 \\ \phi_{1,y}^{1e} \\ \phi_{1,z}^{1e} \end{array} \right\} dr \tag{B.79}$$

The eleventh element is obtained by computing the virtual work corresponding to a virtual displacement in the eleventh degree of freedom, which is given below.

$$M(11,6) = \int_0^R \left(m(r)[T]_{26}^{B1} \left(\left\{ \begin{array}{c} 0 \\ 0 \\ 1 \end{array} \right\} \times \left\{ \begin{array}{c} r_x \\ r_y \\ r_z \end{array} \right\} \right) \right) \cdot \left\{ \begin{array}{c} 0 \\ \phi_{1,y}^{2f} \\ \phi_{1,z}^{2f} \end{array} \right\} dr \tag{B.80}$$

The twelfth element is obtained by computing the virtual work corresponding to a virtual displacement in the twelfth degree of freedom, which is given below.

$$M(12,6) = \int_0^R \left(m(r)[T]_{26}^{B2} \left(\left\{ \begin{array}{c} 0 \\ 0 \\ 1 \end{array} \right\} \times \left\{ \begin{array}{c} r_x \\ r_y \\ r_z \end{array} \right\} \right) \right) \cdot \left\{ \begin{array}{c} 0 \\ \phi_{2,y}^{1f} \\ \phi_{2,z}^{1f} \end{array} \right\} dr \tag{B.81}$$

The thirteenth element is obtained by computing the virtual work corresponding to a virtual displacement in the thirteenth degree of freedom, which is given below.

$$M(13,6) = \int_0^R \left(m(r)[T]_{26}^{B2} \left(\left\{ \begin{array}{c} 0 \\ 0 \\ 1 \end{array} \right\} \times \left\{ \begin{array}{c} r_x \\ r_y \\ r_z \end{array} \right\} \right) \right) \cdot \left\{ \begin{array}{c} 0 \\ \phi_{2,y}^{1e} \\ \phi_{2,z}^{1e} \end{array} \right\} dr \tag{B.82}$$

The fourteenth element is obtained by computing the virtual work corresponding to a virtual displacement in the fourteenth degree of freedom, which is given below.

$$M(14,6) = \int_0^R \left(m(r)[T]_{26}^{B2} \left(\left\{ \begin{array}{c} 0 \\ 0 \\ 1 \end{array} \right\} \times \left\{ \begin{array}{c} r_x \\ r_y \\ r_z \end{array} \right\} \right) \right) \cdot \left\{ \begin{array}{c} 0 \\ \phi_{2,y}^{2f} \\ \phi_{2,z}^{2f} \end{array} \right\} dr \tag{B.83}$$

The fifteenth element is obtained by computing the virtual work corresponding to a virtual displacement in the fifteenth degree of freedom, which is given below.

$$M(15,6) = \int_0^R \left(m(r)[T]_{26}^{B3} \left(\left\{ \begin{array}{c} 0 \\ 0 \\ 1 \end{array} \right\} \times \left\{ \begin{array}{c} r_x \\ r_y \\ r_z \end{array} \right\} \right) \right) \cdot \left\{ \begin{array}{c} 0 \\ \phi_{3,y}^{1f} \\ \phi_{3,z}^{1f} \end{array} \right\} dr \tag{B.84}$$

The sixteenth element is obtained by computing the virtual work corresponding to a virtual displacement in the sixteenth degree of freedom, which is given below.

$$M(16,6) = \int_0^R \left(m(r)[T]_{26}^{B3} \left(\left\{ \begin{array}{c} 0 \\ 0 \\ 1 \end{array} \right\} \times \left\{ \begin{array}{c} r_x \\ r_y \\ r_z \end{array} \right\} \right) \right) \cdot \left\{ \begin{array}{c} 0 \\ \phi_{3,y}^{1e} \\ \phi_{3,z}^{1e} \end{array} \right\} dr \qquad \text{(B.85)}$$

The seventeenth element is obtained by computing the virtual work corresponding to a virtual displacement in the seventeenth degree of freedom, which is given below.

$$M(17,6) = \int_0^R \left(m(r)[T]_{26}^{B3} \left(\left\{ \begin{array}{c} 0 \\ 0 \\ 1 \end{array} \right\} \times \left\{ \begin{array}{c} r_x \\ r_y \\ r_z \end{array} \right\} \right) \right) \cdot \left\{ \begin{array}{c} 0 \\ \phi_{3,y}^{2f} \\ \phi_{3,z}^{2f} \end{array} \right\} dr \qquad \text{(B.86)}$$

Seventh column:

A unit acceleration is given in the seventh degree of freedom and the corresponding inertia loads are calculated.

The first element is the same as that of the seventh element in the first column because of the symmetry, ie, $M(1,7) = M(7,1)$ and similarly $M(5,7) = M(7,5)$.

The second, third, fourth, sixth and eighth elements in the seventh column are zero since a unit acceleration in the seventh degree of freedom does not produce any inertia forces in these degrees of freedom.

Seventh element in the seventh column is the virtual work by giving a virtual displacement in the seventh degree of freedom, which implies the following equation.

$$M(7,7) = m_{ts} \qquad \text{(B.87)}$$

The ninth element is obtained by computing the virtual work corresponding to a virtual displacement in the ninth degree of freedom, which is given below.

$$M(9,7) = \int_0^R \left(m(r)[T]_{46}^{B1} \left\{ \begin{array}{c} 0 \\ 0 \\ 1 \end{array} \right\} \right) \cdot \left\{ \begin{array}{c} 0 \\ \phi_{1,y}^{1f} \\ \phi_{1,z}^{1f} \end{array} \right\} dr \qquad \text{(B.88)}$$

The tenth element is obtained by computing the virtual work corresponding to a virtual displacement in the tenth degree of freedom, which is given below.

$$M(10,7) = \int_0^R \left(m(r)[T]_{46}^{B1} \left\{ \begin{array}{c} 0 \\ 0 \\ 1 \end{array} \right\} \right) \cdot \left\{ \begin{array}{c} 0 \\ \phi_{1,y}^{1e} \\ \phi_{1,z}^{1e} \end{array} \right\} dr \qquad \text{(B.89)}$$

The eleventh element is obtained by computing the virtual work corresponding to a virtual displacement in the eleventh degree of freedom, which is given below.

$$M(11,7) = \int_0^R \left(m(r)[T]_{46}^{B1} \left\{ \begin{array}{c} 0 \\ 0 \\ 1 \end{array} \right\} \right) \cdot \left\{ \begin{array}{c} 0 \\ \phi_{1,y}^{2f} \\ \phi_{1,z}^{2f} \end{array} \right\} dr \qquad \text{(B.90)}$$

The twelfth element is obtained by computing the virtual work corresponding to a virtual displacement in the twelfth degree of freedom, which is given below.

$$M(12,7) = \int_0^R \left(m(r)[T]_{46}^{B2} \left\{ \begin{array}{c} 0 \\ 0 \\ 1 \end{array} \right\} \right) \cdot \left\{ \begin{array}{c} 0 \\ \phi_{2,y}^{1f} \\ \phi_{2,z}^{1f} \end{array} \right\} dr \tag{B.91}$$

The thirteenth element is obtained by computing the virtual work corresponding to a virtual displacement in the thirteenth degree of freedom, which is given below.

$$M(13,7) = \int_0^R \left(m(r)[T]_{46}^{B2} \left\{ \begin{array}{c} 0 \\ 0 \\ 1 \end{array} \right\} \right) \cdot \left\{ \begin{array}{c} 0 \\ \phi_{2,y}^{1e} \\ \phi_{2,z}^{1e} \end{array} \right\} dr \tag{B.92}$$

The fourteenth element is obtained by computing the virtual work corresponding to a virtual displacement in the fourteenth degree of freedom, which is given below.

$$M(14,7) = \int_0^R \left(m(r)[T]_{46}^{B2} \left\{ \begin{array}{c} 0 \\ 0 \\ 1 \end{array} \right\} \right) \cdot \left\{ \begin{array}{c} 0 \\ \phi_{2,y}^{2f} \\ \phi_{2,z}^{2f} \end{array} \right\} dr \tag{B.93}$$

The fifteenth element is obtained by computing the virtual work corresponding to a virtual displacement in the fifteenth degree of freedom, which is given below.

$$M(15,7) = \int_0^R \left(m(r)[T]_{46}^{B3} \left\{ \begin{array}{c} 0 \\ 0 \\ 1 \end{array} \right\} \right) \cdot \left\{ \begin{array}{c} 0 \\ \phi_{3,y}^{1f} \\ \phi_{3,z}^{1f} \end{array} \right\} dr \tag{B.94}$$

The sixteenth element is obtained by computing the virtual work corresponding to a virtual displacement in the sixteenth degree of freedom, which is given below.

$$M(16,7) = \int_0^R \left(m(r)[T]_{46}^{B3} \left\{ \begin{array}{c} 0 \\ 0 \\ 1 \end{array} \right\} \right) \cdot \left\{ \begin{array}{c} 0 \\ \phi_{3,y}^{1e} \\ \phi_{3,z}^{1e} \end{array} \right\} dr \tag{B.95}$$

The seventeenth element is obtained by computing the virtual work corresponding to a virtual displacement in the seventeenth degree of freedom, which is given below.

$$M(17,7) = \int_0^R \left(m(r)[T]_{46}^{B3} \left\{ \begin{array}{c} 0 \\ 0 \\ 1 \end{array} \right\} \right) \cdot \left\{ \begin{array}{c} 0 \\ \phi_{3,y}^{2f} \\ \phi_{3,z}^{2f} \end{array} \right\} dr \tag{B.96}$$

Eighth column:

A unit acceleration is given in the eighth degree of freedom and the corresponding inertia loads are calculated.

The first seven elements in column 8 are zero since a unit acceleration in the eighth degree of freedom does not produce any inertia forces in these degrees of freedom.

Eighth element in the eighth column is the virtual work by giving a virtual displacement in the eighth degree of freedom, which implies the following equation.

$$M(8,8) = 3 \int_0^R m(r) r^2 dr \tag{B.97}$$

The ninth element is obtained by computing the virtual work corresponding to a virtual displacement in the ninth degree of freedom, which is given below.

$$M(9,8) = \int_0^R \left(m(r) \left([T]_{56} \left\{ \begin{array}{c} 0 \\ 0 \\ 1 \end{array} \right\} \times \left\{ \begin{array}{c} r \\ \phi_{1,y}^{1f} \\ \phi_{1,z}^{1f} \end{array} \right\} \right) \right) \cdot \left\{ \begin{array}{c} 0 \\ \phi_{1,y}^{1f} \\ \phi_{1,z}^{1f} \end{array} \right\} dr \qquad \text{(B.98)}$$

The tenth element is obtained by computing the virtual work corresponding to a virtual displacement in the tenth degree of freedom, which is given below.

$$M(10,8) = \int_0^R \left(m(r) \left([T]_{56} \left\{ \begin{array}{c} 0 \\ 0 \\ 1 \end{array} \right\} \times \left\{ \begin{array}{c} r \\ \phi_{1,y}^{1e} \\ \phi_{1,z}^{1e} \end{array} \right\} \right) \right) \cdot \left\{ \begin{array}{c} 0 \\ \phi_{1,y}^{1e} \\ \phi_{1,z}^{1e} \end{array} \right\} dr \qquad \text{(B.99)}$$

The eleventh element is obtained by computing the virtual work corresponding to a virtual displacement in the eleventh degree of freedom, which is given below.

$$M(11,8) = \int_0^R \left(m(r) \left([T]_{56} \left\{ \begin{array}{c} 0 \\ 0 \\ 1 \end{array} \right\} \times \left\{ \begin{array}{c} r \\ \phi_{1,y}^{2f} \\ \phi_{1,z}^{2f} \end{array} \right\} \right) \right) \cdot \left\{ \begin{array}{c} 0 \\ \phi_{1,y}^{2f} \\ \phi_{1,z}^{2f} \end{array} \right\} dr \qquad \text{(B.100)}$$

Since the blades are identical, the remaining mass elements in column 8 are one and the same as that in blade 1, ie, $M(15,8) = M(12,8) = M(9,8)$, $M(16,8) = M(13,8) = M(10,8)$ and $M(17,8) = M(14,8) = M(11,8)$.

Ninth column:

A unit acceleration is given in the ninth degree of freedom and the corresponding inertia loads are calculated.

The first eight elements in column 9 are the same elements corresponding to the symmetric terms, ie, $M(1,9) = M(9,1)$, $M(2,9) = M(9,2)$, $M(3,9) = M(9,3)$, $M(4,9) = M(9,4)$, $M(5,9) = M(9,5)$, $M(6,9) = M(9,6)$, $M(7,9) = M(9,7)$ and $M(8,9) = M(9,8)$.

The diagonal element is the virtual work by giving a virtual displacement in the ninth degree of freedom, which implies the following equation.

$$M(9,9) = \int_0^R \left(m(r) \left(\left(\phi_{1,y}^{1f} \right)^2 + \left(\phi_{1,z}^{1f} \right)^2 \right) \right) dr \qquad \text{(B.101)}$$

All the other elements in the ninth column are zero since the inertia force on the first flapwise degree of freedom on blade 1 does not influence the other degrees of freedom in the blade 1 and other blades and hence no virtual work done is present.

Tenth column:

Similar to the ninth column, apart from the symmetric elements (M(1,10) to M(8,10)), only diagonal element (which corresponds to the first edgewise degree of freedom of blade 1) is present, which is given below. All other terms are zeros.

$$M(10,10) = \int_0^R \left(m(r) \left(\left(\phi_{1,y}^{1e} \right)^2 + \left(\phi_{1,z}^{1e} \right)^2 \right) \right) dr \qquad \text{(B.102)}$$

Eleventh column:

Similar to the ninth column, apart from the symmetric elements (M(1,11) to M(8,11)), only diagonal element (which corresponds to the second flapwise degree of freedom of blade 1) is present, which is given below. All other terms are zeros.

$$M(11,11) = \int_0^R \left(m \left(\left(\phi_{1,y}^{2f} \right)^2 + \left(\phi_{1,z}^{2f} \right)^2 \right) \right) dr \tag{B.103}$$

From 12th to 17th columns only the first eight symmetric terms and the diagonal terms are only present. The diagonal terms for blade 2 and 3 are the same as that of blade 1 since the blades are identical, ie, $M(15,15) = M(12,12) = M(9,9)$, $M(16,16) = M(13,13) = M(10,10)$ and $M(17,17) = M(14,14) = M(11,11)$.

Hence all of the terms in the generalized mass matrix are derived.